FRICTION STIR WELDING AND PROCESSING X

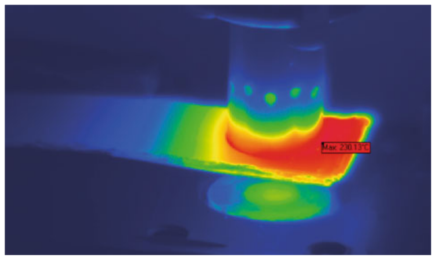

Edited by
Yuri Hovanski · Rajiv Mishra · Yutaka Sato
Piyush Upadhyay · David Yan

TMS

Springer

The Minerals, Metals & Materials Series

Yuri Hovanski · Rajiv Mishra ·
Yutaka Sato · Piyush Upadhyay ·
David Yan
Editors

Friction Stir Welding and Processing X

TMS

Springer

Editors
Yuri Hovanski
Brigham Young University
Provo, UT, USA

Yutaka Sato
Tohoku University
Sendai, Japan

David Yan
San Jose State University
San Jose, CA, USA

Rajiv Mishra
University of North Texas
Denton, TX, USA

Piyush Upadhyay
Pacific Northwest National Laboratory
Richland, WA, USA

ISSN 2367-1181 ISSN 2367-1696 (electronic)
The Minerals, Metals & Materials Series
ISBN 978-3-030-05751-0 ISBN 978-3-030-05752-7 (eBook)
https://doi.org/10.1007/978-3-030-05752-7

Library of Congress Control Number: 2018964037

Cover illustration: Top left: From Chapter 'Welding Multilayer Materials by Refill Friction Stir Spot Welding', Uceu Suhuddin, Dennis Gera, Nelson Alcantara, Jorge dos Santos, Pages 245–253, Figure 2: Infrared image of temperature measurement during welding. https://doi.org/10.1007/978-3-030-05752-7_23.
Top right: From Chapter 'Copper-Graphite Composite Wire Made by Shear-Assisted Processing and Extrusion', Xiao Li, Glenn Grant, Chen Zhou, Hongliang Wang, Thomas Perry, James Schroth, Pages 163–169, Figure 4, Macrostructure of copper-graphite wire and disc made by ShAPE. Solid cylinder precursor, transverse cross-section of wire. https://doi.org/10.1007/978-3-030-05752-7_15.
Bottom: From Chapter 'Comparison of Dissimilar Aluminum Alloys Joined by Friction Stir Welding with Conventional and Bobbin Tools', Paul Goetze, Mateusz Kopyściański, Carter Hamilton, Stanisław Dymek, Pages 3–12, Figure 2a: Optical micrograph for the AS-2024C configuration. https://doi.org/10.1007/978-3-030-05752-7_1.

This Springer imprint is published by the registered company Springer Nature Switzerland AG
The registered company address is: Gewerbestrasse 11, 6330 Cham, Switzerland

Preface

These proceedings represent the tenth symposium on Friction Stir Welding and Processing (FSW/P) held under the auspices of TMS. The continued interest and participation in this symposium is an indirect testimony of the growth of this field. For 2019, a total of 73 abstracts were accepted, which include 8 oral sessions and 13 unique posters. There are 25 papers included in this volume, which when combined with the previous nine proceedings' publications represent more than 300 papers over a 20-year period. These submissions cover all aspects of friction stir technologies including FSW of high melting temperature materials, FSW of lightweight materials, FSW of dissimilar materials, simulation of FSW/P, controls and inspection of FSW/P, and derivative technologies like friction stir processing, friction stir spot welding, additive friction stir, and friction stir extrusion.

Friction stir welding was invented by TWI (formerly The Welding Institute), Cambridge, UK and patented in 1991, although the real growth in this field started several years later. In the last 27 years, FSW has seen significant growth in both technology implementation and scientific exploration. The original patent has led to hundreds of additional patents issued globally, as various solid-state processing techniques have derived from the original FSW concept. In addition to the tremendous number of derivative technologies that have been developed based on the concept of friction stirring, thousands of papers have been published characterizing and documenting the commercial and scientific benefits of the same.

The organizers would like to thank the Shaping and Forming Committee of the Materials Processing and Manufacturing Division for sponsoring this symposium.

Yuri Hovanski
Rajiv Mishra
Yutaka Sato
Piyush Upadhyay
David Yan

Contents

Part I Dissimilar Materials

Part II High Melting Temperature Materials

Part III Lightweight Materials

Part IV Simulation

Part V Controls and Inspection

Part VI Derivative Technologies

Part VII Friction Stir Processing

Part VIII Friction Stir Spot Welding

Part IX Poster Session

About the Editors

Yuri Hovanski is an Associate Professor of Manufacturing Engineering at Brigham Young University. He earned a B.S. Degree in Mechanical Engineering at Brigham Young University, and then completed his Masters and Doctorate degrees at Washington State University. As a member of numerous professional societies, he actively participates in AWS, ASM, SME, and TMS serving in numerous leadership roles at the technical committee and division levels. He is the Past-chair of the TMS Shaping and Forming Committee, the secretary for the ASM Joining Committee, and the programming representative for the Material Processing and Manufacturing Division in TMS. He has participated in research related to friction stir technologies for more than a decade as a senior research engineer at Pacific Northwest National Laboratory where he developed low-cost solutions for industrial implementation of friction stir technologies. Working with numerous industrial suppliers around the world, Dr. Hovanski has introduced cost efficient solutions for thermal telemetry, new low-cost tool materials, high volume production techniques for aluminum tailor-welded blanks, and new methodologies for joining dissimilar materials. As an active researcher, Dr. Hovanski received the R&D 100 award in 2011 and again in 2017, the DOE Vehicle Technologies Office Distinguished Achievement award in 2015, and a western region FLC award for technology transfer in 2015. He actively reviews friction stir related literature for numerous publications and has documented his work in more than 75 publications and proceedings and three U.S. patents.

Rajiv Mishra is a Distinguished Research Professor of Materials Science and Engineering in the Department of Materials Science and Engineering at the University of North Texas, and is Director of the Advanced Materials and Manufacturing Processes Institute (AMMPI). He is also the UNT Site Director of the NSF I/UCRC for Friction Stir Processing and a Fellow of ASM International. His highest degree is Ph.D. in Metallurgy from the University of Sheffield, UK (1988). He has received a number of awards including the Firth Pre-doctoral Fellowship from the University of Sheffield, the Brunton Medal for the best Ph.D. dissertation in the School of Materials from the University of Sheffield in 1988, the Young Metallurgist Award from the Indian Institute of Metals in 1993, Associate of the Indian Academy of Sciences in 1993, the Faculty Excellence Award from the University of Missouri-Rolla each year from 2001 to 2007. He is a Past-chair of the Structural Materials Division of TMS and served on the TMS Board of Directors (2013–2016). He has authored/coauthored 312 papers in peer-reviewed journals and proceedings and is principal inventor of four U.S. patents. His current publication based h-index is 60 and his papers have been cited more than 19,000 times. He has coauthored two books: (1) *Friction Stir Welding and Processing*, and (2) *Metallurgy and Design of Alloys with Hierarchical Microstructures*. He has edited or co-edited 15 TMS conference proceedings. He serves on the editorial board of *Materials Science and Engineering A*, *Science and Technology of Welding and Joining*, and *Materials Research Letters*. He is the founding editor of a short book series on friction stir welding and processing published by Elsevier and has coauthored seven short books in this series.

Yutaka Sato is a Professor in the Department of Materials Processing at Tohoku University, Japan. He earned a Ph.D. in Materials Processing at Tohoku University (2001). His Ph.D. thesis was titled "Microstructural Study on Friction Stir Welds of Aluminum Alloys." He participated in friction stir research of steels at Brigham Young University for a year in 2003. He is a member of Sub-commission III-B WG-B4 at IIW, which is a working group to build international standardization of friction stir spot welding. His work has focused on metallurgical studies of friction stir welding and processing for about 20 years. He has obtained fundamental knowledge on development of grain structure, texture evolution, joining mechanism, behavior of oxide-layer on surface, and properties-microstructure relationship. Recently he has focused on developing friction stir welding of steels and titanium alloys, and new tool materials. He has received a number of awards including the Kihara Award from the Association for Weld Joining Technology Promotion (2008), Prof. Koichi Masubuchi Award from AWS (2009), Murakami Young Researcher Award from the Japan Institute of Metals (2010), Aoba Foundation Award (2010), Honda Memorial Young Researcher Award (2011), and The Japan Institute of Metals and Materials Meritorious Award (2015). He has authored or coauthored more than 250 papers in peer-reviewed journals and proceedings.

Piyush Upadhyay is a scientist at Pacific Northwest National Laboratory. He obtained his Ph.D. in Mechanical Engineering from University of South Carolina in 2012 in "Boundary Condition Effects on Friction Stir Welding of Aluminum Alloys." For the past decade he has been primarily involved in research and development of FSW and allied technologies to join similar and dissimilar materials. Currently, he leads efforts on friction stir welding of alloys in dissimilar thickness and dissimilar materials including combinations of aluminum, magnesium, steels, and polymers for automotive application. He has received several awards and recognitions including Aid Nepal Scholarship for undergraduate study (2001), Happy House Foundation Research Fellowship at Kathmandu University (2007), the DOE Energy Efficiency and Renewable Energy Recognition for Innovation (2015), and the R&D 100 award (2018). He has authored or coauthored more than 25 papers in peer-reviewed journals and proceedings and is actively involved as a reviewer for several technical journals and conference sub-committees.

David Yan is an Assistant Professor of Manufacturing Engineering Technology at San Jose State University. He earned his Ph.D. degree in Mechanical Engineering from Deakin University, Australia (2014). Prior to that, he received his M.Phil. (1st Hons) and B.E. (Hons) degree in Mechanical Engineering from Auckland University of Technology, New Zealand. His current research focuses on friction stir additive manufacturing. Previously, he centered his postgraduate research on the characterizations of material flow formation during scroll tool friction stir welding Al alloys and has gained more than 10 years of research experience in friction stir welding and processing. In addition, he is actively involved in ASME, SME, and TMS, serving as a member in the TMS Shaping and Forming Committee, Additive Manufacturing Committee, and Powder Materials Committee, and as a symposium co-organizer. Dr. Yan reviews machining and solid-state joining related literature for several journals and has authored more than 15 publications including books, journal papers, and peer-reviewed conference proceedings. He has received a number of awards including Research for Industry Awards (2008), Australian Postgraduate Awards (2010), and Grants-In-Aid of Research Award (2016).

Part I
Dissimilar Materials

Comparison of Dissimilar Aluminum Alloys Joined by Friction Stir Welding with Conventional and Bobbin Tools

Paul Goetze, Mateusz Kopyściański, Carter Hamilton and Stanisław Dymek

Abstract Dissimilar aluminum alloys 2024-T351 and 7075-T651 were friction stir welded utilizing a conventional tool and a bobbin-style tool. The welds produced with the conventional tool yielded higher mechanical properties than those produced with the bobbin tool, and fracture of all tensile specimens occurred on the 2024 side of the weld regardless of the tool or weld configuration. Temperature data and modeling demonstrated that the temperature distribution from either tool skews toward the advancing side. Ultimately, the mechanical properties and hardness profiles across the welds correlated with the temperature distribution and the associated precipitation behavior of the alloys. Optical microscopy revealed distinct layers of the alloys interwoven within the stir zone and identical grain sizes in both alloys. Grain boundary orientations from the stir zone followed the Mackenzie plot, suggesting complete recrystallization and a lack of texture within this zone.

Keywords Friction stir welding · Dissimilar metals · Tool comparison
Material comparison

P. Goetze (✉) · C. Hamilton
Department of Mechanical and Manufacturing Engineering, College of Engineering
and Computing, Miami University, Oxford, OH, USA
e-mail: goetzepa@miamioh.edu

C. Hamilton
e-mail: hamiltbc@miamioh.edu

M. Kopyściański · S. Dymek
Faculty of Metal Engineering and Industrial Computer Science, AGH University
of Science and Technology, Krakow, Poland
e-mail: mateusz.kopyscianski@gmail.com

S. Dymek
e-mail: gmdymek@cyfronet.pl

Y. Hovanski et al. (eds.), *Friction Stir Welding and Processing X*, The Minerals, Metals & Materials Series, https://doi.org/10.1007/978-3-030-05752-7_1

Introduction

The process of friction stir welding (FSW) is relatively unique and was first developed in the early 1990s. It was primarily intended for the joining of aluminum alloys and the process has become very cost-effective in several transportation industries. Standard friction stir welding, friction stir processing, and friction stir spot welding are beginning to displace traditional welding methods because of their tendency toward lower heat inputs and the longevity of tooling. In the case of welding aluminum, a hardened steel tool may last millions of cycles and can be considered non-consumable.

The tool enters the material with a controlled velocity and transverse speed, producing heat through friction and plastic deformation of the material. This heat allows the material to flow around the tool creating a mixed zone, known as the weld nugget or stir zone, along the centerline of the weld. Because the material is stirred with a unidirectional rotating tool, there are distinct regions around the weld that exhibit various material properties. The heat input and physical deformation of the material produce the weld zone where stirring occurs (SZ), a thermo-mechanically affected transition zone (TMAZ) where there are both thermal and mechanical changes, and a heat affected zone (HAZ) where the heat input alters the properties of the material. Additionally, due to the distinct material flow associated with tool rotation and advancement on either side of the weld, the tool produces an advancing and retreating side that have different characteristics.

The low heat input of friction stir welding makes it an attractive method for joining high strength aluminum alloys such as the 2XXX and 7XXX series that are very difficult to join with traditional fusion welding. Thus, much prior work has been done to characterize the properties of these alloys joined with FSW. Works by Mahoney, Jones, and Mishra [1–3] outline these topics well.

Dissimilar alloy welding is a developing interest within the field of friction stir welding. It is the process of joining two different alloys together such as 2024 and 7075. This technique is potentially useful for creating structures that utilize the properties of multiple alloys. Da Silva, Cavaliere, and Khodir and Shibayanagi [4–6] provide useful bases for this topic. However, there is a need to examine the effects of certain variables on the process because of the asymmetric nature of the produced joints. Specifically, there is limited research comparing the conventional and bobbin tool geometries and the effects of material placement on either the advancing or retreating side of the weld line.

Experimental Procedure

The objective of this study was to examine the properties of friction stir welded butt joints of 2024-T3 and 7075-T6. The design of the experiment contains two primary elements. First, performance characteristics are compared between the bobbin and

Table 1 Summary of experimental configurations and welding trial designations

Trial	AS Mat.	Tool
AS-2024B	2024	Bobbin tool
AS-7075B	7075	
AS-7075C	7075	Conv. tool
AS-2024C	2024	

conventional tool geometries when they are used with dissimilar alloys. Second, the effect of the placement of the 2024 and 7075 alloys on the retreating (RS) or advancing side (AS) was assessed. Table 1 summarizes the experimental configurations and provides identifying nomenclature for each welding trial.

Tensile testing, micro-hardness maps, and optical microscopy were used to fully characterize each weld trial and compare the effect of tool choice and material placement on weld quality. Aluminum sheets of 2024-T351 and 7075-T6 were selected, conforming to the ASTM B209 standard, at a thickness of 6.35 mm. Each sheet was 101.6 mm wide by 609.6 mm long before processing and the mating surfaces were machined for proper alignment. The welding was done in two stages at the University of South Carolina on an MTS ISTIR PDS machine to ensure the process validity for each material and tool configuration. After the first half of each trial was completed, a three-point bend test was done to test for process defects. Then, each trial was finished using the same or corrected parameters if needed. In practice, a crosshead feed of 127 mm/min and a spindle speed of 120 RPM was used for all material configurations with the bobbin (self-reacting) tool. A feed of 203.2 mm/min and speed of 300 RPM was used with the conventional tool geometry for all material configurations. The machine operated with a 0-degree tool tilt angle. The bobbin tool was designed with 17 mm shoulders and 6.35 mm pin and the conventional tool had a 17.78 mm shoulder diameter with a 4.1 mm scroll pitch and a 6.35 mm threaded pin. Temperature measurements were made in configurations with the bobbin tool by embedding a thermocouple in the base sheet near the weld nugget and the conventional tool had a thermocouple embedded in the center of the tool body.

A Zeiss Axio Imager M1 light optical microscope was used to observe the microstructural features of a cross section from each weld configuration. Each specimen was prepared through standard polishing practice and etched with Barker's Reagent (1.8 ml HBF_4 and 100 ml H_2O) for 2 min at 20 V DC. For all welding configurations, the advancing side is always presented on the left-hand side of the image.

Vickers micro-hardness testing of the weld cross sections for each configuration was performed using 1 kg load for 10 s on a Wolpert-Wilson Tukon 2500 machine. For the conventional tool configurations, one measurement row was taken along the mid-thickness line of each cross section. Measurements with a 1 mm spacing interval were taken to a 20 mm distance on each side of the weld centerline. A total of three measurement rows were taken for each bobbin tool configuration: 1 mm below the top surface of the cross section (upper shoulder), the mid-thickness line, and 1 mm above the bottom surface of the cross section (lower shoulder). As before, a 1 mm spacing was used between indentations out to 20 mm on each side of the weld centerline.

Tensile specimens were machined transverse to the weld direction on a Haas TM-1 CNC milling machine. A sub-size sheet-type specimen design was selected to conserve space on the welded sheets and to ensure the tensile trials could be accomplished on an MTS Exceed E44 with flat, mechanical grips. The specimen design conformed to the ASTM E8-04 standard. Five specimens were machined for each material configuration and each was engraved with a serial number for later identification. The tensile testing was performed after four months of natural aging at a strain rate of 0.012/min. An MTS 634.12E-54 extensometer with a gage length of 25.4 mm was used during each trial. All welded material and samples were kept below 0 °C after completion of the tension testing to prevent further natural aging before or during the subsequent hardness experiments.

Results and Discussion

Optical Microscopy

The microstructures of the welds utilizing the bobbin tool geometry are presented in Fig. 1a and b where 2024 is on the advancing side and retreating side respectively. Figure 1 shows the 2024 as optically darker compared to the 7075. Both configurations contain the typical stir, thermal mechanical, heat affected and base material zones that characterize most friction stir welds. Fine grain refinement occurs in the stir zone, likely due to dynamic recrystallization as described by Reynolds [7]. Both configurations show abrupt transitions between the SZ and TMAZ on the AS compared to the RS which do not depend on material location. However, the AS TMAZ in the AS-2024B configuration is reduced in size compared to the same feature in the AS-7075B weld. Measurements of the grain transformation between the recrystallized and base zones on the AS in the AS-2024B weld occurs within 0.4 mm whereas the AS-7075B weld transitions for 1.5 mm. A similar trend is seen on the RS with the AS-2024B transition being more gradual than that of AS-7075B. Here the transformation occurs over 6.5 mm and 5.0 mm respectively, measuring on the midsection lines of each cross section. Overall, the optical microscopy shows the 2024 alloy transitions between fine recrystallized grains in the stir zone to unaffected grains over less distance on both the AS and RS than the 7075 alloy. Little material mixing is observed in both material configurations, with the most complete mixing occurring along the midsection line. Bands of material are present throughout the stir zone, indicating that some material traversed across the centerline during processing.

The optical micrographs of the conventional tool welds show similar patterns to the micrographs of the bobbin tool configurations. Figure 2 presents these results with 2024 appearing darker than 7075. The advancing side transition between the SZ and TMAZ is more abrupt than the corresponding retreating side for both the AS-2024C and AS-7075C welds. Like the welds in the bobbin tool configuration, the

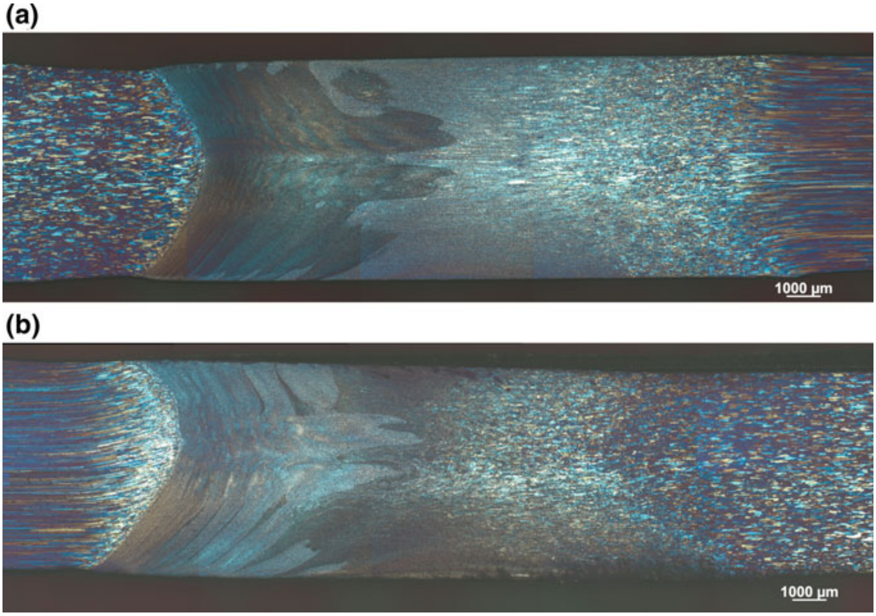

Fig. 1 Optical micrograph for: **a** the AS-2024B configuration, **b** the AS-7075B configuration

2024 microstructure transitions over less distance than that of 7075 when compared on the same side. Figure 2a shows that it takes around 0.1 mm for 2024 to transition on the AS and 3.0 mm for 7075 to transition on the RS. Conversely, the opposite configuration shown in Fig. 2b indicates the 7075 takes between 0.7 mm in the shoulder affected region and 0.2 mm near the bottom of the pin to transition on the AS. The 2024 transitions over 1.5 mm on the RS.

In all welding configurations, the 2024 transition from stir zone to base material grain structure occurs over less distance than that of 7075, regardless of advancing or retreating side placement. The bobbin tool configuration produced a wider region of dynamically recrystallized grains due to the symmetric shoulder affected regions and simpler mixing patterns of the dissimilar alloys compared to the conventional tooling. However, grain size and orientation within the stir zone are identical for both tool geometries. Similar patterns are found in the TMAZ zones of configurations of both tool geometries where the advancing side exhibits a significantly more abrupt transition between the stir zone and base material than the retreating side. Additionally, both tool configurations show advanced stir patterns in the shoulder affected region of the advancing side when 2024 is placed on the retreating side before welding. In these configurations, bands of 2024 are observed penetrating deeper into the center of the cross sections and may indicate more thorough material mixing in these cases. Works from Reza-E-Rabby et al. [8] and Koilraj et al. [9] support these observations by concluding that in dissimilar welding situations, placing the harder material on the advancing side can reduce stirring defects and can improve mechanical properties of the joint.

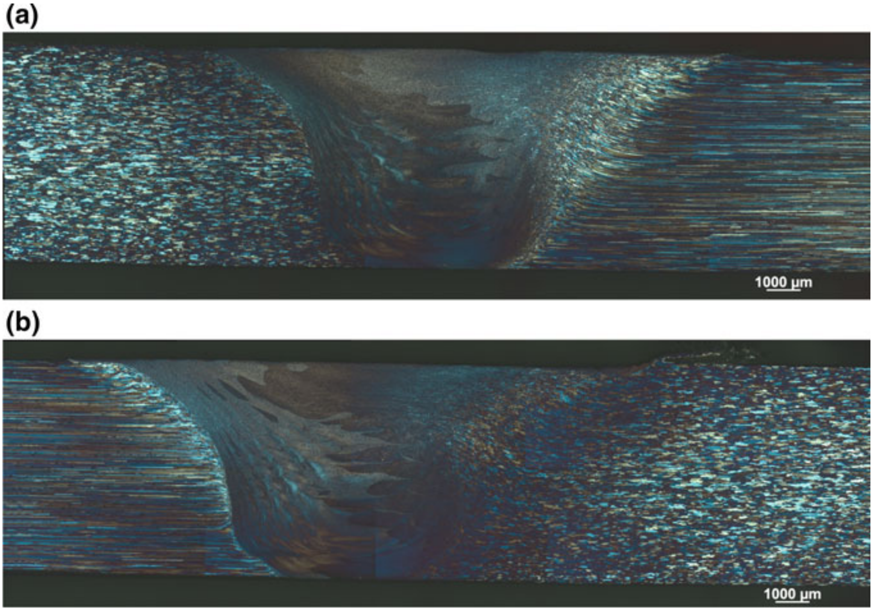

Fig. 2 Optical micrographs for: **a** the AS-2024C configuration, **b** the AS-7075C configuration

Micro-hardness Distributions

The micro-hardness profiles of the bobbin tool configuration AS-2024B are presented in Fig. 3a. Two hardness minima are recognized on the advancing and retreating edges of the weld with values of 110 HV and 120 HV, respectively. Their locations indicate that the maximum material softening occurs near the edge of the SZ, otherwise marking the HAZ of the weld. Moving toward the outward edges of the profiles, the material gradually returns to the material properties of the base material. Additionally, the profiles indicate a degree of hardness recovery in the SZ from dynamic recrystallization and the material reaching the solidus temperature of 2024 and/or 7075. Figure 3a shows a distinct hardness step across the weld centerline from AS to RS. The shoulder dominated profiles mark the midpoint step as biased 3–4 mm to the AS from the centerline while the midsection profile records the step occurring 1–2 mm toward the AS from the centerline. The range of measurements taken across the midsection step is less severe than in the shoulder dominated profiles, indicating better material mixing in the region. This is reinforced by the optical micrographs above.

The micro-hardness profiles of the bobbin tool configuration AS-7075B are presented in Fig. 3b. This weld configuration produced profiles similar to its counterpart (AS-2024B) with two hardness minima near the edges of the SZ with values of 121 HV and 108 HV on the advancing and retreating sides, respectively. The precise locations of the minima are shifted slightly toward the AS and the base material on

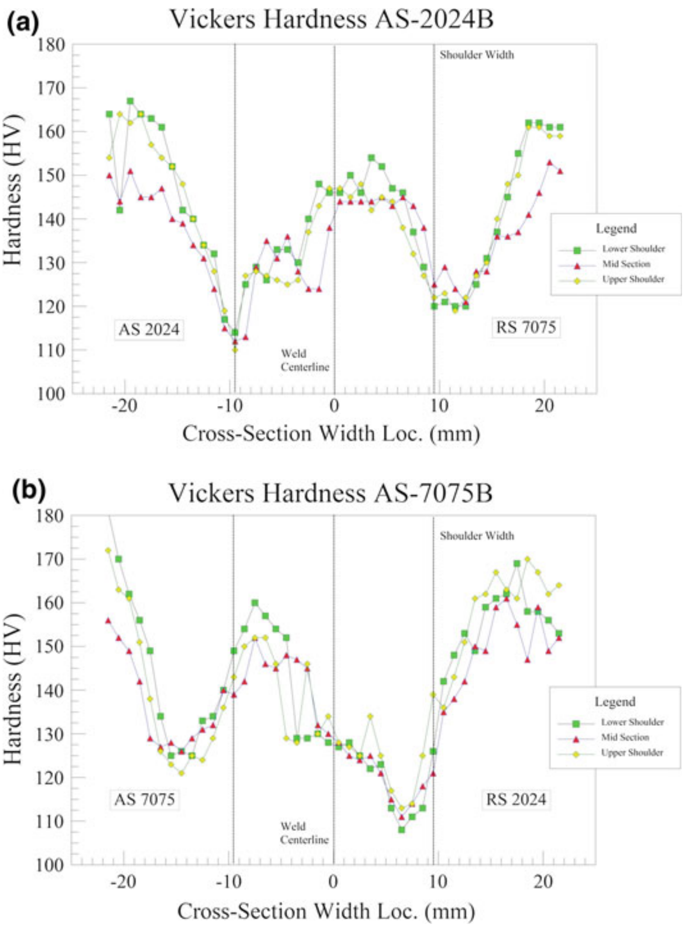

Fig. 3 Vickers hardness profiles for: **a** the AS-2024B configuration, **b** the AS-7075B configuration

the 7075 side of the weld achieves better recovery compared to the counterpart weld. In both the AS-2024B and AS-7075B configurations, the lowest hardness minimum was found accompanying the 2024 side of the weld. The same hardness step occurrence is present in Fig. 3b but shows better dynamic recovery of the 7075 and gradual decline of the 2024. Again, a less severe step is present along the midsection profile than in the shoulder dominated regions.

The conventional tool configuration AS-2024C produced the midsection hardness profile shown in Fig. 4a. Here, one absolute hardness minimum was recorded on the 2024 side of the weld near the edge of the pin diameter with a value of 129 HV. A smaller local minimum is also present on the 7075 side outside of the pin diameter but within the shoulder diameter. Inside the SZ, measurements varied significantly and indicate some material mixing along the midsection of the weld. This is supported

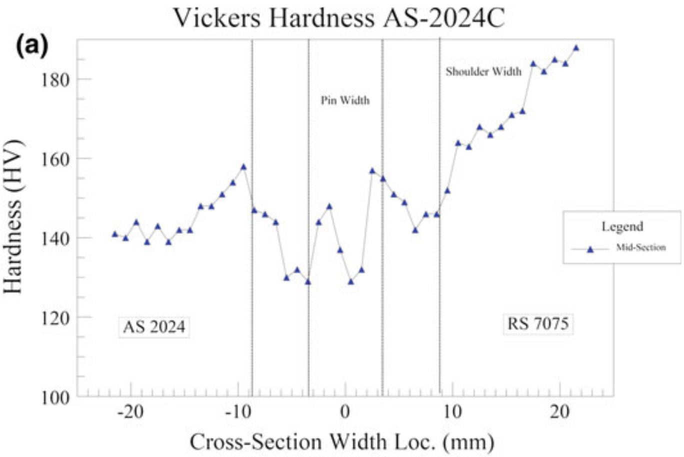

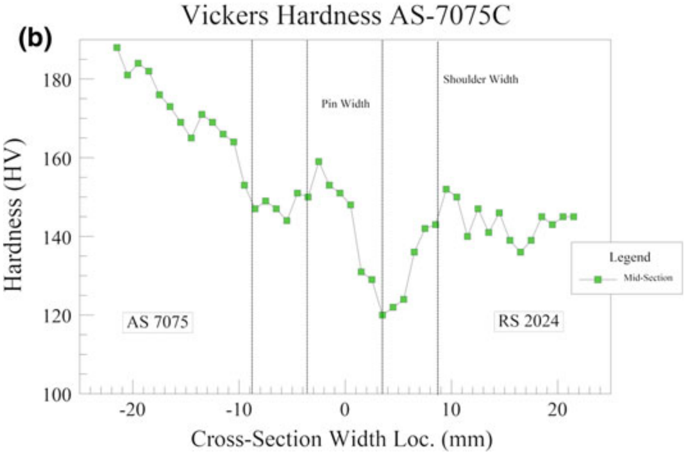

Fig. 4 Vickers hardness profiles for: **a** the AS-2024C configuration, **b** the AS-7075C configuration

by the optical micrograph showing bands of material present across the width of the stir zone.

The midsection hardness profile for the AS-7075C conventional tool configuration exhibits similar characteristics to the AS-2024C weld, shown in Fig. 4b. One absolute hardness minimum is present on the 2024 side measured at 120 HV and a local minimum is present on the 7075 side between the extents of the shoulder and pin geometries. The profile of this configuration also shows a hardness step across the midsection of the weld, highlighting the interface between 2024 and 7075. The same trend is likely to present in the AS-2024C weld, but the presence may be hidden because of measurements in different material bands across the SZ obscuring the bulk trend.

Both conventional weld configurations show one absolute hardness minimum on the 2024 side and a local minimum in the 7075. This is distinctly different from the bobbin tool configurations where there is a hardness minimum on both the 2024 and 7075 sides. This difference is likely due to contrasting heat inputs by the two tool geometries. A higher machine input power was recorded during the conventional tool trials than the bobbin tool trials which suggests a higher heat input into the weld. Temperature data taken at the center of the conventional tool was near 450 °C and very close to the solution treatment temperature for 7075. This may explain the smaller hardness reduction of the 7075 in the conventional configurations compared to the bobbin tool trials. If the peak temperature in the bobbin tool did not approach the solution temperature for 7075, significant precipitate coarsening is expected in the HAZ of the weld. Future complete temperature models of both tool configurations will help to fully explain and confirm the material hardness profiles shown above.

Tensile Testing

The average result for the tensile testing of each welding configuration is presented below in Table 2. All trials produced failures on the 2024 side of the weld. The conventional tool welds with 2024 on the advancing side had higher yield (YS) and ultimate tensile strength (UTS) values than those with 2024 on the retreating side. The failures occurred inside the shoulder width and close to the edge of the stir zone for both material configurations.

The bobbin tool configuration testing produced higher UTS results with 7075 on the advancing side than with 2024, but the YS values were similar across both material configurations. The failures in the bobbin tool configuration also occurred along the edge of the SZ. Additionally, the standard deviations among the sampling groups suggest that the conventional tool welds were more consistent than the joining performed with the bobbin tool.

Table 2 Tensile testing results for all material and tool configurations

Trial	Description	UTS (MPa)	YS (MPa)	Fracture location	St. dev.
AS-2024B	Bobbin, 2024 AS	359	245	Edge of SZ 2024	2.46
AS-7075B	Bobbin, 7075 AS	383	246	Edge of SZ 2024	2.41
AS-2024C	Conventional, 2024 AS	444	302	Edge of SZ 2024	0.44
AS-7075C	Conventional, 7075 AS	426	287	Edge of SZ 2024	0.20

Conclusions

A comparative study investigating the effects of material placement (AS vs. RS) and tool type (conventional vs. bobbin) on the joining of dissimilar alloys 2024-T3 and 7075-T6 has been performed. The friction stir welds were examined through optical microscopy, micro-hardness measurements, and tensile testing. These results indicate that placement of 2024 on the retreating side during processing for both tool geometries produces more material banding in the shoulder dominated stir regions. Identical grain size is also found within the SZ regardless of tool type. Conversely, the different geometries and process parameters for each tool produced contrasting heat inputs to the weld. This affected the hardness profiles across the weld cross section especially with respect to hardness minima and location. As a result, the tensile testing results showed higher joint strength in welds processed with the conventional tool and placement of 2024 on the advancing side. Further work on temperature modeling of each weld configuration may help explain the trends shown in hardness and tensile results.

Acknowledgements Special thanks to Dr. Anthony Reynolds and Mr. Dan Wilhelm at the University of South Carolina for their expertise and facilities in the production of all welding configurations used in this study. Additionally, Dr. Mateusz Kopyściański and the Department of Metal Engineering and Industrial Computer Science at the AGH University of Science and Technology were very generous in their assistance and guidance during the examination phase of the study.

References

1. Mahoney MW, Rhodes CG, Flintoff JG, Bingel WH, Spurling RA (1998) Properties of friction-stir-welded 7075 T651 aluminum. Metall Mater Trans A 29(7):1955–1964
2. Jones MJ, Heurtier P, Desrayaud C, Montheillet F, Allehaux D, Driver JH (2005) Correlation between microstructure and microhardness in a friction stir welded 2024 aluminium alloy. Scr Mater 52(8):693–697
3. Mishra RS, Ma ZY (2005) Friction stir welding and processing. Mater Sci Eng R Rep 50(1):1–78
4. da Silva AAM, Arruti E, Janeiro G, Aldanondo E, Alvarez P, Echeverria A (2011) Material flow and mechanical behaviour of dissimilar AA2024-T3 and AA7075-T6 aluminium alloys friction stir welds. Mater Des 32(4):2021–2027
5. Cavaliere P, Nobile R, Panella FW, Squillace A (2006) Mechanical and microstructural behaviour of 2024–7075 aluminium alloy sheets joined by friction stir welding. Int J Mach Tools Manuf 46(6):588–594
6. Khodir SA, Shibayanagi T (2008) Friction stir welding of dissimilar AA2024 and AA7075 aluminum alloys. Mater Sci Eng B 148(1):82–87
7. Mishra RS, Mahoney MW (2007) Friction stir welding and processing. ASM International, Materials Park, Ohio
8. Reza-E-Rabby M, Tang W, Reynolds AP (2015) Effect of tool pin features on process response variables during friction stir welding of dissimilar aluminum alloys. Sci Technol Weld Join 20(5):425–432
9. Koilraj M, Sundareswaran V, Vijayan S, Koteswara Rao SR (2012) Friction stir welding of dissimilar aluminum alloys AA2219 to AA5083—optimization of process parameters using Taguchi technique. Mater Des 42:1–7

Promising High-Speed Welding Techniques for Joining Polymers to Metals and Underlying Joining Mechanisms

F. C. Liu and P. Dong

Abstract Strong dissimilar material welds (DMW) of PA66 and 6061 Al was produced by friction lap welding (FLW) at welding speeds as high as 5 m/min. The temperature difference at various locations of the welds did not affect the local joining strength. In an attempt of explaining the joint strengths, special samples were made by evaporation of aluminum oxide onto a polyamide 66 (PA66) substrate to form metal/polymer interface. X-ray photoelectron spectroscopy (XPS) analysis showed that the key chemical bond developed across the PA66/alumina interface is of Al–O–C type which would have very likely contributed to good joint strengths in such metal/polymer joints. Elevated temperatures are not essential for formation such chemical bonds as long as a fully intimate atomic contact between the PA66 and Al plates can be achieved.

Keywords Dissimilar material welds · Friction lap welding · High welding speed X-ray photoelectron spectroscopy · Joining mechanism

Introduction

Lightweight and high performance are the emerging trends of tomorrow's vehicles. Carbon fiber reinforced polymers (CFRP), as a new engineering polymer composites, have been used and are expected to have more application in aerospace, automotive and naval architecture due to their lightweight and high performance. Welding of CFRP to the traditional metallic workpiece allows exploiting the advantages of each material of the hybrid components. The metal in the hybrid components can provide

---

F. C. Liu (✉) · P. Dong
Department of Naval Architecture and Marine Engineering, University of Michigan,
Ann Arbor, MI 48109, USA
e-mail: liufc@umich.edu

P. Dong
Department of Mechanical Engineering, University of Michigan,
Ann Arbor, MI 48109, USA

Y. Hovanski et al. (eds.), *Friction Stir Welding and Processing X*, The Minerals, Metals & Materials Series, https://doi.org/10.1007/978-3-030-05752-7_2

high stiffness and strength while the plastic material can offer excellent functional integration. However, it is still a great challenge to produce sound hybrid welds of metal and plastic because metal and plastic materials have a significant difference in physical and chemical properties at both room temperature and elevated welding temperatures [1, 2].

Traditionally, mechanical fastening and adhesive bonding have been used to join metal and plastic components together in some applications. Both methods have their unique advantages but also have their limitations. The structural integrity can be assured by mechanical fastening when well-established prediction methods and analysis was applied [3]. Therefore, mechanical joints are commonly used in highly critical and safety-rated components, such as aircraft frames, automotive, etc. [4, 5]. However, the third component in mechanical joins, such as rivets or bolts, increased the structure weight. The stress concentration around the fastener is also a critical issue in practical application. Adhesive bonding is also an option for joining dissimilar materials in some applications. It enables sealing and good surface finishing [6]. Nonetheless, this process is very time-consuming as extensive surface preparation before joining and long curing time is necessary for achieving strong adhesive bonds. Also, accidental disassembly may occur in service as adhesive suffers from thermal and environmental degradation [1, 6].

Various welding processes, such as friction lap welding (FLW) [1, 7], Laser direct joining (LDJ) [8], resistance spot welding [9], refill friction stir spot welding [10], and ultrasonic spot welding [11], have been developed recently to produce metal/plastic dissimilar materials welds. Among these welding methods, only FLW and LDJ provide can produce strong liner lap welds. The lap joints produced by LDJ usually contains a high volume of bubbles along the joining interface [12, 13], which is not allowed in some of the highly required industry applications. In contrast, FLW can squeeze out most of the bubbles out of the weld zone under the forging effect of the FLW tool [7].

The concept of joining metal and thermoplastic using FLW is schematically illustrated in Fig. 1. A nonconsumable cylindrical tool is set to rotate at a desirable speed (Fig. 1a) and then moved to press against the metal sheet sitting on the thermoplastic plate (Fig. 1b). Once the desired pressure and temperature are attained, the cylindrical tool is set to travel along the welding direction at a fixed speed (Fig. 1c). The primary function of the cylindrical tool is to generate frictional heat while exerting a sufficient local pressure to form a sound joint between the plastic and metal piece. A strong bond forms at the interface after the melted plastic solidifies under pressure (Fig. 1d).

The investigations about the dissimilar materials welding of metal and polymers have been limited at linear velocities of less than 1 m/min [14–16]. It is in urgent need to develop a high-speed dissimilar welding technology for metal and polymer joints that could enable the more excellent use of dissimilar material welds in high-volume production applications.

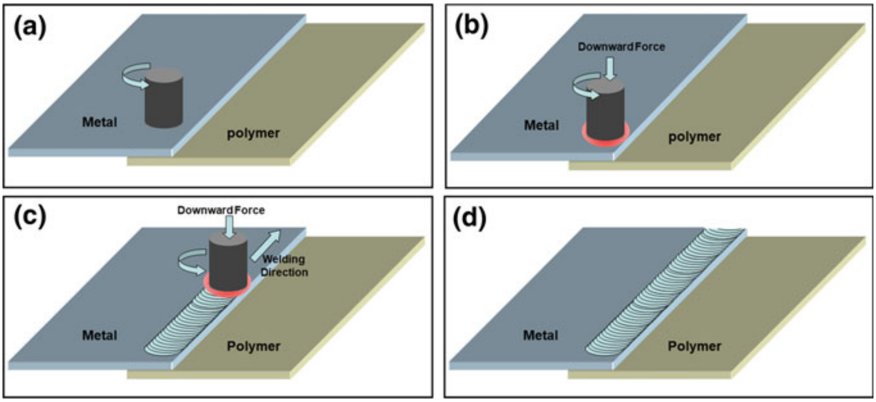

Fig. 1 Schematic illustration of friction lap welding: **a** rotating tool prior to contact with the plate; **b** rotating tool presses against the plate while expanding the hot zone; **c** the rotating tool moves relative to the plates, creating local heating and high pressure at the interface between metal and polymer; and **d** the rotating tool moves away from the plates, producing a strong bonding between metal and polymer

Experimental Procedures

6061-T6 aluminum alloy and polyamide 66 (PA66) sheets with dimensions of 600 × 75 × 2 mm were subjected to welding. A specially designed cylindrical tool with an embedded thermocouple was used to make the welds. The tip of the thermocouple is 1 mm away from the tool bottom surface. The tool diameter was 20 mm. The overlap width was 16 mm. The FLW processes were operated under position control. The plunging depth was set to be 0.45 mm. The cylindrical tool remained perpendicular to the workpiece surface during FLW. The FLW machine monitored the forging force during welding. The rotation rate (R) was set to be 3000 rpm for all the welds.

Lap shear tensile samples with a width of 20 mm were removed from the as-welded samples for testing. The tensile shear test was carried out using a tensile test machine (Instron 3366) at a tensile speed of 0.5 mm/min. The grip inserts were used to align the grip centerline with the joining interface. The cross section of the welded samples and fracture surfaces of the tensile samples were subjected to scanning electron microscopy (SEM) analyses.

The simulated interface between 6061Al and nylon was made by depositing alumina onto the PA66 plate surface through physical vapor deposition (PVD). The PA66 plates with alumina coating were taken into another laboratory for XPS analysis. Argon ion beam sputtering was applied in the XPS vacuum chamber before XPS measurement. XPS experiments were carried out in a Kratos Axis Ultra XPS system using monochromatic Al X-ray source at room temperature. All the spectra were calibrated by setting the C1s hydrocarbon peaks to the positions of binding energy of 285.0 eV. All the data were analyzed by the Casa XPS software using the Shirley-type background.

Results and Discussion

The forging forces at the welding speed of 1, 3, and 5 m/min were summarized in Fig. 2. It shows that the forging force applied to each weld maintained the same in the stage of pin plunge and dwelling. This indicated the FSW welder executed the command well in the tool plunge period as the tool plunge speed, plunge depth, and dwelling time before tool traveling have been set to be the same for all the welds. Figure 2 also shows that the forging force during quasi-steady state was significantly affected by the welding speed. With an increase in the welding speed from 1 to 5 m/min, the average forging force increased from ~1 to ~6 kN (Fig. 2). The high forging force at high welding speed could increase the pressure at the metal/polymer interface which is highly desired during FLW to ensure the intimate materials contact and to squeeze the bubbles out of the joining interface. A welding machine with high stiffness is required for high-speed FLW due to the high forging force.

As very high welding speed as selected in this study, it is necessary to check whether the tool indeed traveled at the designed speed. For this purpose, the variation of tool position with time was recorded for validation. Figure 3 shows that the tool indeed has reached the designed welding speed and maintain constant in the majority of the welding route.

Fig. 2 Variation of forging force at different welding speed from the beginning to the end of the welds

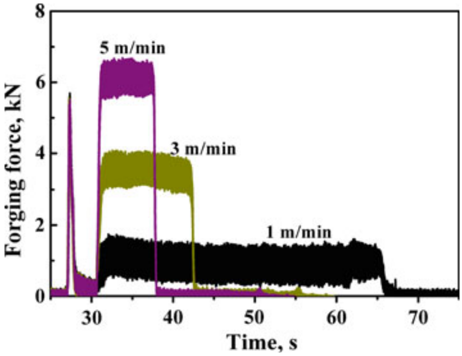

Fig. 3 Variation of tool position with time for difference welding speed

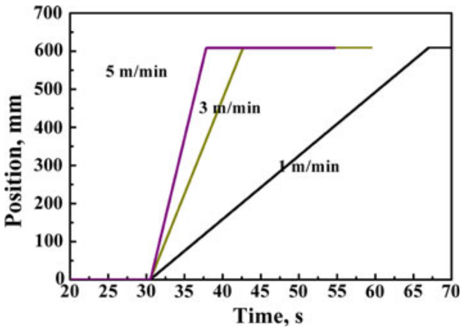

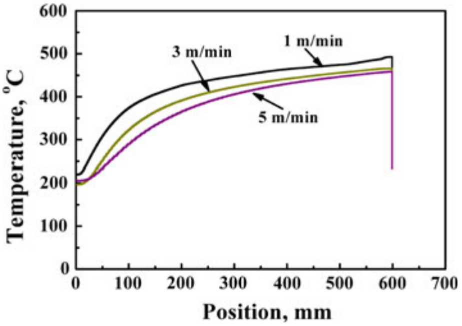

Fig. 4 Variation of tool surface temperature with position for difference welding speed

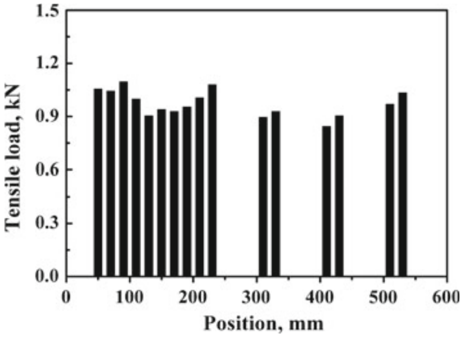

Fig. 5 Tensile shear load for sample extracted from various locations of the weld produced at 5 m/min

The temperature at the tip of the rotating tool was measured by the embedded thermocouple, which was a reference of the local welding temperature. Although the welding speed and forging force maintains constant during the whole path of the liner welding, the welding temperature raised along the welding path during welding (Fig. 4). For all the welds, the temperature increased rapidly in the first 100–200 mm. Following the sharp temperature increase is a moderate increase until the end of the welds. Even after a welding path of 600 mm, the welding temperature did not reach constant at all the invested welding conditions.

Lap shear tensile specimens were extracted at various locations of the weld produced at 5 m/min to investigate the effect of welding temperature on joining strength. The results were summarized in Fig. 5. Al the tensile samples failed along the joining interface instead of a cross-sectional failure, indicating the surface modification of plates is necessary for further increasing the joining strength. Although the local welding temperature increased along the liner direction of the weld, no clear trend of increase or decrease of the joining strength along the welding path was observed. As melted polymer squeezing out of the welding interface has been observed along all the welding path, it is reasonable to believe that the polymer adjacent to the welding interface was melted during welding. These indicated that as long as the welding temperature is high enough to melt the nylon at the welding interface locally, the welding temperature is no longer the dominant factor affecting the joining strength.

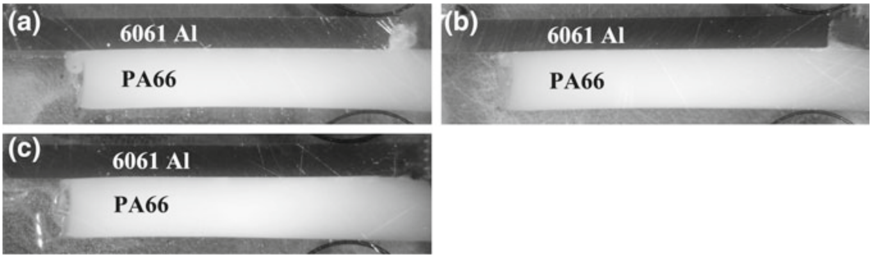

Fig. 6 Cross-sectional macroscope observation of FLW joints produced at **a** 1 m/min, **b** 3 m/min, and **c** 5 m/min

Fig. 7 Cross-sectional SEM observation of FLW joints welded at 5 m/min

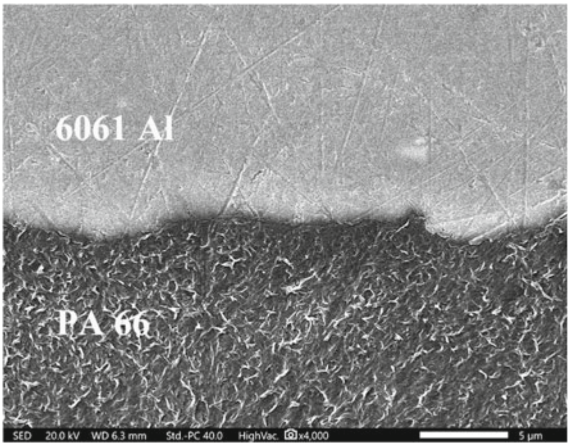

The typical cross sections of the samples welded at different welding speeds were summarized in Fig. 6. As the tool diameter (20 mm) is larger than the overlap width of the sample (16 mm), the joining interface maintained straight and was generally parallel to the top Al surface. Bubbles which commonly existed in samples produced by low welding speed [7] FLW or Laser [8, 16] was not observed along the joining interfaces. An SEM examination at higher magnification along the joining interface shows that the nylon and 6061 Al plates were tightly bonded together along the joining interface (Fig. 6). The bonding cannot be mainly ascribed to the mechanical interlocking as a deep groove or a sharp protrusion was not observed at most parts of the interface, and the tight boning was evident at locations with the relative smooth interface (Fig. 7).

X-ray photoelectron spectroscopy (XPS) has been shown to be a valuable tool for characterizing chemical reactions at the metal/polymer interface [17, 18]. The typical spatial resolution of XPS is larger than several tens of micrometers while the interfacial reaction layer of metal/polymer welds could be less than 1 nm. Thus, interfacial chemical bonds cannot be discerned through a cross-sectional XPS examination of the metal/polymer welds due to the low proportion of the retraction layer in an XPS

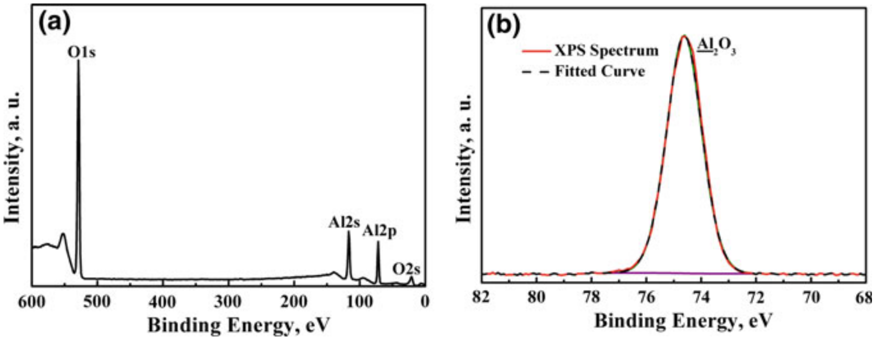

Fig. 8 XPS survey spectrum (**a**) and Al2p core level spectrum (**b**) from a 15 nm thick Al_2O_3 coating on PA66 plate

Table 1 Chemical atomic composition obtained through XPS scan on PA66 with various thickness of coating (without considering hydrogen atoms)

Alumina thickness	O1s (at.%)	N1s (at.%)	C1s (at.%)	Al2p (at.%)	N1s/C1s (at.%)	(O1s − N1s)/Al2p (at.%)
3.2 nm	45.45	3.25	22.10	29.20	0.147	1.45
1.5	32.84	5.98	41.28	19.90	0.145	1.35

spot. In addition, a typical XPS analysis depth is about 3–10 nm. It is very difficult to precisely thin down either the metal or the polymer plates of metal/polymer joints to that size. Due to great difficulties exists in using XPS for determining the interfacial chemistry in polymer/aluminum joints, alumina coatings were deposited onto polyamide 66 (PA66) plates through a physical vapor deposition (PVD) process to form an aluminum alloy/PA66 interface.

The PA66 plate with 15 nm thick alumina deposition was analyzed by XPS first (Fig. 8) to determine the FWHM of the Al2p peak of alumina. Only the peaks of O1s, Al2s, Al2p, and O2s were visible in the XPS survey. No C or N peak was detected, indicating the 15 nm alumina is thick enough so that the photoelectron emitting from PA 66 and possessing characteristic emission energies did penetrate the alumina coating and did not contribute to any peak of the spectrum in Fig. 8. The relative content of components O1s and Al2p was determined by the area under the corresponding components (Fig. 8a). The results were summarized in Table 1 which shows that the atomic percentage of O1s and Al2p are consistent with the content of O and Al atoms in Al_2O_3, confirming that the coating is pure Al_2O_3. As Al2p spectrum in Fig. 8b is solely the result of the Al atoms in Al_2O_3 coating, only a single component Al_2O_3, in which Al atoms are linked to oxygen, was resolved from the Al2p spectrum at 74.6 eV. The FWHM of the Al_2O_3 component is determined to be 1.5 eV.

Figure 9 shows the XPS survey spectra of the samples with a different thickness of alumina coatings. With a decrease in the thickness of the alumina coating, the O1s,

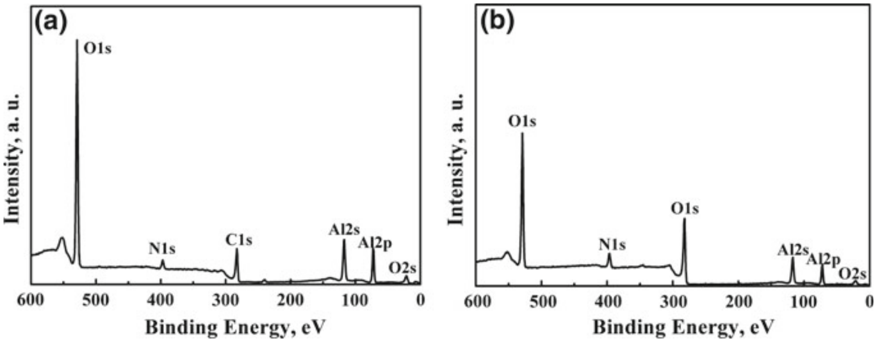

Fig. 9 XPS survey spectra (0–600 eV) as a function of Al_2O_3 coating: **a** 3.2 nm and **b** 1.6 nm

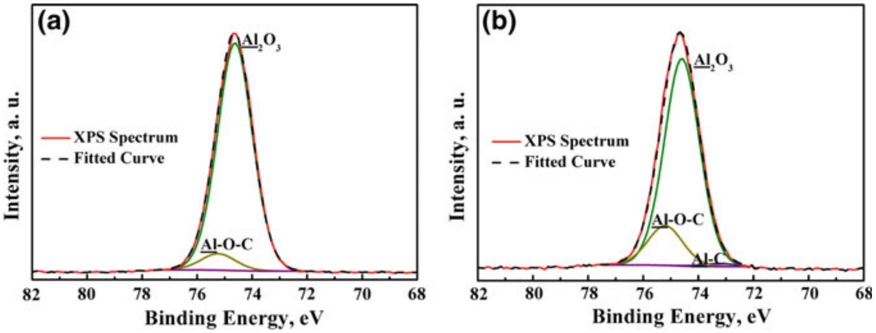

Fig. 10 Al2p core level spectra recorded as a function of Al coating: **a** 3.2 nm and **b** 1.6 nm

Al2s, and Al2p intensities declined while emission signals of N1s and C1s became stronger. The attenuation of O1s, Al2s and Al2p intensities is ascribed to less alumina to emit photoelectrons. The intensification of N1s and C1s peaks can be explained by the screening effect that is more photoelectrons possessing characteristic emission energies come from the PA66 surface have penetrated the thinner alumina coating.

The fitted Al2p spectra obtained from the PA66 plates with 3.2 and 1.5 nm alumina coating were shown in Fig. 10. The FWHM of all the resolved components from Al2p spectra is 1.5 eV. Figure 10a shows that in addition to the component of Al_2O_3 at 74.6 eV, a distinct component at 75.2 eV also appeared in the Al2p spectrum of the sample with 3.2 nm Al2O3 coating. This new component was in the form of Al–O–C bonds and expressed as Al–O–C. Another new component at 73.0 eV was observed the spectrum collected from the samples with 1.5 nm alumina coating (Fig. 10b). This new component involving the Al atoms linked directly to C atoms was denoted as Al–C.

An increased proportion of Al–O–C components were detected when the alumina coating became thinner (Fig. 10). This phenomenon indicated that more photoelectron possessing characteristic emission energies of the Al–O–C bonds formed at the

Fig. 11 Appearance of FLW sample welded at 5 m/min

PA66/alumina interface could penetrate the thinner alumina coating. All the Al2p spectra in Fig. 10 have confirmed that the dominant new bond developed across the interface of PA66/alumina is of the Al–O–C type. It should be noticed that such Al–O–C components formed the PA66/alumina interface at room temperature PVD process, demonstrating that elevated temperature is not necessary for the formation of such chemical bonds. To build a strong FLW joint of PA 66 and Al plate, locally melting of PA 66 is still necessary for developing Al–O–C components at the joining interface as the two materials need to achieve a fully intimate atomic contact along the join interface to develop enough Al–O–C bonds.

This study shows that metal and thermal plastic cab be joined together at very high welding speed by FLW. In addition to mechanical interlocking, the high joining strength can be contributed to the formation of Al–O–C components at the joining interface. In addition to boosting productively, high-speed welding also exhibited other advantages, such as reducing the bubble volume in the joints (Fig. 6) and reduced welds distortion (Fig. 11).

Conclusion

1. Strong dissimilar materials welds of PA66 and 6061 Al was produced by friction lap welding at welding speeds as high as 5 m/min.
2. The average plunge force remained at the same level over the entire weld at a fixed welding parameter but increased with an increase in the welding speed. A welding machine with high stiffness is required for high-speed FLW.
3. The temperature at the surface of aluminum plates increased as the tool traveled along the path of the liner welding. The temperature variation at different locations of the weld did change the joining strength of the weld as elevated temperatures are not essential for forming Al–O–C bond at the joining interface.

References

1. Liu FC, Liao J, Nakata K (2014) Joining of metal to plastic using friction lap welding. Mater Des 54:236–244
2. Martinsen K, Hu SJ, Carlson BE (2015) Joining of dissimilar materials. Cirp Ann-Manuf Technol 64(2):679–699
3. Amancio ST, dos Santos JF (2009) Joining of polymers and polymer-metal hybrid structures: recent developments and trends. Polym Eng Sci 49(8):1461–1476
4. Kweon JH, Jung JW, Kim TH, Choi JH, Kim DH (2006) Failure of carbon composite-to-aluminum joints with combined mechanical fastening and adhesive bonding. Compos Struct 75(1–4):192–198
5. Lambiase F, Paoletti A, Grossi V, Di Ilio A (2017) Friction assisted joining of aluminum and PVC sheets. J Manuf Process 29:221–231
6. Baldan A (2004) Adhesively-bonded joints in metallic alloys, polymers and composite materials: mechanical and environmental durability performance. J Mater Sci 39(15):4729–4797
7. Liu FC, Nakata K, Liao J, Hirota S, Fukui H (2014) Reducing bubbles in friction lap welded joint of magnesium alloy and polyamide. Sci Technol Weld Join 19(7):578–587
8. Katayama S, Kawahito Y (2008) Laser direct joining of metal and plastic. Scr Mater 59(12):1247–1250
9. Ageorges C, Ye L (2001) Resistance welding of metal/thermoplastic composite joints. J Thermoplast Compos 14(6):449–475
10. Amancio-Filho ST, Camillo APC, Bergmann L, dos Santos JF, Kury SE, Machado NGA (2011) Preliminary investigation of the microstructure and mechanical behaviour of 2024 aluminium alloy friction spot welds. Mater Trans 52(5):985–991
11. Balle F, Wagner G, Eifler D (2007) Ultrasonic spot welding of aluminum sheet/carbon fiber reinforced polymer-joints. Materialwiss Werkst 38(11):934–938
12. Jung KW, Kawahito Y, Takahashi M, Katayama S (2013) Laser direct joining of carbon fiber reinforced plastic to aluminum alloy. J Laser Appl 25(3)
13. (2000) Direct diode laser welds expand plastics joining. Prof Eng 13(23):48–48
14. Jung DJ, Cheon J, Na SJ (2016) Effect of surface pre-oxidation on laser assisted joining of acrylonitrile butadiene styrene (ABS) and zinc-coated steel. Mater Des 99:1–9
15. Nagatsuka K, Kitagawa D, Yamaoka H, Nakata K (2016) Friction lap joining of thermoplastic materials to carbon steel. ISIJ Int 56(7):1226–1231
16. Lambiase F, Genna S (2017) Laser-assisted direct joining of AISI304 stainless steel with polycarbonate sheets: thermal analysis, mechanical characterization, and bonds morphology. Opt Laser Technol 88:205–214
17. Cueff R, Baud G, Benmalek M, Besse JP, Butruille JR, Jacquet M (1997) X-ray photoelectron spectroscopy studies of plasma-modified PET surface and alumina/PET interface. Appl Surf Sci 115(3):292–298
18. Sandrin L, Sacher E (1998) X-ray photoelectron spectroscopy studies of the evaporated aluminum corona-treated polyethylene terephthalate interface. Appl Surf Sci 135(1–4):339–349

Ultrasound Enhanced Friction Stir Welding (USE-FSW) of Hybrid Aluminum/Steel Joints

Marco Thomä, Guntram Wagner, Benjamin Straß, Bernd Wolter, Sigrid Benfer and Wolfram Fürbeth

Abstract Ultrasound Enhanced Friction Stir Welding (USE-FSW) is an innovative hybrid method for solid-state joining. This process resulted in remarkably positive findings in the successful realization of hybrid aluminum/magnesium joints as well as in first investigations on the microstructure of aluminum/steel joints due to the parallel and synchronous transmission of power ultrasound into one of the joining partners. The present work investigates the impact of additional power ultrasound on the mechanical properties of AA6061/SAE1006-joints by comparing FSW and USE-FSW. Therefore, light microscopy, as well as scanning electron microscopy, was carried out for examining the microstructure of the joints. Furthermore, mechanical tests on the microhardness of the weld zone of the joints as well as tensile and first fatigue tests were examined. The investigations proved an influence of the power ultrasound by a change in the morphology of the nugget. It showed to be more cleared up and also contains a thinner intermetallic phase of $FeAl_3$ at the interface aluminum to steel. Furthermore, an

---

M. Thomä (✉) · G. Wagner
Institute of Materials Science and Engineering, Chemnitz University of Technology,
09107 Chemnitz, Germany
e-mail: marco.thomae@mb.tu-chemnitz.de

G. Wagner
e-mail: guntram.wagner@mb.tu-chemnitz.de

B. Straß · B. Wolter
Fraunhofer Institute for Nondestructive Testing IZFP, Campus E3 1,
66123 Saarbrücken, Germany
e-mail: benjamin.strass@izfp.fraunhofer.de

B. Wolter
e-mail: bernd.wolter@izfp.fraunhofer.de

S. Benfer · W. Fürbeth
DECHEMA-Forschungsinstitut, Theodor-Heuss-Allee 25,
60486 Frankfurt am Main, Germany
e-mail: benfer@dechema.de

W. Fürbeth
e-mail: fuerbeth@dechema.de

Y. Hovanski et al. (eds.), *Friction Stir Welding and Processing X*, The Minerals, Metals & Materials Series, https://doi.org/10.1007/978-3-030-05752-7_3

increase in the tensile strength of the joints of about 15% could be observed. First stepwise load increase tests resulted in slightly different stress levels for the estimated fatigue limit.

Keywords Friction stir welding · Ultrasound enhancement · Dissimilar metals
Fatigue

Motivation

The need for innovative and powerful joining techniques for joining high-performance materials or realizing material compounds of different materials is steadily increasing. Therefore, established conventional joining methods such as fusion welding or brazing and soldering do not fulfill the necessary requirements for joining materials of different groups or categories like dissimilar metals [1]. Thereby, the formation of brittle intermetallic phases (IM phases) due to a high heat input is the main problem. Facing this challenge new joining techniques have been developed. Thus, the pressure welding process of friction stir welding (FSW) showed great potential for realizing such dissimilar joints of metals as well as polymers or composites due to its characteristic reduced heat input [2]. Industrial interesting material combinations are aluminum/steel joints due to their big differences in physical properties. Considering their densities of 7.8 g/cm^3 for steel and 2.7 g/cm^3 for aluminum the substitution of steel through aluminum at relevant areas of components will result in a significant decrease in weight. This is of great interest for lightweight and ecological efforts in several industrial areas like the transportation sector. Using friction stir welding several scientific investigations have been made regarding the microstructure of Al/steel joints as well as their mechanical properties and the process parameters themselves [3–8]. The majority of the research work concentrates on the presence of intermetallic phases at the interface of aluminum/steel joints due to their high mostly negative impact on the resulting mechanical properties [4–6]. This shows that the comparatively low heat input of FSW reduces the amount of IM phases compared to, e.g., fusion welding, but cannot avoid them completely. Mostly, the intermetallics occur as a continuous layer over the whole thickness of the joints at the interface [7, 8], whereas different morphologies and thicknesses lead to different results for the mechanical properties. By studying the literature, it is obvious that a small intermetallic phase results in the highest tensile strengths [3, 6, 8]. So by optimizing the process parameters values of 86 and 80% of the tensile strength of the weaker base material, aluminum could be observed [6, 8]. For increasing the possible tensile strengths of Al/steel joints and making them more attractive for the industrial field's new approaches of hybrid joining techniques were developed like gas tungsten arc welding assisted FSW [9], laser-assisted FSW [10] or electrically assisted FSW [11]. All of these hybrid versions are based on an additional heating or preheating of the base materials. This leads to reduced welding forces as well as higher feed rates. Another promising approach is the additional transmission of power ultrasound in the friction stir welding process. For this, several transmission methods were developed [12–17]. The patented ultrasound enhanced friction stir welding (USE-FSW) introduces the power ultrasound in one of the sheet base materials and was carried out on aluminum/magnesium—as well as on aluminum/steel joints [18–20]. Thereby, the welding results were mostly positive regarding microstructure as well as mechanical properties. USE-FSW joints showed a better stirring of the nugget for Al/Mg joints as well as a reduction of continuous brittle intermetallic phase layers at the interface nugget/magnesium [21]. Furthermore, the fatigue limit could be increased by a factor of 3.5 using additional power ultrasound [22]. Regarding the corrosion characteristics of these dissimilar joints, the enhanced stirring led to a stronger corrosive attack [23]. For aluminum/steel USE-FSW showed a similar impact. The nugget appeared more cleared up and an IM phase of $FeAl_3$ developed at the interface of the base materials was reduced in its thickness. Here, the transmission of power ultrasound showed no significant influence on the resulting corrosion properties [20].

The present work investigates the influence of additional power ultrasound on the resulting aluminum/steel joints of AA6061 and SAE1005. For these joints, the microstructure was investigated by light and scanning electron microscopy (SEM). The quasi-static mechanical properties of the joints were investigated by micro hardness mappings and tensile tests. In addition to this, first, dynamic stepwise load increase tests were carried out as well.

Experimental Procedure

The deep-drawing steel SAE1006 (1.0338; cold rolled) and the aluminum wrought alloy AA6061 T6 (AlMg1SiCu; cold rolled) were used to realize the dissimilar joints. They were cut into a sheet geometry of 280 mm length, 100 mm width and 3 mm thickness. A four-axis universal machining center DMU80T from DMG Mori was used to realize the friction stir welding. It is additionally equipped with four load cells from Kistler to run the process force-controlled and uses a pneumatic clamping to fix the metal sheets in a butt joint configuration. For the aluminum/steel joints, the steel was always placed on the advancing side. The FSW tool had a diameter of 16 mm for the shoulder, a 2.8 mm probe length with a metric thread of M6 and it consisted of a tungsten-based alloy with 1% lanthanum oxides (Fig. 1b). The design of experiment method of Taguchi was used to find parameters maximizing the tensile strength of the joints [24]. Therefore, the rotational speed, the feed rate, the tilt angle and the lateral offset of the probe surface to the faying surface were considered. The final parameters were a rotational speed of 1250 rpm, a feed of 30 mm/min, a tilt angle of 2°, a welding force of 2.5 kN in vertical direction (Z) and a lateral offset of the center of the probe to the faying surface of the steel of 3 mm. A scheme of the hybrid method of USE-FSW is shown in Fig. 1.

An ultrasonic roll seam module of Schunk Sonosystems was installed additionally on the universal machining center. It runs synchronously and parallel to the FSW tool within the process and introduces the power ultrasound with a resonance frequency

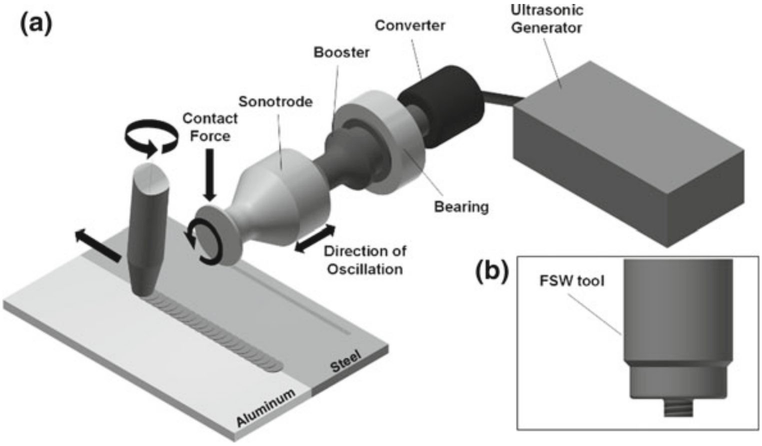

Fig. 1 **a** USE-FSE setup and **b** used FSW-Tool

of 20 kHz, a generator maximum power of 3000 W and an amplitude of 38 μm. The advancing side of the joints was always chosen for the transmission of the ultrasound. The tensile tests were performed on a 20 kN Zwick Roell tensile testing machine at room temperature. The specimen geometry was shape E of DIN 50125 and three specimens of each joint were tested. For the determination of the estimated fatigue, limit stepwise load increase tests were performed on a servohydraulic testing machine MTS Landmark 100 kN. The fatigue tests ran force controlled at room temperature with a stress ratio of $R = 0.1$, a frequency of 5 Hz and a number of 10,000 cycles for each step before increasing the load by 2.5 MPa per step. The initial stress level was estimated from the respective stress–strain curves. The elongation of the specimens was determined using a clip gage. The geometry of the specimens was designed following DIN EN 3987. The materials measured for the estimated fatigue lifetime of 2×10^6 cycles was the plastic strain. Whenever no explicit reaction for the plastic strain curve could be detected, a third-degree polynomial was used to fit the values to a mathematical function. Afterward, the first derivative was calculated and used to place tangents at its minimum (linear rise) and maximum (exponential rise). The intersection point of these two tangents was presumed as the estimated fatigue limit [25].

Results and Discussion

Light microscopic investigations were used for a first comparison of the microstructure for FSW- and USE-FSW joints. Figure 2 depicts the cross section of the AA6061/SAE1006-FSW joint.

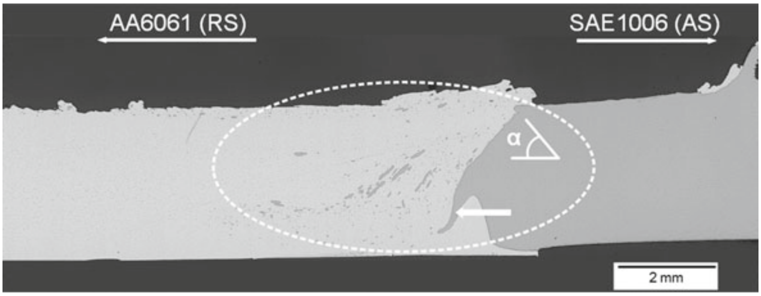

Fig. 2 Cross section image of an AA6061/SAE1006-FSW joint

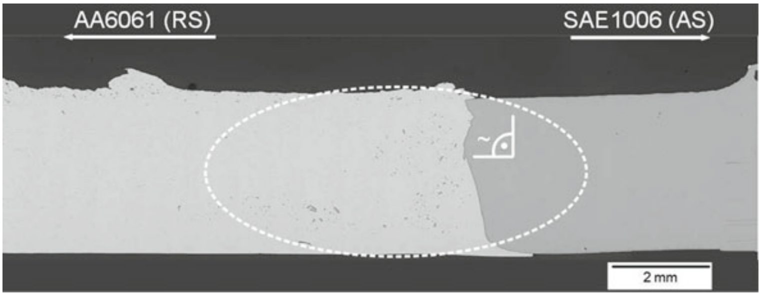

Fig. 3 Cross section image of an AA6061/SAE1006-USE-FSW joint

The image shows a complete bonding over the whole interface without any defects. The upper part of the interface runs under an angle α of about 50° against the horizontal. It is assumed that the characteristic higher heat input in the upper region leads to an enhanced material softening resulting in the depicted morphology. Moreover, a clearly visible about 1 mm long hook (white arrow) from the steel base material has developed at the center of the interface aluminum/steel, which assures a mechanical interlocking. Concentrating on the nugget of the joint particles in different sizes and with different morphologies is present which are assumed to consist of the base material SAE1006. Figure 3 shows the cross section image of an ultrasound-enhanced joint.

Also for the USE-FSW joint, a complete through-weld was achieved without visible failures. The interface appears more uniform than for the FSW joint with an almost perpendicular shape. So, the behavior differs from the FSW joint. Regarding the nugget, zone particles are also present, but this time smaller and less. So the USE-FSW joint in general is more cleared up. This microstructural differences caused by the additional transmission of power ultrasound in the welding zone corresponds with the findings of Thomä et al. [20]. Taking a closer look on the interface of the aluminum/steel joints, scanning electron microscopy was carried out. A comparison of both joints is depicted in Fig. 4.

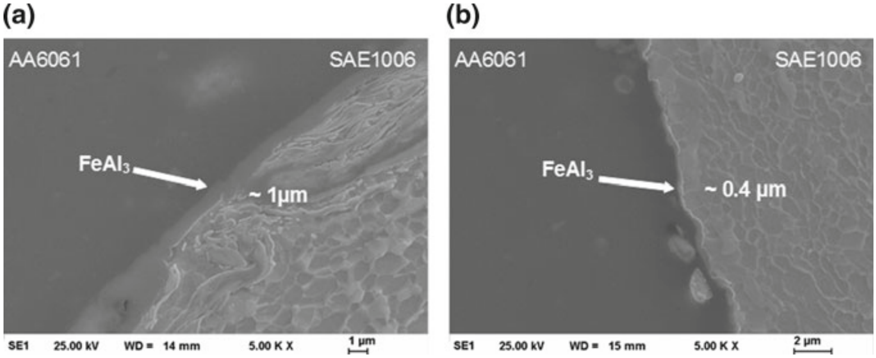

Fig. 4 Scanning electron microscopy image of **a** FSW joint and **b** USE-FSW joint

Image (a) shows the presence of a continuous intermetallic phase layer between aluminum and steel which was typically expected and is in accordance with the literature [3, 6, 8, 20]. Various EDX spot measurements lead to the assumption that the IM phase layer with a thickness of about 1 µm consists of the aluminum-rich $FeAl_3$. This finding is also in good accordance with earlier research work and is assumed to be a dominating factor for the resulting mechanical properties of the dissimilar joints. In comparison to FSW, the ultrasound enhancement (Fig. 4b) also shows a continuous intermetallic layer, also assumed to consist of $FeAl_3$. But this time it is considerably thinner reaching only about 40% of the thickness of FSW. Furthermore, the particles in the nugget found in light microscopic investigations were determined to consist of the steel base materials SAE1006. To get information about the quasi-static behavior of the Al/steel joints with and without power, ultrasound tensile tests were carried out leading to the diagram for the comparison of tensile strengths depicted in Fig. 5.

The diagram also contains the tensile strengths for the two base materials SAE1006 with 294 MPa as well as AA6061 with 203 MPa. The FSW joint reached 122 MPa which correspondents to about 60% of the aluminum base material. Additional power ultrasound increases the tensile strength up to 139 MPa, leading to an improvement of about 15%. Compared to the findings in the literature, the achieved strengths are slightly lower, whereas it is important to look after the specific alloys which were joined in the concerned investigations. Beside quasi-static tensile tests first dynamic examinations have been carried out through first stepwise load increase tests on the different joints. Figure 6 shows the behavior of the AA6061/SAE1006-FSW joint under cyclic loading.

The stepwise load increase tests started each at a stress level of 10 MPa due to the brittle failure character of the joints. The FSW joint reached a stress level of about 50 MPa where its fatigue limit is assumed to be regarding the reaction behavior of the plastic mean strain. This correspondent to about 41% of the tensile strength of the FSW joint. Regarding the literature Straß carried out similar investigations on aluminum/magnesium joints, whereas his FSW joint reached a lower assumed fatigue limit of 22.5 MPa [21]. For the USE-FSW joints of Straß a fatigue limit of

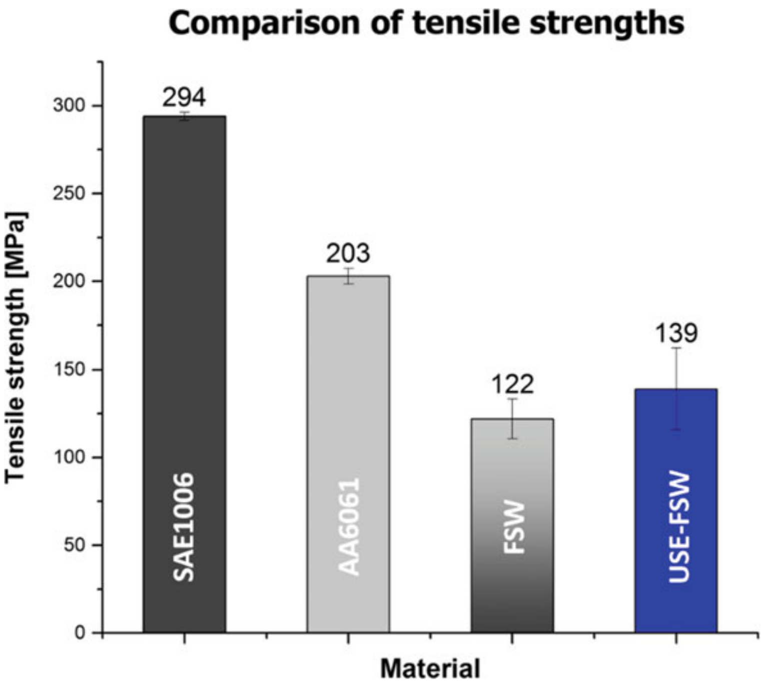

Fig. 5 Comparison of tensile strengths of base materials, FSW-and USE-FSW joints

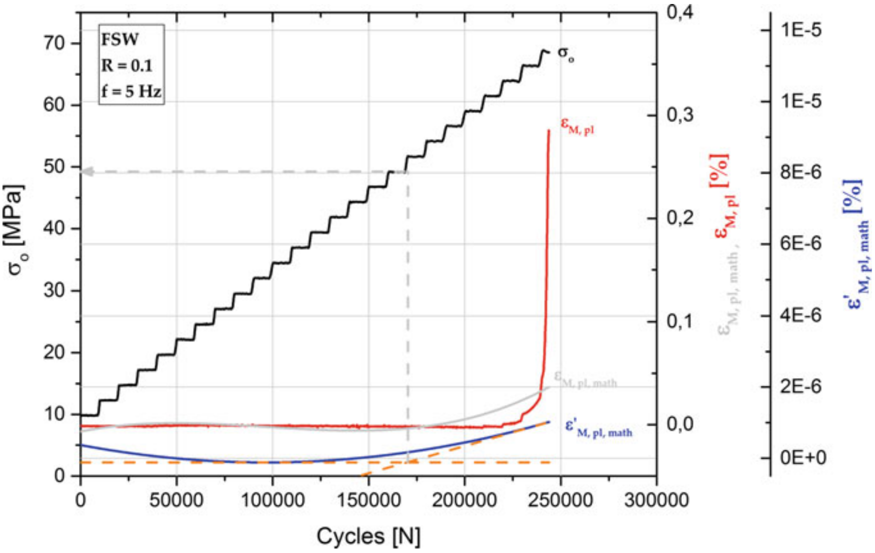

Fig. 6 Stepwise load increase test of a FSW joint

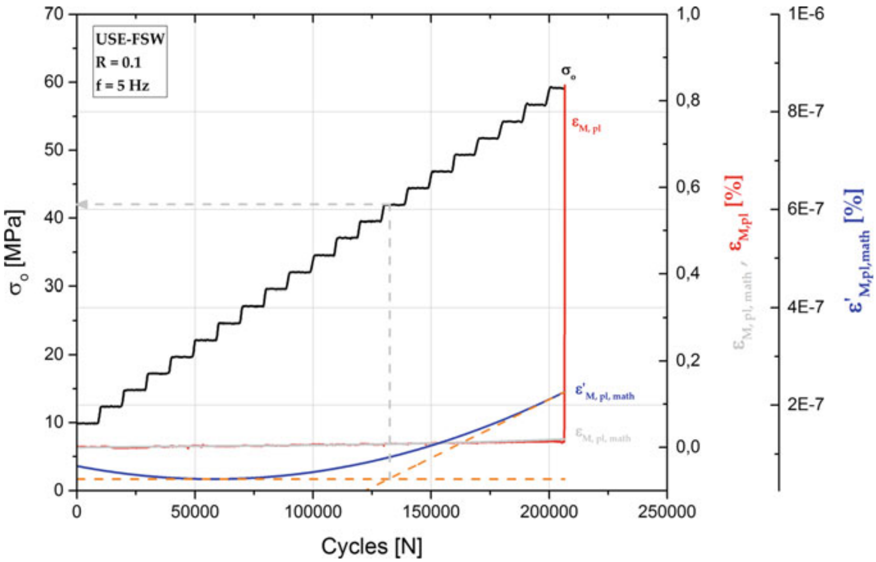

Fig. 7 Stepwise load increase test of an USE-FSW joint

25 MPa was assumed. Figure 7 shows the stress cycles diagram for the USE-FSW joints of AA6061/SAE1006.

The estimated fatigue limit is detected to be at around 42.5 MPa, which is 7.5 MPa lower than the value for the FSW. This is in contrast to the findings of the quasi-static tensile tests of AA6061/SAE1006 where USE-FSW reached higher strengths in comparison to the investigations of Straß, who found a higher fatigue limit for his USE-FSW joints. The reason for this could be on one hand that the joints have a very brittle failure characteristic resulting in a bigger scattering of the measurements and on the other hand that this method gives an assumption about the fatigue limit, which was in good accordance to previous investigations in the literature. Only monotonic load tests can determine the real fatigue limit.

Summary and Outlook

The present work investigated the influence of additional power ultrasound during friction stir welding on the microstructure as well as on the mechanical properties of dissimilar AA6061/SAE1006 joints. The optical microscopic investigations showed defect free welds for both joint types. Additionally, differences in the developing microstructure were obvious regarding the nugget, which appeared more cleared up for the USE-FSW joint. The power ultrasound enhanced joint contained less and smaller particles of the steel base material SAE1006. Furthermore, a different morphology of the interface aluminum/steel was found in the form of a nearly perpendicular form for USE-FSW compared to an angle of about 50° against the horizontal for the FSW. During SEM examinations, a continuous intermetallic layer probably consisting of the aluminum-rich $FeAl_3$ could be detected for both joint types, whereas the thickness was reduced by about 40% for the ultrasound enhanced joint. The tensile tests showed that the realized FSW joint reached about 60% of the strength of the aluminum base material, whereas the addition of power ultrasound led to an improvement in the tensile strength of about 15% for the mean values. Regarding the behavior of the joints under cyclic loading through stepwise load increase tests slightly different assuming fatigue limits were achieved, where the FSW joint reached higher values of 50 MPa compared to 42.5 MPa for USE-FSW. This finding will be investigated by further cyclic monotonic load tests, to examine the fatigue limits of both joint types and verify their accordance with the assumed values.

Acknowledgements We would like to thank the German Research Foundation (DFG) for the support of the present work as a part of the Priority Program 1640 “Joining by Plastic Deformation”.

References

1. Givi M, Asadi P (2014) Advances in friction-stir welding and processing. Elsevier Science & Technology, Cambridge
2. Mishra RS, De PS, Kumar N (2014) Friction stir welding and processing. Springer International Publishing, Cham
3. Tanaka T, Morishige T, Hirata T (2009) Scr Mater 61:756–759
4. Uzun H, Dalle Donne C, Argagnotto A, Ghidini T, Gambaro C (2005) Mater Des 26:41–46
5. Shen Z, Chen Y, Haghshenas M, Gerlich AP (2015) Eng Sci Technol Int J 18:270–277
6. Watanabe T, Takayama H, Yanagisawa A (2006) J Mater Process Technol 178:342–349
7. Pourali M, Abdollah-zadeh A, Saeid T, Kargar F (2017) J Alloy Compd 715:1–8
8. Coelho RS, Kostka A, dos Santos JF, Kaysser-Pyzalla A (2012) Mater Sci Eng A 556:175–183
9. Bang H, Bang H, Jeon G, Oh I, Ro C (2012) Mater Des 37:48–55
10. Merklein M, Giera A (2008) Int J Mater Form 1:1299–1302
11. Ferrando WA (2008) The concept of electrically assisted friction stir welding (EAFSW) and application to the processing of various metals. Defense Technical Information Center, Fort Belvoir, VA
12. Lai R, He D, Liu L, Ye S, Yang K (2014) Int J Adv Manuf Technol 73:321–327
13. Liu XC, Wu CS (2015) J Mater Process Technol 225:32–44
14. Rostamiyan Y, Seidanloo A, Sohrabpoor H, Teimouri R (2015) Arch Civ Mech Eng 15:335–346
15. Shi L, Wu CS, Liu XC (2015) J Mater Process Technol 222:91–102
16. Park K (2009) Development and analysis of ultrasonic assisted friction stir welding process. PhD thesis, The University of Michigan
17. Amini S, Amiri MR (2014) Int J Adv Manuf Technol 73:127–135
18. Strass B, Wagner G, Conrad C, Wolter B, Benfer S, Fürbeth W (2014) Adv Mater Res 521–535
19. Klag O (2013) Mikrostruktur, mechanische Eigenschaften und Korrosionsverhalten rührreibgeschweißter AZ91, AZ91- und AZ91, AlMg3Mn-Verbunde, vol 31. Techn. Univ. Kaiserslautern, Kaiserslautern
20. Thomä M, Wagner G, Straß B, Wolter B, Benfer S, Fürbeth W (2018) J Mater Sci Technol 34:163–172
21. Straß B (2015) Ultraschallunterstütztes Rührreibschweißen von Al/Mg-Verbunden. Dissertation, Technische Universität Kaiserslautern

22. Strass B, Wagner G, Eifler D (2014) MSF 783–786:1814–1819
23. Benfer S, Straß B, Wagner G, Fürbeth W (2016) Surf Interface Anal 48:843–852
24. Kleppmann W, Versuchsplanung (2016) Produkte und Prozesse optimieren, 9th edn. Hanser, München, Wien
25. Ebel-Wolf B, Walther F, Eifler D (2008) Mater Sci Eng A 486:634–640

Effect of Stress Concentration on Strength and Fracture Behavior of Dissimilar Metal Joints

Tianhao Wang and Rajiv Mishra

Abstract Dissimilar metal joints tend to fracture along the welded interface during tensile testing, particularly in butt joint configuration. A common explanation relates formation of brittle intermetallic compound layer at dissimilar weld interface to crack initiation and propagation. This typically leads to lower strength and ductility of the dissimilar material joint. However, another critical aspect determining strength and fracture behavior of dissimilar material joints is the existence of stress concentration at the welded interface during mechanical loading. Mismatch of elastic modulus of dissimilar materials creates stress concentration at the initial stage of mechanical loading, which facilitated crack initiation at the welded interface. In this overview, factors leading to stress concentration and their impact on dissimilar joint strength and fracture behavior have been highlighted.

Keywords Dissimilar joining · Fracture · Stress concentration

Introduction

Joining of the dissimilar metals can increase the design flexibility in industries [1]. Dissimilar metals can be divided into two main categories: miscible or immiscible systems. For miscible system, brittle intermetallic compound (IMC) layer generally form, which led to crack initiation and propagation during deformation-based testing. Therefore, solid-state joining methods have been applied for miscible systems, which require less heat input and resultant thin IMC layer. For instance, ultrasonic welding [2], roll bonding [3], diffusion welding [4], friction welding [5], and friction stir welding (FSW) [6, 7] have been applied for Al/steel joining. A widely accepted conclusion is that thicker IMC layer leads to lower joint strength [8]. While for

---

T. Wang · R. Mishra (✉)
Department of Materials Science and Engineering, Center for Friction Stir Processing
and Advanced Materials and Manufacturing Processes Institute, University of North Texas,
Denton, TX 76207, USA
e-mail: Rajiv.Mishra@unt.edu

Y. Hovanski et al. (eds.), *Friction Stir Welding and Processing X*, The Minerals,
Metals & Materials Series, https://doi.org/10.1007/978-3-030-05752-7_4

immiscible system, weak interactions resulted in poor joints. Immiscible combination of magnesium alloy and steel was bonded via either high-power density welding process such as laser welding [9] or ultrasonic spot welding with zinc interlayer [10]. In addition, FSW has proved to be an effective method for immiscible combination of magnesium/steel [11] and copper/steel [12, 13].

Result shows that joints generally fracture at the weld interface even when dissimilar materials are immiscible and no IMC layer existed at welded interface. In such cases, stress concentration is the main factor resulting in interfacial failure [12]. In this analysis, three combinations: copper/steel, magnesium alloy/steel, and aluminum alloy/steel are summarized to separate the effect of IMC and stress concentration on joint strength and fracture behavior.

Experimental Procedures

110-O copper, AZ31 magnesium alloy, and AA2024-T4 aluminum alloy sheets (thickness ~ 6.0 mm) and 316 stainless steel (316 SS) sheet (thickness ~ 5.75 mm) were friction stir butt welded using a W-Re tool. During FSW, steel sheet was placed on the advancing side (AS), while Cu (Mg, Al) sheet was positioned on the retreating side (RS) (Fig. 1a). The tool offset was positioned from the Cu (Mg, Al)/steel interface to favor the Cu (Mg, Al) side by 2.2 or 2.5 mm. The W-Re tool had a threaded conical pin of pin length, pin diameter at root and tip, and shoulder diameter of 4.0 mm, 7.6 mm, 5.0 mm, and 16.0 mm, respectively. And, image of the tool was shown in a previous study [14]. Standard tensile testing (ASTME8-04) and mini tensile testing were conducted to evaluate Cu (Mg, Al) alloy/steel joint strength and weld stir zone (SZ) strength, respectively (Fig. 1b). The width, thickness, and gage length of the mini tensile samples were 1.0, 1.0, and 3.0 mm, respectively. The chemical compositions of all the base materials are listed in Table 1. Welding parameters for joints 1–4 including rotation rate (R), traverse speed (T), plunge depth in steel (P_d), tool tilt angle, and tool offset are listed in Table 2. Scanning electron microscopy

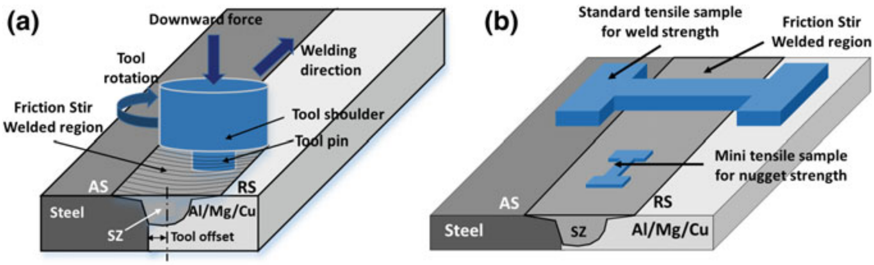

Fig. 1 Schematic of **a** friction stir butt welding of Cu (Mg, Al) and steel sheets and **b** fabrication of standard and mini tensile samples

Table 1 Chemical composition of base materials

Base materials	Elements (wt%)										
	Al	Zn	Cu	Mg	C	Mn	Si	Cr	Ni	Mo	Fe
110-Cu	–	–	Bal.	–	–	–	–	–	–	–	–
AZ31	2.83	0.80	0.002	Bal.	–	–	–	–	–	–	–
AA2024	Bal.	–	4.4	1.5	–	0.6	–	–	–	–	–
SS316	–	–	–	–	0.08	2.0	0.03	17.0	12.0	2.50	Bal.

Table 2 Welding parameters for joints 1–4

Joint number	Composition	R (RPM)	T (in./min)	P_d (mm)	Tilt angle (°)	Tool offset (mm)
1	110 Copper/SS316	500	1.0	4.75	2.5	2.5
2	AZ31/SS316	600	1.0	4.75	2.5	2.5
3	AA2024-T4/SS316	400	2.0	4.75	2.5	2.5
4	AA2024-T4/SS316	400	2.0	4.75	2.5	2.2

(SEM) was used to investigate the microstructure of cross section of welded joints and welded interface.

Results and Discussion

Mechanical properties including elastic modulus, yield strength, and ultimate tensile strength of base materials are plotted in Fig. 2. As compared with SS316, 110 Copper, AZ31 magnesium alloy, and AA2024-T4 aluminum alloy have lower modulus, yield strength, and ultimate tensile strength. Therefore, strain concentrated on 110 copper, AZ31, and AA2024-T4 part during testing on welded 110 copper/SS316, AZ31/SS316, and AA2024-T4/SS316.

Cross sections of butt joints 1–4 are displayed in Fig. 3a–d. There is no IMC layer at 110 copper/SS316 (joint 1) interface due to immiscibility between Cu and Fe (enlarged picture in Fig. 3a). For AZ31/SS316 (joint 2), there is a very thin IMC layer at the interface due to the fact that AZ31 magnesium alloy contains 3 wt% Al in the matrix which can diffuse to weld interface and react with Fe forming Al–Fe IMCs [11]. For AA2024/SS316, IMC layer thicknesses are ~0.2 and ~0.6 μm for joints 3 and 4, respectively, at AA2024-T4/SS316 interface. Reduced tool offset in Al and resultant excess deformational heat on steel results in increase of IMC layer thickness. In addition, the amount of steel fragments increase with decreasing tool offset in Al (Fig. 3c, d).

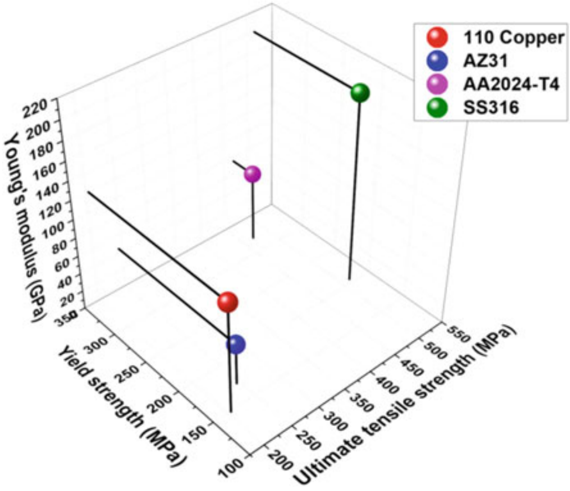

Fig. 2 Mechanical properties of base 110-O copper, AZ31 magnesium alloy, AA2024-T4 aluminum alloy, and 316 stainless steel

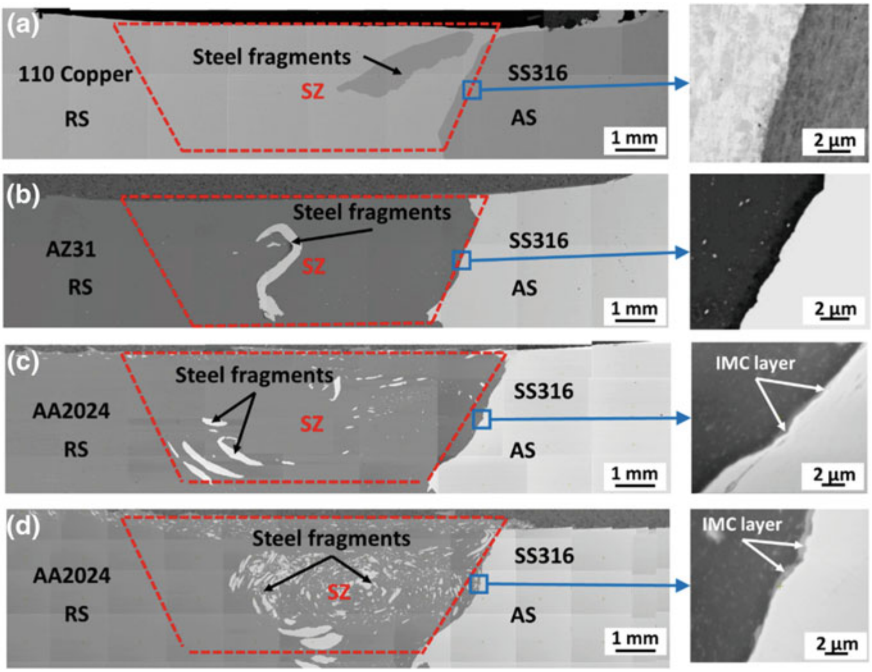

Fig. 3 Cross section of **a** joint 1 (110 copper/SS316), **b** joint 2 (AZ31/SS316), **c** joint 3 (AA2024/SS316), and **d** joint 4 (AA2024/SS316)

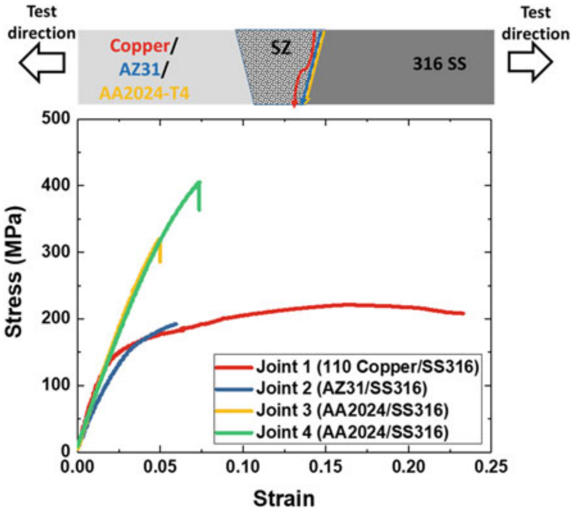

Fig. 4 Stress–strain curves of welded 110-copper/SS316, AZ31/SS316, and AA2024-T4/SS316 specimens

Tensile testing of butt-welded joints 1–4 shows that joint 1 fractured along the copper next to weld interface and joints 2–4 fractured along the weld interface. As shown in Fig. 4, joint 1 shows ductility due to no IMC existing at weld interface. Additionally, joints 2–4 show limited ductility due to IMC layer at the weld interface. As compared with joint 3, joint 4 has a thicker IMC and a higher joint strength. This is contrary to a well-accepted conclusion that higher IMC layer thickness leads to lower joint strength. The increase in joint strength of joint 4 results from the strengthened SZ, which was due to the existence of steel fragments [14]. Yield strength and ultimate tensile strength of base materials, joints 1–4 and SZ of joints 1–4 are plotted in Fig. 5. It displays that the joint strength is influenced by strength of SZ. Since SZ of joint 4 has higher strength than SZ of joint 3, the crack initiation in joint 4 was delayed due to lower stress concentration at the interface. It is important to consider the elastic modulus mismatch. The SZ with dispersed steel fragments (joint 4) make the transition smoother and result in better overall distribution of plastic strain. This finding can guide further development of dissimilar material joining.

Conclusions

(1) Joint strength for dissimilar materials was determined not only by IMC layer thickness but also by strength of the SZ when the joints fractured along the welded interface.

(2) Stress concentration at the weld interface initiated the crack, and joint strength increased with strength enhancement of the SZ.

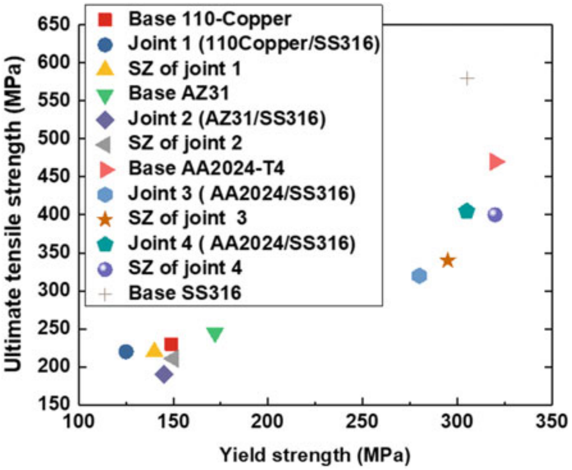

Fig. 5 Comparison of yield strength and ultimate tensile strength of base materials and dissimilar joints

(3) SZ strength was enhanced via dispersal of steel fragments, which reduced mechanical property mismatch between two sides of the welded interface.

Acknowledgements This work was supported under the NSF-IUCRC grant for Friction Stir Processing (NSF-IIP 1157754). The additional support of Boeing, General Motors, Pacific Northwest National Laboratory, Army Research Laboratory and Korea Aerospace Research Institute for the UNT CFSP site is acknowledged. This report was prepared as an account of work sponsored by an agency of the US Government. The views and opinions of the authors expressed herein do not necessarily state or reflect those of the US Government or any agency thereof. We also acknowledge the UNT Materials Research Faculty (MRF).

References

1. Kumar N, Yuan W, Mishra RS (2015) Friction stir welding of dissimilar alloys and materials. Butterworth-Heinemann
2. Tsujino J, Hidai K, Hasegawa A, Kanai R, Matsuura H, Matsushima K, Ueoka T (2002) Ultrasonic butt welding of aluminum, aluminum alloy and stainless steel plate specimens. Ultrasonics 40(1–8):371–374
3. Nezhad MSA, Ardakani AH (2009) A study of joint quality of aluminum and low carbon steel strips by warm rolling. Mater Des 30(4):1103–1109
4. Peng L, Yajiang L, Juan W, Jishi G (2003) Vacuum brazing technology and microstructure near the interface of Al/18-8 stainless steel. Mater Res Bull 38(9–10):1493–1499
5. Taban E, Gould JE, Lippold JC (2010) Dissimilar friction welding of 6061-T6 aluminum and AISI 1018 steel: properties and microstructural characterization. Mater Des 31(5):2305–2311
6. Uzun H, Dalle Donne C, Argagnotto A, Ghidini T, Gambaro C (2005) Friction stir welding of dissimilar Al 6013-T4 to X5CrNi18-10 stainless steel. Mater Des 26(1):41–46
7. Coelho RS, Kostka A, Dos Santos J, Pyzalla AR (2008) EBSD technique visualization of material flow in aluminum to steel friction-stir dissimilar welding. Adv Eng Mater 10(12):1127–1133

8. Tanaka T, Morishige T, Hirata T (2009) Comprehensive analysis of joint strength for dissimilar friction stir welds of mild steel to aluminum alloys. Scr Mater 61:756–759
9. Liu LM, Zhao X (2008) Study on the weld joint of Mg alloy and steel by laser-GTA hybrid welding. Mater Charact 59(9):1279–1284
10. Patel VK, Bhole SD, Chen DL (2013) Formation of zinc interlayer texture during dissimilar ultrasonic spot welding of magnesium and high strength low alloy steel. Mater Des 45:236–240
11. Kasai H, Morisada Y, Fujii H (2015) Dissimilar FSW of immiscible materials: steel/magnesium. Mater Sci Eng A 624:250–255
12. Wang T, Shukla S, Nene SS, Frank M, Wheeler RW, Mishra RS (2018) Towards obtaining sound butt joint between metallurgically immiscible pure Cu and stainless steel through friction stir welding. Metall Mater Trans A 49(7):2578–2582
13. Sahlot P, Nene SS, Frank M, Mishra RS, Arora A (2018) Towards attaining dissimilar lap joint of CuCrZr alloy and 316L stainless steel using friction stir welding. Sci Technol Weld Join 23(8):715–720
14. Wang T, Mageshwari K, Liu K, Mishra RS (2018) Friction stir butt welding of strain-hardened aluminum alloy with high strength steel. Mater Sci Eng A

Part II
High Melting Temperature Materials

Friction Stir Welding of Fibre-Reinforced Titanium Composites for Aerospace Structures

Jonathan Martin, Craig Blacker, Kathryn Beamish and Advenit Makaya

Abstract Composite materials consisting of a titanium alloy reinforced with continuous silicon carbide fibres, called TiSiC, are currently being investigated to enhance performance for applications where titanium alloys are used. Conventional fusion welding techniques create difficulties due to the detrimental impact of high temperature on the fibre/metal interfaces. This study describes the application of stationary shoulder friction stir welding (SS-FSW) technique to join TISIC components to monolithic titanium. Microscopic investigations had shown flaw-free welding, until the SSFSW tool started to mechanically interact with the SiC fibres. When subjected to tensile testing, the weld properties were superior to the parent monolithic titanium. The comprehensive investigation of fracture toughness, residual stress and fatigue properties of the weld components are presented and potential advantages discussed.

Keywords Stationary shoulder · Titanium · TiSiC

J. Martin (✉)
TWI Technology Centre (Yorkshire), Wallis Way, Catcliffe, Rotherham S60 5TZ, UK
e-mail: jonathan.martin@twi.co.uk

C. Blacker
TISICs Ltd, 22 Invincible Road, Farnborough GU14 7QU, UK
e-mail: cjblacker@tisics.co.uk

K. Beamish
TWI Ltd, Granta Park, Great Abington, Cambridge CB21 6AL, UK
e-mail: kathryn.beamish@twi.co.uk

A. Makaya
European Space Agency, 2201 AZ Noordwijk, Netherlands
e-mail: advenit.makaya@esa.int

Y. Hovanski et al. (eds.), *Friction Stir Welding and Processing X*, The Minerals, Metals & Materials Series, https://doi.org/10.1007/978-3-030-05752-7_5

Background

Titanium composite materials consisting of a titanium alloy reinforced with continuous silicon carbide (SiC) fibres, called ‘TiSiC’, are currently being investigated to enhance performance in applications where conventional titanium alloys are currently used. The silicon carbide fibres are lighter, stronger and stiffer than the metallic matrix, thereby offering the possibility of significant weight savings when manufacturing aerospace components such as xenon propellant tanks. TiSiC meets or exceeds the performance of many high-strength titanium alloys, is equally corrosion resistant, with superior fatigue properties and crack arrest capabilities. Components can be 30 to 70% lighter than monolithic titanium versions based on how much the design is tailored for the composite material [1].

Joining of the composite to manufacture components is challenging. Conventional fusion welding techniques create difficulties due to the detrimental impact of elevated temperatures on the fibre/metal interfaces. Decomposition of the SiC allows for a reaction of titanium with silicon and carbon, resulting in the formation of brittle phases which significantly reduce joint strength.

Hot isostatic press (HIP) diffusion bonding techniques have been used successfully in research demonstrator components [2]; tooling cost, complexities and size limits have hindered further practical application of the TiSiC material to date. As such, potentially lower cost alternative solid-state joining techniques such as friction stir welding (FSW) are being investigated.

The TiSiC used in this study consists of layers of 140-micron diameter SM3256 silicon carbide (SiC) fibres with a 14-micron tungsten core supplied by TISICS Ltd. The fibres are arranged in layers embedded in a matrix of titanium alloy Fig. 1. The fibre orientation provides directional improvement in mechanical strength. This material is also commonly referred to in other literature as TMC or Ti-MMC.

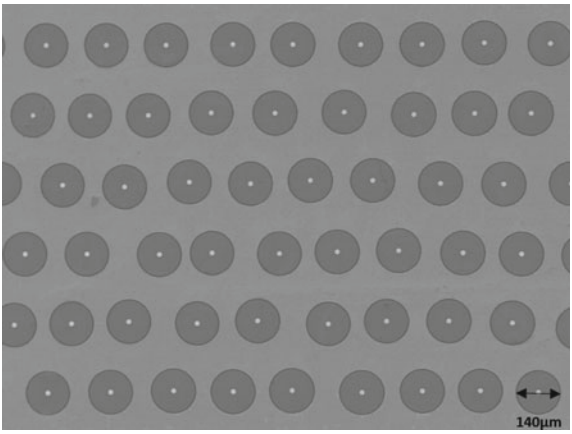

Fig. 1 Layers for SiC fibres in a titanium alloy matrix: TiSiC composite [3]

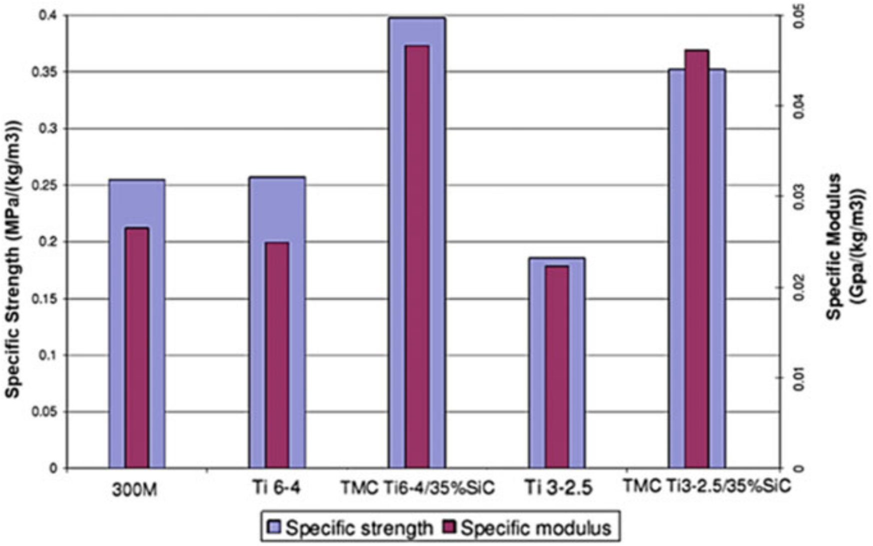

Fig. 2 Comparison of typical specific properties for monolithic and uniaxial TiSiC (i.e. TMC) materials [4]

The specific strength and specific modulus of Ti-6Al-4 V and Ti-3Al-2.5 V with and without fibres are compared in Fig. 2. The specific properties of TiSiC are at least 50% higher than monolithic material.

This paper describes the feasibility of using FSW to join TiSiC to a monolithic titanium alloy without damaging the reinforcing fibres and resultant weld properties.

Friction Stir Welding

Friction stir welding was invented by TWI in 1991 [5]. It has been demonstrated that FSW can join monolithic titanium alloys with very good mechanical performance across the weld and very narrow heat-affected zones. This offers the potential for narrow mass efficient weld regions for attaching TiSiC to monolithic design features and for closure of composite pressure vessels and tanks. Due to the lower thermal conductivity of titanium, the use of conventional FSW tools is problematic, due to uneven heat generation leading to component surface overheating. TWI developed a new technique in 2005 [6] called stationary shoulder FSW (SS-FSW). The near vertical weld nugget interface offers the potential to present a consistent thermal profile to the fibres in the TiSiC material being joined.

Initial FSW Trials

The initial work undertaken aimed to establish the effect of the SS-FSW technique on the TiSiC fibres and the impact of fibre orientation. Two TiSiC plates (3 mm thick) with both TiSiC and monolithic regions were fabricated, consisting of eight layers of SiC fibres in a Ti-3Al-2.5 V matrix. In one panel, the fibres were orientated parallel to the welding direction (Panel 'W5') and the other perpendicular (Panel 'W6'), as shown in Fig. 3.

At the start of the weld, the outside diameter of the probe was positioned 7 mm away from the fibres and then traversed through the plate, such that it was 7 mm into the fibres at the weld end. The advancing side of the weld was placed on the TiSiC side of the panel.

Macrograph samples and tensile specimens were extracted from each panel and assessed every 1–2 mm in tool position change, relative to the fibres, throughout the weld length. The results of the visual assessment are shown in Fig. 4 and the tensile results are shown graphically in Fig. 5.

The tensile specimens where the FSW probe was +7 to +1 mm away from the fibres failed within the TiSiC region. This was not unexpected, since tensile strength perpendicular to SiC fibres has previously been shown to be weaker than equivalent monolithic material.

The results from Panel W6 are shown in Fig. 6. The tensile specimens where the FSW probe was +7 to −1 mm away from the fibres failed within the parent monolithic plate. This conforms to the expected failure position since the TiSiC panels are longitudinally reinforced, and therefore stronger than the monolithic material. This also demonstrated that the weld region was also stronger than the monolithic material.

In both trials, the FSW probe exhibited severe tool wear, due to the abrasive action of the SiC fibres as it entered and welded in the TiSiC region. From this initial investigation, it was decided that subsequent trials would focus on TiSiC laid perpendicular to the weld, with the FSW tool probe traversing at a position +2 mm from the SiC fibre ends.

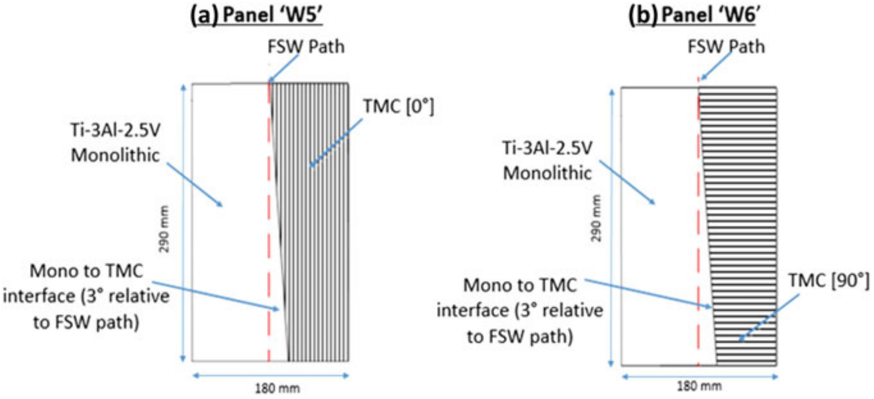

Fig. 3 Fibre orientation in the two test panels

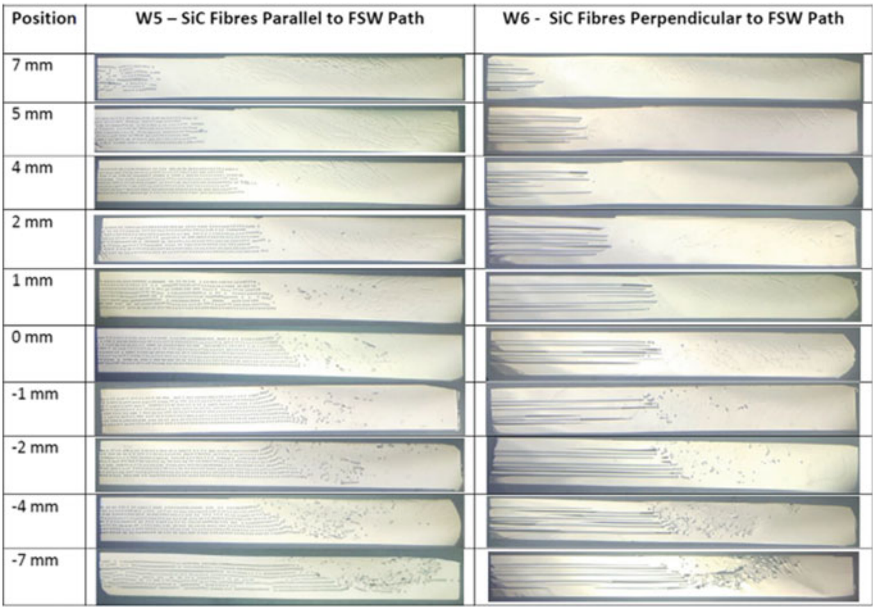

Fig. 4 Macrographs taken from Panels W5 and W6

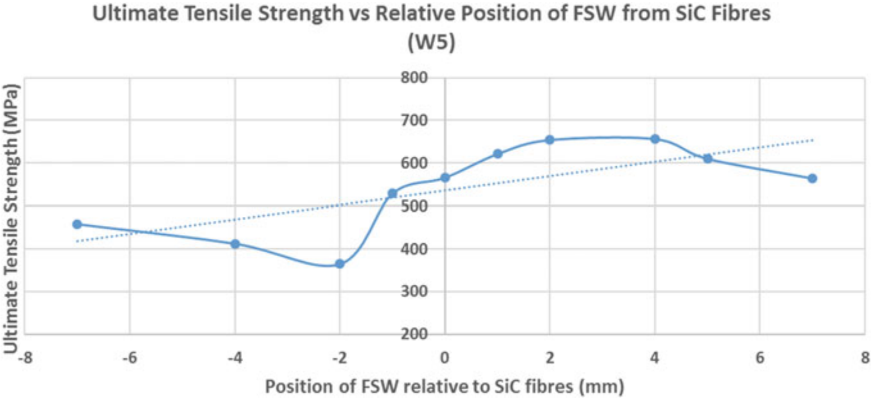

Fig. 5 UTS plotted as a function of distance of the FSW probe from the fibres

Manufacture of Test Panel

The configuration of the test panel (butt weld) is shown in Fig. 7. This consisted of monolithic Ti-3Al-2.5 V plates for the run on and run off tabs and the plate on the weld retreating side. To ensure a consistent fibre end termination position, a TiSiC panel was initially fabricated and then wire cut to exact dimensions, incorporated and subsequently hipped into a monolithic frame producing a hybrid panel with a 7 mm wide Ti-3Al-2.5 V margin to abutt to the monolithic plate on the weld retreating side.

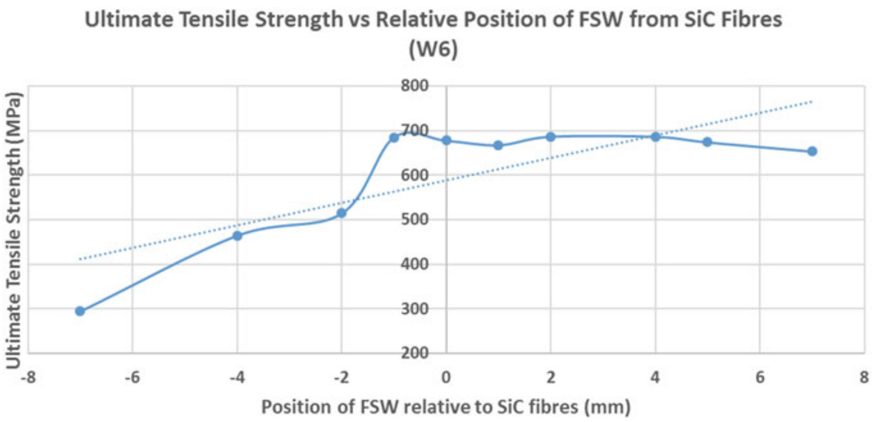

Fig. 6 UTS plotted as a function of distance of the FSW probe from the fibres

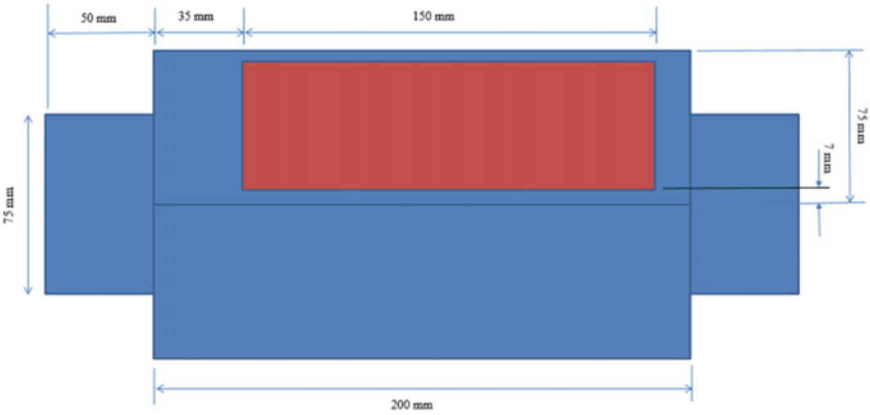

Fig. 7 Schematic of the test panels. Red zone indicating TiSiC material and blue monolithic Ti-3Al-2.*5 V*

As the FSW probe diameter was 10 mm, this would place its edge 2 mm from the fibre ends when traversing the tool in the joint line of the abutting plates.

Three plates were fabricated for assessment using a tool probe rotation speed of 900 rpm and a welding speed of 100 mm/min.

Plate Assessment

The following section presents properties of the friction stir welded specimens. All test specimens were extracted from the welded plates via wire EDM.

Tensile Strength

Tensile tests were performed on three specimens according to ASTM standard E8-15a (WMTR W6 ‘dog bone’ specimen design). The specimens were each extracted from the three different weld plates and had a nominal gauge width of 6.0 mm and a 25.0 mm gauge length. Strains were measured using a dual averaging extensometer and an optical strain measuring device for measurement for the total duration of the test. The testing was carried out in strain rate control at an initial rate of 0.0025 strain/min, beyond yield, a second rate of 0.050 strain/min was adopted and the extensometer removed.

Table 1 shows a summary of the results from the three FSW specimens and Table 2 shows a summary of the baseline testing results on diffusion bonded (DB) specimens. The tensile strength of the FSW was on average 6.4% (yield) and 5.89% (UTS) stronger compared to the equivalent DB specimens. The FSW results also indicated a net 12% increase in joint stiffness compared with the DB joints. This is unlikely to be the genuine weld material modulus and is most likely an artefact due to the specimen configuration (i.e. artificial reduction in specimen gauge length). These relative results are promising; however, they highlight the need for further work if the absolute properties of the welded alloy are to be determined. Part-level testing may be a more appropriate engineering method for identifying weld performance in real-world components.

Figure 8 presents a comparison of the stress versus strain curves for both the diffusion bonded (DB) and friction stir welded (Friction Stir Welding (FSW)) specimens. In general, the consistency of both sets of results is good, but compared with the DB specimens, there is a slightly broader spread amongst the data for the friction stir welding (FSW) specimens (5.7 versus 17 MPa UTS standard deviation). The TiSiCs friction stir welding (FSW) process development is in its early stages and such vari-

Table 1 Tensile test results for Ti-3Al-2.5 V alloy to TiSiC friction stir welded joints

Sample ID	Modulus (GPa)	0.2% PS (MPa)	UTS (MPa)	Total elong. (%)	R of A (%)
W17	128	620	723	9.68	41.7
W18	131	623	737	10.11	38.8
W19	129	597	696	10.26	41.8
Average:	**129**	**613**	**719**	**10.0**	**40.8**
Stdev:	1.2	11.6	17.0	0.2	1.4

Table 2 Tensile test results for Ti-3Al-2.5 V alloy to TiSiC diffusion bonded joints

Sample ID	Modulus (GPa)	0.2% PS (MPa)	UTS (MPa)	Total elong. (%)	R of A (%)
T1	118	588	676	19	47.6
T2	114	575	687	20.1	47.3
T3	114	564	674	17.6	47.8
Average:	**115**	**576**	**679**	**18.9**	**47.6**
Stdev:	1.9	9.8	5.7	1.0	0.2

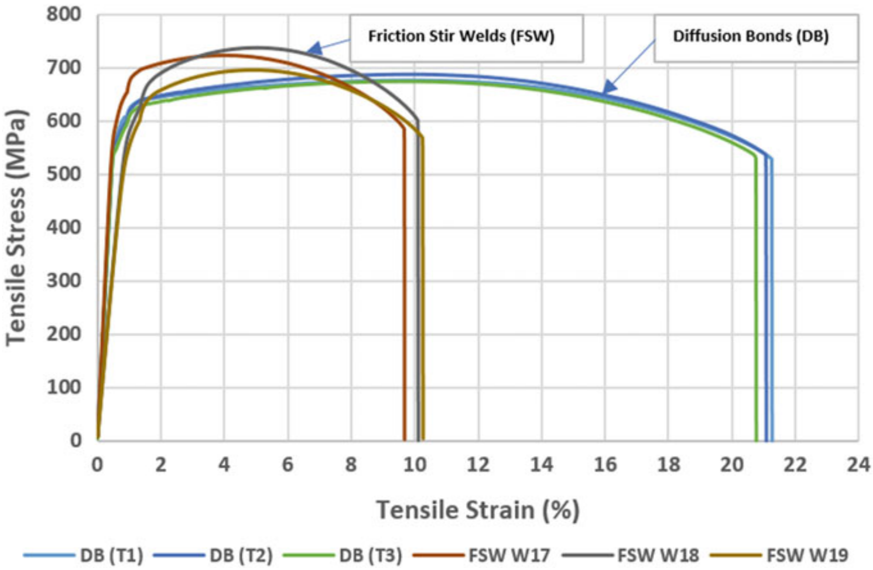

Fig. 8 Comparison of stress versus strain behaviour for monolithic Ti-3Al-2.5 V to TiSiC friction stir welded or diffusion bonded joints

ations in strength would be expected depending on the proximity of the peak stress relative to the weld heat-affected zone (HAZ).

The FSW joint results also suggested a 43% reduction in strain to failure compared with the DB specimens. This is a significant reduction, but at 10% strain to failure, the FSW specimen behaviour is still relatively ductile and is, in fact, a closer match to the typical 1% strain to failure of 0° reinforced TiSiCs. However, as with the modulus data, this measurement is most likely an artefact due to the specimen configuration. Obtaining representative elongation/stain measurement on FSWs is a known challenge. Due to the non-homogenous nature of the weld HAZ, specimen deformation tends to be concentrated in a localised area, thus artificially reducing the effective gauge length and resulting in lower overall elongation measurement compared with more homogenous materials (i.e. diffusion bond).

Fatigue

Fatigue testing was performed to ASTM standard E466-07. Testing was undertaken at four load levels, specifically, 80%, 70%, 60% and 50% of the load corresponding to the ultimate tensile strength of the material, with three repeat tests at each level. As shown in Fig. 9, the FSW fatigue performance was found to be comparable to that of the baseline monolithic Ti-3Al-2.5 V alloy.

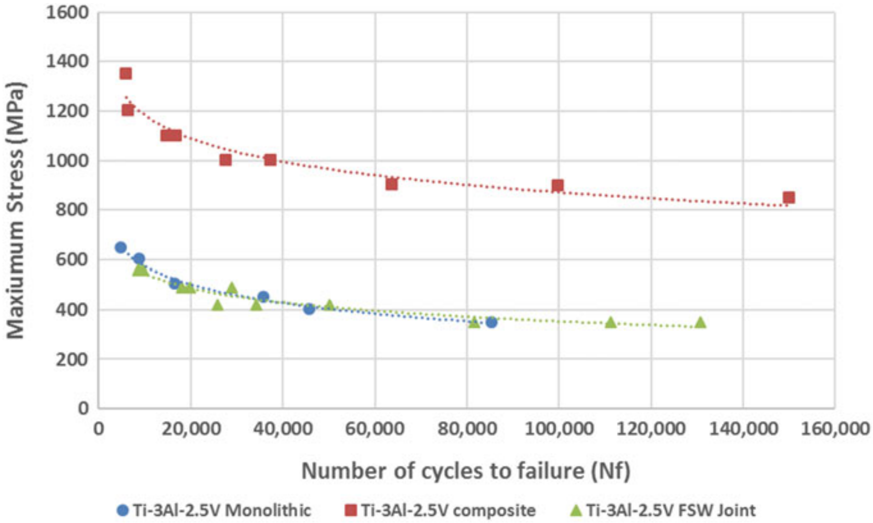

Fig. 9 Comparison of fatigue behaviour for friction stir welded Ti-3Al-2.5 V joints versus as-HIPed Ti-3Al-2.5 V alloy and TiSiCs materials

Residual Stress

Surface residual stress characterisation was completed on a Ti-3Al-2.5 V flat plate friction stir weld using the centre hole drilling technique (Table 3). Five residual stress measurements were performed in the weld nugget, HAZ and parent material of a Ti-3Al-2.5 V flat plate friction stir weld. The highest tensile residual stresses were measured in the weld nugget. These measured between 312 MPa and 318 MPa in the longitudinal direction and 25 MPa and 67 MPa in the transverse direction. Residual stress measurements in the HAZ and parent material were low, the maximum principal stresses were measured between −23 MPa and 16 MPa.

Table 3 Residual stress measurement results

Results: Ti6AL4 V flat plate FSW					
Measurement position (hole—region)	Residual stress, (MPa)				Principal stress angle measured CW from transverse direction (degrees)
	Max	Min	Transverse	Longitudinal	
Hole depth = 0.5–0.8 mm Hole diameter = 0.75–0.85 mm					
1—Weld nugget	318	67	67	318	89
2—HAZ	−23	−71	−28	−67	18
3—Parent material	11	−8	11	−8	2
4—Weld nugget	315	22	25	312	96
5—HAZ	16	−23	14	−21	14

Fracture Toughness

Three compact tension (CT) specimens with SiC fibres were sent for J-integral testing per ASTM E1820-17a. The specimens were wire eroded and machined to a nominal width (W) measuring 10.16 × 10.16 mm and were fatigue pre-cracked to a final a/W of approximately 0.5. The results from the baseline diffusion bonded specimens are shown in Table 4, whilst the latest results from the friction stir welded specimens are shown in Table 5. It should be reiterated for J1C testing that the J parameter is a measure of energy needed to drive a crack under monotonic loading conditions. This value is calculated at several points along a loading curve. The load line compliance and the area under the load versus clip gauge opening displacement curve are used in calculating the crack length and J values. A plot of J versus the change in crack length is then plotted. A least squares curve is then plotted through the valid data set. Where this regression line crosses an offset line, a qualification J is chosen and called Jq. A series of nine validity checks are then run. If these checks pass, the qualification J is then termed J1C.

For most of the specimens tested, both baseline and FSW, the test results obtained did not pass all criteria to qualify as J1C values. However, one of the FSW results, from W18, passes all criteria, and thus represents a J1C data point. Due to the one-off aspect of this result, all fracture data have been presented as Jq values, although a comment is placed in Table 5 stating which value passed the J1C validity checks.

The three-specimen average for the FSW samples was 137.14 MPa$\sqrt{}$m which is an approximate 18.5% increase over the diffusion bonded specimen average of 115.75 MPa$\sqrt{}$m. However, given the spread in the data and accounting for standard deviations, this result cannot be described as a significant difference. Due to the high level of variation in fracture toughness data, it is recommended that a larger number

Table 4 Baseline fracture toughness data for TiSiCs to monolithic Ti-3Al-2.5 V DB joints

Specimen	Testlog no.	JQ (kJ/m^2)	KJQ (MPa$\sqrt{}$m)	Unstable
J1	25709H	141.58	131.69	No
J2	25701H	102.22	108.63	No
J3	25702H	89.92	106.91	No
	Average	111.24	115.74	
	Stdev	22.03	11.30	

Table 5 Fracture toughness for FSW joints between TiSiCs and monolithic Ti-3Al-2.5 V

Specimen	Testlog no.	JQ (kJ/m^2)	KJQ (MPa$\sqrt{}$m)	Unstable	Comments
W17	3579H	120.99	122.53	No	
W18	3580H	122.48	123.88	No	J1C data
W19	3581H	210.57	165.02	No	
	Average	151.35	137.14		
	Stdev	41.88	19.72		

of specimens be tested in future studies. What this initial data does suggest is that the FSW has a beneficial impact with regards to fracture toughness of the joint and is at least just as good as the diffusion bonded baseline. Due to the nature of the test, the variation observed is likely due to the specific nature of how the cracks deflected during the test. For example, the TiSiCs material has superior crack arrest capabilities compared with monolithic materials, thus, any cracks trying to propagate through the TiSiCS side of the joint would likely be deflected, resulting in higher toughness values. Such results have not been excluded from the average calculation because, ultimately, this is the nature of this joint configuration. From inspection of the failed specimens, all fractures appeared normal.

Fatigue Crack Growth Rate (FCGR)

One compact tension (CT) specimen was subject to fatigue crack growth rate testing per ASTM E647-15. The specimen was initially wire eroded and then machined from the welded plate material to a width and length measuring 30 × 30 mm. The specimen was pre-cracked and then tested at room temperature in laboratory air, with a stress ratio of 0.1 at a cyclic frequency of 30 Hz. An electric potential system consisting of a constant current supply was used to continuously monitor the physical crack length (a) on the specimen. Electric potential probes were attached to the front face of the specimen on either side of the specimen's notch. Test results from both the FSW specimen and diffusion bond specimen can be seen in Fig. 10.

In general, both sets of results are consistent with each other, which are also consistent with the expected behaviour for the monolithic Ti-3Al-2.5 V alloy. This provides excellent confidence in the fatigue behaviour of the fibre termination region, as this is a frequent area of concern of TiSiC components.

Structural Component Comparison

As a minimum, the material performance of the FSW joint as implemented into the structural component (xenon tank) should meet or exceed that of the current technology (i.e. diffusion bonding). As such, the structural component performance requirements are the same as the diffusion bonded, i.e. baseline material performance. Table 6 presents both the baseline and FSW joint performance data for comparison. The FSW joint meets or exceeds the diffusion bond in all aspects apart from strain to failure; therefore, the FSW joint can be considered to satisfy the structural component requirements in each of these areas. When considering the strain to failure, the structure itself will consist of both composite body and monolithic ends. Given that the composite has a strain to failure of 1% despite the FSW joint being 50% that of a diffusion bond, in absolute terms, a strain to failure of approximately 10%, as with the FSW joint, would be satisfactory.

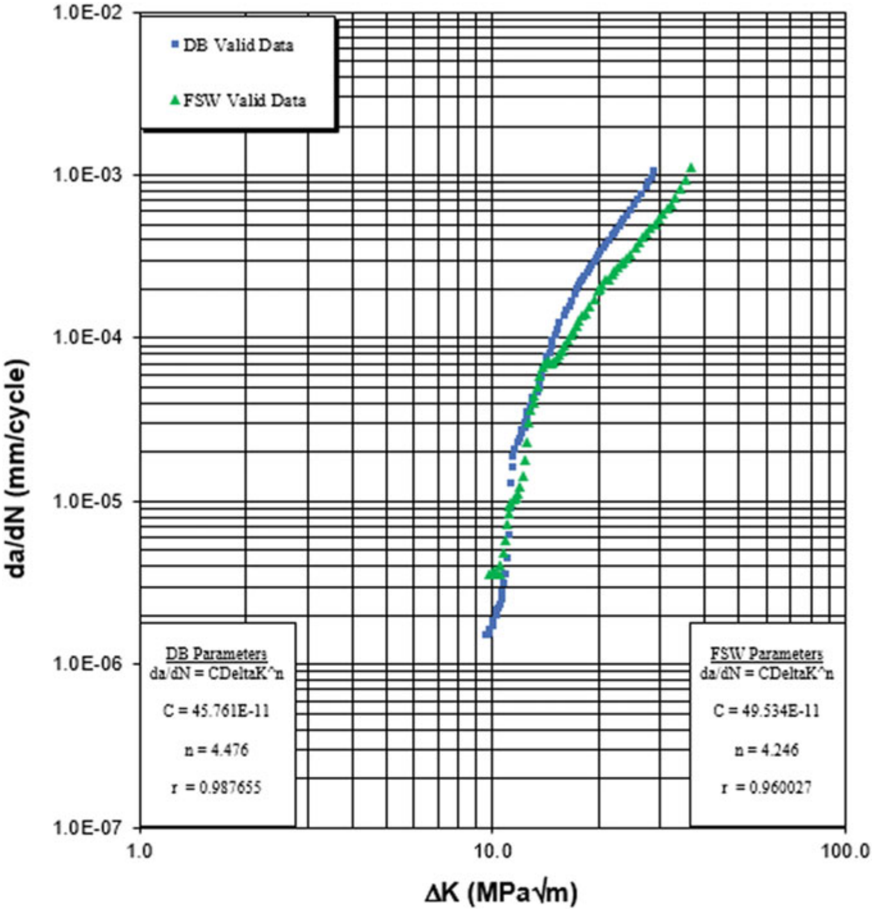

Fig. 10 Comparison of fatigue crack growth rate for diffusion bonded and friction stir welded TiSiCs to monolithic Ti-3Al-2.5 V joints

The quantitative property values obtained for the FSW joint can now be used in future studies to help select the appropriate thickness of the monolithic regions. Since the performance of the FSW has been shown to be comparable or superior to that of a diffusion bond, there is no specific requirement for an additional knockdown factor to account for the presence of the FSW. In other words, the thickness of the monolithic regions does not need to be increased beyond what is required for a diffusion bonded joint. A two-step manufacturing route to diffusion bond a monolithic Ti-6Al-4 V strip onto the edge of a pre-consolidated TiSiC panel is recommended. The TiSiC preform should be wire eroded for controlled fibre termination and position control. The thickness of the Ti-6Al-4 V monolithic strip should be greater than that of the bulk TiSiC plate, with a gradual taper leading from the TiSiC plate to the maximum monolithic thickness. The thickness increase will be such that the tensile failure

Table 6 Comparison of WP5 results against the baseline and structural component requirements

Parameter	Baseline	FSW	Target component requirement	Acceptable
Visual	Seamless	Slight distortion	Properties dictate	N/A
Microstructure	Homogenous, coarse grains	Non-homogenous, fine grain	Properties dictate	N/A
Micro-hardness (Hv)	280	290	Non-critical	Yes
Ultimate tensile (MPa)	679	719	Same or higher	Yes
Yield strength (MPa)	576	613	Same or higher	Yes
Strain to failure (%)	20%+	~10%	1%<	Yes
Young's modulus (GPa)	115	129	Same or higher	Yes
Fatigue	See Fig. 9	Comparable	Same or higher	Yes
Fracture Toughness (MPa$\sqrt{}$m)	115	137	Same or higher	Yes
Fatigue crack growth rate	See Fig. 10	Comparable	Same or higher	Yes
Residual stress (MPa)	11	318	Up to 450 MPa	Yes

load of the monolithic region will exceed that of the higher strength TiSiC plate. The Ti-6Al-4 V monolithic plate for welding should be purchased from commercial suppliers. Any run on and run off required should be provided by separate monolithic plates. In addition, the process development trials have identified that a 2 mm probe to fibre distance is satisfactory when welding 3 mm thick material with a 10 mm diameter probe.

Two weld configurations are available; the first is to have a double taper, where there is a transition to a thicker monolithic region on both faces of a TiSiC plate. This is a more balanced configuration, but the initial plate manufacture and fixturing would be more complex. Option 2 is to have a sufficiently large taper on only one of the TiSiC panel faces. This is not symmetrical, but would be easier to manufacture and fixture during the FSW process (see Fig. 11).

Conclusions

- The SSFSW technique successfully produced sound welds in monolithic Ti32.5 to TiSiC plates, with the highest ultimate tensile strength of 768 MPa achieved.
- The monolithic width of 7 mm on the abutting edge of TiSiC plates is sufficient to avoid any damage to SiC fibres during welding.
- The control over dimensional accuracy of TiSiC plates is critical to the successful performance of the SSFSW process.
- Friction stir welded joints between TiSiC and monolithic Ti-3Al-2.5 V plates have been characterised using a range of tests. The FSW results were comparable or

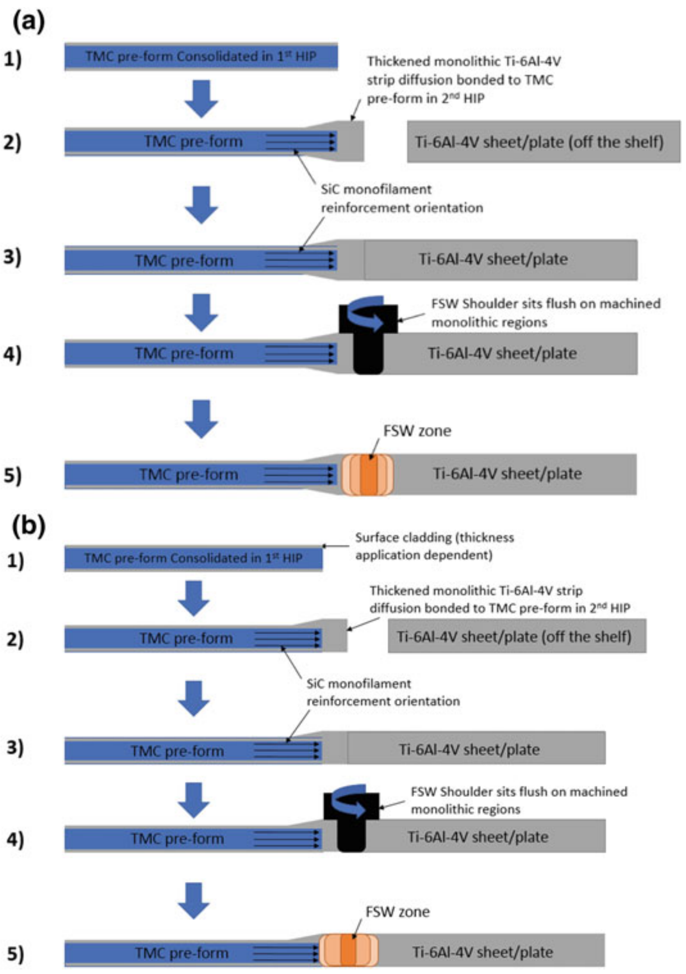

Fig. 11 Recommended TMC panel configuration for FSW: **a** Option 1 double taper; **b** Option 2 single taper

higher than the baseline (i.e. diffusion bond) in every metric tested apart from strain to failure, which was approximately 50% that of the baseline.

- A comparison between the FSW performance was done to target structural component performance needs for a xenon tank. The structural component requirements are based on the baseline performance, thus, as expected, the FSW results satisfied the necessary criteria in every tested metric. This also included strain to failure because, although the FSW was approximately 50% that of a diffusion bond, given that the TiSiCs material has a strain to failure of 1%, a strain to failure higher than this would still be satisfactory.

Acknowledgements This activity is supported by ESA's TRP programme under contract number 4,000,116,110/15/NL/BJ/gp.

References

1. Kyle-Henney S. Recent advances in titanium metal matrix composite technology in the UK, n.d. Internal Document, Farnborough, TISICS Ltd
2. Kyle-Henney S (2007) One small step for titanium, materials world, pp 22–23
3. Kyle-Henney S (2017) SME Engagement with ESA, UK space conference 2017 presentation, slide 2. Farnborough, TISICS Ltd
4. Kyle-Henney S (2015) Metal composites for light weighting, LVC 2015 presentation, slide 4. Farnborough, TISICS Ltd
5. Thomas WM, Nicholas ED, Needham JC, Murch, MG, Templesmith P, Dawes CJ (1991) GB patent no. 9125978.8. International Patent Application No. PCT/GB92/02203, pp 826–827
6. Russell MJ, Threadgill PL, Thomas MJ, Wynne BP (2007). In: Niinomi M, Akiyama S, 830 Ikeda M, Hagiwara M, Maruyama K (eds) 829 Ti-2007 science and technology. The Japan Institute 831 of Metals, pp 1095–98

Wear Mechanism for H13 Steel Tool During Friction Stir Welding of CuCrZr Alloy

Pankaj Sahlot, R. S. Mishra and Amit Arora

Abstract Wear affects shape and size of the friction stir welding (FSW) tool, and leads to unexpected weld properties and shorter tool life. Understanding wear mechanisms during FSW is important to prevent or reduce tool wear and ensure longer tool life for joining of high melting point metallic (HMPM) materials. Severe tool wear is a consequence of extreme thermo-mechanical environment around the tool during welding. The macroscopic and microscopic investigations of wear mechanism are conducted by performing 3D profilometer and scanning electron microscopy (SEM) with energy dispersive spectroscopy (EDS). Analysis of the scratch formation on the tool surface is used to ascertain the presence of abrasive wear mechanism. Adhesive wear is confirmed by investigating the tool–workpiece interface layer, which features diffusion of copper. This understanding of tool wear mechanism during FSW of high melting point metallic materials will enable selection of better tool materials and improved weld properties.

Keywords Friction stir welding · Tool wear · Wear mechanism · Adhesive wear
Abrasive wear

P. Sahlot · A. Arora (✉)
Advanced Materials Processing Research Group, Materials Science and Engineering,
Indian Institute of Technology Gandhinagar, Palaj, Gandhinagar 382355, India
e-mail: amitarora@iitgn.ac.in

P. Sahlot
Department of Mechanical Engineering, School of Technology, Pandit Deendayal Petroleum
University, Gandhinagar 382007, India

R. S. Mishra
Department of Materials Science and Engineering, Center for Friction Stir Processing,
University of North Texas, Denton, TX 76203, USA

Y. Hovanski et al. (eds.), *Friction Stir Welding and Processing X*, The Minerals,
Metals & Materials Series, https://doi.org/10.1007/978-3-030-05752-7_6

Introduction

Friction stir welding (FSW) is gaining wide acceptance due to solid state and eco-friendly joining process [1]. This technique is very promising for welding of low strength materials such as aluminum and magnesium alloys. However, tool wear continues to thwart the commercial application of FSW to join high-strength materials such as steel, copper alloys (CuCrZr), and titanium alloys [2–4]. Wear affects the shape and size of the FSW tool, and thus leads to unexpected weld properties and shorter tool life [5–7]. Understanding tool wear and wear mechanism during FSW is important to obtain consistent weld properties, as well as longer tool life for joining of high-strength materials. Tool wear during FSW of materials such as aluminum alloys (AMG5 M alloy), metal matrix composites (MMC), steel, copper alloy, and titanium alloys has been studied [7–10]. These studies focus mainly on measurement of wear during the process and the effect of process parameters on tool wear and wear rate. Researchers also investigated the wear mechanism for various sets of materials such as MMC, steel, aluminum alloys and titanium alloys.

Tarasov et al. [11] investigated tool wear mechanism of steel tool during FSW of aluminum alloy (AMG5 M alloy) and observed wear due to diffusion of aluminum and steel at high temperature. Prado et al. [5] reported severe wear during FSW of metal matrix composite (Al6061 + 20% Al_2O3) using a steel tool. Tool wear occurred mainly due to the interaction of abrasive particles with the steel tool. The major wear mechanism during FSW of MMC is abrasive wear due to the interaction of abrasive particles with the tool material. Wang et al. [12] investigated wear mechanism of WC-Co tool for FSW of Ti-6Al-4 V and observed an adhesive wear mechanism during the process. An interaction layer was formed due to decarburization of WC. Farias et al. [13] conducted a wear study for WC tool during FSW of commercial titanium Ti-6Al-4 V. They observed wear due to hot adhesion and noticed strong sticking of workpiece material over the tool surface. Weld qualities were also affected by tool wear during the process. Park et al. [3] investigated the tool wear study of polycrystalline cubic boron nitride (pcBN) tool for FSW of stainless steel and observed the effect of tool wear on the formation of boron and nitrogen due to severe stresses at elevated temperature. Tool wear leads to the formation of Cr-rich borides as a result of the reaction between boron and nitrogen with matrix. Choi et al. [41] compared the effect of tool wear on mechanical weld properties and studied wear mechanism during FSSW of low carbon steel by using two WC-alloy tools. They investigated three main mechanisms of tool wear—oxidation wear of WC, fatigue of Co binder and the formation of a ternary W-Fe-O compound. They also reported that joint strength was influenced by a change in the shape of the tool due to wear. However, currently no wear mechanism study is available for H13 steel tool during FSW of copper alloys such as CuCrZr alloy. Since understanding tool wear mechanism for these materials is important, here we conduct a wear mechanism study during FSW. Our research is intended to reveal the mode of the wear mechanism during the process.

Experimental Methodology

The material used in the present study was CuCrZr alloy (Cu-0.8 wt%Cr-0.1 wt%Zr) plates with 6 mm thickness. CuCrZr was used in peak aged condition by aging a solutionized plate at 450 °C for 3 h, followed by water quenching [14–16]. H13 steel (Fe-5.27 wt%Cr-1.25 wt%Mb) tool was used to perform bead-on-plate method to investigate wear study during FSW of CuCrZr alloy. The tools had a tapered pin length of 4.6 mm and pin diameter of 10.4 mm and 4.4 mm at pin root and pin tip, respectively; with a shoulder diameter of 19.6 mm. Complete experiment details have been reported [14]. The microstructural study was carried out by performing SEM with EDS. 3D profile projector were also used to analyze surface features. For abrasive wear mechanism, the tool surface was investigated to observe the scratches and grooves using 3D profile projector. A section view is used for the adhesive wear study to investigate tool–workpiece interface layer. In this study, the microstructure of the tool–workpiece interface was investigated to determine the mode of adhesive wear mechanism in this system. The main focus was to examine tool–workpiece interface layer. Mirror polishing was done for tool–workpiece interface microstructural study by SEM-EDS. The elemental study was also performed at tool–workpiece interface and generated line and area elemental maps.

Results and Discussion

Figure 1a shows the H 13 steel tool used for welding of CuCrZr alloy and Fig. 1b shows the used tool after removal of sticking workpiece material. Surface morphology of used tool is analyzed to investigate abrasive wear mechanism. The scratches and grooves form due to the interaction of flowing workpiece material with the

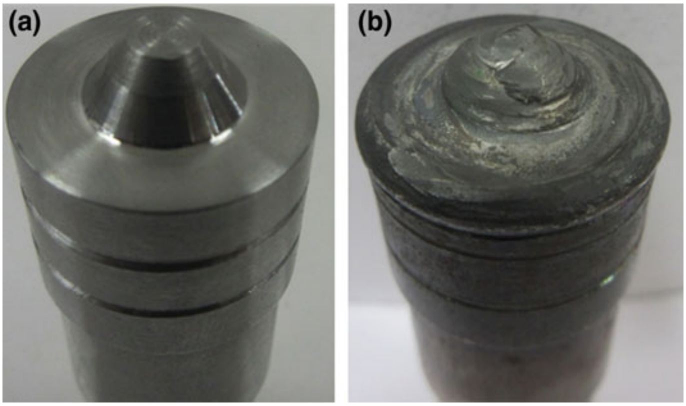

Fig. 1 Tool images **a** unused tool **b** used tool after removal of sticking copper alloy

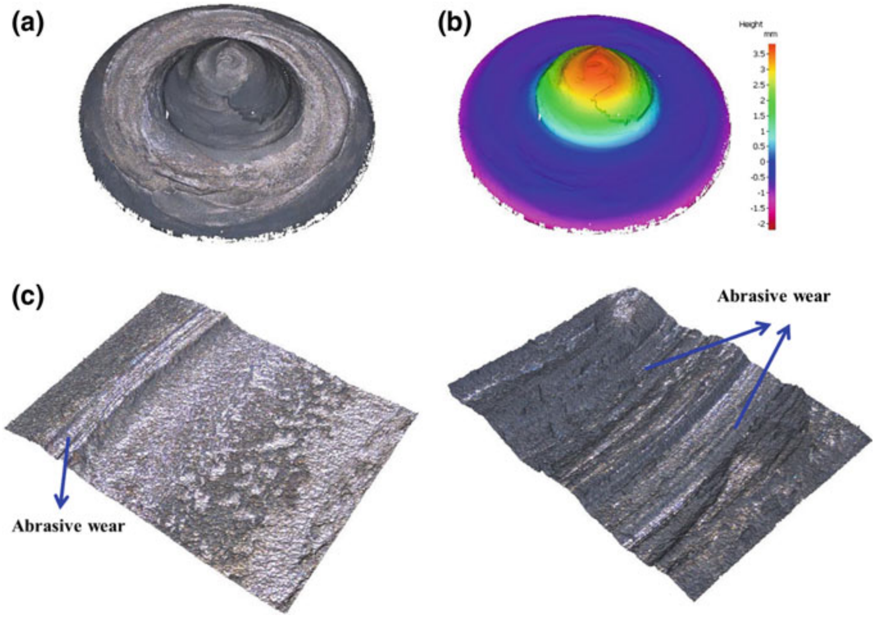

Fig. 2 3D profile projector image of the used tool **a** surface map, **b** color contour map and c formation of scratches and grooves

tool at high axial pressure and elevated temperature. Sticking of workpiece over the tool and the formation of scratches and grooves lead to adhesive and abrasive wear respectively.

The 3D profile projector is used to generate a 3D profile of unused tool. Figure 2a, b show 3D surface and color contour map of the used tool surface. The 3D contours or profile show the formation of micro-machining grooves at all surfaces as shown in Fig. 3c. Micro-grooves are localized locations of stress concentration to initiate wear. The initial grooves consist of peak and valleys and behave like a cantilever beam. These cantilever beams like features are weak and fail during material stirring at high temperature. The flowing material also follows the trajectory of some of these grooves and increases the size of grooves. These formations of scratches and grooves result from the abrasive wear.

The tool–workpiece interface is also investigated to understand adhesive wear mechanism and the features which increase wear during FSW. The sticking of copper alloy on steel occurs due to diffusion bonding between copper and steel [14]. Figure 3a shows BSE image of adhered CuCrZr alloy with the steel at the tool–workpiece interface. The interface layer is highlighted to distinguish between steel and copper. EDS elemental line and area map scans are performed to investigate diffusion of elements across the interface line as shown in Fig. 3b, c. The EDS line scan across the interface shows diffusion of both copper and iron into each other with a diffusion length of 3 μm [14]. This diffusion length depends on the diffusivity of the copper

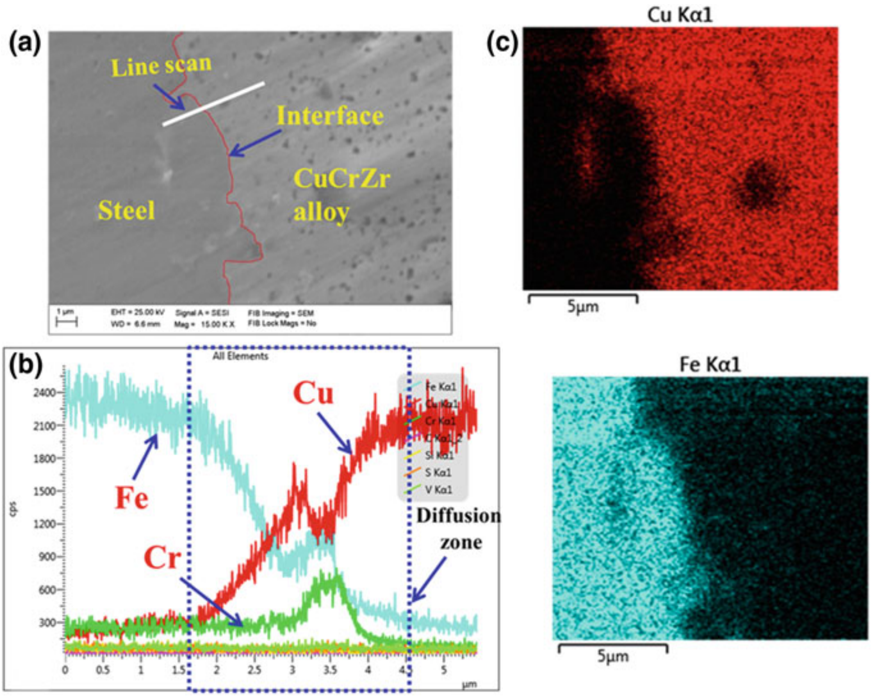

Fig. 3 Tool–workpiece interface images of the used tool at sticking copper location **a** BSE image at the tool–workpiece interface, **b** EDS line scan elemental distribution perpendicular to the interface location and **c** EDS elemental area map at the tool–workpiece interface [14]

and steel in each other at the processing temperature and conditions. Copper and iron also significant diffusivity within this temperature range to form a diffusion bond [17].

Conclusions

Some key findings from this study are given below.

1. Severe tool wear is observed for H13 steel tool during FSW of CuCrZr alloy due to high stresses at elevated temperature.
2. Macroscopic surface investigation shows copper alloy gets stuck at localized locations over the used tool surface due to diffusion bonding. Scratches and grooves were also observed at localized locations at the used tool surface.
3. Microscopic investigation of tool surface shows formation of grooves and scratches due to interaction of flowing workpiece material with a rotating tool.

The machining grooves behave like localized wear areas and interaction of flow material with tool results in abrasive wear.

4. The sticking of copper alloy over tool material surface occurred due to diffusion bonding between copper and steel.

Acknowledgements Authors would like to acknowledge Board for Research in Nuclear Sciences (BRNS), (36(2)/20/02/2014-BRNS/). Authors are also grateful to Dr. G. K. Dey, Materials Group and Mr. Kaushal Jha, Engineering Design & Development Division for their support to use the research facilities available at BARC. Authors would also like to thanks Dr. Ramesh Singh for permission use the research facility at IIT Bombay.

References

1. Thomas WM, Nicholas ED, Needham JC, Murch MG, Templesmith P, Dawes CJ (1991) Great Britain patent application no. 9125978.8
2. Thompson B, Babu SS (2010) Tool degradation characterization in the friction stir welding of hard metals. Weld J 89(December):256–261
3. Park SHC, Sato YS, Kokawa H, Okamoto K, Hirano S, Inagaki M (2009) Boride formation induced by pcBN tool wear in friction-stir-welded stainless steels. Metall Mater Trans A 40(3):625–636
4. Rai R, De A, Bhadeshia HKDH, DebRoy T (2011) Review: friction stir welding tools. Sci Technol Weld Join 16(4):325–342
5. Prado RA, Murr LE, Shindo DJ, Soto KF (2001) Tool wear in the friction-stir welding of aluminum alloy 6061 + 20% Al2O3: a preliminary study. Scr Mater 45(1):75–80
6. Choi D, Lee C, Ahn B, Choi J (2009) Frictional wear evaluation of WC–Co alloy tool in friction stir spot welding of low carbon steel plates. Int J Refract Met Hard Mater 27(6):931–936
7. Liu HJ, Feng JC, Fujii H, Nogi K (2005) Wear characteristics of a WC–Co tool in friction stir welding of AC4A + 30 vol%SiCp composite. Int J Mach Tools Manuf 45(14):1635–1639
8. Prado R, Murr L, Soto K, McClure J (2003) Self-optimization in tool wear for friction-stir welding of Al 6061 + 20% Al 2 O 3 MMC. Mater Sci Eng A 349:156–165
9. Gan W, Li ZT, Khurana S (2007) Tool materials selection for friction stir welding of L80 steel. Sci Technol Weld Join 12(7):610–613
10. Sato YS, Miyake M, Susukida S, Kokawa H, Omori T, Ishida K (2015) Performance enhancement of co-based alloy tool for friction stir welding of ferritic steel. In: Friction stir welding symposium and processing VIII, pp 39–46
11. Tarasov SY, Rubtsov VE, Kolubaev EA (2014) A proposed diffusion-controlled wear mechanism of alloy steel friction stir welding (FSW) tools used on an aluminum alloy. Wear 318:130–134
12. Wang J, Su J, Mishra RS, Xu R, Baumann JA (2014) Tool wear mechanisms in friction stir welding of Ti – 6Al – 4 V alloy. Wear 321:25–32
13. Farias A, Batalha GF, Prados EF, Magnabosco R, Delijaicov S (2013) Tool wear evaluations in friction stir processing of commercial titanium Ti–6Al–4V. Wear 302(1–2):1327–1333
14. Sahlot P, Jha K, Dey GK, Arora A (2017) Quantitative wear analysis of H13 steel tool during friction stir welding of Cu-0.8%Cr-0.1%Zr alloy. Wear 378–379:82–89
15. Sahlot P, Arora A (2018) Numerical model for prediction of tool wear and worn-out pin profile during friction stir welding. Wear 408–409:96–109
16. Sahlot P, Jha K, Dey GK, Arora A, Wear-induced changes in FSW tool pin profile: Effect of process parameters. Metall Mater Trans A 1–12
17. Rothman SJ, Peterson NL, Walter CM, Nowicki LJ (1968) Diffusivity of copper in Iron. J Appl Phys 39(11):5041–5044

Part III
Lightweight Materials

High-Speed Friction Stir Lap Welding of Al Alloys

Piyush Upadhyay, Xiao Li and Tim Roosendaal

Abstract Friction stir lap welding (FSLW) with linear speed of 1 m/min or higher can open up opportunities for industrial implementation. This paper will provide an overview of several challenges and mitigation strategies to produce effective joints between several Al alloys. FSLW of Al alloys at high speed presents challenges including interface hook features and defects at the interface. 5xxx, 6xxx, and 7xxx Al alloys were joined and characterized. Load-bearing capacity in excess of 80% of base material strength has been demonstrated at the welding speed of 2 m/min for 6xxx and 5xxx similar lap joints. The effects of parameters like welding speed, RPM, tool geometry in material flow features, void volume, and hook geometry is investigated and this knowledge base is applied to improve the joint strength of 7xxx lap welds.

Keywords Friction stir lap welding · High speed · AA7xxx · AA5xxx · AA6xxx

Background and Introduction

Unlike butt joint, friction stir lap joint interface is oriented perpendicular to the axis of tool rotation. Consequently, FSLW has a tendency for inadequate mixing of the multi-sheet stack-ups. Furthermore, undispersed surface oxide at the interface can lead to undesirable material upturn on either side of the nugget, often referred to as "hooks". Additionally, the bonded area for FSLW is more dependent on pin diameter rather than the much larger shoulder diameter as is the case in butt joining; thus material flow around the bottom of the pin (i.e., faying interface) is critical for FSLW. Lap geometry inherently has crack-like structures at both the edges of the overlap. This hook feature can either deviate towards top or bottom of the joint, reducing the effective sheet thickness concurrently, acting as a site for crack initiation

---

P. Upadhyay (✉) · X. Li · T. Roosendaal
Pacific Northwest National Laboratory, 902 Battelle Boulevard, Richland, WA 99354, USA
e-mail: piyush.upadhyay@pnnl.gov

Y. Hovanski et al. (eds.), *Friction Stir Welding and Processing X*, The Minerals, Metals & Materials Series, https://doi.org/10.1007/978-3-030-05752-7_7

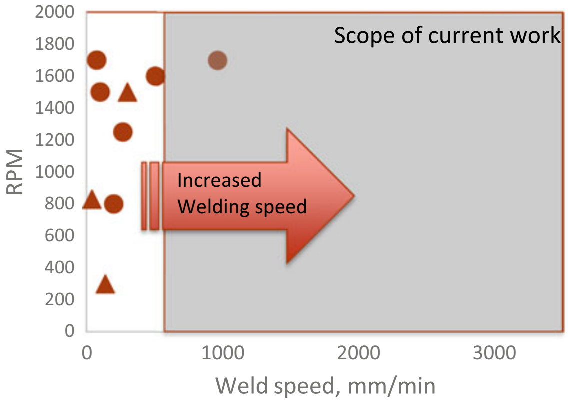

Fig. 1 Different welding speeds for FSLW reported in the literature versus scope of this work

and propagation, thus affecting mechanical properties of the joint. Management of this interface is key to obtaining acceptable static and dynamic joint performance.

While first-order estimates regarding how weld parameters can affect the above-mentioned joint morphology are understood, functional relationships between control parameters, tool design and the resulting interface that are critical to joint strength remain elusive. It is observed that in some instances the presence of hook features are especially detrimental when on the advancing side of the joint. The problem is exacerbated when the hook is deviated towards the sheet with a lower load carrying capacity.

Certain combinations of welding control parameters and tool geometries have been shown to produce superior welds in the literature; however these parameters are highly specific to a chosen material stack-up [1–3]. The reported joint strength values have large scatter and can range anywhere between 20 and 60% of the base metal. Aside reported variation in weld strength, another important issue persists as a primary obstacle to commercialization. The welding speeds reported in the literature are relatively low (Most of the welds are performed at around 0.3–0.6 m/min while only few show capabilities up to 1 m/min (See Fig. 1) and do not justify commercial investment nor a switch to FSLW technology unless a significant improvement in welding speed can be demonstrated.

An ongoing project at Pacific Northwest National Laboratory (PNNL), in close collaboration with an original equipment manufacturer and a material supplier is focused on evaluating and developing FSLW such that Al alloys relevant to automotive assembly line can be effectively lap welded. We present an overview of the process, progress made, and challenges associated with lap joining at high speeds.

Fig. 2 Representative FSLW tools with different shoulder and pin features

Materials and Experimental Details

FSL welds were made between similar aluminum sheets. The pair of FSLW reported in this paper include 7055–7055s and 5754–5754. All the tools were made using heat-treated H-13. Tools with various designs were employed in this study. Examples of a few tools used in this work is shown in Fig. 2. Joints were produced on a high precision Manufacturing Technology, Inc., gantry-type FSW machine at PNNL. The FSW system can measure several process responses in real time including tool forces in all three directions, tool torque, and position. All the welds were ~280 mm long, made with 100 mm × 300 mm flat panel sheets with an overlap of 20 mm.

After welding, the joints were cut transversely into metallographic and lap shear test specimens using water jet milling. Select weld cross sections were then ground and polished for optical macro/micrographs. A series of unguided lap shear tensile tests were performed using a universal test frame. For each case, several samples from different regions of the joints were tested. Appropriate shims were added to the grips to ensure that samples were aligned during testing and bending stress in the samples was minimized. For the sake of simple comparison with the base material, load-bearing capacity per unit joint length is used in this work.

Results and Discussion

Owing to inherent asymmetrical material flow, the top sheet of a lap welded sample can be either loaded on (1) advancing side or (2) retreating side. Usually, the two configurations can be obtained by placing top sheet's trim edge on either retreating or advancing side respectively. Figure 3 shows a sequence of images during lap shear test of a FSLW made between 7055 (2.5 mm) and 7055 (2.5 mm). Strain evolution during the lap shear test was captured using Digital Image Correlation (DIC). The color map on the first two images shows distribution of Lagrangian strains on the edge of the sample. As the test progresses, strain localizes at two locations on either side of the lap weld. Except in the case of interfacial fracture, the joints fracture in these two regions. The performance of the joint in mechanical test consequently depends on local mechanical properties and macro-structure in these two areas.

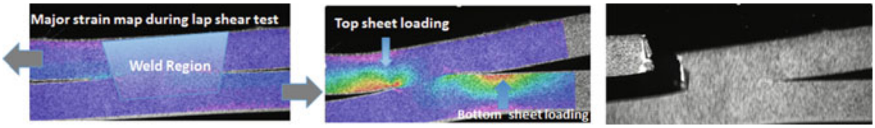

Fig. 3 Images obtained from lap shear test of AA7055 (2.5 mm)–AA7055 (2.5 mm). The first two images show Lagrangian strain overlay obtained using VIC3D utilizing digital image correlation. The last image shows weld fracture

A series of welding trials were conducted in both material sets by varying parameters including welding speed, tool rotation rate, and tool geometry. A large number of welding conditions were thus obtained. Figure 4 shows an overview of different types and extent of joint defects observed in this study. Several observations have been made about the types of defects. For instance, the hook-type interface is typically observed on the retreating side of the weld for both 7xxx and 5xxx series alloys. There are cases where a hook feature is present on the advancing side (see Fig. 4a) however, the extent of retreating side hooking (towards the root, thus decreasing the effective thickness of top sheet) is significantly higher. Additionally, the use of a shorter pin (2.7 mm) resulted in a lack of material mixing and defective interface (Fig. 4b). Inadequate/excessive material mixing both resulted in wormhole defect in the advancing side. While higher power weld (0.25 m/min at 1950 rpm) resulted in

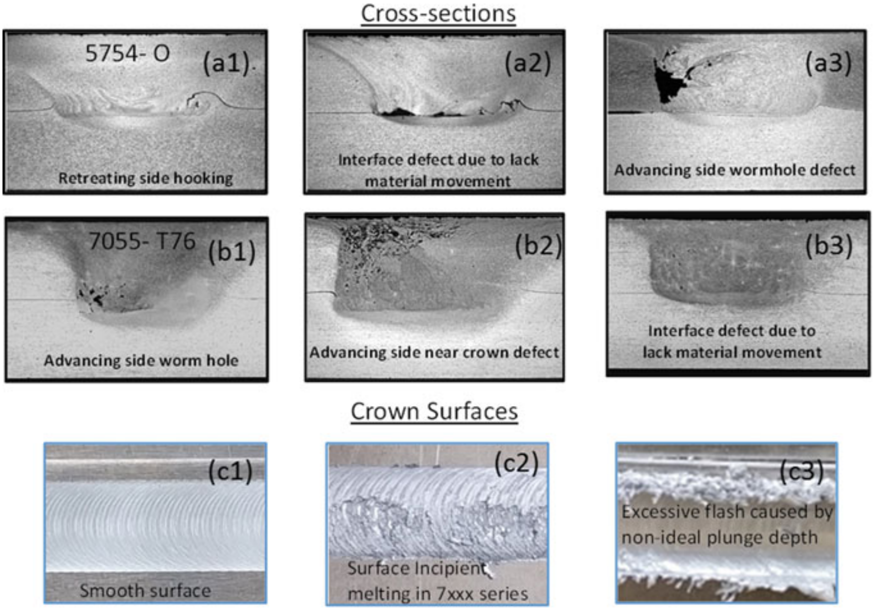

Fig. 4 An overview of types of weld defects observed in FSLW. **a** 5754-0 Lap joints, **b** 7055-T76 lap joints, **c** 7055 crown surface

large adv. side wormhole defect (Fig. 5b), no such defect was observed in welds ran at 3 m/min, 1950 rpm using an identical tool (Fig. 5b).

A load-bearing capacity of ~84% corresponding to the base material was obtained at the welding speed of 3 m/min (See Fig. 6). The top sheet was loaded on the advancing side such that the fracture occurred via the advancing side root region traveling up to the crown.

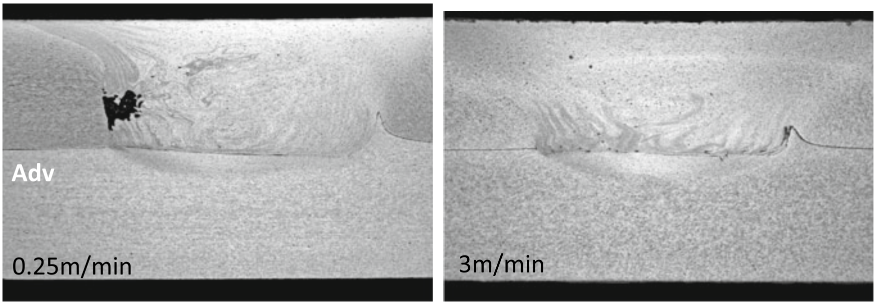

Fig. 5 FSLW made between 5754 (2.5 mm) and 5754 (2.5 mm) sheet at 1950 rpm using identical tooling at the welding speed of 0.25 m/min and 3 m/min

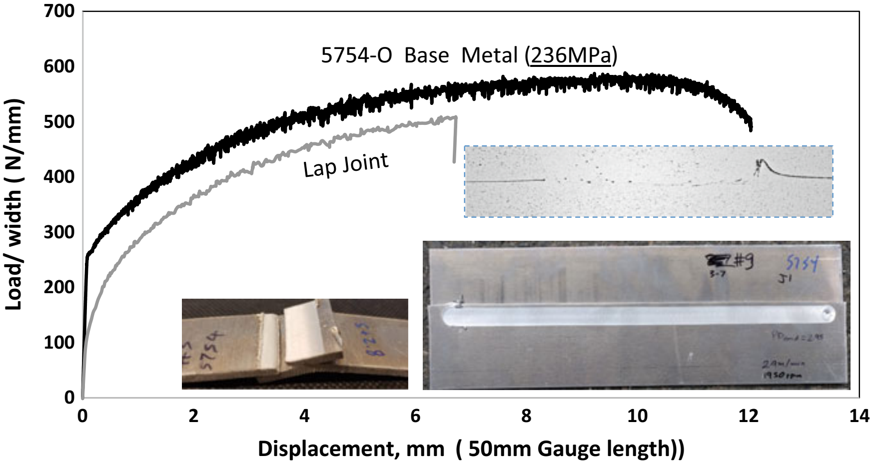

Fig. 6 Load-bearing capacity of AA5754-O lap joint (2.5–2.5 mm) compared with that of base AA5754-o (2.5 mm) sheet. Full weld panel and a close up the joint interface is also shown. The sheet was loaded on advancing side (left on the cross section)

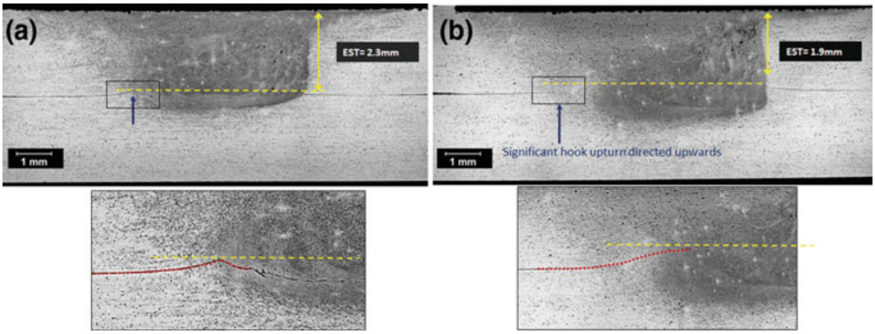

Fig. 7 Joint cross section showing hook upturn and effective sheet thickness for welds made between AA7055 (2.5 mm) and AA7055 (2.5 mm) using **a** 3.1 mm long pin **b** 3.4 mm long pin

Effect of Pin Length

Figure 7 demonstrates the effects of pin length on resulting interface/hook geometry. All other things being equal, a joint made with effective pin length of PL = 3.4 mm (Fig. 7b) resulted in a significant hook upturn compared to that made using PL = 3.1 mm (Fig. 7a). The shorter pin length resulted in an adequate amount of interface mixing without being affected by the vertical flow field of the tool. In contrast, for welds made with PL = 3.4 mm, the retreating side was significantly affected by vertical flow field as a result of greater engagement into the bottom sheet. An approximate, effective thickness of the top sheet was measured and is indicated on the respective figures for each of the two cases. A direct effect of this is observed in the lap shear testing. Whereas sample shown in Fig. 7b showed a load-bearing capacity of 581 ± 30 N/mm, the sample in Fig. 7b with EST = 1.9 mm showed a joint strength of 466 ± 15 N/mm.

AA 7055 Lap Joints

Owing to its high hardness AA 7055 presented a unique set of challenges in Friction stir lap welding. As is well known compared to 5xxx and 6xxx series, 7xxx series material required significantly greater power input. The welding parameters and tool design that produced "good" welds in 6xxx and 5xxx series resulted in various types of defects including advancing side wormhole defect either near the root region (Fig. 4b1) or near the crown (Fig. 4b2). At greater welding speeds (2 m/min and beyond), an intermittent crown surface breach indicative of incipient melting in 7xxx series was also observed. In many cases, this type of crown defect resulted in nugget fracture of the top sheet with poor mechanical property. Nevertheless, the use of less aggressive shoulder features in concert with lower power input allowed to minimize surface defect.

Figure 8 shows the result of lap shear test performed for FSLW between 7055(2.5 mm) and 7055(2.5 mm). At a welding speed of 0.5 m/min and 1200 rpm, a joint load-bearing capacity of 49 ± 5% (standard deviation based on three samples extracted from near start, middle, and end of the weld) was achieved. The fracture mode was similar to the one shown in Fig. 2 (far left). The fractured sample is also shown in Fig. 10. For comparison, a bead on plate tensile test result is also shown in Fig. 8. 20% knockdown in load-bearing capacity is observed by simply friction stir welding through the base material (Fig. 9).

Full field hardness distribution of the FSLW joint discussed above is plotted in Fig. 10. The fracture location is coincident with the location of HAZ minimum hardness location on the advancing side. While not shown, some high performing

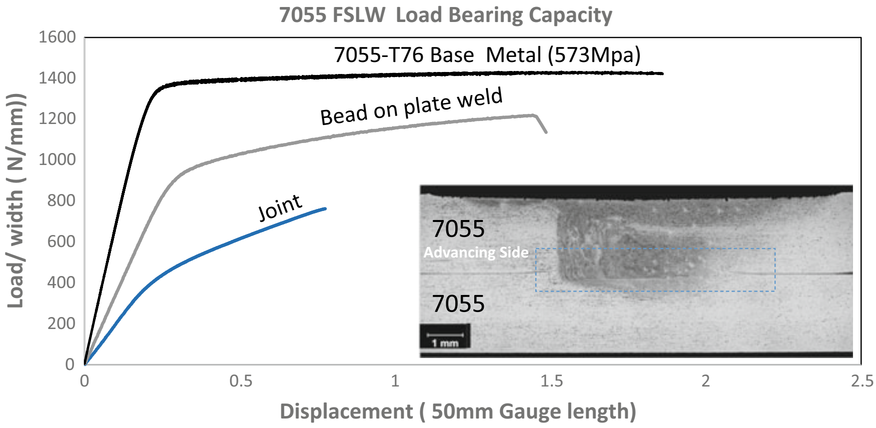

Fig. 8 Load/unit width versus displacement for FSLW lap joint (2.5–2.5 mm), bead on plate weld (2.5 mm) and base material

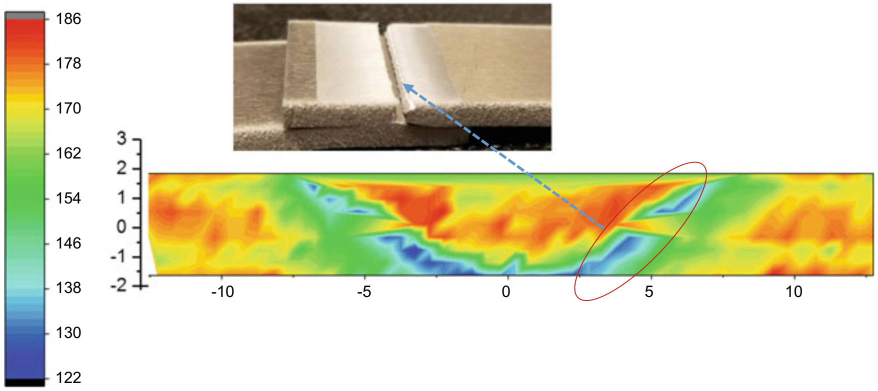

Fig. 9 Full field micro-hardness distribution across FSLW between 7055 (2.5 mm) and 7055 (2.5 mm). Fracture location of lap shear sample coincides with HAZ minimum hardness location

samples have also fractured through the bottom sheet on the retreating side (also consistent with HAZ minimum location on the retreating side. This indicates that fracture propagation can be limited by increasing the strength around the interface region. One of the ways to increase the joint strength beyond the demonstrated 50% is to increase the welding speed [4]. Increase in the welding speed has been shown to increase the HAZ minimum hardness by decreasing level of coarsening of precipitates. Figure 11 shows hardness traverse from two beads on plate weld sample showing that a significant improvement in HAZ minimum hardness can be attained welding speed increasing welding speed (from 0.5 to 3 m/min in this case). The current challenge is to increase the welding speed beyond 0.5 m/min while avoiding surface and wormhole type defects. Efforts are underway in evaluating several tool design and parameters set towards this goal.

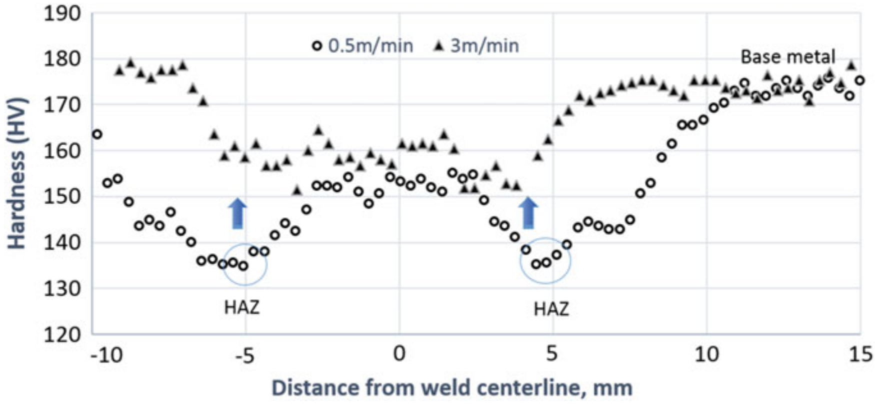

Fig. 10 Micro-hardness traverse on bead on plate 7055 sheet showing significant improvement In HAZ minimum hardness with the use of higher welding speed everything else remaining constant

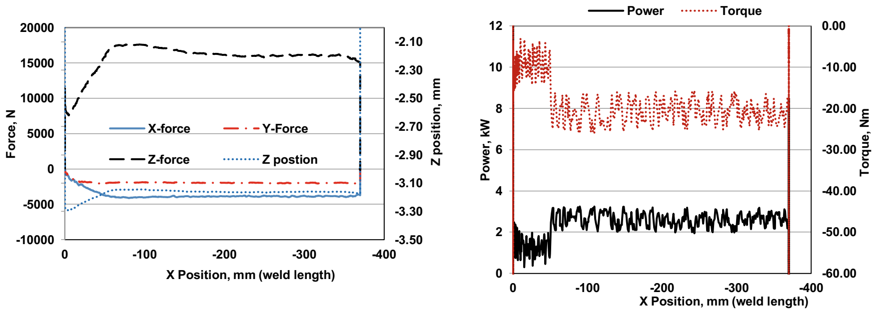

Fig. 11 Process forces plotted against weld distance. Weld power and torque plotted versus the X position

Summary

This project aims to develop Friction stir lap welding technique in automotive Al sheets such that effective joints can be made at industrially viable welding speed for commercialization. By studying a wide variety of welding parameters including tool geometry, welding speeds and rotational speeds, correlations between welding parameters, FSLW microstructure and mechanical property is being evaluated. Thus far, a joint efficiency corresponding to 84% (at the welding speed of 3 m/min) AA5754-O–AA5754-O (2.5–2.5 mm) and 50% (at the welding speed of 0.5 m/min) for AA7055-T765–AA7055-T765 (2.5–2.5 mm) have been attained in lap shear testing.

Acknowledgements PNNL is operated by Battelle Memorial Institute for the U.S. Department of Energy under contract DE-AC05-76RL01830. This work was sponsored by S. Kleinbaum in association with the U.S. Department of Energy Office of Vehicle Technologies as part of the Lightweight Materials program along with contributions from participating entities including Honda R&D Americas, and Arconic Inc.

References

1. Cederqvist L, Reynolds AP (2001) Factors affecting the properties of friction stir welded aluminum lap joints. Weld J New York 80(12):281-s
2. Song Y, Yang X, Cui L, Hou X, Shen Z, Xu Y (2014) defect features and mechanical properties of friction stir lap welded dissimilar AA2024–AA7075 aluminum alloy sheets. Mater Des 55:9–18. https://doi.org/10.1016/j.matdes.2013.09.062
3. Threadgill PL, Leonard AJ, Shercliff HR, Withers PJ (2009) Friction stir welding of aluminium alloys. Int Mater Rev 54(2):49–93
4. Upadhyay P, Reynolds AP (2010) Effects of thermal boundary conditions in friction stir welded AA7050-T7 sheets. Mater Sci Eng A 527(6):1537–1543. https://doi.org/10.1016/j.msea.2009.10.039

Friction Stir Welding of Lap Joints Using New Al–Li Alloys for Stringer-Skin Joints

Egoitz Aldanondo, Ekaitz Arruti, Alberto Echeverria and Iñaki Hurtado

Abstract The aeronautic industry is continuously looking for new structural concepts with the aim of reducing dangerous gas emissions as well as reducing manufacturing costs and times. The development of advanced lightweight structures is an effective alternative to achieve the mentioned goals. Reinforced panels produced by the third generation aluminum–lithium alloys and Friction Stir Welding (FSW) can bring new solutions for more efficient aircrafts. This work presents the results obtained in the development and characterization of FSW joints directed to reinforced panel manufacturing. FSW lap joints were produced using aluminum–lithium alloys AA2099-T83 extrusions and AA2060-T8E30 sheets. Several welding parameter combinations and FSW tool designs were used to produce the joints. Joint properties were investigated by metallographic examination, microhardness tests as well as mechanical strength testing. The appropriate FSW conditions to optimize joint properties were established.

Keywords Friction stir welding · Lap joints · Al–Li

Introduction

Riveting has been the dominant joining technology for reinforced panel manufacturing for aircraft structures. However, there are some disadvantages in the riveting processes such as low productivity and lack of potential for weight reduction [1]. Welded integral structures represent benefits such as reductions in the number of necessary parts, weight saving potential as well as significant reductions in manufacturing times and costs. The main welding technologies developed have been

---

E. Aldanondo (✉) · E. Arruti · A. Echeverria
IK4 LORTEK, Arranomendia Kalea 4A, 20240 Ordizia, Spain
e-mail: Egoitz@lortek.es

I. Hurtado
Faculty of Engineering (MU-ENG), Mondragon Unibertsitatea,
Loramendi Kalea 4, 20500 Arrasate-Mondragon, Spain

Y. Hovanski et al. (eds.), *Friction Stir Welding and Processing X*, The Minerals, Metals & Materials Series, https://doi.org/10.1007/978-3-030-05752-7_8

Laser Beam Welding (LBW) and Friction Stir Welding (FSW) [2, 3], resulting in the implementation of some applications in real aircrafts [4–6]. Thus, FSW technology was proposed and investigated as alternative joining technology to riveting for lap joints in stringer to skin applications [7, 8].

Joining stringers to skin by FSW generally requires welding in the lap joint configuration, which has been investigated and reported by several authors using aeronautic aluminum alloys [9–16]. Probably the most important conclusion of these investigations is the importance of the FSW tool design to minimize the main welding imperfections [17] that are typical in FSW lap joints: Hook features and cold lap defects.

Another important aspect to be considered in aircraft structure innovation is the maturation and launch of third-generation aluminum–lithium alloys, which offer high strength, low density and excellent corrosion resistance [18]. These Al–Li alloys such as AA2099 extrusions and AA2060 sheets have been promising candidates for stringer-skin applications and, although some recent investigations have been reported on FSW of these alloys [19], further work is needed to understand the FSW process applied to them.

The work presented in this article reports on investigations of the FSW process applied to lap joints using AA2099-T83 extrusions and AA2060-T8E30 sheets, the understanding of the joint formation mechanism and the evaluation of the resulting lap joint properties.

Experimental Details

Z-shaped extrusions of aluminum alloy AA2099-T83 and sheets of alloy AA2060-T8E30 were used in this work as stringer and skin materials to perform FSW joints in the overlap configuration. The chemical composition of these alloys is shown in Table 1. The thickness of the extrusion in the joining zone was 2 mm and the thickness of the sheet was 2.5 mm. Two different tools were employed to produce the lap joints as shown in Fig. 1. The general dimensions of both tools were similar having a plain shoulder of 10 mm in diameter, a probe diameter of 4 mm and a probe length of 2.5 mm. The difference between the tools was the probe design, one having a conventional threaded cylindrical probe (Fig. 1a) and the other a probe with three flats and a mixed neutral thread (Fig. 1b). Lap joints were produced combining several welding parameters, using rotational speeds between 800 and 1200 rpm and welding speeds between 150 and 250 mm/min. All investigated joints were produced in force control using an I-STIR PDS 4 FSW system adjusting the axial force for each welding parameter condition. Thus, FSW lap joints were produced using weld pitches between 0.125 and 0.31 mm/rev. The type of FSW lap joints produced is shown in Fig. 1c.

Samples for metallographic examination were cut perpendicular to the welding direction, polished to a mirror like finish, etched using Keller's reagent, rinsed in water and dried in a warm airflow. Weld cross-sectional features of the FSW lap

Table 1 Chemical compositions of base materials, wt%

Alloy	Al	Si	Fe	Cu	Mn	Mg	Zn	Ti	Ag	Li	Zr
2060-T8E30	Bal.	0.07	0.07	3.4–4.5	0.1–0.5	0.6–1.1	0.3–0.5	0.1	0.05–0.5	0.6–0.9	0.05–0.15
2099-T83	Bal.	0.05	0.07	2.4–3.0	0.1–0.5	0.1–0.5	0.4–1	0.1	–	1.6–2.0	0.05–0.12

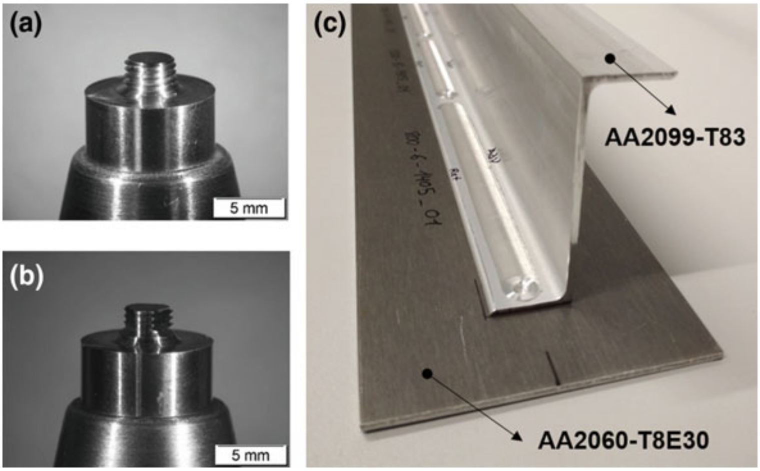

Fig. 1 FSW tools used to produce the FSW joints; **a** conventional threaded cylindrical tool; **b** three flats + neutral thread tool; and **c** FSW lap joint formed by AA2099-T83 extrusion and AA2060-T8E30 sheet

joints were examined by optical microscopy using an Olympus GX51 light optical microscope.

Microhardness tests were performed using a Vickers indenter, a load of 500 g and load application time of 15 s. Scans of indentations of approximately 20 mm in length were carried out, investigating the extension of about 10 mm from the weld centerline in both directions. The spacing between indentations was 0.5 mm. The scans were located in the mid-thickness of the AA2099-T83 extrusion as well as at a distance of 0.5 mm from the joint interface of the AA2060-T8E30 sheet. The microhardness tests were performed in the as welded condition and allowing a time of approximately 60 days between the production of the welds and the measurements.

The static mechanical strength of the FSW lap joints was investigated by pull-out tests, using a special fixture to hold the AA2060-T8E30 sheet firmly and pulling from the AA2099-T83 extrusion in the vertical-perpendicular direction to the sheet surface. All tests were performed at room temperature using a Zwick Roell Z100 tensile testing machine at a constant speed of 1.6 mm/min.

Results and Discussion

The quality of the FSW lap joints produced using different tools and welding parameters was evaluated based on their as welded surface quality, severity of welding imperfections as well as mechanical properties. The following sections summarize the main results obtained in this work:

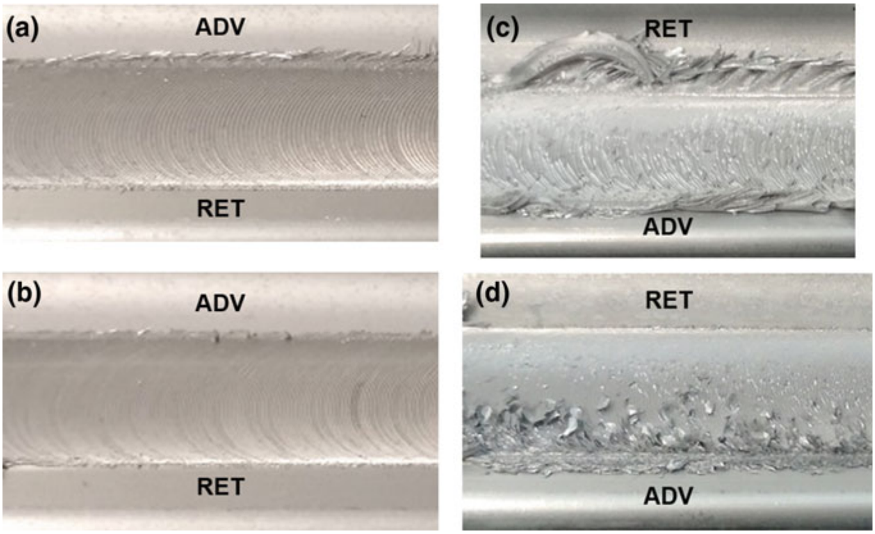

Fig. 2 Close-up images showing the surface quality of welds performed by a tool with three flats at 800 rpm and 250 mm/min; b tool with three flats at 1200 rpm and 250 mm/min; c conventional threaded tool at 800 rpm and 250 mm/min; d conventional threaded tool at 1200 rpm and 250 mm/min

Surface Quality

The surface appearance of FSW lap joints produced by the two tools and different welding parameters is shown in Fig. 2. As a general result, the joints produced by the tool with three flats presented a superior surface quality than those produced with a conventional threaded tool. This can be concluded seen in the images shown in Fig. 2a, b which contain a minimal amount of toe flash in comparison with Fig. 2c, d, which were produced with the conventional threaded tool and presented a larger amount of flash. Thus, it could be concluded that the implementation of flats on the probe produced favorable material flow and consolidation capacity of the FSW tool. This conclusion is in agreement with previous results obtained in FSW lap joining [12, 13], showing that the weldability window and the quality of the lap joints can be higher for tools featuring flats.

Metallographic Examination

Cross-sections of FSW lap joints produced under different welding parameters with both tools are presented in Figs. 3, 4, and 5. No volumetric defects were observed in the welds performed within the range of investigated welding parameters. However, significant differences were observed in typical FSW imperfections [17] of lap joints

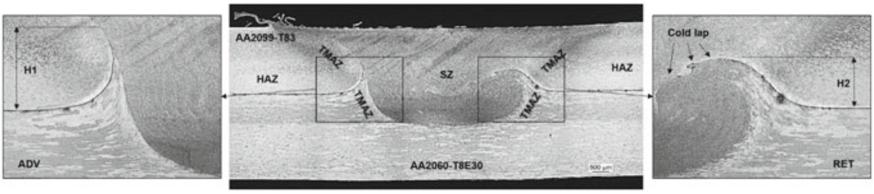

Fig. 3 Cross-section of FSW lap joint produced at 1200 rpm and 250 mm/min by a conventional threaded tool

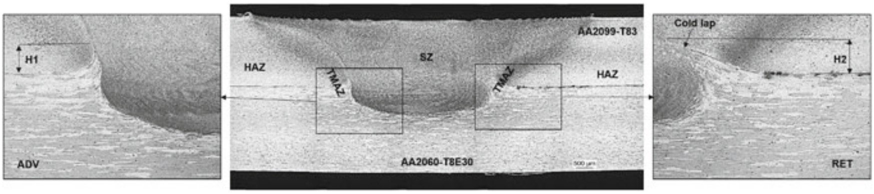

Fig. 4 Cross-section of FSW lap joint produced at 1200 rpm and 250 mm/min by a tool with three flats

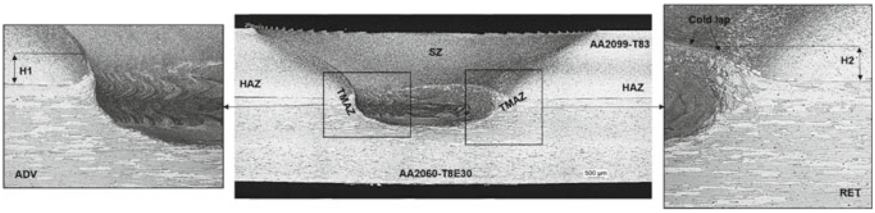

Fig. 5 Cross-section of FSW lap joint produced at 800 rpm and 250 mm/min by a tool with three flats

such as hooks and cold lap defects. Relatively large hook features were observed in both the advancing and the retreating side in joints produced by the conventional threaded tool as it is shown in Fig. 3. The magnified images of the sides show the hook features in the thermomechanically affected zone (TMAZ) regions in the advancing side (or H1) in the left as well as the hook in the retreating side (or H2) in the right. The highly deformed grain orientations of AA2060-T8E30 sheet material of the TMAZ regions are indicative of the vertical material flow induced by the conventional threaded tool, which is the main formation mechanism of the hook features. In addition to this, a cold lap defect feature was observed in the retreating side progressing from the tip of the hook towards the stir zone (SZ).

A reduction on the severity and size of the hook features was observed in FSW lap welds performed by the tool with three flats as shown in Figs. 4 and 5. In addition to that the hook size remained practically the same regardless the rotational speed used to perform the joints. This effect can be observed comparing the hook features in Figs. 4 and 5, which show equivalent FSW lap joints performed at 1200 rpm and

800 rpm, respectively. Thus, it is feasible to increase the rotational speed, without increasing the hook size, in order to produce a higher deformation at the interface, promoting a more extensive mixing of material and limiting the cold lap defect formation. Similar conclusions were obtained in previous works carried out with other aeronautic aluminum alloys [12].

The hooks (H1, H2) of FSW lap joints performed using the two tools previously described herein, and several welding parameters are represented as a function of the weld pitch in Fig. 6. It is clearly shown that the hook features produced by the conventional threaded tool are significantly larger, especially when low weld pitch values are employed. The hook size decreases as the weld pitch increases for the conventional threaded tool due to the less intensive vertical material flow induced at lower rotational speeds and higher welding speeds. This is not the case for the tool with three flats + neutral thread as the hook remains equivalent for all the investigated weld pitch range. The globally neutral nature of the three sections of threads present on the probe eliminates a preferential vertical flow of plasticized material resulting in limited hook formation.

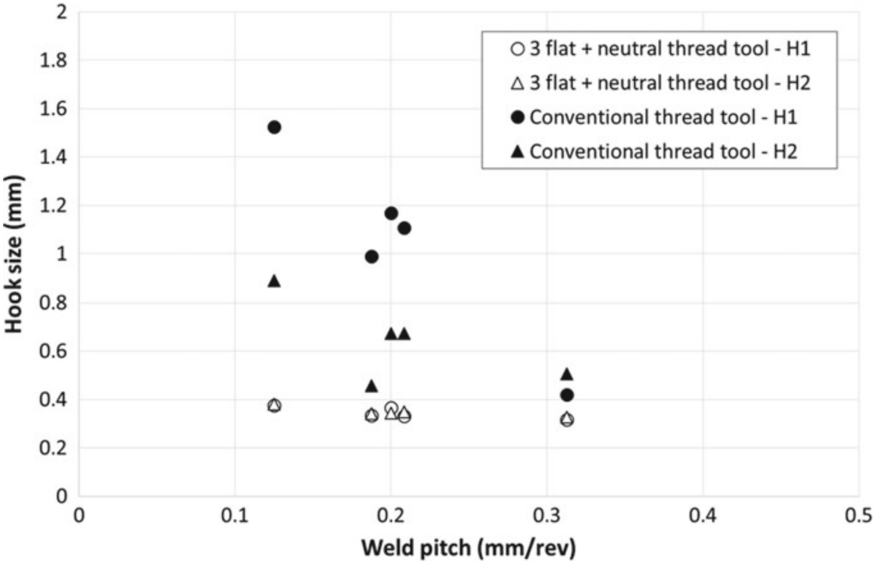

Fig. 6 Representation of the hook size measured in FSW lap joints produced using different welding parameters and weld pitches

Microhardness Testing

The microhardness distribution of different microstructural regions of FSW lap joints in the extrusion AA2099-T83 and the sheet AA2060-T8E30 are presented in Figs. 7 and 8 respectively. The obtained results are in agreement with the conclusions reported by Huang et al. [19], where FSW lap joints with AA2099-T83 and AA2060-T8E30 were investigated. A significant hardness reduction in the HAZ, TMAZ and SZ regions was observed which is typical in FSW of precipitation hardening aluminum alloys [13]. Microstructural phenomena such as dissolution, coarsening and precipitation of the precipitates, which are induced by the complex thermomechanical cycle by the FSW process, directly influence the hardness. Therefore, the hardness distribution usually depends on the FSW parameters used to produce the joints.

A nonsymmetric hardness distribution was observed in the scans performed in the AA2099-T83 extrusion as shown in Fig. 7. A HAZ extension of approximately 9 mm was observed at the advancing side, while the retreating side showed a larger HAZ. The heat accumulation at the edge of the stringer in the retreating side could be the reason for a larger HAZ, producing a more severe overaging effect at this region. In addition to that, the FSW lap joint produced using a weld pitch of 0.21 mm/rev also presented a larger HAZ in comparison with the one performed at 0.31 mm/rev. The higher temperatures and heat accumulation produced by the weld pitch of 0.21 mm/rev could be again the reason for that. This effect was not observed at the advancing side of these FSW lap joints. A maximum hardness reduction of 74 HV0.5 was measured, from 168 HV0.5 of the base material to 94 HV0.5 of the minimum hardness at the HAZ at the advancing side, which represents a ~44% drop.

Figure 8 shows the hardness distribution of the AA2060-T8E30 sheet, where a symmetric HAZ of approximately 16 mm was observed. A maximum hardness drop

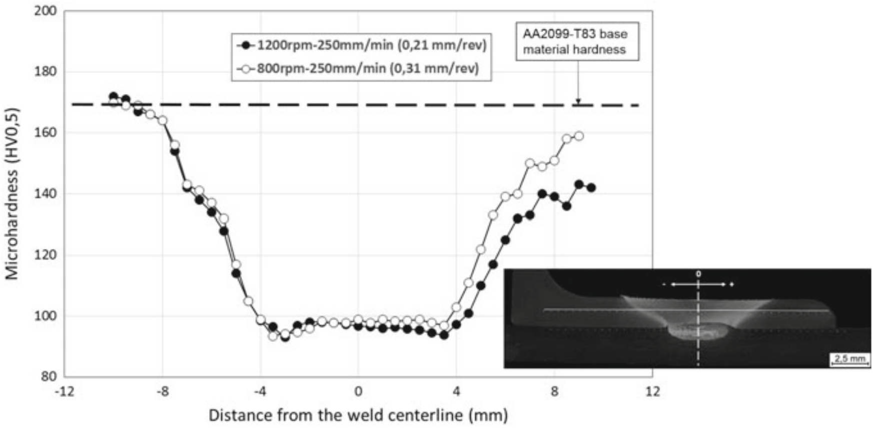

Fig. 7 Microhardness value distributions in the AA2099-T83 extrusion of FSW joints performed using 0.21 mm/rev and 0.31 mm/rev weld pitches and a tool with three flats

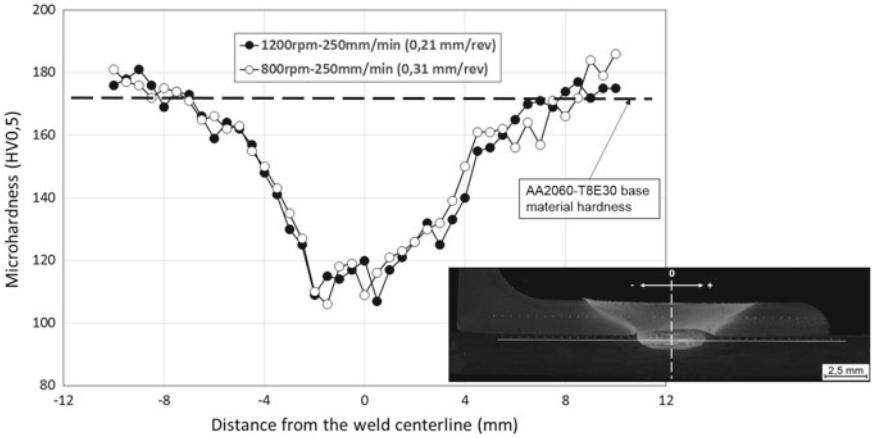

Fig. 8 Microhardness value distributions in the AA2060-T8E30 sheet of FSW joints performed using 0.21 and 0.31 mm/rev weld pitches and a tool with three flats

of ~38% was estimated from 172 HV0.5 of base material to 106 HV0.5 measured at the SZ region boundaries. No significant differences were observed between FSW lap joints performed at 0.21 and 0.31 weld pitches.

Mechanical Strength Testing

Pull-out tests were performed with the aim of evaluating the static mechanical strength of the FSW lap joints produced using several welding parameters and both tools. Figure 9 shows two limit cases that represent the critical influence of the FSW lap joint quality on the joint strength. A maximum pull-out load of 2.8 kN was observed for the FSW lap joint produced by the tool with three flats + neutral thread and welding parameters of 1200 rpm and 250 mm/min. The small hooks and the effective reduction of the cold lap defect shown in Fig. 4 are representative of an appropriate stirring and mixing of materials, producing a good quality weld that presented a failure in the stringer outside the weld. On the other hand, a FSW lap joint produced by the conventional threaded tool at 800 rpm and 150 mm/min presented an interfacial failure, as shown in the top-right image in Fig. 9, with an ultimate pull-out load of 1.95 kN. In this case, the larger size of the hooks and the presence of the cold lap defect in the weld were found to be the main factors that reduced the joint quality and load carrying capacity.

In general, FSW lap joints produced by the tool with three flats + neutral thread presented superior mechanical strength in comparison with the conventional threaded tool, with average ultimate pull-out load values of 2.62 kN and 2.18 kN, respectively.

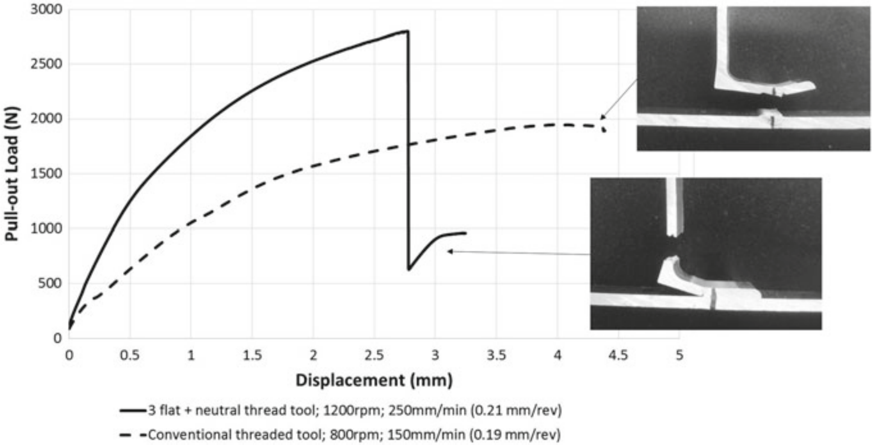

Fig. 9 Pull-out strength and failure mode of FSW lap joints produced by different tools and welding parameters

Thus, it could be concluded that superior weld quality and load carrying capacity can be obtained by the tool with three flats + neutral thread.

Conclusions

In this work, FSW lap joints were performed with AA2099-T83 extrusions and AA2060-T8E30 sheet materials, using different tools and welding parameters, and the joint properties were investigated. The following conclusions could be obtained:

- The tool with three flats + neutral thread can produce FSW lap joints with superior surface quality than the conventional threaded tool.
- The FSW lap joints produced by the tool with three flats + neutral thread present superior weld quality (reduced hooks and cold lap defects) than the ones produced by the conventional threaded tool.
- The tool with three flats + neutral thread allows to increase the rotational speed without promoting vertical flow of plasticized material nor increasing the hook size.
- Hardness drops of approximately 44% and 38% were observed for AA2099-T83 extrusion and AA2060-T8E30, respectively.
- An average ultimate pull-out load of 2.62 kN with a failure outside the joint was achieved in FSW lap joints produced by the tool with three flats + neutral thread. This is a ~20% higher than the values obtained with the joints performed by the conventional threaded tool.

Thus, the main conclusion is that the tool with three flats + neutral thread has the capability to produce FSW lap joints of superior quality and higher load carrying capacity, showing a larger weldability window. Within this window, 1200 rpm and 250 mm/min were identified as the best welding parameters that resulted in the highest weld quality.

Acknowledgements This work has been performed in the frame of the project ecoTECH within the AIRFRAME ITD of the Clean Sky 2 programme of the H2020. The authors acknowledge the funding received for this project under the project ID 807083 of the call H2020-IBA-CS2-GAMS-2017.

References

1. Rendings KH (2001) Aluminium structures used in aerospace—status and prospects. Mater Sci Forum 242:11–24
2. Mendez P, Eagar T (2002) New trends in welding in the aeronautic industry. In: Proceedings of 2nd conference of new manufacturing trends, Bilbao, Spain
3. Talwar R et al (2000) Friction stir welding of airframe structures. In: Proceedings of 2nd international symposium on friction stir welding, Gothenburg, Sweden, pp 27–29
4. Assler H, Telgkamp J (2006) Design of aircraft structures under special consideration of NDT. In: Proceedings of 9th European conference on NDT, Berlin (Germany)
5. Christner B (2016) A friction stir welded jet aircraft: from concept to reality. In: Proceedings of 11th international symposium on friction stir welding, Cambridge, UK, 17 May 2016
6. Fernandez F (2010) FSW applied on mid-size aircraft. In: Proceedings of 8th international symposium on friction stir welding, Timmendorfer Strand, Germany, 18–20 May 2010
7. Tavares SM (2011) Design and advanced manufacturing of aircraft structures using friction stir welding. PhD thesis, Universidade do Porto (Portugal)
8. Freeman J, Moore G, Thomas B, Kok L (2006) Advances in FSW for commercial aircraft applications. In: 6th international symposium on friction stir welding, Toronto (Canada)
9. Cederquist L, Reynolds AP (2001) Factors affecting the properties of friction stir welded aluminium lap joints. Weld J Res Suppl 80:281
10. Dubourg L et al (2010) Process optimisation and mechanical properties of friction stir lap welds of 7075-T6 stringers on 2024-T3 skin. Mater Des 31:3324–3330
11. Buffa G et al (2009) Friction stir welding of lap joints: Influence of process parameters on the metallurgical and mechanical properties. Mater Sci Eng A 519:19–26
12. Aldanondo E et al (2016) Microstructural features in friction stir welded lap joints. In: Proceedings of 10th international conference on trends in welding research, Tokyo, Japan, 10–14 Oct 2016
13. Aldanondo E, Arruti E, Echeverria A (2017) Friction stir weld lap joint properties in aeronautic aluminium alloys. In: Proceedings of 148th friction stir welding and processing X, in annual meeting and exhibition TMS2017, San Diego (USA)
14. Ji S et al (2016) Effect of reverse-threaded pin on mechanical properties of friction stir lap welded alclad 2024 aluminum alloy. J Mater Sci Technol 32:671–675
15. Yang X et al (2014) Defect features and mechanical properties of friction stir lap welded dissimilar AA2024-AA7075 aluminum alloy sheets. Mater Des 55:9–18
16. Liu H et al (2016) The effect of interface defect on mechanical properties and its formation mechanism in friction stir lap welded joints of aluminum alloys. J Mater Process Technol 238:244–254

17. ISO, ISO25239 (2011) Friction stir welding—aluminium, Geneva (Switzerland)
18. Eswara Prasad N, Gokhale AA, Wanhill R (2014) Aluminium-lithium alloys: processing, properties and applications. Elsevier-BH, Oxford, UK
19. Huang Y et al (2018) Interface characteristic and tensile property of friction stir lap welding of dissimilar aircraft 2060-T8 and 2099-T83 Al–Li alloys. Int J Adv Manuf Technol 94:1253–1261

Part IV
Simulation

Probing Tool Durability in Stationary Shoulder Friction Stir Welding

B. Vicharapu, H. Liu, H. Fujii, N. Ma and A. De

Abstract The effect of process parameters on temperature distribution in stationary shoulder friction stir welding (SSFSW) and conventional FSW of AA7010-T6 alloy are studied using a three-dimensional heat conduction analysis. The computed results are validated from experimentally measured results reported in independent literature. The tool torque, traverse force and the mechanical stresses on the FSW tool were evaluated analytically using mechanics based principles. The estimated results showed that the tools used in the SSFSW process were more likely to early failure.

Keywords Stationary shoulder friction stir welding · Torque · Traverse force
Tool durability factor

Introduction

Friction stir welding (FSW) is increasingly considered as an alternate joining technology for welding of Al–Cu and Al–Zn alloys since solidification cracking and hot cracking in joints, which are common in fusion welding of these alloys, can be avoided in FSW [1–4]. Several variants of FSW were attempted in the recent past [2]. Stationary shoulder friction stir welding (SSFSW) is found as an efficient variant that involves the rotation of only the tool probe with its shoulder remaining stationary during welding [5–7].

The SSFSW offers several potential advantages over the conventional FSW process that include improved joint properties, lower level of residual stresses, and narrower stir zone (SZ), thermo-mechanically affected zone (TMAZ) and heat affected zone (HAZ) [5–7]. SSFSW improves the surface finish of the weld and reduces the

---

B. Vicharapu (✉) · H. Liu · H. Fujii · N. Ma
Joining and Welding Research Institute, Osaka, Japan
e-mail: buchibabu@jwri.osaka-u.ac.jp

A. De
Indian Institute of Technology, Mumbai, India

Y. Hovanski et al. (eds.), *Friction Stir Welding and Processing X*, The Minerals, Metals & Materials Series, https://doi.org/10.1007/978-3-030-05752-7_9

workpiece thinning with a further energy saving of 20–30% over the conventional FSW process [5–7]. However, the stationary tool shoulder resulted reduced rate of heat generation in comparison to the conventional process and thus, the tool probe would experience colder and stronger alloy. As a result, the longevity of the FSW tool in SSFSW process could remain a concern. [5–11]. For example, Wu et al. [7] used a very high tool probe rotational speed of 1500 rpm in SSFSW of 6.3 mm thick AA7050 plates to avoid the tool failure in contrast to a tool rotational speed of 700 rpm in the conventional process [6]. Sun et al. [8] employed nearly 25% larger-diameter tool probes to avoid tool failure in SSFSW of 6.35 mm thick AA7050. These tools were selected by trial and error approach [6–8]. Very few studies are dedicated till date to assess the stresses experienced by tool probe based on principles of mechanics in FSW and no such studies are reported for SSFSW [9–11].

A prior estimation of the peak temperature and mechanical stresses experienced by the tool probe is found useful in design for FSW process and a similar approach is required for SSFSW [9–11]. The well designed tools could ensure uninterrupted welds, and more importantly, these tools could offer great cost savings. Therefore, an attempt is made here for the assessment of torque, traverse force and tool life in SSFSW and the results are compared with the FSW.

Numerical Modeling

A transient three-dimensional heat conduction based numerical model, *JWRIAN©* is developed indigenously at *Joining and Welding Research Institute (JWRI)©* is utilized to simulate the FSW process [12]. The governing equation can be stated as

$$\frac{\partial}{\partial x}\left(k\frac{\partial T}{\partial x}\right)+\frac{\partial}{\partial y}\left(k\frac{\partial T}{\partial y}\right)+\frac{\partial}{\partial z}\left(k\frac{\partial T}{\partial z}\right)+\dot{Q}=\rho C_p\frac{\partial T}{\partial t} \tag{1}$$

where k, ρ, C_p, T and t represent thermal conductivity, density, specific heat, temperature and time variable, respectively. The x-, y- and z-coordinates represent the longitudinal, transverse and thickness directions, respectively. The term, $\dot{Q}$, accounts for the rate of volumetric heat generation and can be expressed as [13–15]

$$\dot{\mathrm{Q}}=\eta_h\times[\eta_m(1-\delta)\tau_y+\delta\mu_f P_N](\omega r-U_1\sin\theta)(A/V) \tag{2}$$

where η_h and η_m refer to percentage of heat transferred to the workpiece and mechanical efficiency, respectively, and δ and μ_f depict fractional sliding and coefficient of friction, respectively. The τ_y, P_N, ω and r refer to the shear yield strength of workpiece as function of temperature, axial pressure, angular velocity of the tool and radial distance from the tool center, respectively, U_1 is the welding speed, θ is the orientation of the tool with the welding direction, and A and V are the tool pin–workpiece contact area and the presumed shear volume around the tool pin. The local variations in δ and μ_f are considered as [13–17]

$$\delta = -0.026 + 0.31\exp(r\omega/1.87); \tag{3}$$

$$\mu_f = 0.51\exp(-\delta r\omega) \tag{4}$$

The heat generation due to the viscous dissipation of the plasticized workpiece material is neglected.

The solution domain is discretized using a three-dimensional eight node brick elements with the temperature as the nodal degrees of freedom.

The torque (M) experienced by the FSW tool is estimated analytically as $M = M_L + M_T$ where M_L and M_T refer to the sliding and sticking components of the torque and are given as [13, 14]

$$\mathrm{M_L} = \int_{\mathrm{R_P}}^{\mathrm{R_S}} \mathrm{r} \times \delta\mu_f \mathrm{P_N} \times (2\pi \mathrm{rdr}) + \int_{0}^{\mathrm{R_P}} \mathrm{r} \times \delta\mu_f \mathrm{P_N} \times (2\pi \mathrm{rdr}) \tag{5}$$

$$\mathrm{M_T} = \int_{\mathrm{R_P}}^{\mathrm{R_S}} \mathrm{r} \times (1-\delta)\tau_y \times (2\pi \mathrm{rdr}) + \int_{0}^{\mathrm{L}} \mathrm{r} \times (1-\delta)\tau_y \times (2\pi \mathrm{rdl}) + \int_{0}^{\mathrm{R_P}} \mathrm{r} \times (1-\delta)\tau_y \times (2\pi \mathrm{rdr}) \tag{6}$$

where, $\mathrm{R_S}$, $\mathrm{R_P}$, L and τ_y refer to the shoulder radius, tool probe radius, probe length, and the temperature dependent shear yield strength of the deforming material, respectively. The sum of the first two terms in Eqs. (5) and (6) contributes to the shoulder torque ($\mathrm{M_S}$) and the remaining terms represent the probe torque.

The traverse force (F) experienced by the tool is estimated as $F = F_S + F_P$ where $\mathrm{F_S}$ and $\mathrm{F_P}$ refer to the components of forces on the tool shoulder and the pin, and can be given as [13, 14]

$$\mathrm{F_S} = \int_{\mathrm{R_P}}^{\mathrm{R_S}} [(1-\delta)\tau_y + \delta\mu_f \mathrm{P_N}] \times (2\pi \mathrm{rdr}); \tag{7}$$

$$\mathrm{F_P} = \int_{0}^{\mathrm{L}} \sigma_y \times (\mathrm{dA}) + \int_{0}^{\mathrm{R_P}} [(1-\delta)\tau_y + \delta\mu_f \mathrm{P_N}] \times (2\pi \mathrm{rdr}) \tag{8}$$

where dA refers to the projected area of the probe.

The mechanical stresses on tool probe are estimated considering the pin as a cantilever beam [13, 14] undergoing a combined bending and torsion due to the traverse force and torque, respectively. As a result, the components of stresses acting on the tool pin include the normal and shear stresses due to bending (σ_B, τ_B), and the shear stress (τ_T) due to torsion. The resultant maximum shear stress (τ_{max}) at any point on the pin profile can be expressed analytically as [11, 13]

$$\tau\text{max} = \sqrt{\left(\frac{\sigma_B}{2}\right)^2 + (\tau_B + \tau_T \cos\beta)^2 + (\tau_T \sin\beta)^2} \tag{9}$$

where β is the angle between τ_T and τ_B, measured in a counter-clockwise direction from τ_T to τ_B.

The tool durability index (*I*) is defined as the ratio between the maximum resultant shear stress at the tool probe root to the shear yield strength of tool material at the computed peak temperature (T_P). Thus, *I* becomes a non-dimensional variable.

The solution domain with a size of L (300) × W (70) × Th (6.35) mm^3 is discretized with an eight noded brick element with temperature as the nodal degrees of freedom. Only a half-symmetric model was considered here by considering the symmetry along the original weld joint interface. Finer mesh (~0.9 mm^3) in the vicinity of the tool and gradually coarser mesh away from the tool are used to reduce the computation time. To account the heat loss from the solution domain, heat transfer coefficients, 60 W/m^2 and 10 W/m^2 are used respectively from the workpiece bottom surface, and the rest of the surfaces. The heat loss along the symmetric plane is arrested.

Materials and Methods

Table 1 shows the tool dimensions and the process input conditions considered for the current study. Table 2 shows the thermo-physical properties employed for the numerical simulations and analytical calculations. The thermal cycles were extracted approximately 5.0 mm away from the weld center line and 2.0 mm below the workpiece top surface on the advancing side and used for validation of the computed results [6].

Results and Discussion

Figure 1 compares the computed isotherms between FSW and SSFSW. The tool rotational speeds 700 rpm and 1500 rpm were used respectively for FSW and SSFSW at a constant welding speed of 100 mm/min. The computed isotherms shown in

Table 1 Tool dimensions and input process conditions considered for the study [6]

Variant	Tool dimensions (mm)				Welding conditions	
	DSH	DPR	DPT	LP	N (rpm)	v (mm/min)
FSW	18	6.2	4.0	6.1	700	100
SSFSW					1500	

DSH, DPR and DPT refer to shoulder, pin root and pin tip diameters, respectively, and LP is pin height. The N and v refer to tool rotational and welding speeds, respectively

Table 2 Thermo-physical properties of AA7010-T6 [13]

Density (kg/m^3)	2750
Solidus temperature (K)	775
Th. conductivity (W/m K)	$83.86 + 0.20 \times T - 3.413e{-}7 \times T^2$
Sp. heat (J/kg K)	$859.02 + 1.21 \times T - 4.13e{-}4 \times T^2$
Yield strength (MPa)	$3.22 + 4846.31 \times \exp(-T/118.48)$

T is temperature in Kelvin

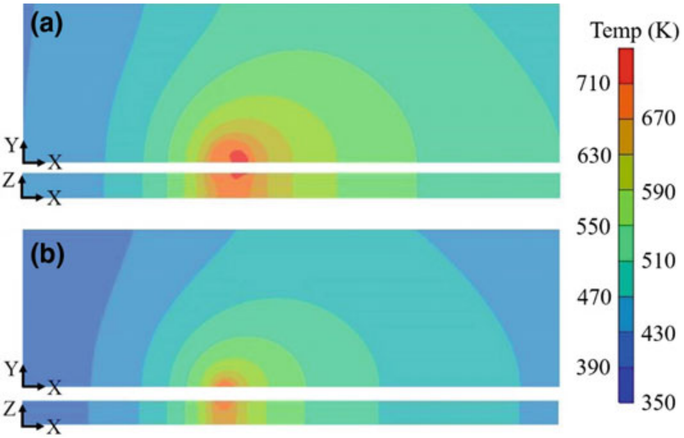

Fig. 1 Computed isotherms at tool rotational speed (rpm) of **a** 700 during friction stir welding, and **b** 1500 during stationary shoulder friction stir welding, at a welding speed of 100 mm/min

Fig. 1a are apparently wider in FSW due to the additional heat generated along the tool shoulder—workpiece interface, whereas heat generated by the shoulder is none in SSFSW due to the stationary shoulder. Therefore, the computed peak temperatures are also higher in the conventional FSW. For example, the computed peak temperatures in conventional FSW and SSFSW are 748 K and 660 K, which are ~0.8Ts and ~0.7Ts, respectively, where T_S is the solidus temperature of the workpiece material. The peak temperatures between ~0.7Ts and ~0.9Ts are widely reported in FSW of aluminum alloys [11, 13]. Figure 2 shows the computed and corresponding measured thermal cycles for two different welding conditions. In both FSW and SSFSW, the computed peak temperatures at the measured locations are found to be lower than the corresponding measured ones. The percentages of error between the computed and corresponding measured results are well below 10% that is attributed to simplified assumptions in the model. For example, the rate of heat generation due to viscous dissipation is neglected, and the effect of tool tilt angle on the rate of heat generation is also not considered in the calculations. The computed thermal cycles are in fair agreement with the corresponding measured results.

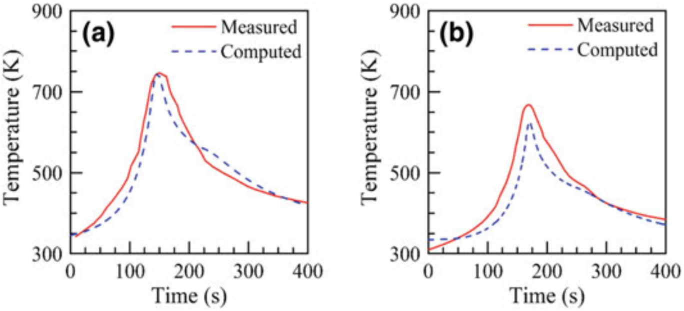

Fig. 2 Computed and corresponding measured thermal cycles at tool rotational speed (rpm) of **a** 700 during friction stir welding, and **b** 1500 during stationary shoulder friction stir welding, at a welding speed of 100 mm/min

Table 3 shows the computed torque and traverse force in both FSW and SSFSW. The computed tool torque and traverse force in FSW and SSFSW are around 24.3 Nm and 6.0 Nm, and around 0.9 kN and 1.2 kN, respectively. Wu et al. [7] reported the measured toque value of ~29 Nm in FSW of 6.35 mm thick AA7050-T6 plates for the similar welding conditions [6]. The difference in torque is attributed to the difference in yield strength of these two alloys at the computed peak temperature and the difference in contact conditions between the tool workpiece [13]. It is worth mentioning here that the slip (refer Eq. (3)) between tool workpiece varies significantly within aluminum alloys, and the torque is more sensitive to the slip [13]. Therefore, the computed values shown in Table 3 are reasonable.

Figure 3 shows the analytically estimated components of stresses (σ_B, τ_B, τ_T, τ_{max}) on the tool probe. All four components of stresses on tool probe are found to be higher in SSFSW, since the torque and force experienced by the tool probe are higher. Figure 3 depicts the normal stress due to bending is maximum at 0° and 180°, and shear stress due to bending is maximum at 90° and 270°, in both FSW and SSFSW. Since, shear stress due to bending at the tool probe periphery is constant, the highest maximum resultant shear stresses are found at 90° (refer Eq. 9), where the normal stress due to bending is 0.0. The highest maximum resultant shear stresses are found as 92 MPa and 122 MPa, respectively in FSW and SSFSW. Table 3 further compares

Table 3 Computed peak temperature, torque, traverse force, maximum resultant shear stress and tool durability index (I) in both FSW and SSFSW

Variant	T_P (K)	Toque (Nm)			Traverse force (kN)			τ_{Max} (MPa)	I
		M_S	M_P	M	F_S	F_P	F_T		
FSW [7, 13]	750	21.3	3.0	24.3	0.3	1.11	1.45	92	5.7
SSFSW	660	0.0	6.0	6.0	0.0	1.61	1.61	122	4.1

M_S and M_P refer to the shoulder torque and probe torque, and $M = M_S + M_P$. F_{sT} and F_{PT} refer to the shoulder force and probe force, and $F_T = F_S + F_P$. I refers to the estimated tool durability index

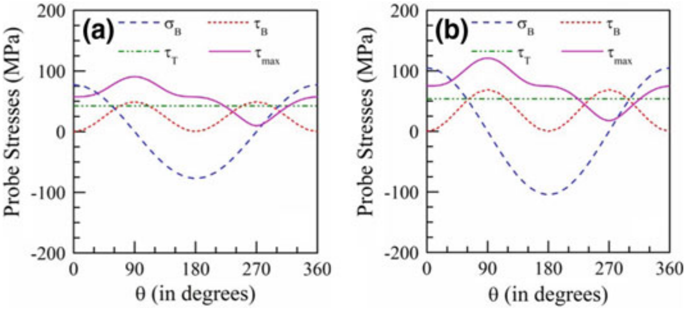

Fig. 3 Analytically estimated values of the components of stresses around the tool probe root at tool rotational speed (rpm) of **a** 700 during friction stir welding, and **b** 1500 during stationary shoulder friction stir welding, at a welding speed of 100 mm/min

the estimated maximum resultant shear stress (τ_{max}) and tool durability index (*I*) in FSW and SSFSW. The computed *I* in FSW and SSFSW are 5.7 and 4.1, respectively for the given welding conditions. The computed values of *I* is much lower in SSFSW since the tool has to traverse through the colder and stronger alloy thereby experiencing greater stresses and susceptibility to early failure. It is presumed that the early fracture of tool is the most likely with the computed value of *I* tending towards lower than unity, i.e. when the maximum resultant shear stress acting on the tool probe is higher than the shear yield strength of the tool material [10]. Therefore, as per the calculations provided in Table 3, the tools considered for the experiments are safe. However, at higher welding speeds and lower tool rotational speeds, the tool material should advance through colder and harder workpiece material. Therefore, the tool probe in SSFSW is more susceptible to premature failure under such conditions. Buchibabu et al. [13] also opined same in FSW of 9.5 mm thick AA7075-T6. Further studies which focus on the influences of tool probe rotational speed, welding speed and plate thickness and workpiece alloy strength on tool durability factor will be useful. The detailed investigation on coupled experimental and numerical investigations on the above mentioned subject in SSFSW of AA7xxx series is underway.

Conclusions

In stationary shoulder friction stir welding, the traverse force experienced by the tool probe is ~45% higher in comparison with the friction stir welding for the welding conditions considered here. As a result, the maximum resultant shear stress is ~33% higher, and tool durability index is ~31% lower in stationary shoulder friction stir welding. Apparently, the tool durability is presumed to decrease further at higher welding speeds and lower tool rotational speeds, which increases the susceptibility to early failure of tools in stationary shoulder friction stir welding. Therefore, it is concluded that the susceptibility of the tools to failure is higher in stationary shoulder friction stir welding even when the probe rotational speed is more than twice to that in friction stir welding.

Acknowledgements This article is based on the results obtained from a future pioneering project commissioned by the New Energy and Industrial Technology Development Organization (NEDO). Dr. B. Vicharapu would like to express his deep sense of gratitude to Mr. K. Narasaki for helping in the development of FSW code.

References

1. Cai W, Daehn G, Anupam V, Li J, Khan H, Mishra R, Komarasamy M (2018) A state-of-the-art review on solid state metal joining. J Manuf Sci Eng. https://doi.org/10.1115/1.4041182
2. Mishra RS, Ma ZY (2005) Friction stir welding and processing. Mater Sci Eng R 50:1–78
3. Fujii H, Cui L, Maeda M, Nogi K (2006) Effect of tool shape on mechanical properties and microstructure of friction stir welded aluminum alloys. Mater Sci Eng A 419:25–31
4. Buchibabu V, Reddy GM, Kulkarni DV, De A (2016) Friction stir welding of thick Al-Zn-Mg alloy plate. J Mater Eng Perform 25(3):1163–1171
5. Padhy GK, Wu CS, Gao S (2015) Auxialary energy assisted friction stir welding—status review. Sci Technol Weld Join 20(8):631–649
6. Davies PS, Wynne BP, Rainforth WM, Thomas MJ, Threadgill PL (2011) Development of microstructure and crystallographic texture during stationary shoulder friction stir welding of Ti-6Al-4V. Metal Mater Trans A 42A:2278–2289
7. Wu H, Chen YC, Strong D, Prangnell P (2015) Stationary shoulder FSW for joining high strength aluminum alloys. J Mater Process Technol 221:187–196
8. Sun T, Roy MJ, Strong D, Withers PJ, Prangnell PB (2018) The effect of shoulder coupling on the residual stress and hardness distribution in AA7050 in friction stir butt welds. Mater Sci Eng A 735:218–227
9. Sun T, Roy MJ, Strong D, Withers PJ, Prangnell PB (2017) Comparison of residual stress distributions in conventional and stationary shoulder high-strength aluminum alloy friction stir welds. J Mater Process Technol 242(1):92–100
10. Rai R, De A, Bhadeshia HKDH, Debroy T (2011) Review: friction stir welding tools. Sci Technol Weld Join 17(4):338–341
11. Arora A, Mehta M, De A, Debroy T (2012) Load bearing capacity of tool pin during friction stir welding. Int J Adv Manuf Technol 61(9):911–920
12. Ma M (2016) An accelerated explicit method with GPU parallel computing for thermal stress and welding deformation of large structure models. Int J Adv Manuf Technol 87:2195–2211
13. Buchibabu V, Reddy GM, De A (2017) Probing traverse force, torque and tool durability in Friction stir welding of aluminum alloys. J Mater Process Technol 241(1):86–92
14. Mehta M, Chatterjee, De A (2013) Monitoring torque and traverse force in friction stir welding from input electrical signatures of driving motors. Sci Technol Weld Join 18:191–197
15. Nandan R, Roy GG, Debroy T (2006) Three-dimensional heat and material flow during friction stir welding of stainless steels. Acta Mater 55(3):883–895
16. Vicharapu B, Kanan LF, Clarke T, De A (2017) An investigation of friction hydro-pillar processing. Sci Technol Weld Join 22(7):555–561
17. Luis FK, Vicharapu B, Bueno AFB, Clarke T, De A (2018) Friction hydro-pillar processing of a high carbon steel: joint structure and properties. Metal Mater Trans B 49(2):699–708

On the Material Bonding Behaviors in Friction Stir Welding

Gaoqiang Chen, Han Li and Qingyu Shi

Abstract The material bonding defects such as root flaws have been an important kind of welding defects in friction stir welds. In recent years, the growing application of friction stir welding (FSW) in fabricating many critical components, e.g., rocket fuel tank, renewed the need for in-depth understanding for the formation of material bonding defects. This study provides a quantitative investigation to access the material bonding behavior via numerical simulation. It is found that the rapid growth of the bonded fraction is developed owing to the localized thermal-mechanical processing during FSW. The thermal-mechanical condition at the root region is deteriorated greatly as the tool rotation rate decreases. The validity of the simulation results at different welding parameters is confirmed by our microstructural observation. The concepts that we develop open up quantitative prospects for the elimination of defects due to insufficient solid state bonding in FSW and similar material processing approaches.

Keywords Friction stir welding · Material bonding
Thermal-mechanical condition · Defect prediction

Introduction

Friction stir welding (FSW) [1] is one typical solid state welding approach for joining many structural materials, such as high strength aluminum alloys [2]. In FSW, the material is welded without fusion. This is crucially important for avoiding solidification defects and reducing the heat input. Although many defects in the welds, such as root flaws [3–5], have been attributed to insufficient material bonding, the material

---

G. Chen (✉) · H. Li · Q. Shi
Department of Mechanical Engineering, Tsinghua University, Beijing 100084,
People's Republic of China
e-mail: cheng3@aliyun.com

Q. Shi
e-mail: shqy@tsinghua.edu.cn

Y. Hovanski et al. (eds.), *Friction Stir Welding and Processing X*, The Minerals,
Metals & Materials Series, https://doi.org/10.1007/978-3-030-05752-7_10

bonding behaviors, regarding how the FSW joins the initial surfaces, have not been fully understood. Insufficient material bonding leads to residual voids or crack at the bonding interface, which results in significant degradation of both the strength and ductility of the welds and thus limits the application of the FSW products. For successful solid state welding of metal surfaces, it is generally required to satisfy certain thermal-mechanical criteria in order to collapse the interfacial asperities and thus heal the interfacial void at the interface between the contacting initial surfaces. If residual interfacial void exists, the material bonding defect occurs. However, very little is known about how the originally separated materials are bonded during FSW due to the lack of observation approaches for the material bonding behaviors and the complex nature of the thermal-mechanical process during FSW. Recent years, the growing application of FSW in fabricating many critical components with exhaustive quality requirement renewed the need for investigation on the material bonding behaviors in FSW. A great interest in the development of reliable technical concept in control the welding defect is greatly desired. Therefore, the clarification of the material bonding behaviors between the initial surfaces would be critically important in order to support the development of new technical concepts for more reliable FSW.

In this paper, we use the three-dimensional numerical simulation to explore the interfacial bonding behavior between the initially separated surfaces (initial butting interface) during FSW. The evolution of the thermal-mechanical state variables such as temperature and pressure, as a function of time during the FSW process is analyzed. This model is shown to predict the bonding state in the welds at different welding parameters which is validated by the experimental observation.

Methods

In the experiment, the butt welding of 3 mm AA2024 plate was carried out. The dimensions of each workpiece were 145 mm × 55 mm × 3 mm (length × width × thickness). The welding tool shoulder was 13 mm in diameter, and length of the pin was 2.4 mm. The pin had a cylinder-like geometry. The diameter of pin was 4 mm near the shoulder and 3.5 mm at the tip. The welding process was conducted in different welding parameters. The tool rotation rate ranges from 500 rpm to 800 rpm, while the welding speed was 40 mm/min in each experiment. The position control is employed during the welding process. The employed plunge depth was 0.5 mm, and no tilt angle was adopted. The specimens for examination of the cross-sectional macrostructure were grounded, polished, and etched with Keller's solution (95 ml water, 1.5 ml hydrochloric acid, 2.5 ml nitric acid, 1 ml hydrofluoric acid) for 60 s. After that, the cross-sectional macrostructure of specimens was observed by optical microscope.

Numerical simulation was carried out to analyze the temperature and material flow field during FSW. The analysis is based on computational fluid dynamics (CFD). In the numerical simulation, the processing parameters, the dimensions of the workpiece, and the geometry of welding tool were taken as the same as those in the experiment. The three-dimensional simulation method was published in our previous paper [6]. The simulated 3D temperature field and velocity field are denoted as a function of the spatial coordination,

$$\text{Temperature} : T(x, y, z) \tag{1}$$

$$\text{Velocity} : \begin{cases} v_x(x, y, z) \\ v_y(x, y, z) \\ v_y(x, y, z) \end{cases} \tag{2}$$

The analysis of flow path is required to generate the thermal-mechanical condition experienced by the original butting interface. For a specific point located at $[x_{w0}, y_{w0}, z_{w0}]$ in the workpiece in the front of the tool before FSW, the flow path is represented by the location of the point $[x_w(t), y_w(t), z_w(t)]^T$ as a function of time, which is calculated by using

$$\begin{bmatrix} x_w(t) \\ y_w(t) \\ z_w(t) \end{bmatrix} = \begin{bmatrix} x_{w0} \\ y_{w0} \\ z_{w0} \end{bmatrix} + \begin{bmatrix} \int_0^t v_x(x_w(t), y_w(t), z_w(t))\mathrm{d}t \\ \int_0^t v_y(x_w(t), y_w(t), z_w(t))\mathrm{d}t \\ \int_0^t v_z(x_w(t), y_w(t), z_w(t))\mathrm{d}t \end{bmatrix} \tag{3}$$

where the $[x_{w0}, y_{w0}, z_{w0}]^T$ is the coordinate of the original location, and the second term at the right side is the integral term calculating the locations along the flow path. Integration along the flow paths is employed to calculate the bonded fraction by using the mathematical approaches in Ref. [7].

Results

Material Flow Pattern at the Butting Interface

The primary goal of welding is to join the initially separate surfaces of different parts. When the separate material surfaces at the butting interface flows through the vicinity of the welding tool, the separate surfaces are joined as a result of the thermal-mechanical processing. Figure 1 shows the material flow paths for the material at the butting interface in the vicinity of the welding tool. It can be found that the material flow path is influenced by the tool rotation, and thus the material flows around the welding tool from the retreating side. Finally, the deposition location is quite different

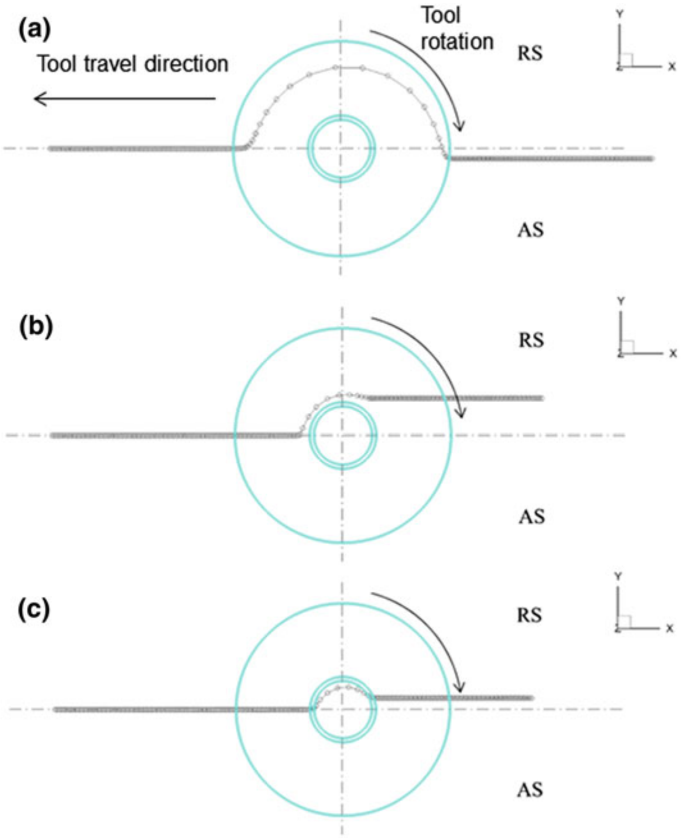

Fig. 1 Material flow paths at the butting interface. The start location of the flow paths are located at **a** 0.5 mm below the shoulder, **b** 1.5 mm below the shoulder and **c** 0.4 mm below the pin bottom

Table 1 Start and end locations of the material path analysis for material bonding

No.	Probing location	Start location (mm)		End location (mm)	
		Y	Z	Y	Z
1	0.5 mm below shoulder	0.00	1.00	−0.60 (AS)	1.06
2	1.5 mm below shoulder	0.00	0.00	2.24 (RS)	0.08
3	0.4 mm below pin bottom	0.00	−1.30	0.71 (RS)	−1.30

from the start locations of butting locations because of the complexity of the flow field. The start and end locations of these flow paths are shown in Table 1.

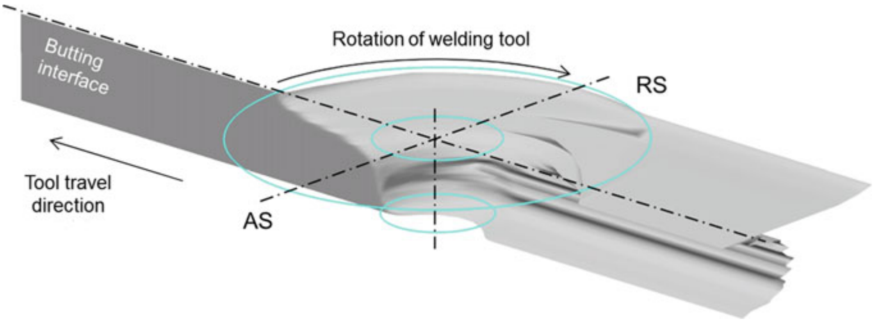

Fig. 2 Morphology of the butting interface during FSW. The corresponding tool rotation and welding speed during FSW is 800 rpm and 40 mm/min. AS denotes the advancing side, while RS denotes the retreating side

Morphology of the Butting Interface

Due to the complexity of the flow field, the butting surfaces at different positions in the FSW process, the 3D morphologies of the original butting interface before and after the FSW has been significantly changed. In this part, based on the analysis of the material flow path on the original butt interface, the 3D morphology of the entire butting surface in the welding process is reconstructed, as shown in Fig. 2. It can be found that in the FSW process, the material at the butting interface is extruded by tool pin and deposited behind the pin thus forming the weld. The butting interface in the weld is not a flat and straight surface, which has a very complex curved geometry. The predicted geometry here is similar to the experimental morphology [8] of the Zigzag line in the weld, which has been considered as the remnants of the oxide layer of the initial butting surface [9].

Thermal-Mechanical Condition for the Material Bonding at the Butting Interface

The influencing thermal-mechanical condition for the material includes the temperature, pressure, and bonding time. In the manufacturing processes, such as FSW, the temperature and pressure at the butting interface are not constant. Figure 3 depicts the predicted temperature evolution at the butting interface during FSW of materials. Figure 3a, b shows the temperature as a function of time at the two positions near the shoulder and under the pin bottom, which are 0.5 mm below the shoulder and 0.4 mm below the pin bottom respectively. It could be found from Fig. 3a that the material at the butting interface experience a continuous heating and cooling process during FSW. The peak temperature and the heating/cooling rate are quite similar at different tool rotation rates, while the hold time at high temperature is influenced by

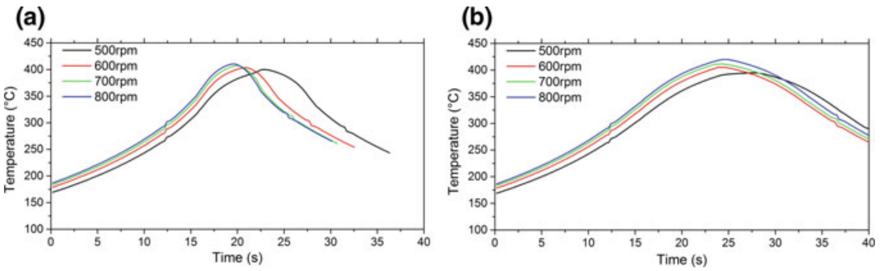

Fig. 3 Temperature evolution at the butting interface. **a** 0.5 mm below shoulder; **b** 0.4 mm below pin bottom

the tool rotation rate. In comparison, the material that is located at the pin bottom experiences similar temperature histories at different tool rotation rates, but the peak temperature increases with the increase of the rotation rate of the welding tool.

The interfacial pressure is another important factor that influences the material bonding behaviors for the solid state material. The material under the welding tool is mechanically loaded due to the axial welding force, which induces an anisotropic stress condition under the welding tool. The equation, which is used to determine the interfacial bonding pressure as a function of the spatial orientation, is given as

$$p_{bonding} = \begin{cases} p_{axial} \cdot \cos\theta_Z, \, \textit{under the shoulder} \\ 0, \, \textit{outside the shoulder} \end{cases} \tag{4}$$

where p_{axial} is the axial welding pressure and θ_Z is the orientation difference between the interface normal and the Z+ direction. Figure 4a, b shows the change of interfacial bonding pressure over time at different locations at the bonding interface. As shown in Fig. 4a, the interfacial pressure at the bonding interface in the vicinity of the shoulder for different rotation rates has a certain similarity. The material at the bonding

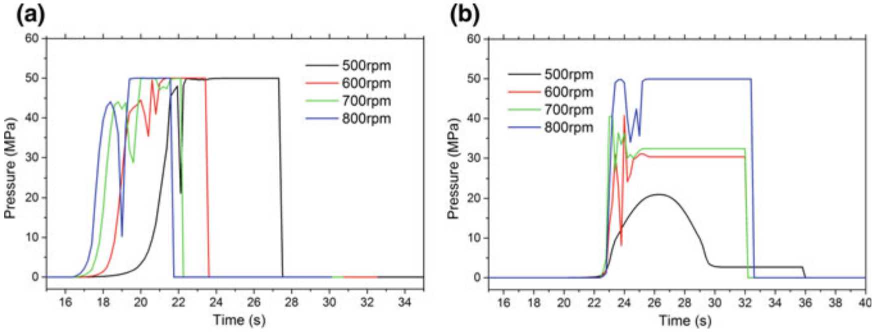

Fig. 4 Bonding pressure at the butting interface. **a** 0.5 mm below the shoulder. **b** 0.4 mm below the pin bottom

interface undergoes an increasing period of the interfacial pressure starting from 0, and then enters a period of intense oscillation; finally, the material stops flowing and is still under the shoulder, so it undergoes a period of relatively stable interfacial pressure. As shown in Fig. 4b, the interfacial material at the space between the pin bottom and the backing plate experiences relatively lower pressure for the material bonding. This is caused by the insufficient plastic flow of the bonding surface and thus the reduced change of spatial orientation.

Material Bonding Behaviors at the Butting Interface

Figure 5 shows the evolution of the bonded fraction at the butting interface under the action of the thermal-mechanical processing during FSW. Figure 6 compares the bonded fraction after welding of the butting surface near the shoulder and the backing plate. It can be seen from the figure that the bonded fraction on the butting surface of the FSW is significantly influenced by the thermal-mechanical process experienced

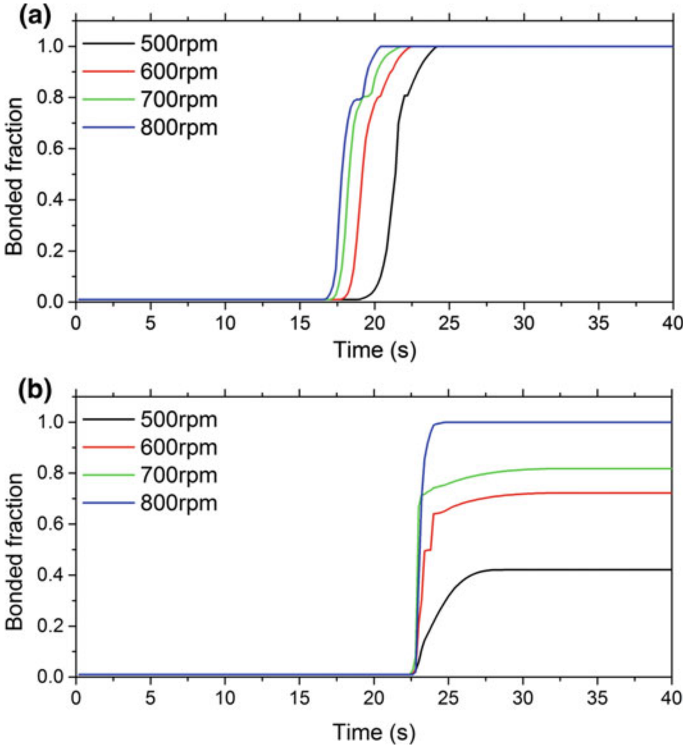

Fig. 5 Bonded fraction evolution during FSW. **a** 0.5 mm below shoulder; **b** 0.4 mm below pin

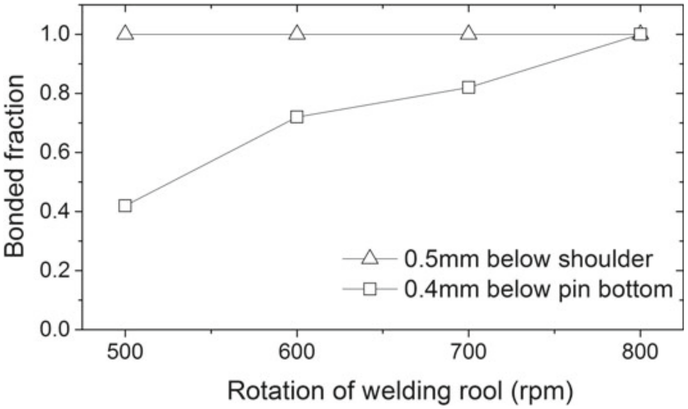

Fig. 6 Bonded fraction after FSW

during the welding process. In the area near the shoulder, the plastic flow results in significant change in the spatial orientation of the butting surface, which induces an increased interfacial pressure under the combined action of temperature and pressure. We found that full bonding can be achieved at the butting surface near the shoulder in a wide range of welding parameters. On the contrary, when the tool rotation rate is low, the plastic flow between the pin and the backing plate is insufficient. This is because the space orientation of the butting interface changes little due to the material flow difficult [6], which results in the fact that the pressure on the interface is insufficient. It could be found from Fig. 4b that the bonded fraction on the butting interface near the backing plate decreases with the tool rotation rate. The numerical prediction is also confirmed by the experimental micrograph at the weld root shown in Fig. 7. It is indicated that the bonding difficulties in the vicinity of the backing plate are induced by the insufficient interfacial bonding, which is further attributed the inadequate bonding pressure caused by the adverse orientation of the local butting interface due to the material flow difficulty.

In addition, it should be clarified that the real FSW process is complex and the material bonding behaviors may be influenced by many factors. For example, the plunge depth plays a very important role in governing the formation of the root flaw. When the plunge depth is insufficient, the distance between the pin bottom and the backing plate increases, which may further increase the length of root flaw in the weld. In the case that the heat input is low during FSW, the material flow becomes difficult. The flow difficulty causes increase in the axial load on the welding tool, which may lead to small deformation of the welder body because the welder is not ideally rigid. This must have occurred in our experiment, which explains why the length of the root flaw is longer than the gap (which is supposed to be 0.1 mm) between the pin bottom and the backing plate. In the present work, we investigate the effect of the tool rotation rate on the material bonding behaviors by numerical simulation while the plunge depth is assumed to be 0. The numerical model succeeded in predict the

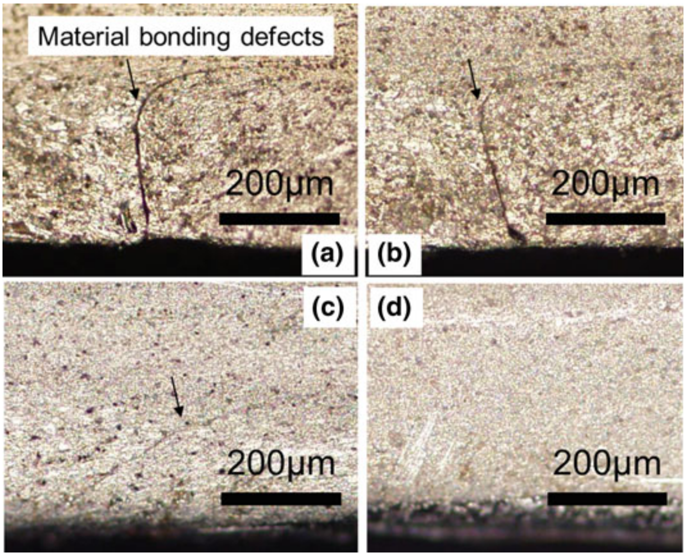

Fig. 7 Micrograph at the root region. The tool rotation rate is **a** 500 rpm, **b** 600 rpm, and **c** 700 rpm and 800 rpm. The welding speed is 40 mm/min

formation of the root flaw but may cause overprediction on the length of root flaw. In future work, we will include more processing factors, such as the plunge depth, and enlarge the range of the welding parameter range in the numerical simulation thus making a better computational tool for analyzing the material bonding behavior in FSW.

Conclusions

Solid state bonding (SSB) occurs at a relatively short time scale in FSW and similar SSB technologies. The material bonding behaviors during FSW is studied in this paper. It was demonstrated that the bonded fraction at the initially butting interface could be predicted by analyzing the evolution of the interfacial thermal-mechanical variables during FSW. Significant orientation change of the original butting interface in companion with the material flow in FSW was reported, which had major impact on the bonding pressure at the butting interface. The temporal evolution of the temperature and the pressure at the butting interface was obtained to analyze their roles in the growth of the bonded fraction. By numerical simulation, it was shown that bonding difficulties in the vicinity of the backing plate were induced by the insufficient interfacial bonding, which is further attributed the inadequate bonding pressure caused by the adverse orientation of the local butting interface due to the material flow difficulty.

Acknowledgements This study was financially supported by the National Natural Science Foundation of China (grant no. 51705280 and 51375259) and the State Key Laboratory of Tribology (no. SKLT 2015D07). The State Key Laboratory of Tribology is managed by the Ministry of Science and Technology of China with support from the Tsinghua University, China.

References

1. Mishra RS, Ma ZY (2005) Friction stir welding and processing. Mater Sci Eng R Rep 50(1–2):1–78
2. Xu WF, Luo YX, Fu MW (2018) Microstructure evolution in the conventional single side and bobbin tool friction stir welding of thick rolled 7085-T7452 aluminum alloy. Mater Charact 138:48–55
3. Sato YS et al (2004) FIB-assisted TEM study of an oxide array in the root of a friction stir welded aluminium alloy. Scripta Mater 50(3):365–369
4. Dickerson T, Przydatek J (2003) Fatigue of friction stir welds in aluminium alloys that contain root flaws. Int J Fatigue 25(12):1399–1409
5. Zhou CZ, Yang XQ, Luan GH (2006) Effect of root flaws on the fatigue property of friction stir welds in 2024-T3 aluminum alloys. Mater Sci Eng Struct Mater Prop Microstruct Process 418(1–2):155–160
6. Chen G et al (2018) Computational fluid dynamics simulation of friction stir welding: a comparative study on different frictional boundary conditions. J Mater Sci Technol 34(1):128–134
7. Chen G et al (2017) Analytical approach for describing the collapse of surface asperities under compressive stress during rapid solid state bonding. Scripta Mater 128:41–44
8. Dai QL et al (2015) Microcavities accompanying a zigzag line in friction stir welded A6082-T6 alloy joint. Sci Technol Weld Join 20(1):68–74
9. Sato YS et al (2005) Characteristics of the kissing-bond in friction stir welded Al alloy 1050. Mater Sci Eng A 405(1–2):333–338

Investigation of Interfacial Diffusion During Dissimilar Friction Stir Welding

Nikhil Gotawala and Amber Shrivastava

Abstract The objective of this study is to predict the thickness of intermetallic compound at the weld interface of dissimilar friction stir weld of Al 1050 and copper. The mechanical properties of the dissimilar friction stir weld are significantly affected by the intermetallic compounds formed during the process. The formation of intermetallic depends on the concentrations of the dissimilar materials, which are determined by their diffusion across the weld interface. A numerical model is developed which consists of Fick's second law based diffusion model in conjunction with a thermo-mechanical model. The numerical model captures the movement of the interfaces between intermetallic species due to the diffusion of the Al. A representative friction stir butt weld is performed with Al 1050 alloy and pure copper. The thickness of the intermetallic layer at the weld interface is determined by scanning electron microscopy and energy dispersive spectroscopy mapping of the weld cross sections. Predicted intermetallic compound thickness is compared well against the experimental observation.

Keywords Friction stir welding · Dissimilar joining · Intermetallic compounds
Interfacial diffusion

Introduction

Friction stir welding (FSW) is a joining method in which workpieces are plastically deformed and mechanically intermixed under mechanical pressure at elevated temperatures. However, these joints are created below the solidus temperature of the workpiece, which makes FSW a solid state welding process. This ability of FSW process to join materials without melting allows the venues for welding/joining of dissimilar materials [1]. Researchers have studied the dissimilar FSW of different

---

N. Gotawala · A. Shrivastava (✉)
Department of Mechanical Engineering, Indian Institute of Technology Bombay,
Mumbai 400076, India
e-mail: ashrivastava.me@iitb.ac.in

Y. Hovanski et al. (eds.), *Friction Stir Welding and Processing X*, The Minerals,
Metals & Materials Series, https://doi.org/10.1007/978-3-030-05752-7_11

combinations of materials, such as aluminium alloys with Cu alloys, Mg alloys, steel and Ti alloys, etc.

Lan et al. [2] studied the FSW of TRIP 780 steel to Al 6061 alloy. To encourage the mixing of steel and Al alloy, FS tool probe was partially present in the Al alloy. Unevenly distributed steel particles with intermetallic compounds at the particle periphery were observed throughout the stir zone. Similarly, Xue et al. [3] noticed many intermetallic compound particles in the friction stir welded joints of Cu and Al 1060 alloy. The authors acknowledged that the formation of the intermetallic compounds during FSW of dissimilar materials is inevitable. The stir zone showed relatively high tensile strength and increased hardness. This observation was attributed to the strengthening effect of the Al–Cu intermetallic compound particles. In an interesting work, Xue et al. [4] attempted to vary the extent of the material mixing by varying the FS tool probe offset across friction stir welds of Cu and 1060 Al alloy. The authors reported that defect free welds were obtained for the larger FS tool offset into the Al 1060 alloy. This observation was attributed to the relatively easy conditions for the material movement, with the large FS tool probes offset into the Al alloy. In order to avoid excessive material mixing, Lee et al. [5] performed the FSW of Al 6056 and 304 steel, with FS tool probe completely offset into the Al side. A very thin (~250 nm) intermetallic layer of Al_4Fe was reported at the steel-Al alloy interface. Similarly, Fe_2Al_5 intermetallic compound was observed in the friction stir welded joints of Al 6181 and high speed steel.

Girard et al. [6] performed FSW of Al 1050 and A284 steel and Al 1050 and C12200 H01 copper. The FS tool probe was positioned tangential to the interface of the dissimilar materials in these friction stir welds. The material mixing was not observed in these welds. And the formation of intermetallic compounds due to diffusion at the dissimilar material interface was reported. The presence of Fe_2Ti intermetallic in friction stir lap welded joints of Ti6Al4 V and 304 steel was confirmed by Campo et al. [7]. The authors also suggested that the intermetallic compounds formed due to the diffusion of the elements at the interface.

Bisadi et al. [8] investigated the influence of the rotational speed on the weld quality of FSW of Al 5083 alloy and copper (lap weld configuration). Relatively low and high stir zone temperatures (rotational speed) during FSW resulted in the formation of defects in the welds. Also, a reduction in tensile strength with increase in the stir zone temperature was attributed to higher intermetallic compound formation. The defect formation at low rotational speeds (temperature) was due to inadequate material movement. There have been many attempts at modelling the temperature distribution during FSW. These attempts range from solving a moving coordinate system based thermal model using finite difference method [9] to solving thermo-mechanical model using finite element method with Lagrangian [10, 11], arbitrary Lagrangian [12] or coupled Eularian lagrangian mesh [13].

There have been many parametric studies of dissimilar friction stir welding of different material combinations. These studies indicate that the material mixing and intermetallic compound formation (type and quantity) are the major factors which affect the quality of the friction stir welded dissimilar joints. However, limited literature is available on the prediction/modelling of the intermetallic compound formation

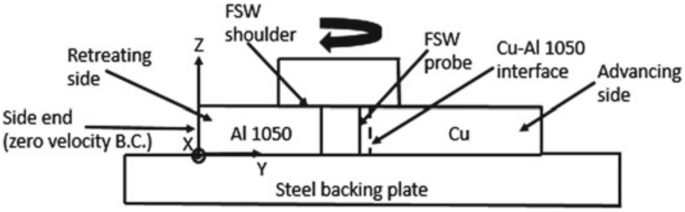

Fig. 1 Schematic diagram of FSW of Al and Cu

during dissimilar FSW. Beside other parameters, intermetallic compound formation primarily depends on the atomic diffusion at the weld interface, which is driven by the temperature during FSW. The objective of this study is to numerically predict the thickness of intermetallic compound at the weld interface of dissimilar friction stir weld of Al 1050 and copper.

Methodology

Figure 1 shows a schematic of the FSW of dissimilar material, with copper on advancing side and aluminium 1050 on retreating side. The FS tool probe is completely in the aluminium 1050 and clear from the Cu–Al 1050 interface. This position of the FS tool is chosen purposefully to avoid the material mixing. So that only diffusion during FSW and associated intermetallic compounds can be investigated. FSW of copper and Al 1050 is performed, and the thickness of the intermetallic layer is measured and compared against the numerical estimation. The details of the numerical model and experimental methods are presented in the following subsections.

Numerical Methodology

First, a thermo-mechanical model is developed to predict the temperature distribution during dissimilar FSW of copper and Al 1050. Next, a diffusion-based model is presented to estimate the thickness of the intermetallic compounds layer.

Thermo-mechanical Model

The steady state velocity field is calculated by solving the momentum conservation equations. The pressure variation in the stir zone is assumed to be negligible. The equations for conservation of momentum are as follows:

$$\rho\left(\frac{\partial u}{\partial t}+u\frac{\partial u}{\partial x}+v\frac{\partial u}{\partial y}+w\frac{\partial u}{\partial z}\right)=\frac{\partial \tau_{xx}}{\partial x}+\frac{\partial \tau_{xy}}{\partial y}+\frac{\partial \tau_{xz}}{\partial z} \quad (1)$$

$$\rho\left(\frac{\partial v}{\partial t}+u\frac{\partial v}{\partial x}+v\frac{\partial v}{\partial y}+w\frac{\partial v}{\partial z}\right)=\frac{\partial \tau_{xy}}{\partial x}+\frac{\partial \tau_{yy}}{\partial y}+\frac{\partial \tau_{yz}}{\partial z} \quad (2)$$

$$\rho\left(\frac{\partial w}{\partial t}+u\frac{\partial w}{\partial x}+v\frac{\partial w}{\partial y}+w\frac{\partial w}{\partial z}\right)=\frac{\partial \tau_{xz}}{\partial x}+\frac{\partial \tau_{yz}}{\partial y}+\frac{\partial \tau_{zz}}{\partial z} \quad (3)$$

where u, v and w are the velocity components in x-direction, y-direction and z-direction. τ_{ij} is the shear stress tensor. A zero-velocity boundary condition is applied at the side ends of the workpieces. The velocity boundary conditions at the FS tool shoulder and probe surfaces are as follows:

$$u=(1-\delta)\left(\frac{2\pi N}{60}\right)rcos\theta-V \quad (4)$$

$$v=(1-\delta)\left(\frac{2\pi N}{60}\right)rsin\theta \quad (5)$$

$$w=0 \quad (6)$$

where δ is slip factor between tool and material surface. A value of 0.4 for δ is used in this study [14]. N is the FS tool rotational frequency in revolutions per min. r is distance from the FS tool centre. θ is the angle between an FS tool velocity component and feed direction (x-direction, Fig. 1). V is the FS tool feed in m/s. The strain rates are calculated from the velocity field as below:

$$\varepsilon^{\cdot}_{ij}=\frac{\partial u_i}{\partial x_j}+\frac{\partial u_j}{\partial x_i} \quad (8)$$

and the strain rate tensor is related to the stress tensor as per the following relationship:

$$\tau_{ij}=\mu\varepsilon^{\cdot}_{ij} \quad (7)$$

where μ is the dynamic viscosity of material during FSW and is given by

$$\mu=\frac{\bar{\sigma}}{3\overline{\varepsilon^{\cdot}}} \quad (9)$$

where $\bar{\sigma}$ is the effective stress and $\overline{\varepsilon^{\cdot}}$ is the effective strain rate. The effective strain rate is calculated using Eq. 10 and the effective stress is estimated from the Johnson–Cook model (Eq. 11).

$$\overline{\varepsilon^{\cdot}}=\sqrt{\frac{2}{3}\varepsilon^{\cdot}_{ij}\varepsilon^{\cdot}_{ij}} \quad (10)$$

$$\bar{\sigma}=\left(A+B\bar{\varepsilon}^{n}\right)\left(1+C\ln\left(\frac{\overline{\varepsilon^{\cdot}}}{\overline{\varepsilon^{\cdot}_{o}}}\right)\right)\left(1-\left(\frac{T-T_0}{T_m-T_0}\right)^{m}\right) \quad (11)$$

Table 1 Johnson-Cook parameters [15]

Material	A (Mpa)	B (Mpa)	C	n	m	T_m(K)
Al 1050	110	150	0.014	0.36	1	918
Pure copper	90	292	0.025	0.31	1.09	1331

In Eq. 11, $\overline{\varepsilon^{\cdot}_{o}}$ is the reference strain rate (taken as 1), T is the temperature of material, T_0 is the room temperature and T_m is the melting temperature. A, B, C, n and m are the material constants. For Al 1050 and pure copper, material constants are given in Table 1.

The conservation of energy equation (Eq. 12) is solved to determine the temperature field.

$$k\left(\frac{\partial^2 T}{\partial x^2} + \frac{\partial^2 T}{\partial y^2} + \frac{\partial^2 T}{\partial z^2}\right) + \frac{q_g}{\rho c} + \rho c u\frac{\partial T}{\partial x} + \rho c v\frac{\partial T}{\partial y} + \rho c w\frac{\partial T}{\partial z} = 0 \tag{12}$$

where k is the thermal conductivity, c is the specific heat and ρ is the density of material. These material properties for Cu and Al 1050 are listed in Table 2. q_g is the heat dissipation due to the plastic deformation during FSW. It is assumed that 90% of the plastic deformation work is dissipated in the form of heat and the same is calculated as below

$$q_g = 0.9\bar{\sigma}\overline{\varepsilon^{\cdot}} \tag{13}$$

The heat transfer coefficients of 1000 W/m^{2}K and 10 W/m^{2}K are used at the bottom surface and at the surfaces exposed to air, respectively. The initial temperature of the Cu and Al 1050 workpieces is 298 K.

Diffusion Model and Intermetallic Layer Thickness

Figure 2 shows the phase diagram of Al and Cu [16]. It can be noticed that the maximum solubility of Cu in Al and Al in Cu is approximately 2% and 20%, respectively. So Al_2Cu and Al_4Cu_9 are primarily formed due to limited solubility of Cu and Al in each other (Fig. 2). For the formation of other Al–Cu intermetallic compounds, it would require relatively larger incubation periods (time spent at elevated temper-

Table 2 Material properties of Cu and Al 1050

Material	Thermal conductivity (W/mK)	Specific heat (J/kgK)	Density (kg/m^3)
Al 1050	205	900	2700
Pure Copper	385	376.812	8960

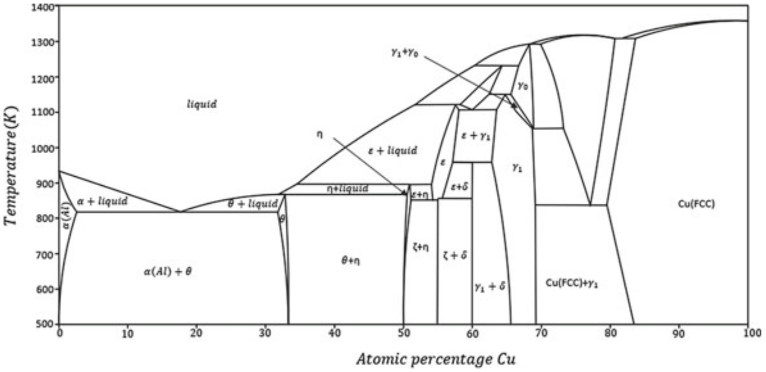

Fig. 2 Phase diagram of Al and Cu [16]

ature). However, in FSW, the incubation time is very limited. Xue et al. reported that Al_2Cu and Al_4Cu_9 are the most common intermetallic compounds formed at the weld interface of friction stir welded joints of Al 1060 and copper [4]. So it is assumed that Al_2Cu and Al_4Cu_9 are the only intermetallic compounds which are formed during FSW of Cu and Al 1050 in the current work.

Initially, it is assumed that very small layer thicknesses (0.03 μm) of Al_2Cu towards the Al side and Al_4Cu_9 towards the Cu side of the Cu–Al 1050 interface are present. This leads to three interfaces: Al–Al_2Cu, Al_2Cu–Al_4Cu_9 and Al_4Cu_9–Cu. A concentration boundary condition of 100% Al at the side end of the Al plate (Fig. 1) and 0% at the side end of the Cu plate are applied. The initial concentrations of Al and Cu at all the interfaces are estimated in accordance with the phase diagram (Fig. 2). A Fick's second law of diffusion-based one-dimensional equation (in y-direction, Eq. 14) is solved at the Al side of Al–Al_2Cu and the Cu side of Al_4Cu_9–Cu interface, to determine the Al concentration profile along x-direction with respect to time.

$$\frac{\partial C}{\partial t} = \frac{\partial}{\partial y}(D\frac{\partial C}{\partial y}) \tag{14}$$

where C is the Al concentration and D is the diffusion of Al (Table 3). It is assumed that the Al concentration varies linearly in between the Al–Al_2Cu and Al_2Cu–Al_4Cu_9 interfaces and Al_2Cu–Al_4Cu_9 and Al_4Cu_9–Cu interface. And as stated earlier, the Al concentration at the interfaces is determined in accordance with the Al–Cu phase diagram. Next, Kajihara's model (Eq. 15) is used to determine the movement of the interfaces in y-direction with respect to time [17].

$$\left(C_{ij} - C_{ji}\right)\frac{dy_{ij}}{dt} = J_{ij} - J_{ji} \tag{15}$$

Table 3 Diffusion coefficient of Al

	Diffusion coefficient of Al (m^2/s)	Reference
D_{Al}^{Al}	$0.137 * 10^{-4} * \exp(-\frac{14866.490}{T})$	[18]
D_{Al}^{Cu}	$\exp(-\frac{22162.38}{T} - 11.60)$	[19]
$D_{Al}^{Al_4Cu_9}$	$1.7 * 10^{-7} * \exp(-\frac{13921.113}{T})$	[20]
$D_{Al}^{Al_2Cu}$	$0.4 * 10^{-4} * \exp(-\frac{14501.160}{T})$	[20]

where C_{ij} is the concentration of Al at interface, y is the location of the interface during intermetallic compound formation and J_{ij} is the diffusion flux such that $J_{ij} = D_i \frac{\partial C}{\partial y}$. Table 3 shows the diffusion coefficients of Al in different intermetallic phases.

Experimental Methodology

In order to validate the thermo-mechanical model (Sect. 2.1), a representative friction stir weld of Al 1050 and Cu was performed on a 3-axis CNC mill (Hardinge VMC 600 II: 13 kW—maximum spindle power and 8000 rpm—maximum spindle speed). Al 1050 and Cu workpieces were 250 mm long, 90 mm wide and 3 mm thick. FS tool made of H13 tool steel with 12 mm shoulder diameter, 3 mm probe diameter and 2.5 mm probe height was used to perform the weld. The FS tool tilt angle was zero degree from the vertical axis. The FS tool offset was 2 mm into the Al 1050 side from the Al–Cu interface. The 220 mm long weld was performed at feed of 50 mm/min, tool rotation frequency of 1000 rpm and plunge depth of 0.3 mm. A mild steel backing plate was placed below the workpieces during the weld. During FSW, temperatures were measured with k-type thermocouple at two points on the workpieces: 10 mm both ways (perpendicular to feed direction) from the tool centre at mid-length of the workpieces. Scanning electron microscopy samples are prepared by sectioning the friction stir weld at the mid-length and mechanical polishing till the mirror finish is achieved. The scanning electron microscopy and energy dispersive spectroscopy are performed using Zeiss Gemini 300 system.

Results and Discussion

Figure 3 shows the temperature distribution at the top surface of the workpiece, as predicted from the thermo-mechanical model. It can be noticed that within stir zone, temperatures are higher in the Al 1050 side as compared to the Cu side. This is expected as the FS tool probe is completely in the Al 1050 side. However outside the stir zone, at the locations equidistant from the tool centre, the temperatures are

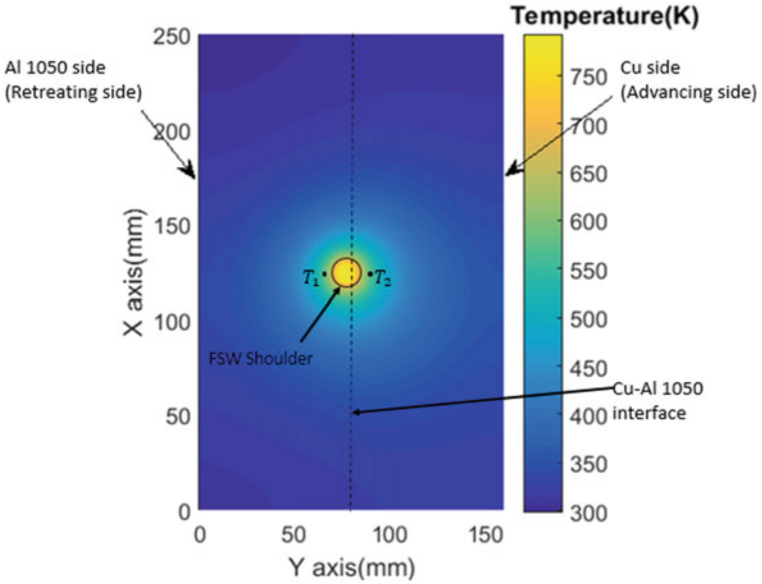

Fig. 3 Predicated temperature distribution during FSW of Cu and Al 1050 at 1000 rpm, 50 mm/min feed and 0.3 mm plunge depth

higher in the Cu side as compared to the Al 1050 side. This is primarily due to higher thermal diffusivity (higher thermal conductivity, lower specific heat, Table 2) of Cu as compared to Al 1050. Due to relatively higher thermal conductivity, heat travels faster through the bulk of copper workpiece as compared to the Al 1050 workpiece. And due to lower specific heat, it takes relatively lower amount of heat to raise the temperature at any location in Cu as compared to the Al 1050.

The temperature history at two locations (10 mm on either side of the tool centre and the mid-length of the workpieces, Fig. 3: T1 and T2) is extracted from the three-dimensional temperature distribution. Figure 4 compares the numerical and experimental temperature histories at these locations. It can be noticed that the temperature history matches well for the Cu side. However, the peak temperature is over-predicted at the Al 1050 side. There are multiple assumptions involved with the simple model developed in this study, which can result in the observed over-prediction of the temperature. All the thermo-physical properties are treated as constant values (at room temperature of 298 K). However, these properties vary with change in temperature. Particularly, the thermal diffusivity decreases with increase in the temperature. A significant decrease in thermal diffusivity would lead to decrease in the experimentally observed peak temperature, which the current numerical model would not capture. Also, the slip factor would vary for different materials. However, a constant slip factor value of 0.4 is used in the current model. This can also contribute to the discrepancy between the numerically and experimentally observed peak temperatures.

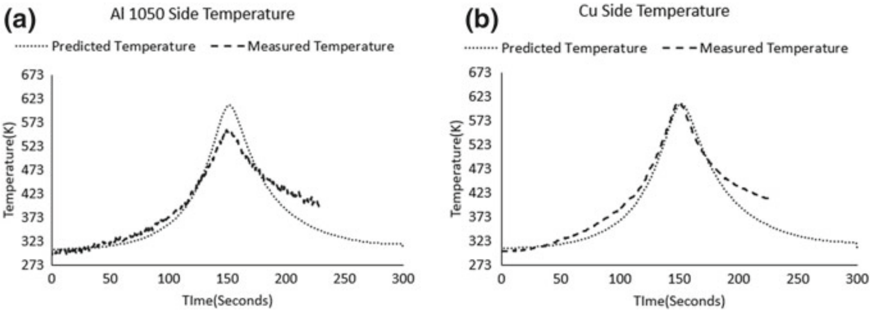

Fig. 4 Predicted and measured temperature at **a** Al 1050 side (T1, Fig. 2). **b** Cu side (T2, Fig. 2)

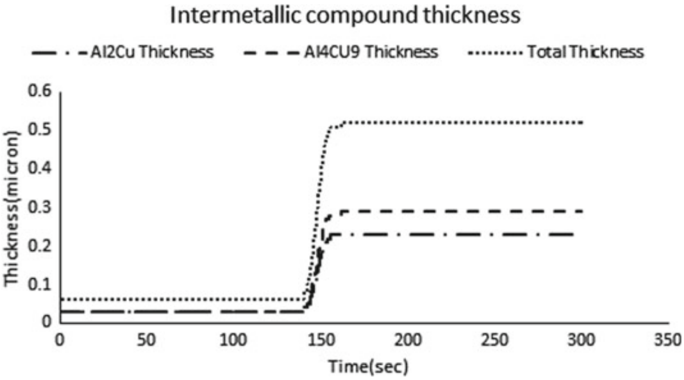

Fig. 5 Predicted layer thicknesses of Al_2Cu, Al_4Cu_9 and total intermetallic

The diffusion model (Sect. 2.1.2) in conjunction with the thermo-mechanical model is used to predict the location of the Al-Al_2Cu, Al_2Cu–Al_4Cu_9 and Al_4Cu_9–Cu interfaces with respect to time. The distances between these interfaces provide the thicknesses of the intermetallic compound layers at any instance. Figure 5 shows the predicted values of the Al_2Cu layer thickness, Al_4Cu_9 thickness and total intermetallic layer thickness (Al_2Cu thickness + Al_4Cu_9 thickness) at the mid-length of the friction stir weld, with respect to time. The total intermetallic layer thickness is predicted to be 0.52 μm. Figure 6 shows the scanning electron microscopy (SEM) image, and the Al and Cu mapping images obtained from the energy dispersive spectroscopy (EDS). An average intermetallic compound layer thickness of 1 μm is measured from the SEM image. It can be noticed that the intermetallic layer thickness from numerical model compares well against the experimental result from the SEM image. The Al and Cu mapping from the EDS shows the significant presence of Al and Cu at the interface, strongly indicating the presence of intermetallic compounds.

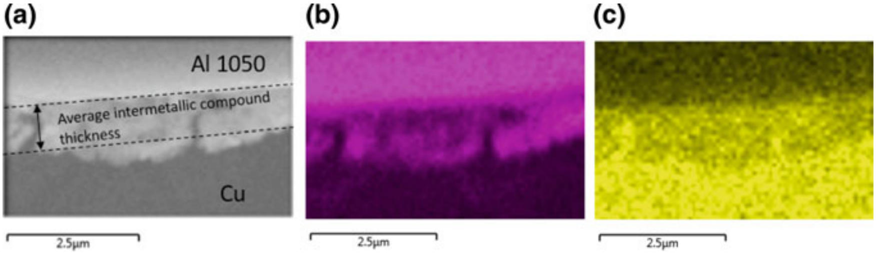

Fig. 6 **a** SEM, **b** EDS-Al mapping and **c** EDS-Cu mapping of friction stir welded Cu–Al 1050 interface

Conclusions and Future Work

In this work, a numerical model is presented to predict the intermetallic layer thickness at the weld interface of dissimilar friction stir weld of Al 1050 and copper. The numerical model consists of a fick's second law based diffusion model in conjunction with a thermo-mechanical model. The numerical model captures the movement of the interfaces between intermetallic species due to the diffusion of the Al. For a representative friction stir weld of Al 1050 and copper, the intermetallic layer thickness from the numerical result compares well against the experimental result. This work shows the significance of the atomic diffusion at the weld interface, towards the intermetallic layer formation. Also, the diffusion phenomenon significantly depends on the temperature during the process.

Further TEM studies are required to confirm the intermetallic species formed during friction stir welding. This will allow the comparison of the layer thickness of individual intermetallic compounds. In this study, the numerical result is compared against the experimental result for a representative friction stir weld. Further validation of the numerical model is required by comparing the predicted results and experimental results, for a series of experiments performed at different weld conditions and different combinations of the dissimilar materials.

Acknowledgements The authors gratefully acknowledge the partial support of this work by the Science & Engineering Research Board, Department of Science & Technology, Government of India (File No. ECR/2017/000727/ES), Department of Mechanical Engineering, Microstructural Mechanics and Microforming Lab and Machine Tools Lab at Indian Institute of Technology.

References

1. Mishra RS, Ma ZY (2005) Friction stir welding and processing. Mater Sci Eng R Rep 50(1–2):1–78
2. Lan S, Liu X, Ni J (2016) Microstructural evolution during friction stir welding of dissimilar aluminum alloy to advanced high-strength steel. Int J Adv Manuf Technol 82(9–12):2183–2193

3. Xue P, Xiao BL, Ni DR, Ma ZY (2010) Enhanced mechanical properties of friction stir welded dissimilar Al–Cu joint by intermetallic compounds. Mater Sci Eng A 527(21):5723–5727
4. Xue P, Ni DR, Wang D, Xiao BL, Ma ZY (2011) Effect of friction stir welding parameters on the microstructure and mechanical properties of the dissimilar Al–Cu joints. Mater Sci Eng A 528(13–14):4683–4689
5. Lee WB, Schmuecker M, Mercardo UA, Biallas G, Jung SB (2006) Interfacial reaction in steel–aluminum joints made by friction stir welding. Scripta Mater 55(4):355–358
6. Girard M, Huneau B, Genevois C, Sauvage X, Racineux G (2010) Friction stir diffusion bonding of dissimilar metals. Sci Technol Weld Join 15(8):661–665
7. Campo KN, Campanelli LC, Bergmann L, dos Santos JF, Bolfarini C (2014) Microstructure and interface characterization of dissimilar friction stir welded lap joints between Ti–6Al–4V and AISI 304. Mater Des (1980–2015) 56:139–145
8. Bisadi H, Tavakoli A, Sangsaraki MT, Sangsaraki KT (2013) The influences of rotational and welding speeds on microstructures and mechanical properties of friction stir welded Al5083 and commercially pure copper sheets lap joints. Mater Des 43:80–88
9. Song M, Kovacevic R (2003) Thermal modeling of friction stir welding in a moving coordinate system and its validation. Int J Mach Tools Manuf 43(6):605–615
10. Thermo-mechanical model with adaptive boundary conditions for friction stir welding of Al 6061. Int J Mach Tools Manuf 45(14):1577–1587
11. Chen CM, Kovacevic R (2003) Finite element modeling of friction stir welding—thermal and thermomechanical analysis. Int J Mach Tools Manuf 43(13):1319–1326
12. Zhang Z, Chen JT, Zhang ZW, Zhang HW (2011) Coupled thermo-mechanical model based comparison of friction stir welding processes of AA2024-T3 in different thicknesses. J. Mater Sci 46(17):5815
13. Al-Badour F, Merah N, Shuaib A, Bazoune A (2013) Coupled Eulerian Lagrangian finite element modeling of friction stir welding processes. J Mater Process Technol 213(8):1433–1439
14. Arora A, Nandan R, Reynolds AP, DebRoy T (2009) Torque, power requirement and stir zone geometry in friction stir welding through modeling and experiments. Scripta Mater 60(1):13–16
15. Rajak A, Kore S (2017) Electromagnetic hemming of aluminum sheets using FEM. ICMMD-2016 Adv Intel Syst Res 77–82
16. Kim HJ, Lee JY, Paik KW, Koh KW, Won J, Choe S, Park YJ (2003) Effects of Cu/AI intermetallic compound (IMC) on copper wire and aluminum pad bondability. IEEE Trans Comp Packag Manuf Technol 26(2):367–374
17. Kajihara M (2004) Analysis of kinetics of reactive diffusion in a hypothetical binary system. Acta Mater 52(5):1193–1200
18. Neumann G, Tuijn C (2011) Self-diffusion and impurity diffusion in pure metals: handbook of experimental data, vol 14. Elsevier
19. Liu D, Zhang L, Du Y, Xu H, Liu S, Liu L (2009) Assessment of atomic mobilities of Al and Cu in fcc Al–Cu alloys. Calphad 33(4):761–768
20. Hentzell HTG, Tu KN (1983) Interdiffusion in copper–aluminum thin film bilayers. II. Analysis of marker motion during sequential compound formation. J Appl Phys 54(12):6929–6937

Part V
Controls and Inspection

Developing and Deploying FSW&P Through Standardization

Dwight A. Burford

Abstract Key advancements in friction stir welding and processing (FSW&P) have been chronicled in these biennial symposia. Insights gained through fundamental and applied research published in symposia proceedings hold significant value in maturing and furthering the development and deployment of FSW&P. However, not all of this research can be replicated scientifically to enable this purpose due to insufficient information provided in the published articles. Providing more complete process information in symposium papers will serve to advance broader acceptance of FSW&P by industry and regulatory agencies. This objective can be facilitated by including appropriate detail required by national and international standards in published research. Without such detail, the maturity of FSW&P will remain in question throughout the different industry sectors due to a lack of uniformity and consistency in published results. A study carried out in coordination with the Metallic Materials Properties Development and Standardization (MMPDS) handbook steering committee illustrates the value of such discipline. The study was undertaken to investigate the potential for developing design data for FSW. Also, because successful implementation of FSW&P is reliant upon understanding and controlling the local metalworking conditions around the weld tool (both thermally and mechanically), utilizing process feedback signals is needed to confirm the consistency and effectiveness, and thus the maturity, of these technologies to organizations and agencies charged with quality assurance.

Keywords Welded aluminum alloys · Friction stir welding (FSW)
Friction stir processing (FSP) · Friction stir spot welding (FSSW)
Industry standards · Specifications · Process parameters and controls

---

D. A. Burford (✉)
Joining Innovations, LLC, 6321 N. Ulysses St, Wichita, KS 67219, USA
e-mail: Dwight.Burford@JoinInv.com

Y. Hovanski et al. (eds.), *Friction Stir Welding and Processing X*, The Minerals, Metals & Materials Series, https://doi.org/10.1007/978-3-030-05752-7_12

Motivation

Over the past 20 years, significant advancements in friction stir related technologies have been chronicled in the proceedings of symposia held at TMS Annual Meetings and Exhibitions. In the nine previous biennial friction stir welding and processing (FSW&P) symposia in particular [1–9], papers have been presented which cover a wide scope of research and development, ranging from experimental studies to case histories for a diverse array of applications. Critical insights have been gained especially through fundamental research involving modeling and advanced measurement techniques. The accumulation of this body of knowledge and information brings opportunities to further advance the development and deployment of the various friction stir processes and derivatives.

Not all of the work presented in the FSW&P symposia can be replicated in a scientific manner, however, due to the lack of sufficient detail in information defining critical aspects of the process or processes reported on in individual papers. For those papers which are meant mainly to showcase an application of the technologies while yet maintaining the proprietary nature of the work, the limitation of detail presented is understandable. However, for those papers that are presented to examine certain engineering and scientific aspects of FSW&P, there is often a lack of sufficient process information to replicate the work presented according to the scientific method. In either case, proprietary or nonproprietary, the application of certain process controls and analysis disciplines is needed to advance the reliability and credibility of the FSW&P literature for broader acceptance of the technology by industry and governing agencies.

A prominent measure of the maturity of a given technology is whether or not there are mature industry standards and specifications in place to outline and guide its use. Such documents are directed at ensuring that manufacturing goods and services meet their designated purposes. How published standards and specifications represent that the technology is crucial to the maintenance and further deployment of that technology. Not only are existing engineering and manufacturing entities impacted by industry-wide standards and specifications, but also potential new areas of application may be enabled or hindered depending upon the information contained within these documents.

In the United States, standards and specifications which provide requirements and guidelines for friction stir welding (FSW) of aluminum alloys, the most widely friction stir processed materials, have been published in AWS D17.3:2016, "*Specification for Friction Stir Welding of Aluminum Alloys for Aerospace Applications*" [10], and in Section 7 of AWS D1.2:2014, "*Structural Welding Code—Aluminum*" [11]. Additional AWS specifications are on track to be published in the near term, e.g., AWS C6.3/C6.3M, "*Recommended Practices for Friction Stir Welding*" [12], and AWS D8.17M, "*Specification for Automotive Weld Quality—Friction Stir Welding*" [13]. International standards for aluminum alloys include ISO 25359:2011, "*Friction stir welding—Aluminium*," Parts 1 [14] through 5, and ISO/FDIS 18785, "*Friction stir* *spot welding—Aluminium*," Parts 1 [15] through 5, which is currently in the final stages of publication.

Manufacturing companies that build marine shipping vessels and aerospace launch vehicles have incorporated friction stir welded structures in their products for two decades now [16, 17]. Enabling this extended period of use has been the establishment and maintenance of requirements and guidelines that outline the safe and best practices for the incorporation of FSW in these industries. Examples include the American Bureau of Shipping "*ABS Guide for the Approval of Friction Stir Welding in Aluminum, 2011*" [18], and The National Aeronautics Space Administration (NASA) "*PRC-0014 Rev. D, Process Specification for Friction Stir Welding*" [19]. While other specifications could be cited, the standards and specifications listed above demonstrate that friction stir welding is a maturing technology, partly because it offers reduced manufacturing costs and efficient product designs [20, 21].

Such standards and specifications also hold the potential for adversely influencing the implementation of FSW. AWS D17.3:2016 and ISO 25359:2011, for instance, include tabulated values that intentionally guide and thus influence design engineers. Consider Table 6.4 of AWS D17.3:2016 and Table 3 of ISO 25359:2011 (Part 4). Joint efficiencies (based on transverse tensile strength) are listed in these tables as low as 0.6 and 0.7 tempers for "heat treatable alloys." It should be kept in mind that AWS D17.3:2016, in particular, is written specifically for use within the aviation and aerospace industries which rely heavily on this general class of high strength aluminum alloys. As such, this is a document that airframe designers are expected to consult when considering designing and sizing structural components with FSW joints. In trade studies including FSW and other joining technologies, the low allowable property minimums for FSW joints of "heat treatable alloys" listed in Table 6.4 of AWS D17.3:2016 may be expected to influence a designer to favor other, more well-known joining technologies that perhaps do not have such an adverse effect on the microstructure of high strength heat treatable aluminum alloys. This may be anticipated for at least several reasons.

Given the lean (tight) margins of safety in aircraft and aerospace design, relatively low joint efficiency values are indicative of added weight to a given component or structure. This concern is somewhat complicated by a footnote to Table 6.4 of AWS D17.3:2016 which suggests that a significant amount of work would be required by designers if they were to pursue incorporating FSW in designs utilizing 2000 and 7000 series aluminum alloys. Footnote "g" clarifies that the joint efficiency values listed in the table apply only to 6000 series "heat treatable alloys" in the respective tempers. Because 6000 alloys are typically considered more weldable than the other "heat treatable alloys" listed in footnote "g" (i.e., 2000 and 7000 high strength aerospace alloys), these other aluminum alloys could be viewed as having even lower joint efficiencies than the values listed for 6000 series alloys by way of a footnote. This directly adds to risk assessment considerations for deciding whether or not FSW joints (having low published efficiencies) should be incorporated in a given aircraft or aerospace design.

Since joint efficiency minimums are not given for 2000 and 7000 series alloys in Table 6.4 of AWS D17.3:2016, the needed values must come from other sources.

Footnote “g” states that the stated values must be “in accordance with the Referencing Document” (e.g., the engineering drawing). In practical terms, this means that designers and engineers must locate and/or generate the needed values from one or more other sources, such as a design data allowables program, or “point design,” focused on their specific application and alloys. Such a program may be expected to cause delays and additional costs to an overall product development program.

Furthering a potentially adverse view of FSW joints by designers may come from the general values included in Table 6.4 of AWS D17.3:2016 and Table 3 of ISO 25359:2011 (Part 4) simply because they are not categorized by parent material thickness. As a result, designers new to FSW may be left with the impression that FSW joint efficiencies are independent of material thickness and therefore the same knockdown factors must be applied to all joint thicknesses in their designs. In reality, joint properties are typically highest in thinner gauge sections of heat treatable aluminum alloys and decrease with an increasing joint cross section [22, 23]. This trend most often results from a decrease in achievable weld travel speeds for increased material thickness. The slower travel rates required for thicker materials result in longer exposure times of the joint material to the transient thermal peak as the tool passes along the joint line.

None of the above discussion is intended to discredit in any way the referenced specifications or standards or the subcommittees or subcommissions who develop and update these documents. Each has done a commendable job which has enabled their publications. Stated another way, the low joint efficiency values listed in Table 6.4 of AWS D17.3:2016 and Table 3 of ISO 25359:2011 (Part 4) do not stem from a deficiency in developing either specification. Rather, these deficiencies stem from a lack of vetted data to be incorporated in the table from reproducible processes. In an effort to address the concerns with tabulated data, the members of working group IIW C-III-B-WGB1 have proposed a change to Table 3 of ISO 25359:2011 (Part 4) which lists higher joint efficiencies for heat treatable alloys equal to and below 5 mm weld penetration [24]. This level of precision is still recognized to be too coarse based on the technical papers presented in these symposia proceedings and other publications.

A number of researchers have reported significantly higher joint efficiencies for 2000 and 7000 series alloys than those listed in the existing as well as the proposed tables [22, 25, 26]. The influence of process variables has been known since the beginning of this series of symposia [27]. For a specific example, Mahoney et al. [28] reported joint strengths for 6.3 mm AA7075-T6 plate of nominally 80% following a post-weld heat treatment (PWHT). The post-weld heat treatment step is needed for AA7075 and similar series alloys because they continue to harden significantly in the as-welded condition [22]. Similar values for AA7075-T6 were developed for an aerospace program by Burford [29, 30]. From these and numerous other sources, it is evident that the standards and specifications can and should be updated to incorporate the higher, more representative joint efficiency values for friction stir welded precipitation strengthened aluminum alloys.

When fully matured, joint efficiencies based on transverse tensile strengths listed in Table 6.4 of AWS D17.3:2016 and Table 3 of ISO 25359:2011 (Part 4) will be the result and thus reflect the full implementation of the respective specification and standard. That is, the values listed will be traceable directly to FSW processes that were carried out in accordance with the respective document for the alloys represented within the table.

Approaches that hold potential for maturing the joint efficiency data in the respective tables are in place elsewhere for other processes and product forms. One approach has been formalized in the *Metallic Materials Properties Development and Standardization* (MMPDS) handbook (formerly MIL-HDBK-5) [31]. This handbook, like others, incorporates a detailed and disciplined methodology for developing allowable design data (or simply "allowables") that provide representative property values which are traceable directly to processes controlled by industry standards and specifications (and internal standards that often exceed the industry standards). Without this traceability, manufactured metallic products are not included or considered for inclusion in the handbook.

Currently, design values are included in the MMPDS handbook for rolled, forged, cast, extruded, and welded product forms as well as mechanical fasteners [32]. Applying the same or a similar methodology used in this or another handbook would greatly improve the value of Table 6.4 of AWS D17.3:2016 and Table 3 of ISO 25359:2011 (Part 4) to designers and stress engineers. With the procedure for regularly updating standards and specifications published by the American Welding Society and the International Organization for Standardization, the potential exists for updating tables with vetted data sets once they are established through the applicable protocols and forms of documentation.

Case Study in Review

After the friction stir welded structure described in references [29, 30] was brought into production, it became evident that the mechanical properties which had been achieved in the related development program were similar to values published in the open literature, as recorded in a number of tabulated summaries [22, 25, 26, 28]. This observation prompted further consideration regarding the extent to which the joint properties of sound welds (those without defects or atypical features) could be adjusted in a given FSW process to produce similar values. This consideration was pursued through an evaluation program in which the nonuniqueness or path independence of obtainable joint properties produced by differing tools and machines was evaluated. Results from this study have been described elsewhere [26, 33–40]. The selected weld tool designs tested in this evaluation are shown in Fig. 1. Six weld tools were evaluated, with three based primarily on TWI tool designs and three considered to be nonstandard TWI designs. Also shown are the process windows developed independently for each tool based on systematically optimizing transverse tensile test results. Optimum process windows were established for three of the tools, but not for the remaining three tools (due to FSW machine torque requirements and other limitations).

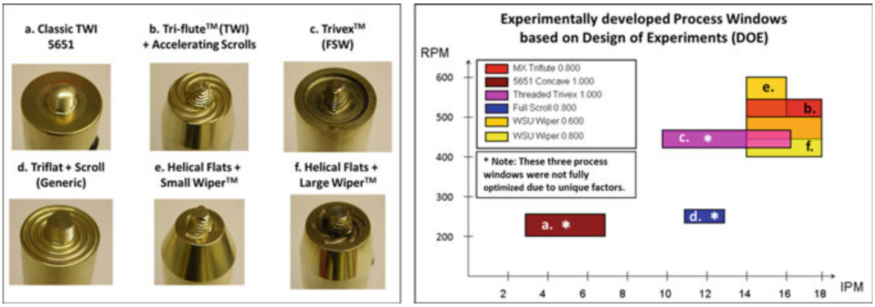

Fig. 1 Selected weld tool designs tested in a path independent study to develop corresponding process windows to produce optimum joint properties based on transverse tensile test results [26, 34]. Three tools produced nearly equivalent process windows: "b," "e," and "f."

One of the major findings of this study is the verification that similar joint properties (as measured by transverse joint tensile strength) can be achieved using a wide range in weld tool designs. Taking full advantage of this approach requires independently optimizing the process for each tool based on the capabilities of the FSW equipment and tool itself. Because different tools have different process windows, the advantage one tool may have over another is generally realized in terms of productivity and robustness (measured in terms of tool wear, process forces, propensity to form defects, etc.). Figure 2 helps illustrate this point. In this figure, transverse tensile test results are plotted for a total of 101 coupons produced by three of the tools shown in Fig. 1. The tool designed marked "e" produced the highest average joint efficiencies among the set of tools tested. Since it also demonstrated faster process speed while producing high joint efficiencies, it may be considered a good candidate for further evaluation for industrial applications, e.g., testing its tool life for selected production runs. Microhardness maps of selected coupons as a function of process basic parameters are presented in Fig. 3 for two of the tool designs evaluated in the cited study [33]. Tool "e," the smaller tool with a threaded frustum-shaped probe and helical flats and a "small" Wiper™ shoulder produced less softening than the standard 5651 tool, "a." These plots further demonstrate the importance of producing FSW joints at as high a travel speed as the tool will reasonably endure without failure.

Based on the results discussed above, including the collections of transverse tensile properties reported in the literature, a proposal was made to the MMPDS coordinating committee to conduct an evaluation of FSW joints using standard MMPDS procedures. A round-robin was subsequently coordinated to evaluate the ability of independent facilities to produce equally sound welds within the process controls and procedures of that facility and evaluate site-to-site variability based on a draft version of AWS D17.3 available at the time. Alcoa and Kaiser provided AA2024 sheet and Alcan provided AA2198 sheet material for the round-robin test program. Airbus, Alcan, Lockheed, and Wichita State University (WSU) then produced FSW coupons independently for evaluation. Once WSU and Westmoreland Mechanical Testing and

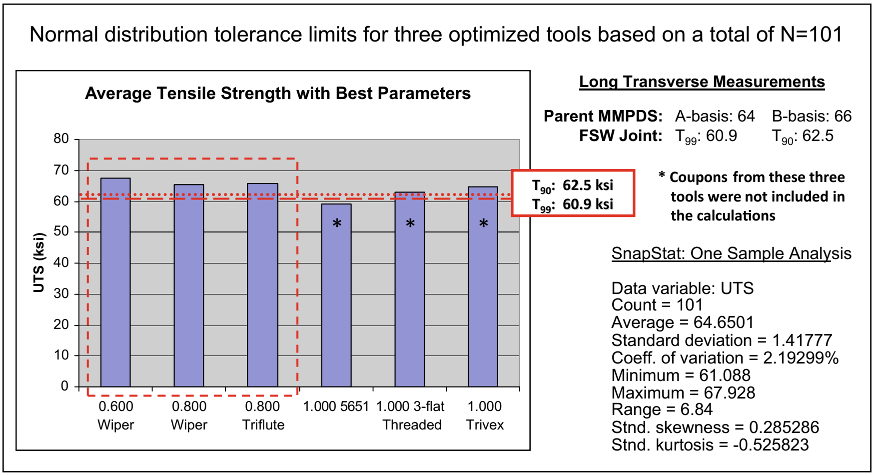

Fig. 2 Transverse tensile test results for a total of 101 coupons produced by three different tools [26, 34]. The tool with a threaded frustum-shaped probe and helical flats and a "small" Wiper™ shoulder produced the highest average joint efficiencies

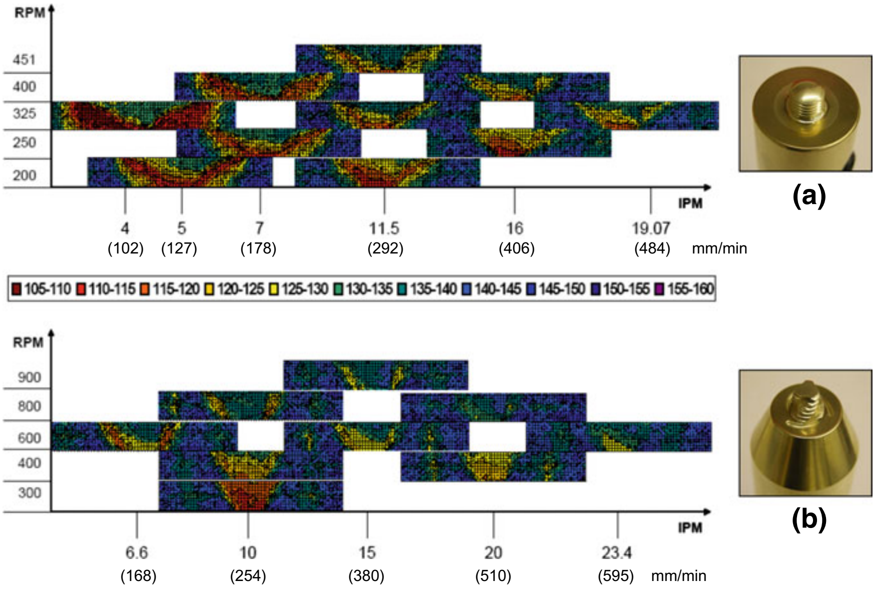

Fig. 3 Microhardness maps of selected coupons as a function of the process window for two tool designs evaluated in the cited study [34]. Tool "e," the smaller tool with a threaded frustum-shaped probe and helical flats and a "small" Wiper™ shoulder produced less softening than the standard 5651 tool, "a." These plots further demonstrate the importance of producing FSW joints at as high a travel speed as the tool will reasonably endure without failure

Research tested the coupons, Battelle evaluated the mechanical test results [41]. The results from the round-robin confirmed the prior path independent findings of WSU. Jurak et al. [37, 38] further evaluated and published the findings of the MMPDS FSW round-robin study.

Because handbooks for allowable design data (allowables) like the MMPDS handbook require a referencing specification with specification minimums, like an Aerospace Material Specification (AMS) material specification, the feasibility of developing one for friction stirred materials and joints was initially proposed to the SAE Aerospace Metals and Engineering Committee (AMEC) [42, 43] in October 2008. The proposal was subsequently approved by AMEC members and specifications based on the MMPDS round-robin program were drafted [44]. The proposed draft, titled Friction Stir Welding and Processing of Aluminum Products and Parts General Minimum Requirements, was subsequently submitted to AMEC in meeting No. 214 on January 21, 2011, by the author [45].

Discussion and Concluding Remarks

Taking a path independent approach, in which different tool designs are evaluated for a given process, is compatible with industry practice. This conclusion is based on how manufacturers typically develop and adjust their internal operations and processes independently of competitors. Such a path independent approach allows each production facility to tailor their process capabilities to meet product quality requirements, tradeoffs in terms of customer expectations and delivery requirements, etc. The alternative is to fix the tool design in a path-dependent approach without realizing potential benefits of tool designs more suited for a given application.

Based on a lack of funding to remain actively involved in the process of developing traceable allowable design data packages, the effort described in the previous section was eventually placed on hold. Nevertheless, significant progress was made toward producing traceable data sets designed for incorporation in specifications and standards like those published by AWS and ISO for FSW and related technologies. While the work has yet to be brought to completion, the efforts already undertaken illustrate a means for maturing as well as assessing the maturity of FSW and its variants.

Ultimately, however, the combined efforts described above demonstrate that FSW of aerospace aluminum alloys can be successfully joined at independent facilities to produce poolable (statistically speaking) joint efficiencies data for FSW. The fact that each of the participants in the MMPDS round-robin program followed a draft version of the AWS D17.3 to produce acceptable welded joints further demonstrates the robustness of the FSW technology when carried out responsibly to produce optimum joint properties for a given alloy without limiting tool design considerations.

The AWS specification was no doubt supplemented by undisclosed company-specific internal process procedures and methods, including proprietary tool designs. This further attests to the robustness of the process and it also identifies the value of having industry standards and specifications that minimize the need for the added cost of internal point design programs. With the incorporation of traceable joint efficiency data, the advanced maturity level of FSW industry specifications will become self-evident and thus promote a greater utilization of the technology.

This work also serves to demonstrate that data packages derived from proprietary research and production operations can be pooled with academic work to form a useful database of material properties for the benefit of both concerns. Therefore, academia can contribute significantly in the technology transfer process by applying similar disciplines to those used in industry-based research work for peer-reviewed symposia like this FSW&P symposia series. This will also enhance the scientific level of technical journals in general. Developing welding procedure specifications (WPS) for academic research does not limit the freedom to innovate and explore new concepts. Rather it is a particular way to promote documenting the essential process variables so research can be represented properly for confirmation and potential statistical pooling of published data. More complete published work holds the potential for more directly implementing repeatable FSW processes, both in the lab and in industry.

By applying the disciplines of having published work include certain information required by established standards, a coherent database of information can be established, not only for reference by researchers but also for advancing the state-of-the-art of FSW&P through standards and process controls development. With a complete and more verifiable dataset, published industry standards and specifications will give a more complete and positive representation of the capabilities of joints produced by FSW relative to fusion welding processes, for example. Without such a coherent set of published data, the perception of maturity will be achieved more slowly due to the lack of uniformity and consistency in published results.

References

1. Friction stir welding and processing. In: 2001 TMS fall meeting, Indianapolis. Indiana, USA, 4–8 Nov 2001
2. Friction stir welding & processing II. In: 2003 TMS Annual Meeting. San Diego, California, 2–6 March 2003
3. Friction stir welding and processing III. In: 2005 TMS annual meeting. San Francisco, California, 13–17 Feb 2005
4. Friction stir welding and processing IV. In: TMS 2007 annual meeting & exhibition. Orlando, Florida, USA, 25 Feb–1 March 2007
5. Friction stir welding and processing V. In: TMS 2009 annual meeting & exhibition. San Francisco, California, USA, 15–19 Feb 2009
6. Friction stir welding and processing VI. In: TMS 2011 annual meeting & exhibition. San Diego, California, USA, 27 Feb–3 March 2011
7. Friction stir welding and processing VII. In: TMS 2013 annual meeting & exhibition. San Antonio, Texas, USA, 3–7 March 2013
8. Friction stir welding and processing VIII. In: TMS 2015 144th annual meeting & exhibition. Orlando, Florida, USA, 15–19 March 2015

9. Friction stir welding and processing IX. In: TMS 2017 146th annual meeting and exhibition. San Diego, California, 26 Feb–2 March 2017
10. AWS D17 Committee on Welding in the Aircraft and Aerospace Industry, AWS D17.3/D17.3M:2016, Specification for Friction Stir Welding of Aluminum Alloys for Aerospace Applications, 2016 ed, The American Welding Society (AWS), Miami, Florida (2016)
11. AWS D1 Committee on Structural Welding, AWS D1.2/D1.2M:2014, Structural Welding Code–Aluminum, The American Welding Society, Miami, Florida (2014)
12. AWS C6 Committee on Friction Welding, AWS C6.3/C6.3M, Recommended Practices for Friction Stir Welding, New Ed, The American Welding Society, Miami, Florida
13. AWS D8 Committee on Automotive Welding, AWS D8.17M, Specification for Automotive Weld Quality—Friction Stir Welding, New Ed, The American Welding Society, Miami, Florida
14. IIW C-III-B-WGB1, Friction Stir Welding Standardisation Working Group, ISO 25239:2011, Friction stir welding—Aluminium, 2011 ed, vol 1, International Organization for Standardization (ISO), Geneva (2011)
15. IIW C-III-B-WGB4 Friction Stir Spot Welding Standardization Working Group, ISO/FDIS 18785, Friction stir spot welding—Aluminium, Geneva: International Organization for Standardization (ISO)
16. Kallee SW, Nicholas ED, Thomas WM (2001) Industrialisation of friction stir welding for aerospace structures. In: Structures and technologies—challenges for future launchers. Strasbourg France
17. Midling T, Kvale JS, Dahl O (1999) Industrialisation of the friction stir welding technology in panels production for the maritime sector. In: 1st international symposium on friction stir welding. Thousand Oaks, CA, USA
18. American Bureau of Shipping, ABS Guide for the Approval of Friction Stir Welding in Aluminum, 2011 Ed, American Bureau of Shipping, Houston, TX
19. NASA LBJ SC Materials and Processes Branch/ES4, Process Specification for Friction Stir Welding, NASA Ed, National Aeronautics and Space Administration, Lyndon B. Johnson Space Center, Houston, TX
20. Arbegast WJ (2007) Friction stir welding: after a decade of development. In: TMS 2007 annual meeting & exhibition. Orlando, Florida, USA
21. Nelson TW (2005) Friction stir welding: a brief review and perspective for the future. In: TMS 2005 annual meeting & exhibition. San Francisco, CA, USA
22. Mahoney MW (2007) Chapter 5: mechanical properties of friction stir welded aluminum alloys, Mishra RS, Mahoney MW (eds), 1st edn, pp 71–110. ASM International, Metals Park, Ohio
23. Dos Santos J, Olea C, Coelho R, Kostka A, Paglia C, Ghidini T, Donne Eads C (2010) Chapter 11—metallurgy and weld performance in friction stir welding, Lohwasser D, Chen ZW (eds), 1st edn, pp 314–410. Woodhead Publishing, Cambridge
24. ISO Central Secretariat, "ISO," International Organization for Standardization. https://www.iso.org/standard/69623.html. Accessed Oct 2018
25. Mishra R, Ma Z (2005) Friction stir welding and processing. Mater Sci Eng 50(1–2):1–78
26. Widener C, Tweedy B, Burford D (2007) Path independence of allowables. In: 7th AIAA aviation technology, integration and operations conference. Belfast, Northern Ireland, Ireland
27. Reynolds P, Tang W (2001) Alloy, tool, geometry, and process parameter effects on friction stir weld energies and resultant FSW joint propertie. In: Friction stir welding and processing. Indianapolis, Indiana, TMS Fall Meeting
28. Mahoney MW, Rhodes CG, Flintoff JG, Spurling RA, Bingel WH (1998) Properties of friction-stir-welded 7075 T651 aluminum. Mater Trans A 29A(7):1955–1964
29. Burford DA (2003) Friction stir welding of airframe structure: from one delivery system to another. SAE Trans 112(Section 1). J Aerosp 295–300
30. Burford DA (2003) SAE technical paper 2003-01-2897. In: Aerospace manufacturing technology conference & exposition, Montreal
31. MMPDS Coordination Committee, MMPDS Handbook, MMPDS-12 ed, Battelle Ed, Metallic Materials Properties Development and Standardization (MMPDS), Current, Columbus, Ohio

32. Metallic Materials Properties Development and Standardization (MMPDS), Battelle, 505 King Ave, Columbus, Ohio 43201. https://www.mmpds.org/about-us/. Accessed Sept 2018
33. Burford D, Tweedy B, Widener C (2007) Evaluation of friction stir weld process and properties for aircraft application. Joint Advanced Materials & Structures Center of Excellence, Atlantic City, NJ
34. Widener CA, Burford DA, Jurak S (2010) Effects of tool design and friction stir welding parameters on weld morphology in aluminum alloys. Mater Sci Forum 638–642:1261–1266
35. Burford DA, Tweedy BM, Widener CA Development of design data for FSW and FSSW. In: 7th international symposium on friction stir welding. Awaji Island, Japan, 20–22 May 2008
36. Widener CA, Tweedy BM, Burford DA An investigation of tool design and welding parameters on fatigue life in FS welded 2024-T3. In: The 7th international friction stir welding symposium. Awaji Island, Japan, 20–22 May 2008
37. Jurak SF (2011) In: Asmatulu R, Burford D, Lankarani H (eds) Statistical analysis of the mechanical properties of friction stir welded AA2024 and AA2198 aluminium alloys. Wichita State University (WSU), Wichita, Kansas
38. Jurak S, Burford D, McCoy M (2013) Analysis of mechanical and metallurgical properties of friction stir butt welded AA2024. In: Mishra R, Mahoney MW, Sato Y, Hovanski Y, Verma R (eds) Friction stir welding and processing VII. Wiley & Sons, San Antonio, TX, pp 183–194
39. Widener C, Tweedy B, Burford D An investigation of tool design and welding parameters on fatigue life in FS welded 2024-T3. In: The 7th international friction stir welding symposium. Awaji Island, Japan, 20–22 May 2008
40. Burford D, Tweedy B, Widener C (2007) Evaluation of friction stir weld process and properties. CECAM & AMTAS, 10 July 2007 [Online]. https://www.jams-coe.org/Presentations/2007-Wichita. Accessed Sept 2018
41. Rice R Statistical analysis of friction stir weld round-robin test data. In: 17th MMPDS coordination meeting: emerging materials working group (ETWG). Atlanta, Georgia, USA, 29 April 2010
42. AMS AMEC Aerospace Metals and Engineering Committee, SAE International. https://www.sae.org/works/committeeHome.do?comtID=TEAAMSAMEC. Accessed Oct 2018
43. Burford D, Widener C, Brown J (2008) Evaluation of friction stir weld process and properties for aircraft application: MMPDS initiatives. The FAA Joint Advanced Materials and Structures Center of Excellence, Everett, Washington
44. Burford DA, Widener CA (2009) Evaluation of friction stir welding process and properties for aerospace application: standards and specifications development. The FAA Joint Advanced Materials and Structures Center of Excellence, Wichita, Kansas
45. Burford D (2011) Material performance/property specifications and standards for friction stir technologies. In: AMEC meeting no. 214, Asilomar Conference Center Pacific Grove, CA, 21 Jan 2011

Advances in Signal Processing for Friction Stir Welding Temperature Control

Brandon Scott Taysom and Carl David Sorensen

Abstract Precise temperature control of FSW benefits from control and manipulated signals that are responsive and smooth. Accurate measurement of tool temperature and spindle speed feedback are important to temperature control, but often noise in these signals prevents optimal control. Two different methods are developed in this paper to improve signal quality. A series of Bezier curves are used to compensate signals which exhibit a periodic but arbitrarily-shaped offset. Least-squares fitting is used to obtain quality derivatives from discrete or noisy signals. The Bezier method is used to decrease the inaccurate temperature fluctuation measurements reported by telemetry collar error and adds no time delay or phase shift. The least-squares approach is used to estimate spindle speed and temperature derivatives and adds only minimal time delay while substantially reducing noise.

Keywords Friction stir welding · Temperature control · Signal processing

Introduction

Friction stir welding (FSW) is a solid-state joining process that is used to join two, usually planar, workpieces to one other. A nonconsumable tool is rotated at the seam of the two pieces, creating friction and sufficient heat to allow for continuous hot deformation. The tool traverses along the seam of the two pieces, creating a joint behind it. Because FSW does not melt, the workpieces, properties such as ductility, strength, and fracture toughness of the weld are better than those resulting from traditional welding [1, 2].

FSW quality is dependent upon temperature [3]. If the temperature of the material during the weld is too low, bonding and consolidation defects can occur. On the other hand, excessive heat can create an enlarged heat-affected zone and incipient melting

---

B. S. Taysom (✉) · C. D. Sorensen
Brigham Young University, Provo, UT, USA
e-mail: scott.taysom@gmail.com

Y. Hovanski et al. (eds.), *Friction Stir Welding and Processing X*, The Minerals, Metals & Materials Series, https://doi.org/10.1007/978-3-030-05752-7_13

[4]. Poor or uncontrolled temperature on either extreme can result in a defective weld [5].

FSW was first performed on modified milling machines, which typically do not have temperature monitoring or control capabilities. Consequently, early welds specified depth, traverse speed, and spindle rotation speed, but did not control temperature [6]. These welds, even when performed at constant input parameters, experience temperature fluctuations due to thermal transients and disturbances [7, 8].

Due to natural temperature variations and temperature-dependent material properties, temperature control is desirable in order to produce more optimized welds. Various researchers have used different inputs such as spindle speed and spindle power to control temperature [8–12], and have used different feedback methods to measure temperature [8, 12–15]. Many algorithms and approaches such as PID, model predictive control, and others have also been used to control temperature in FSW [8–11, 16].

A fundamental limitation to any control scheme is the quality of the feedback signals to the controller. Specifically, if the signals are noisy or have a large time delay, then the maximum achievable control may be limited. When using a low-pass filter to reduce temperature noise, thermal time delays of only 0.3 s can increase to 1.5–3 s [7, 8, 17, 18]. Reducing noise at the cost of time delay and responsiveness is usually acceptable for longer welds with durations ranging from several minutes to an hour. However, adding a significant time delay is unacceptable for processes that are either quick or need tight control. A time delay increase of 1–2 s would be completely unacceptable in the welding of automotive sheets, where total weld times are well under a minute.

This paper develops two different methods to reduce signal noise while adding minimal or zero time delay. A Bezier compensation method is used to account for arbitrary-shaped yet periodic offsets, such as those often observed with a telemetry collar. This method has zero added time delay, and can often reduce the signal-to-noise ratio by a factor of 10. A least-squares method is used to directly calculate derivatives from noisy and discrete signals. This method is applicable to both temperature feedback and spindle motor encoder feedback for calculation of spindle speed and acceleration. The least-squares method adds a small amount of time delay but significantly improves measurements of first and second derivatives.

Software and Equipment

The Matlab language and software was used to perform all initial development and prototyping and was also used to create all figures. The programming environment for the PLC is B&R Automation Studio 4.2, which uses a custom language similar to C. Code in this paper is based upon B&R AS 4.2, with syntactic changes to aid in brevity and readability.

The machine used for all experiments was a TTI High Stiffness RM2 FSW machine with 10 Ton Spindle. The machine has a new Bond Technologies

B&R-based PLC with high-speed data acquisition and control. The PLC tasks operate at rates ranging from 42 to 1250 Hz, with the Bezier method operating at 500 Hz and the derivative method at 1250 Hz. The motor and drive are a semi-custom Yaskawa VFD F7 series, with max capacity of 37 kW, 4500 RPM, 400 N-m torque, a 12-bit encoder, and a 1:2.5 gear ratio to the spindle. The telemetry collar is an ATI 2010i with capabilities for up to three channels, although only one channel was used for these experiments.

Correcting Arbitrary Periodic Signal Offset

Use Case and Purpose—Temperature Measured via Telemetry Collar

Telemetry collars are often employed in FSW to measure the temperature of the rotating tool. These units typically have a collar with thermocouples that rotates with the spindle, and a stationary antenna which provides power and receives the signal wirelessly.

A downside to this system is that measurements can be affected by the position of the collar relative to the antenna loop. Furthermore, minor changes to the tuning and positioning of these units can drastically affect the stability and quality of signal. This is shown below in Fig. 1, where the spindle was rotated in air with a thermocouple embedded in a constant temperature tool.

As Fig. 1a shows, the signal is periodic but of an apparently arbitrary waveform. When plotted against the spindle angle as in Fig. 1b, the measured signal is shown to be linked to the angle of the spindle. The shape of the temperature offset correlates to

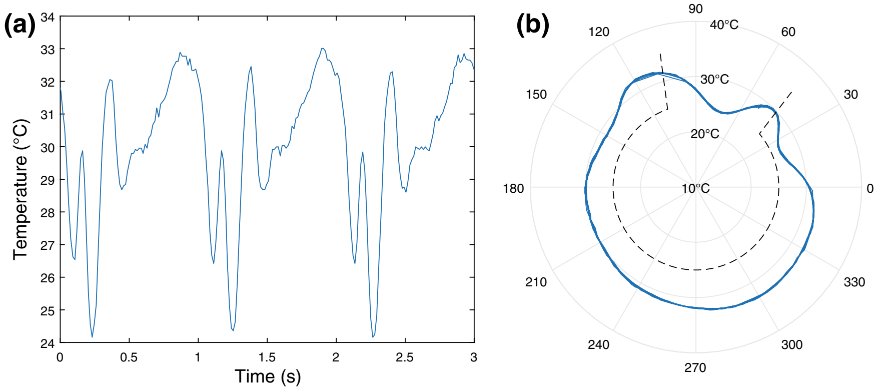

Fig. 1 **a** Measured temperature versus time. **b** Polar plot of temperature versus time, with the spatial orientation of the antenna schematically shown in dashed lines

the antenna position, shown schematically in dashed lines. Each time the telemetry collar is physically adjusted, the shape of the waveform has been observed to change.

Such a signal cannot provide accurate measurements that enable precise temperature control in FSW. The signal can be aggressively filtered, but this induces a large time delay into the system, which limits the responsiveness of temperature control.

A much better approach is to address the underlying signal problem—that the signal is a composite of the true value, plus an offset based upon angular position plus other noise sources. Since the angular position waveform is consistent, this offset can be calculated and compensated for.

Bezier Curves

Bezier curves have gained renewed interest from computer scientists due to their ability to represent arbitrary shapes in computer graphics. Bezier curves can be fitted together smoothly to closely follow data. For a series of Bezier curves to have C^n continuity, the individual curves themselves must be at least $(2n+1)$th order. Thus to have continuous derivatives (C^1), third-order curves are needed. For a domain of [0 1], the equation for the *n*th Bezier curve is

$$B_n(t) = (1-t)^3 P_{0,n} + 3(1-t)^2 t P_{1,n} + 3(1-t)t^2 P_{2,n} + t^3 P_{3,n} \tag{1}$$

The above third-order curve intersects points P_0 and P_3, and is tangent at its ends to the lines connecting P_0–P_1 and P_2–P_3.

Building and Interpolating from Bezier Curves

The spindle was divided into 36 segments, each of which was characterized by a third-order Bezier curve. The curves were linked such that the first and last control points were shared by two curves and thus 108 unique control points were calculated.

Data was collected over time and counted and binned to the nearest control point; thus the 0th bin for the first point used data from positions of 358.33–1.66°. After data was collected, the mean of each span was calculated (M_0, M_1, etc.). The value of control points P_0 and P_3 is simply the mean, thus $P_0 = M_0$ and $P_3 = M_3$. P_1 and P_2 are calculated such that C^1 derivative continuity between the curves is maintained, and are calculated by a central difference derivative between the two curves. Thus control points P_1 and P_2 are:

$$P_{1,n} = M_{0,n} + \left(M_{1,n} - M_{2,n-1}\right)/2 \tag{2}$$

$$P_{2,n} = M_{3,n} - \left(M_{1,n+1} - M_{2,n}\right)/2 \tag{3}$$

Once all of the 108 control points are initially calculated, they need to be converted into offsets. This is accomplished by subtracting the mean of the points from each point individually.

During operation, at each IO cycle, the position of the spindle is used to determine which set of Bezier curves is applicable for that position. Then the 0–360° position is converted into a 0–1 parametric position (t) over that curve and Eq. (1) is used to calculate the offset.

This signal processing method can be used with other filtering techniques. When combined with other methods, this technique should be applied first as it has zero time delay. Afterward, a low-pass filter can be applied to mitigate normally occurring noise. A filter with a low cutoff frequency was used in order to reduce noise without adding a significant phase shift.

Results of Bezier Curve Compensation

The Bezier curve compensation method was tested in two different ways. First, the method was tuned at 60, 240, and 960 rpm, and the spindle was operated at those speeds in air to produce a tightly controlled test. Second, the Bezier method was tuned at 240 rpm, and a temperature control weld was performed at a nominal 240 rpm to test real-world application. The 240 rpm air rotation and actual weld results are shown in Fig. 2. As can be seen in Fig. 2a, the Bezier curves (dashed lines) match the observed variation extremely well, and thus are able to compensate for a vast majority of the deleterious effect.

In order to quantify the effectiveness of the Bezier compensation method, the standard deviations of both the original and compensated signal were taken over an

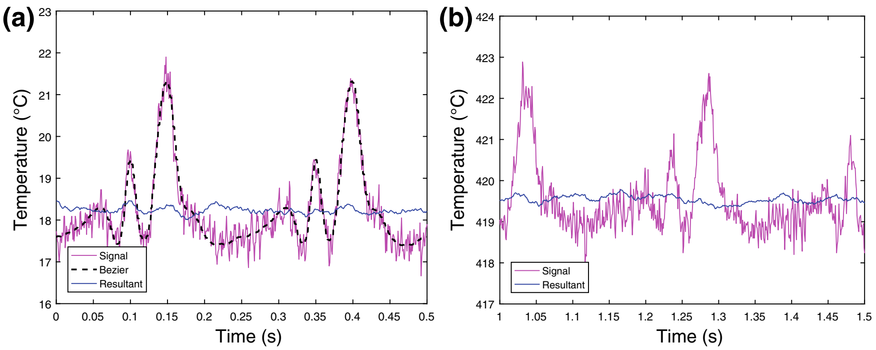

Fig. 2 **a** Bezier temperature filter applied to tool temperature while rotating in air at 240 rpm. **b** Bezier temperature filter in a weld at a constant tool temperature and nominal spindle speed of 240 rpm

Table 1 Variation in measured temperature for several different cases

	60 rpm air	240 rpm air	960 rpm air	240 rpm weld
Original Std. dev. (°C)	1.03	1.01	0.80	0.86
Compensated Std. dev. (°C)	0.07	0.16	0.16	0.08
Ratio of compensated/original	0.07	0.16	0.20	0.10

integer number of rotations. A ratio of the two was calculated to establish how much the signal improved. These results are shown in Table 1.

In all cases, the Bezier compensation method eliminated a majority of the periodic deviation of the telemetry collar. Furthermore, this effect is achieved without adding any time delay. Thus, this method has no negative results on the signal, unlike low-pass filters which reduce noise at the cost of an added time delay.

Calculating Derivatives from Noisy or Discretely Sampled Data

Use Cases and Purpose—Encoder Data and Accurate Derivatives

Spindle speed is a fundamental manipulated variable used to control temperature in FSW. Spindle speed can be determined in two main ways: by the motor drive, or by the encoder. Most drives estimate spindle speed based upon instantaneous voltage and current, but the results can be sluggish, noisy, and have other frequency effects. A servo encoder is highly reliable, has little to no noise, and is very accurate; however, unlike a controller's voltage feedback, the signal is discrete and gives only position, not speed. This discrete nature can present challenges when a medium-accuracy encoder (~12 bits) is sampled quickly and is used to calculate a derivative. Another example occurs when a first or higher derivative must be calculated from noisy data, such as an analog temperature signal.

In both cases, the core problem is the same: uncertainty, truncation, or noise present in the 2 or 3 points used to calculate the derivative(s) greatly affects the resultant derivative. While the time-averaged results are reasonably accurate, the instantaneous results are often noisy and need significant filtering to be useful.

Least-Squares Curve Fitting

Using the nth previous data points to calculate the derivative reduces the influence of noise in any one point, and the signal can be significantly smoothed at the cost of some lag. A least-squares fit can calculate a derivative with higher accuracy and a lower time delay than a two-point derivative method can while spanning the same time. This method can also be easily extended to calculate 2nd derivatives (acceleration) or higher if needed.

While several methods exist to fit curves to data, one of the most straightforward is the classical least-squares approach. If x and y are vectors of data, the unknown coefficients m and b will fully constrain the line $y = mx + b$. In order to perform a linear least-squares regression, vectors/matrices X and Y are first created from data. These are

$$\mathrm{X} = \begin{bmatrix} 1 & x_1 \\ 1 & x_2 \\ \vdots & \vdots \\ 1 & x_n \end{bmatrix} \tag{4}$$

$$Y = \begin{bmatrix} y_1 \\ y_2 \\ \vdots \\ y_n \end{bmatrix} \tag{5}$$

A is then determined by

$$A = \left(X^T X\right)^{-1} X^T Y \tag{6}$$

And m and b (derivative and intercept) coefficients are

$$A = \begin{bmatrix} b \\ m \end{bmatrix} \tag{7}$$

This method can also be extended to a quadratic equation of the form $y = ax^2 + bx + c$. In this case, X is

$$X = \begin{bmatrix} 1 & x_1 & x_1^2 \\ 1 & x_2 & x_2^2 \\ \vdots & \vdots & \vdots \\ 1 & x_n & x_n^2 \end{bmatrix} \tag{8}$$

And A is

$$A = \begin{bmatrix} c \\ b \\ a \end{bmatrix} \tag{9}$$

where the derivative (at time x=0) is $y' = b$, and the second derivative (acceleration) is $y'' = 2a$.

Least Squares via Arrays

Least-squares fitting is traditionally performed with linear algebra, which can be difficult to emulate on many PLCs. Furthermore, matrix inversion is computationally intense, scaling at a rate of n^3 per inversion. However, the precise timing nature of PLCs can be exploited such that the math is reduced to simple arrays, and the repeating computation cost then scaling at a rate of n^1.

When the time step is constant and known, the expression $\left(X^T X\right)^{-1} X^T$ can be calculated once and used for all future calculations. Thus, this method has two parts: (1) One-time; initial calculation and setup of the array version of the matrix $\left(X^T X\right)^{-1} X^T$, and (2) Each cycle; updating the last n points, and multiplying and summing in order to recalculate the regression coefficients.

Initial Setup

For the linear method, the 2×2 matrix $\left(X^T X\right)$ must be calculated and formatted into a 4×1 array. This is

lin_XTX[0] = n
*lin_XTX[1, 2] = −1 * dt * n * (n − 1)/2;*
*lin_XTX[3] = 1/6 * (n − 1) * n * (2 * n − 1) * dt * dt;*

Then, the inverse $\left(X^T X\right)^{-1}$ is calculated:

*lin_det_XTX = 1/(lin_XTX[0] * lin_XTX[3] − lin_XTX[1] * lin_XTX[2]);*
*lin_XTX1[0] = lin_det_XTX * lin_XTX[3];*

```
lin_XTX1[1, 2] = −1 * lin_det_XTX * lin_XTX[1];
lin_XTX1[3] = lin_det_XTX * lin_XTX[0];
```

And the second row of the product $\left(X^T X\right)^{-1} X^T$ can also be calculated once

```
For i = 0: (n − 1)
    lin_XTX1XT_row2[i] : = lin_XTX1 [2] + lin_XTX1[3] * dt * (i − n + 1);
End
```

A similar approach can be used to derive the quadratic forms of the matrix array "*quad_XTX1XT.*" These cannot be included herein due to length restrictions. For the quadratic derivation, it is convenient to first explicitly calculate the determinate before taking the inverse, in contrast to the linear version shown above where that step was combined with the inverse. Parties interested in the full derivation, or worked examples of either of these, are invited to contact the corresponding author.

Each Cycle

Each cycle, y values are shifted, with the newest value stored at the end index. Then, the components are multiplied and summed, which calculates the derivatives:

```
dydt_lin = 0; dydt_quad = 0; d2ydt2_quad = 0;
    For i = 0: (n − 1)
    dydt_lin = dydt_lin + lin_XTX1XT_row2[i] * y_vec [i];
    dydt_quad = dydt_quad + quad_XTX1XT_row2[i] * y_vec [i];
    d2ydt2_quad = d2ydt2_quad + 2 * quad_XTX1XT_row3[i] * y_vec [i];
End
```

The linear estimate of the first derivative is typically more regular, but slightly less responsive, than the corresponding quadratic estimate.

Results of the Least-Squares Method on Calculated Spindle Speed

Spindle speed was measured using four different methods. The first method used to measure spindle speed is the analog output from the spindle drive, which is estimated based upon voltage and current to the motor. The second method is a filtered version of the analog spindle speed. The third method uses the encoder position in a backwards difference derivative, referencing the position five points in the past. The fourth method is the least-squares fit approach developed in this paper, using the most recent 50 data points collected at 1250 Hz.

Table 2 Performance characteristics for four different methods of estimating spindle speed

	Analog	Filtered analog	Encoder—simple 5 point	Encoder—least-squares
Delay (s)	0.01	0.06	0.002	0.02
Std. dev. (rpm)	0.45	0.086	1.04	0.10

The spindle was brought to a nominal speed of 1000 rpm and held steady, while the data acquisition system recorded data at a rate of 0.8 ms or 1250 Hz. In order to estimate the time delay of the system, the estimated spindle speed was compared to a 2-point backwards difference calculation from the encoder during acceleration to 1000 rpm. Average noise in the signal was determined by calculating standard deviation of a 1 s interval of data with nearly zero acceleration or deceleration of the motor. The results are shown below in Table 2.

The least-squares method has noise comparable to a heavily filtered analog signal but has a third the delay. The other two methods have lower time delays, but the noise in the signal is significantly greater than that of the least-squares method. Overall, the least-squares method provides a good balance in its delay and noise properties that make it very useful for a variety of circumstances.

Combined Bezier Compensation and Least Squares Fitting

The Bezier-compensation and least-squares methods were used in tandem to provide estimates of first and second derivatives of temperature in a weld. An adaptive relay autotuning weld was performed to achieve sustained oscillation of temperature. The raw temperature signal, compensated temperature, fit estimate, first derivative, and second derivative were recorded during the process and are shown in Fig. 3.

As the graphs show, the two methods work together extremely well. Even though the original signal had ~3 °C telemetry noise, usable derivative values are calculated. As expected, the second derivative is about ½ period shifted from the original quasi-sine signal. The quality of the second derivative's estimate is impressive considering that the original signal-to-noise ratio is about 1:1.

Future Work and Improvements

Both methods presented here are accompanied by specific use cases; however, the methods themselves can be applied to other situations as well. Applying the least-squares method to temperature measurements yields improved first derivatives, which are useful for the adaptive relay autotuning method and PID temperature control. Improved second derivatives are extremely useful in tuning the acceleration term of

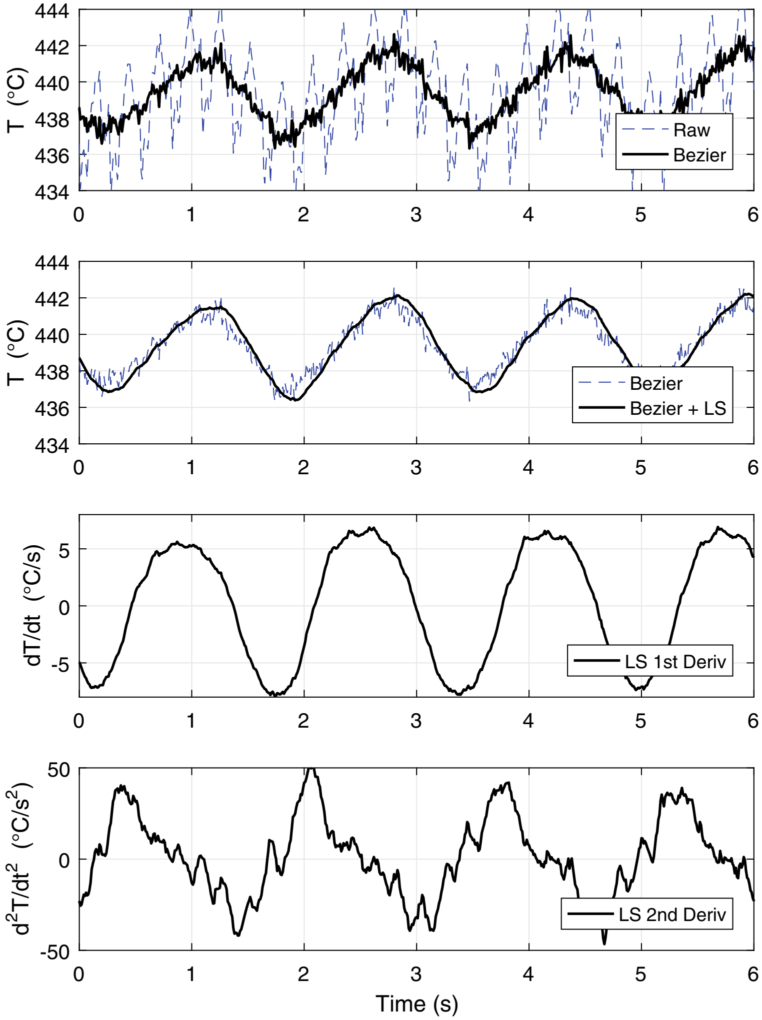

Fig. 3 Estimates of zeroth, first, and second derivatives of temperature during an adaptive relay weld. The first plot shows the raw and compensated temperature, and the second plot shows the compensated and compensated-then-least-squares calculated temperature, with lighter dashed and bolded solid lines, respectively. The third and fourth plots show respectively the first and second derivatives of temperature calculated from the least squares method

PVA controllers. Mathematically, this method can be extended to higher derivatives as well, but noise becomes an increasing problem.

The Bezier curve method works extremely well when calibrated for specific spindle speeds. However, the signal shows an angular/time shift with a drop in amplitude at higher spindle speeds. It is hypothesized that this is caused by an intrinsic low-pass filter in the telemetry system. At low spindle speeds (i.e., 15 vs 60 rpm), there is no perceptible difference. However, a notable change is seen between 60, 240, and 960 rpm. It may be possible to model this electromechanical low-pass filter with a Fouier transform, and then apply this transform to the Bezier compensation to modify the correction curve.

Conclusions

Bezier curves can be used to model and then compensate for the majority of an arbitrarily-shaped periodic offset in a signal. In the studied case of a FSW telemetry collar, this method was used to reduce the noise by a factor of 10. This improvement occurs without increasing the time delay of measurement.

Regression techniques can be used to calculate the velocity and acceleration of the spindle from encoder data, resulting in an estimate of spindle speed that has both a low time delay and decreased noise levels compared to currently used methods. The least-squares method also gives good estimates of the acceleration of the spindle and can be used to calculate derivatives of tool temperature with good results.

References

1. Lakshminarayanan AK, Balasubramanian V, Elangovan K (2009) Effect of welding processes on tensile properties of AA6061 aluminium alloy joints. Int J Adv Manuf Technol 40:286–296
2. Mahoney MW, Rhodes CG, Flintoff JG, Bingel WH, Spurling RA (1998) Properties of friction-stir-welded 7075 T651 aluminum. Metall Mater Trans A 29:1955–1964
3. Fehrenbacher A, Duffie NA, Ferrier NJ, Pfefferkorn FE, Zinn MR (2014) Effects of tool-workpiece interface temperature on weld quality and quality improvements through temperature control in friction stir welding. Int J Adv Manuf Technol 71:165–179. https://doi.org/10.1007/s00170-013-5364-4
4. Robson JD, Cui S, Chen ZW (2010) Incipient melting during friction stir processing of AZ91 magnesium castings. Mater Sci Eng A 527:7299–7304. https://doi.org/10.1016/j.msea.2010.07.093
5. Cederqvist L, Garpinger O, Hagglund T, Robertsson A (2011) Reliable sealing of copper canisters through cascaded control of power input and tool temperature. In: Mishra R, Mahoney MW, Sato Y, Hovanski Y, Verma R (eds) Friction stir welding and processing VI. Wiley, Inc., Hoboken, NJ
6. Chimbli SK, Medlin DJ, Arbegast WJ (2007) Minimizing lack of consolidation defects in friction stir welds. In: Proceedings of 136th TMS annual meeting friction stir welding and processing IV symposia, TMS, pp. 135–142
7. Taysom BS (2015) Temperature control in friction stir welding using model predictive control. Brigham Young University. https://doi.org/10.1017/cbo9781107415324.004
8. Taysom BS, Sorensen CD, Hedengren JD (2017) A comparison of model predictive control and PID temperature control in friction stir welding. J Manuf Process 29:232–241. https://doi.org/10.1016/j.jmapro.2017.07.015
9. Ross KA, Sorensen CD (2013) Effort modulation for process control of friction stir operations. US 20140207274 A1
10. Ross KA (2012) Investigation and implementation of a robust temperature control algorithm for friction stir welding. Brigham Young University

11. Cederqvist L, Garpinger O, Hägglund T, Robertsson A (2012) Cascade control of the friction stir welding process to seal canisters for spent nuclear fuel. Control Eng Pract 20:35–48
12. Fehrenbacher A, Smith CB, Duffie NA, Ferrier NJ, Pfefferkorn FE, Zinn MR (2014) Combined temperature and force control for robotic friction stir welding. J Manuf Sci Eng 136:21007
13. Cederqvist L, Garpinger O, Cervin A, Nielsen I (2015) Improved temperature and depth control during FSW of copper canisters using feedforward compensation. In: Friction stir welding and processing VIII, pp. 69–76. https://doi.org/10.1007/978-3-319-48173-9_7
14. Ross K (2014) Temperature control in friction stir welding for industrial and research applications. In: 10th international symposium on friction stir welding
15. De Backer J, Bolmsjo G, Christiansson A-K (2014) Temperature control of robotic friction stir welding using the thermoelectric effect. Int J Adv Manuf Technol 70:375–383. https://doi.org/10.1007/s00170-013-5279-0
16. Marshall D, Sorensen CD (2013) System parameter identification for friction stir processing. TMS Annu Meet 289–299. https://doi.org/10.1007/978-3-319-48108-1_30
17. Taysom BS, Sorensen CD, Hedengren JD (2016) Dynamic modeling of friction stir welding for model predictive control. J Manuf Process 23. https://doi.org/10.1016/j.jmapro.2016.06.004
18. Marshall D (2013) An alternative system identification method for friction stir processing. Brigham Young University

Intermittent Flow of Material and Force-Based Defect Detection During Friction Stir Welding of Aluminum Alloys

Daniel J. Franke, Michael R. Zinn and Frank E. Pfefferkorn

Abstract The cost limitations of post-weld inspection have driven the need for in situ process monitoring of subsurface defects. Subsurface defects are believed to be formed due to a breakdown in the intermittent flow of material around the friction stir tool once per revolution. This work examines the intermittent flow of material and its relation to defect formation. In addition, advances have been made in a force-based defect detection model that links changes in process forces to the formation and size of defects. A range of aluminum alloys has been examined, showing that softer aluminum alloys produce less distinct changes in process forces during defect formation and harder aluminum alloys produce more distinct changes when using the same tool geometry.

Keywords Aluminum alloys · Nondestructive evaluation
Intermittent material flow · Forces

Introduction

Friction stir welding (FSW) is a solid-state joining process developed at The Welding Institute in 1991 [1]. During FSW, metallic components are plastically deformed and mechanically intermixed under high pressure and elevated temperature. A significant amount of research has shown that FSW can be used as an energy efficient method of creating high-quality joints in lightweight alloys such as aluminum and magnesium [2–5]. The solid-state nature of this process provides several distinct advantages when compared to fusion welding processes. These advantages include the avoidance of hot cracking, minimal residual stresses and distortion, energy efficiency, and improved joint quality due to grain refinement and minimal thermal effects [2, 3].

D. J. Franke · M. R. Zinn · F. E. Pfefferkorn (✉)
Department of Mechanical Engineering, University of Wisconsin-Madison,
1513 University Ave, Madison, WI, USA
e-mail: frank.pfefferkorn@wisc.edu

Y. Hovanski et al. (eds.), *Friction Stir Welding and Processing X*, The Minerals,
Metals & Materials Series, https://doi.org/10.1007/978-3-030-05752-7_14

Disadvantages of FSW, when compared with fusion welding processes, include large process forces and torques and limitations on weld geometry.

One challenge encountered in the application of the friction stir welding process is the avoidance of sub-surface defects (voids). It is believed that sub-surface defects result from a breakdown in material flow around the probe of the friction stir (FS) tool due to an inadequate thermomechanical state. The thermomechanical state of the process is dependent on a wide range of factors including tool rotational rate, tool traverse rate, FS tool geometry, workpiece material, and thermal boundary conditions. Currently, friction stir welding conditions are empirically determined based on a combination of prior knowledge and trial and error. One goal of this research area is to understand the complex flow around the FS tool probe well enough to accurately simulate and predict defect formation, thus streamlining the application of the process. Additionally, in high-reliability applications, post-weld inspection is often cost prohibitive. Therefore, a secondary goal of this work focuses on developing a real-time in-process defect monitoring system based on a numerical model of the process and measured process output (i.e., a cyber-physical system).

The basis of this work focuses on the intermittent flow of material around the FS tool (specifically the probe) during friction stir welding. Ever since the late 1990s, researchers [6–14] have shown evidence of an intermittent extrusion of material around the FS tool probe once per tool revolution during the friction stir welding of low melting temperature alloys. The most direct evidence of this layer-by-layer transfer is the banded microstructure (Fig. 1) that is often observed in the plane of welding. Figure 1 shows this structure within the region of the stir zone driven by the probe: i.e., 2.5 mm below the workpiece surface. The transverse cross section of the banded microstructure is what produces the prominent features referred to as "onion rings" in friction stir welding literature.

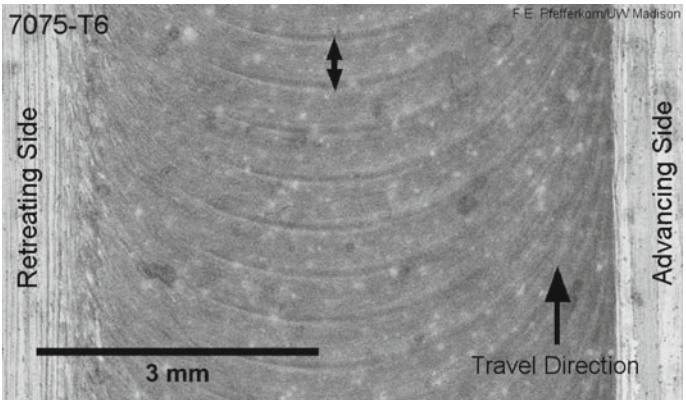

Fig. 1 A reflected light image of the banded microstructure observed in the probe driven region on the stir zone. The double-sided arrow designates the distance the tool travels in one rotation

The underlying physics of how these banded lamellae are formed is a fundamental and unanswered question in the friction stir welding research community. Schmidt et al. [14] and Tongne et al. [15] have both proposed that it stems from a change in contact condition between the tool and workpiece: a change from sticking to sliding or partial sticking/sliding once per tool revolution. Fonda et al. [12] proposed that it stems from a combination of tool runout as well as periodic deflection of the tool (due to the large process forces) once per revolution. Boldsaikhan et al. [16] proposed that a cavity opens up in the wake of the tool probe and is filled in once per tool revolution. Under good welding conditions this cavity is completely filled, and under inadequate conditions, the cavity is not completely filled leaving defects (voids, discontinuities). The most important aspect of the intermittent flow is that several researchers [13, 16–18] have either proposed or shown evidence that the formation of sub-surface defects is directly related to a breakdown of the intermittent flow. This is best exemplified in Fig. 2 which clearly shows the incomplete extrusion of material at a distance equal to the distance the tool moves in one revolution. Therefore, to fully understand sub-surface defect formation mechanisms, the intermittent flow of material must be understood.

Researchers have also linked the intermittent flow of material once per revolution to the oscillation of process forces once per tool revolution. When measuring welding forces in the direction of welding or perpendicular to the direction of welding at a sampling frequency sufficiently greater than the tool rotational frequency, it is evident

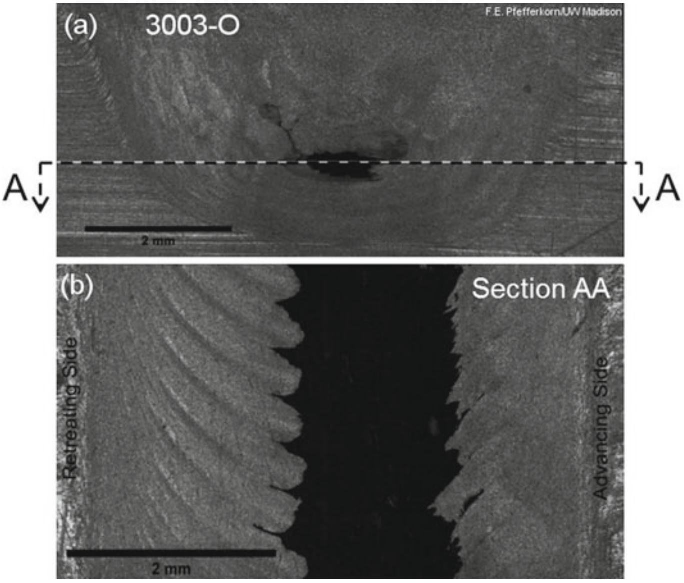

Fig. 2 Reflected light images of **a** transverse cross section of **b** section view in the plane of welding showing the incomplete extrusion of material once per tool revolution resulting in the formation of a void

that the forces tend to oscillate at the tool rotational frequency during friction stir welding. This concept was utilized by Boldsaikhan et al. [17] to develop a force-based method of monitoring weld quality by means of examining the welding forces in the frequency domain. Furthermore, Boldsaikhan et al. [18] developed a heuristic 2D force model that relates the oscillating process forces to the movement of a plasticized shear layer of material that is periodically extruded. Shrivastava et al. [19] built on the work by Boldsaikan et al. by examining the frequency content of the welding forces in depth and provided a physical explanation of what causes changes in process forces during defect formation. The work by Shrivastava et al. utilized the oscillating nature of the process forces to develop a force-based defect detection method that relies on interactions between features on the FS tool and void volumes to produce changes in the process forces. In good welding conditions, the forces in the plane of welding oscillate almost purely sinusoidally as shown in Fig. 3a. This is characteristic of smooth and complete extrusion of material around the FS tool probe once per tool revolution. When examining the force signal in the frequency domain, there is only a significant amplitude at the tool rotational frequency. When using a tool with features on the probe (in this case flats were used), an interaction between the features and the formation of a defect can be captured in the force signal. In the frequency domain, this interaction manifests itself as an amplitude at the harmonic of the tool rotational frequency corresponding to the number of flats on the FS tool probe, e.g., a three flat tool will produce an amplitude at the third harmonic of the tool rotational frequency as shown in Fig. 3b. The amplitude of the third harmonic was correlated to void volume in aluminum alloy 60661-T6 showing good initial agreement. The present study seeks to be a continuation of this method by extending it to other aluminum alloys. This work examines the oscillation of forces in an attempt to further uncover the mechanisms of intermittent flow of material as well as examining how disturbances in the force signals can be used to develop

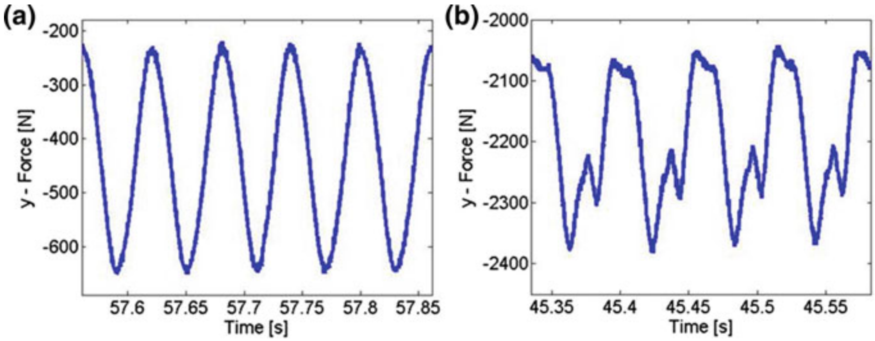

Fig. 3 Measured force signals in the direction of welding in **a** a fully consolidated weld and **b** a weld containing sub-surface defects. Welds were performed in 6061-T6 with a FS tool with three flats on the probe

means of force–measurement-based defect monitoring of the process across different aluminum alloys.

Experimental Methods

Welding was performed on a three-Axis CNC mill (HAAS TM-1). The stiffness of this machine, due to z-axis (plunge) forces, was estimated to be 0.05 mm/kN [20]. Workpieces were mounted on a three-axis piezoelectric force dynamometer (Kistler model 9265). The Dynamometer measures the net force (in each respective direction) that the tool applies to the workpiece. This net force is what is reported in this study. Charge signals from the dynamometer were fed to the charge amplifiers. Outputs from the charge amplifiers were connected to the DAQ system (National Instruments, LabVIEW).

An FS tool made of heat treated H13 tool steel was utilized in this study. It consisted of a concave shoulder with a diameter of 11.6 mm and a threaded, conical probe with three flats. The probe diameter tapered from 7 to 5 mm and was 5 mm in length. All welds were performed with a 3° travel angle. A defined preload was applied to a precision-ground gage block positioned between the trailing edge of the FS tool shoulder and the workpiece in order to establish a consistent plunge depth among welds. This study examined the force signals during defect formation of four different aluminum alloys: 3003-O, 6061-T6, 7075-T6, and 2024-T3. All workpieces were 203 mm (8 in.) long, 102 mm (4 in.) wide and 6.35 mm (0.25 in.) thick. Welding spindle speed was held constant at 1,000 rpm and travel speed was varied between 500 and 600 mm/min. Two replications at both conditions were performed in all four alloys. All welds were 150-mm-long (5.9 in.). Different commanded shoulder plunge depths (specified at the center of the tool) were used in each aluminum alloy in an attempt to produce consistent plunge depths: i.e., position of trailing edge of FS tool shoulder below the workpiece surface. Since the system is compliant, the stiffer and stronger alloys deflect the system more and require a larger commanded shoulder plunge depth to achieve a consistent resultant plunge depth. The commanded plunge depths in the different alloys are listed in Table 1. Material properties believed to

Table 1 List of commanded plunge depths for each specific alloy along with material properties taken from MatWeb [21]

Alloy	Commanded shoulder plunge (mm)	Modulus, E (GPa)	Yield strength (MPa)	Yield strength at temperature (MPa) (°C)
3003-O	0.150	68.9	41.4	12.0 @ 400
6061-T6	0.175	68.9	276	12.0 @ 371
7075-T6	0.525	71.7	503	32.0 @ 371
2024-T3	0.550	73.1	345	28.0 @ 371

be relevant to the plunge depth are also listed in Table 1. The stiffer/stronger alloys produced larger welding forces that generated more deflection in the system. Cross-sectional samples were cut from each weld (25 mm from the end of the weld), polished, and etched. Aluminum alloys 7075-T6 and 2024-T3 were etched with Keller's reagent, whereas 3003-O and 6061-T6 were etched in a modified Poulton's reagent with additional HNO_3.

Results and Discussion

The goal of this work is to examine the application of the force-based defection method developed in 6061-T6 by Shrivastava et al. [19] on different aluminum alloys. This study friction stir welds four different alloys with the same FS tool using the same processing parameters. The parameters were selected to produces defects in all of the alloys so that the change in the process forces in each alloy can be compared (1,000 rpm and 600 mm/min). Figure 4 shows the cross section of a 3003-O sample with the corresponding force data for three rotations of the tool in the region of

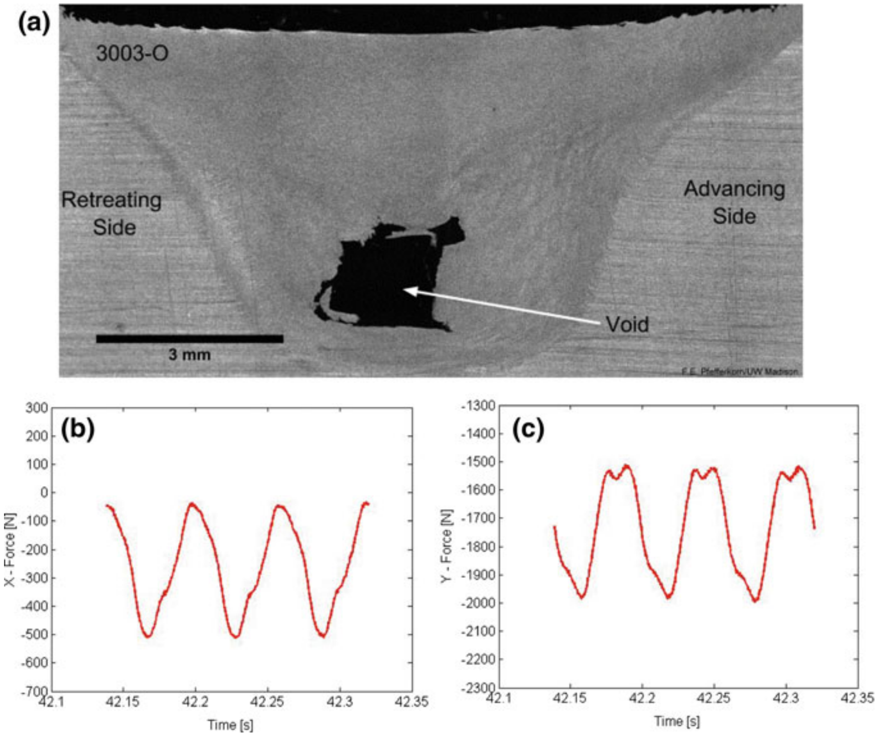

Fig. 4 Results of weld at 1,000 rpm and 600 mm/min in alloy 3003-O: **a** cross section of weld, **b** force signal perpendicular to welding direction, **c** force signal in direction of welding

the weld where the sample was cut from. The Y-direction corresponds to the travel direction of the weld and the X-direction corresponds to the direction in the plane of the workpiece that is perpendicular to the travel direction. A negative Y-direction corresponds to the direction of travel, i.e., the tool will apply an average negative Y-force to the workpiece since the workpiece is resisting the motion of the tool. The negative X-direction corresponds to a force pointing toward the retreating side of the process. Figures 5 through 7 are the corresponding cross sections and force signals for a sample of 6061-T6, 7075-T6, and 2024-T3, respectively. Each force plot shows the time period equal to three rotations of the tool.

Considering that it is not a structural aluminum alloy, 3003-O is the softest and weakest alloy of the four evaluated in this study. The intermediate alloy in this set is 6061-T6, with moderate hardness and hot strength compared to the rest. The two structural alloys, 7075-T6 and 2024-T3, are significantly harder and have a higher hot strength than 3003-O and 6061-T6. These properties govern how the material flows during welding, and how the forces are altered during defect formation. When examining 3003-O, it is clear that the largest defect was produced at these particular welding conditions when compared to the other alloys. It is hypothesized that this occurrence is due to the wide layer of sheared material near the surface of the weld

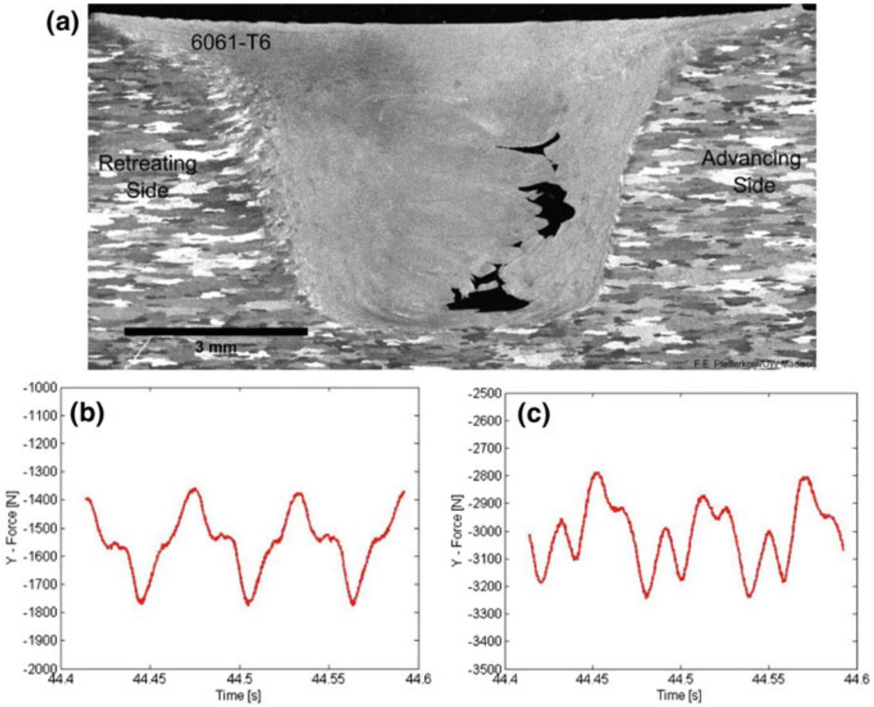

Fig. 5 Results of weld at 1,000 rpm and 600 mm/min in alloy 6061-T6: **a** cross section of weld, **b** force signal perpendicular to welding direction, **c** force signal in direction of welding

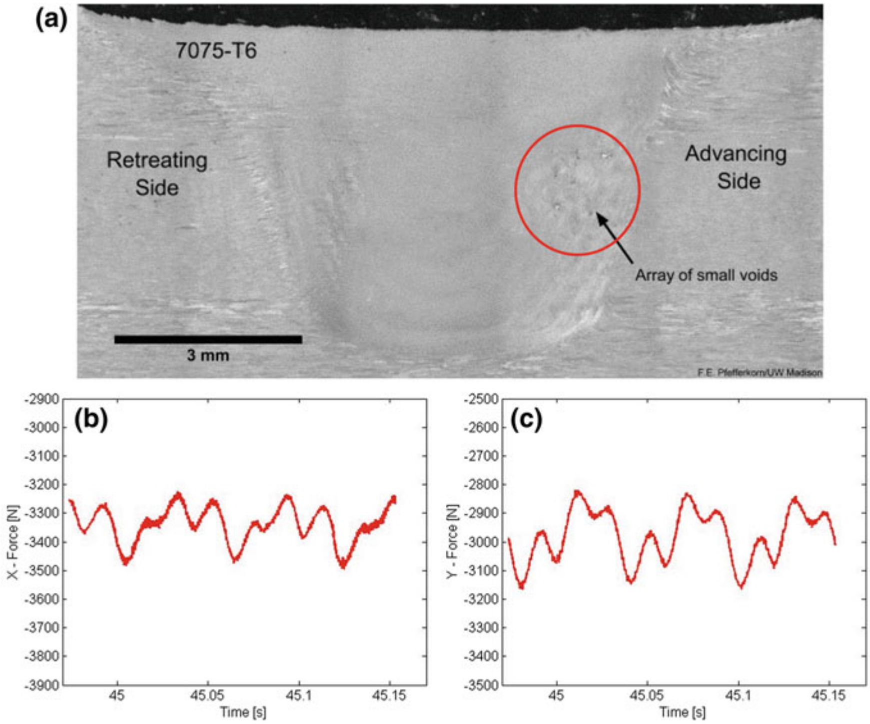

Fig. 6 Results of weld at 1,000 rpm and 600 mm/min in alloy 7075-T6: **a** cross section of weld, **b** force signal perpendicular to welding direction, **c** force signal in direction of welding

(shoulder), which allows the plasticized material to flow up around the shoulder and escape the probe driven region of the stir zone instead of being held and consolidated in the weld. In an application of FSW in 3003-O, an FS tool with a wider shoulder should be used. A larger ratio of the shoulder diameter to probe diameter will allow the shoulder to trap more of the plasticized material generated by the probe. When looking at the harder alloys (2024-T3 and 7075-T6) the stir zone is narrow near the shoulder suggesting that it was harder for material to escape from the weld zone, resulting in smaller defect volumes.

In the study performed by Shrivastava et al. [19] in 6061-T6, larger void sizes correlated with larger amplitudes of the higher harmonic. Interestingly, the 3003-O sample, which has the largest void size, experiences the smallest disturbance in the force signals at the higher harmonic (Fig. 4b, c) when compared to the other alloys tested at the same weld parameters. When examining the harder alloys, even at relatively small void sizes, there is a much more pronounced harmonic. The values of the amplitudes of the force signals at the tool rotational frequency (fundamental frequency) and the third harmonic were extracted from the signals using a discrete Fourier transform, and are reported alongside the average force in Table 2. It is observed that the larger amplitude values of the third harmonic appear to correlate with a larger average force of the harder and stronger alloys. This makes physical sense because there should be a drop in the oscillatory portion of the force when the void is opening up in the weld since the absence of material will lead to an absence of pressure between the tool and workpiece material. It is hypothesized that at a higher average force the sudden change in force will appear more drastic.

Additionally, in all welds performed in this study, it was observed that the location of the defects within the stir zone was consistent with the phase of the force transients for each particular alloy. In 3003-O the voids reside from the centerline of the weld toward the retreating side, in 6061-T6 they reside halfway between the center of the weld and the advancing side edge, and in 2024-T3 they reside all the way at the advancing side edge of the weld (refer to Figs. 4, 5, and 7). This appears to match the phase of the resultant harmonic in relation to the fundamental amplitude. Figure 8 shows the force signals for the three alloys previously mentioned. In Fig. 8, the location of the harmonic (red line) is done by identifying where the force signal deviates from an ideal sinusoid in the region between the large peaks (blue lines). The red lines are located where the force signal begins to decrease even though a sinusoid should be increasing at this location. As can be seen, it appears that phase of the harmonic shifts in accordance to the location of the void within the stir zone. In 3003-O the harmonic is closer to the left-hand side fundamental peak (void closer to the retreating side of weld), in 6061-T6 the harmonic shifts closer to the right-hand side peak (void closer towards advancing side), and in 2024-T3 the harmonic is closest to the right-hand side peak (void all the way towards advancing side). This bolsters confidence that the force oscillation is directly related to the movement of material and that the disruption in the force signal is due to an interaction with the void volume.

Conclusions

The same method of force-based defect detection previously developed for 6061-T6 cannot be directly applied to other aluminum alloys. The disruptions in the force signals at higher harmonics due to interactions with features on the FS tool probe and voids are dependent on the hardness and strength of the alloy. Therefore, a unique approach is required for each alloy.

- For soft alloys, the disruption in the force signal is less pronounced, leading to the challenge of producing good correlations between the harmonic and void size. There is potential to overcome this challenge by using more distinct features on the FS tool probe to produce a more distinct disturbance.
- In harder alloys, there are significant disturbances in the force signal at very small void sizes, or even in fully consolidated welds. This presents the challenge of differentiating between fully consolidated and defective welds.

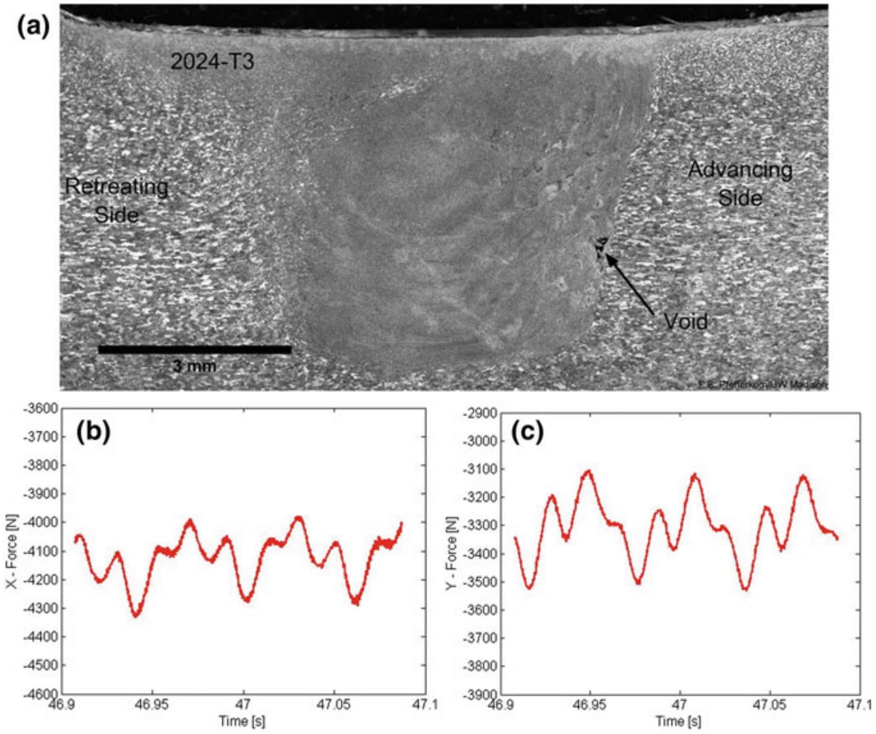

Fig. 7 Results of weld at 1,000 rpm and 600 mm/min in alloy 2024-T3: **a** cross section of weld, **b** force signal perpendicular to welding direction, **c** force signal in direction of welding

Table 2 Average force values as well as amplitudes at the tool rotational frequency and third harmonic derived using a discrete Fourier transform from the force signals shown in Figs. 4, 5, 6, 7

	3003-O			6061-T6		
	Average	Amp. fundamental	Amp. third harmonic	Average	Amp. fundamental	Amp. third harmonic
X-Force (N)	1,710	230	40	3,010	130	80
Y-Force (N)	240	210	30	1,550	140	50
	7075-T6			2024-T3		
	Average	Amp. fundamental	Amp. third harmonic	Average	Amp. fundamental	Amp. third harmonic
X-Force (N)	3,440	130	70	2,940	120	70
Y-Force (N)	4,170	80	50	3,330	70	50

- The same friction stir tool design would not be used to optimally weld the four aluminum alloys used in this study because of their significantly different material flow characteristics. Therefore, future studies should use tools that are better suited for each alloy.

The phase of the higher harmonic appears to match the location of the defect within the stir zone across different alloys. This bolsters confidence in the link between oscillations in force signals and the defect formation process.

Acknowledgements The authors gratefully acknowledge financial support of this work by the Department of Mechanical Engineering at the University of Wisconsin-Madison, the Machine Tool Technology Research Foundation, and the U.S. National Science Foundation through grants CMMI-1332738 and CMMI-1826104.

References

1. Thomas WM, Nicholas ED, Needham JC, Murch MG, Temple-Smith P, Dawes CJ (1991) Friction stir butt welding. GB Patent No. 9125978.8
2. Mishra RS, Ma ZY (2005) Friction stir welding and processing. Mater Sci Eng R Rep 50:1–78

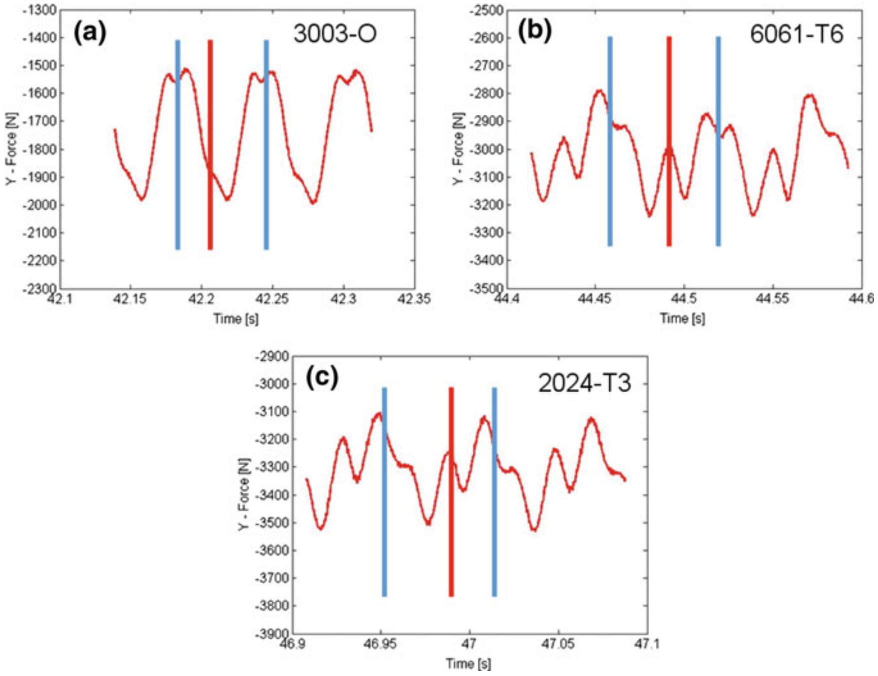

Fig. 8 Force signals in the direction of welding with phase of harmonic identified for **a** 3003-O, **b** 6061-T6, and **c** 2024-T3

3. Threadgill PL et al (2009) Friction stir welding of aluminium alloys. Int Mat Rev 54:49–93
4. Shrivastava A, Overcash M, Pfefferkorn FE (2015) Prediction of unit process life cycle inventory (UPLCI) energy consumption in a friction stir weld. SME J Manuf Proc 18:46–54
5. Shrivastava A, Krones M, Pfefferkorn FE (2015) Comparison of energy consumption and environmental impact of friction stir welding and gas metal arc welding for aluminum. CIRP J Manuf Sci Technol 9:159–168. https://doi.org/10.1016/j.cirpj.2014.10.001
6. Krishnan KN (2002) On the formation of onion rings in friction stir welds. Mater Sci Eng A 327:246–251
7. Colligan K (1999) Material flow behavior during friction stir welding of aluminum. Weld Res Suppl 229–237
8. Kh A, Hassan A, Prangnell PB, Norman AF, Price DA, Williams SW (2003) Effect of welding parameters on nugget zone microstructure and properties in high strength aluminium alloy friction stir welds. Sci Technol Weld Joining 8:257–268
9. Prangnell PB, Heason CP (2005) Grain structure formation during friction stir welding observed by the ‘stop action technique. Acta Mater 53:3179–3192
10. Schneider JA, Nunes AC (2004) Characterization of plastic flow and resulting microtextures in a FSW. Metall Mater Trans B 35(4):777–783
11. Arbegast WJ (2003) Modeling friction stir joining as a metalworking process. In: Jin Z (ed) Hot deformation of aluminum alloys III, TMS (The Minerals, Metals, and Materials Society)
12. Fonda R, Reynolds A, Feng CR, Knipling K, Rowenhorst D (2013) Material flow in friction stir welds. Metall Mater Trans A 44:337–344
13. Abergast WJ (2008) A flow-partitioned deformation zone model for defect formation during friction stir welding. Scr Mater 58:372–376
14. Schmidt H, Dickerson TL, Hattel JH (2006) Material flow in butt friction stir welds in AA2024-T3. Acta Mater 54:1199–1209
15. Tongne A, Jahazi M, Feulvarch E, Desrayaud C (2015) Banded structures in friction stir welded Al alloys. J Mater Process Technol 221:269–278
16. Boldsaikhan E, Burford DA, Gimenez Britos PJ (2011) Effect of plasticized material flow on the tool feedback forces during friction stir welding. Frict Stir Weld Proc VI:335–343
17. Boldsaikhan E, Corwin EM, Logar AM, Arbegast WJ (2011) The use of neural network and discrete Fourier transform for real-time evaluation of friction stir welding. Appl Soft Comput 11:4839–4846
18. Boldsaikhan E, McCoy M (2013) Analysis of tool feedback forces and material flow during friction stir welding. Frict Stir Weld Proc VII:311–320
19. Shrivastava A, Zinn M, Duffie NA, Ferrier NJ, Smith CB, Pfefferkorn FE (2017) Force measurement-based discontinuity detection during friction stir welding. J Manuf Proc 26:113–121
20. Shultz EF, Cole EG, Smith CB, Zinn MR, Ferrier NJ, Pfefferkorn FE (2010) Effect of compliance and travel angle on friction stir welding with gaps. J Manuf Sci Eng 132:0410101–0410109
21. MatWeb (2018) Material property data. www.matweb.com: Aluminum 3003-O, Aluminum 6061-T6; 6061-T651, Aluminum 7075-T6; 7075-T651, Aluminum 2024-T3

Part VI
Derivative Technologies

Copper-Graphite Composite Wire Made by Shear-Assisted Processing and Extrusion

Xiao Li, Glenn Grant, Chen Zhou, Hongliang Wang, Thomas Perry and James Schroth

Abstract Copper-graphite composites wires are manufactured by a novel friction stir processing named Shear-Assisted Processing and Extrusion (ShAPE). Two types of precursors have been prepared respectively: a blend of copper and graphite powder; solid copper cylinders having pre-drill holes filled with graphite powder. The precursor material was consolidated and extruded in one step by ShAPE. Up to 800 mm long defect-free wires were produced. The metallographic inspection on both transverse cross-section and longitudinal cross-section confirms the good integrity of the ShAPE Cu-graphite wires. Energy dispersive spectroscopy and electron backscatter diffraction indicate the graphite particles were reduced to sub-micro size and uniformly dispersed in the copper matrix. The ultrafine graphite particle inhibits the grain growth thus improving the hardness. The processing temperature is below 550 °C which is much lower compared to conventional manufacturing methods.

Keywords Shear-assisted extrusion and processing · Friction extrusion
Metal matrix composite · Wire

Introduction

Metal matrix composites (MMC) are metallic matrices mixed with fibers or particles that improve functional performance. Copper-carbon composites have been applied in many different areas thanks to its high thermal/electrical conductivity and lubricating properties. For example, high conductivity copper-carbon nanotube composites are used in sensitive electronic devices [1]. Copper-graphite composites are used as brusher for starters or welding machines [2]. Yet, there still exist unresolved challenges towards continuously manufacturing bulk MMC with quality that satisfies

---

X. Li (✉) · G. Grant
Pacific Northwest National Laboratory, 902 Battelle Boulevard, Richland, WA 99352, USA
e-mail: xiao.li@pnnl.gov

C. Zhou · H. Wang · T. Perry · J. Schroth
General Motors Research and Development Laboratory, Warren, MI 48090, USA

Y. Hovanski et al. (eds.), *Friction Stir Welding and Processing X*, The Minerals, Metals & Materials Series, https://doi.org/10.1007/978-3-030-05752-7_15

industrial specifications. For instance, a typical defect in MMC produced by melting or solidification MMC is the phase separation due to the density disparity between the matrix and reinforcement phase. The high processing temperature could deteriorate the nanofiber or nanoparticles as in the case of the decomposition of reduced graphene oxide beyond 600 °C [3]. In addition, a fast manufacturing rate is desired for industrial production. Traditional electrochemical deposition or chemical vapor deposition are either not able to produce bulk size composites or suffer from a low throughput.

Shear-Assisted Processing and Extrusion (ShAPE), also known as friction extrusion/consolidation [4–8] or friction stir extrusion/consolidation [9, 10], is a novel manufacturing technology that mixes and consolidates material via plastic deformation. It is capable of producing high-quality wire and discs in a single step [11, 12]. In a typical setup, the precursor material is contained in a billet ring and supported by a backing block. A rotating tool with the scrolled surface is driven by a spindle and pushed against the billet. With the help of shear deformation on the contacting plane normal to the extrusion direction, the filler materials are homogeneously dispersed in the metal matrix [13]. Because this is a solid phase processing and no melting occurs, the peak temperature can be lowered and well-controlled to maintain the quality of the product. In this study, to address the issue of the manufacturing defect and increase the production rate, ShAPE has been adopted as a new method to produce Copper-carbon composite wire. Graphite powder has been selected due to its low cost.

Material and Experiments

Two types of precursor materials were prepared for ShAPE. The first one is copper powder well blended with a small amount of graphite powder. Approximately 25 g of the powder mixture is cold compacted and refilled several times so the billet ring is filled as much as possible. The second one is a solid copper (25.4 mm diameter, 12.7 mm high) cylinder with several non-through holes where graphite powder is filled (shown in Fig. 1). The total mass is about 55 g and no pre-compaction is needed. As a reference, the pure copper cylinder was also used as a precursor to making wire. The details are given in another paper. Although the pre-mixture of disc-filling is not homogeneous, the cost of preparing a solid copper disc is much lower than using pure copper powder.

The ShAPE machine is set up for backward extrusion, presented in Fig. 2. The apparatus consists of the following: a cylindrical die tool with 2.5 mm central hole and scroll pattern on the face, a 25 mm inner diameter billet ring, a square fixture block with cooling channels go around the outside of the ring, a hydraulic spindle hold the tool, a thermocouple embedded in the tip of tool and connected to a wireless transmitter sending real-time tool temperature to the computer during process.

The general operation sequence of the ShAPE can be described as below: (1) move the die above the billet and align the central axis of the spindle with the center of the

Fig. 1 Copper disc with pre-drilled holes

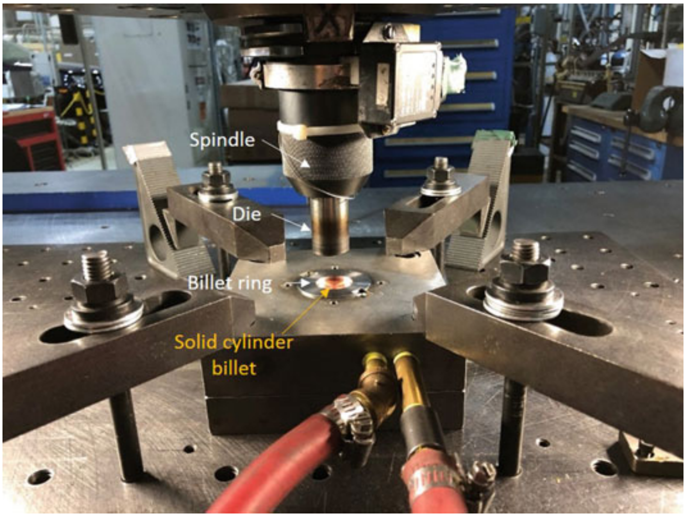

Fig. 2 Machine setup of ShAPE

billet ring; (2) Move the die down till 20 kN force feedback is reached, then start to rotate the die with desired rotational speed and plunge about 8.5 mm deep; (3) the top of the billet material is heated, softened and plastically deformed by the shearing between the tool face and billet; (4) copper and graphite were thoroughly mixed by the stirring and then consolidated; (5) under extrusion pressure, the processed billet material was continuously squeezed into the central orifice and formed a wire; (6) when the plunging has been completed, the die retracted from the billet ring either with the wire in the die or left it on the remnant disc.

Postprocess Analysis and Results

After the process, the wire and remnant disc were carefully removed from the die and billet ring. A 254 mm long copper-graphite composite wire and the consolidated disc made from copper powder and graphite powder are shown in Fig. 3. The wire has a smooth surface finish and uniform diameter. The black oxidation layer is only 20 μm thick and can be easily removed by a sandpaper. 600–800 mm long wires were made from solid cylinder precursor with the same surface finish.

The last extruded part of the wires was cut transversely and longitudinally for metallography inspection. The disc was also cut vertically to show the material flow and the state of consolidation. The macro-structures of both wire and disc are shown in Fig. 4. The transverse cross sections were further examined by 1EDS (Energy Dispersive Spectroscopy) and EBSD (Electron backscatter diffraction) to identify grain structure and elementary distribution.

From the transverse cross sections and longitudinal cross sections, we can see both wires made from powder and solid cylinder are fully consolidated. No carbon aggregation was seen on both wires. The one made from powder forms tree-ring structure which is commonly seen in the friction extrusion wires [14]. Its homogeneous grain size implies the graphite is uniformly distributed in the wire. Interestingly, the wire made from solid disc shows a “galaxy-spirals” pattern in the transverse cross section. In this picture, the region with larger grain size looks brighter and the region has smaller grains looks darker. The phase map identified by EDS plus EBSD is shown in Fig. 5 reveals the distribution of copper and graphite in the wire. The red grain is copper, and the blue is carbon. After ShAPE, the aggregated graphite powders were separated and well dispersed in the entire wire. Besides, the average grain size of copper reduced from about 45–1.2 μm. The size of graphite particles was also reduced from its original size 20 μm to less than 1 μm. The region that copper has a larger size (~4 μm) contains relatively larger but less numbered graphite cluster. On the other hand, the region has a smaller grain size (<1 μm) have more and finer graphite particles. Both have a much smaller grain size compared to the pure copper wire (87 μm) made by ShAPE. This suggests that the graphite powder effectively impedes the movement of the grain boundary. Although the elusive “galaxy-spirals” remains less perfect uniformity of graphite distribution, it could be improved by using a reorga-

Fig. 3 Copper-graphite composite disc and wire made from copper and graphite powder

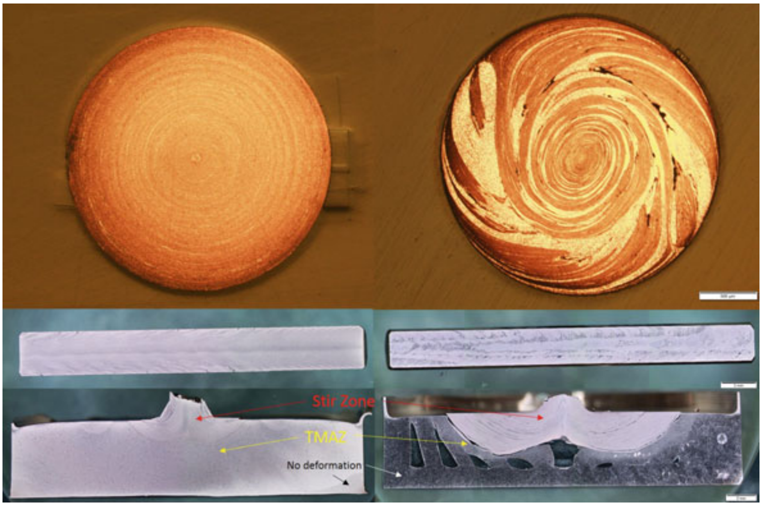

Fig. 4 Macrostructure of copper-graphite wire and disc made by ShAPE. Left: powder precursor; right: solid cylinder precursor. From top to bottom: transverse cross-section of wire, longitudinal cross-section of wire, vertical cross-section of the remnant disc

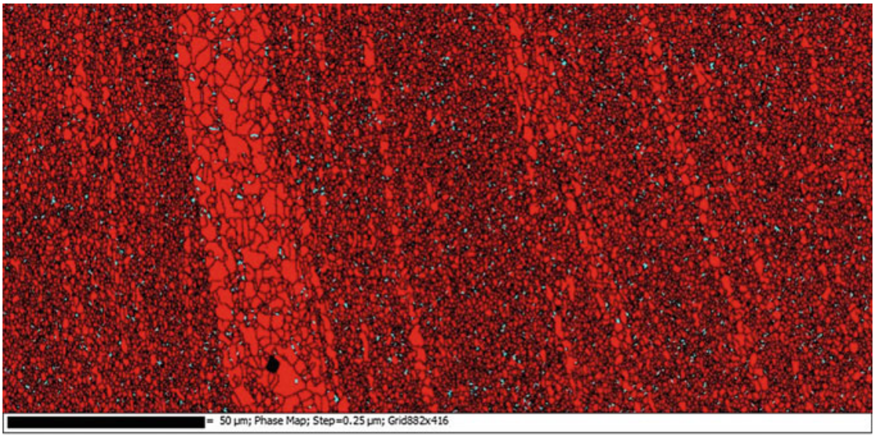

Fig. 5 Phase map with grain structure on the transverse cross-section of the wire made from solid cylinder precursor. The red grains are copper, and the blue is carbon

nized drill pattern on billet cylinder or increasing the die rotational speed to enhance the mixing.

Analogous to the metallurgy on friction stir welding (FSW), the remnant disc can be classified into several zones by microstructure. As shown in the bottom of Fig. 4, the top center has an equiaxial grain structure and banded layers, similar to the stir zone (SZ) in FSW. The region right below SZ was deformed but not recrystallized, which can be defined as TMAZ. Outside the TMAZ is the unstirred

Table 1 Vickers Hardness of ShAPE wires

Precursor material	Average vickers hardness of extruded wire	Standard deviation
Cu powder blended graphite powder	93.6	4.3
Cu cylinder filled with graphite powder	108.6	7.3
Pure Cu cylinder	44.7	2.7

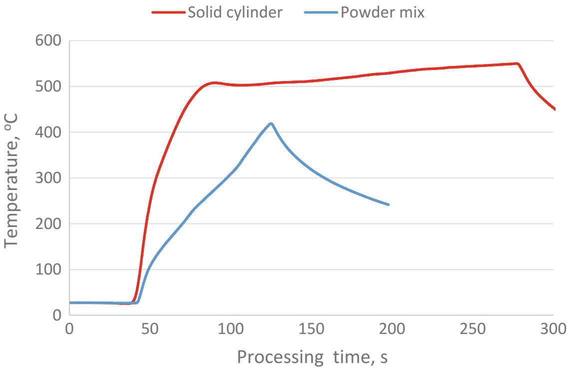

Fig. 6 Die face temperature during ShAPE process

zone where the deformation is not obvious or none. The SZ in the remnant disc made from powder is small but still covers the extrusion hole. This proves that the blended powder was well processed and consolidated prior to the extrusion. The SZ in the remnant disc made from a solid cylinder is much bigger. The mixing in it is obviously effective, compared to the unstirred zone in the bottom corner where the copper and carbon have not been mixed at all.

Vickers hardness test was performed on the transverse cross section of both wires. Five indents were made from center to the edge of wire with the same spacing. The average hardness is shown in Table 1 with the value of pure copper ShAPE wire. The hardness of Copper-graphite ShAPE wire is at least two times of that of the pure copper ShAPE wire. The value has no big variation in different locations.

The history of die face temperature during ShAPE process is presented in Fig. 6. The peak temperature of using ShAPE to make Cu-graphite composite is below 550 °C. It is significantly lower than the melting point of copper 1085 °C and the sintering temperature 700–900 °C [15].

Conclusions

The copper-graphite composite material is successfully manufactured by ShAPE from either blended powder or graphite-filled solid copper cylinder. The friction stirring avoids aggregation and provides a uniform graphite dispersion in the copper matrix. The sub-micro size graphite impedes the copper grain growth and improves the hardness. As a solid phase processing, the peak temperature of ShAPE is much lower than conventional manufacturing methods involved with melting or sintering. Therefore, the materials that are not stable at high temperature now could be utilized to make new MMCs.

References

1. Male KB, Hrapovic S, Liu Y, Wang D, Luong JHT (2004) Electrochemical detection of carbohydrates using copper nanoparticles and carbon nanotubes. Anal Chim Acta 516(1):35–41. https://doi.org/10.1016/j.aca.2004.03.075
2. Mazloum A, Kováčik J, Emmer Š, Sevostianov I (2016) Copper–graphite composites: thermal expansion, thermal and electrical conductivities, and cross-property connections. J Mater Sci 51(17):7977–7990. https://doi.org/10.1007/s10853-016-0067-5
3. Hwang J, Yoon T, Jin SH, Lee J, Kim TS, Hong SH, Jeon S (2013) Enhanced mechanical properties of graphene/copper nanocomposites using a molecular-level mixing process. Adv Mater 25(46):6724–6729
4. Li X, Tang W, Reynolds A, Tayon W, Brice C (2016) Strain and texture in friction extrusion of aluminum wire. J Mater Process Technol 229:191–198
5. Catalini D, Kaoumi D, Reynolds AP, Grant GJ (2013) Friction consolidation of MA956 powder. J Nucl Mater 442(1, Supplement 1):S112–S118. https://doi.org/10.1016/j.jnucmat.2012.11.054
6. Li X, Tang W, Reynolds A (2013) Material flow and texture in friction extruded wire. Friction stir welding and processing VII. Springer, Cham, pp 339–347
7. Whalen S, Jana S, Catalini D, Overman N, Sharp J (2016) Friction consolidation processing of n-type bismuth-telluride thermoelectric material. J Electron Mater 45(7):3390–3399. https://doi.org/10.1007/s11664-016-4454-0
8. Jiang X, Whalen SA, Darsell JT, Mathaudhu S, Overman NR (2017) Friction consolidation of gas-atomized Fe Si powders for soft magnetic applications. Mater Charact 123:166–172
9. Baffari D, Buffa G, Fratini L (2016) Influence of process parameters on the product integrity in friction stir extrusion of magnesium alloys. In: Paper presented at the key engineering materials
10. Li X, Baffari D, Reynolds A (2018) Friction stir consolidation of aluminum machining chips. Int J Adv Manuf Technol 94(5–8):2031–2042
11. Overman NR, Whalen SA, Bowden ME, Olszta MJ, Kruska K, Clark T, Mathaudhu SN (2017) Homogenization and texture development in rapidly solidified AZ91E consolidated by Shear Assisted Processing and Extrusion (ShAPE). Mater Sci Eng A 701:56–68. https://doi.org/10.1016/j.msea.2017.06.062
12. Darsell JT, Overman NR, Joshi VV, Whalen SA, Mathaudhu SN (2018) Shear Assisted Processing and Extrusion (ShAPE™) of AZ91E Flake: a study of tooling features and processing effects. J Mater Eng Perform. https://doi.org/10.1007/s11665-018-3509-1
13. Catalini D, Kaoumi D, Reynolds AP, Grant GJ (2015) Dispersoid distribution and microstructure in Fe-Cr-Al ferritic oxide dispersion-strengthened alloy prepared by friction consolidation. Metall Mater Trans A 46(10):4730–4739. https://doi.org/10.1007/s11661-015-3059-1
14. Li X, Tang W, Reynolds AP (2012) Visualization of material flow in friction extrusion. In: ICAA13 Pittsburgh, pp. 1659–1664. Springer, Cham
15. Bui HT, Tran BT, Le DQ, Than XT, Doan DP, Phan NM (2011) The effect of sintering temperature on the mechanical properties of a Cu/CNT nanocomposite prepared via a powder metallurgy method. Adv Nat Sci Nanosci Nanotechnol 2(1):015006

Joining AA7099 to Ni-Cr-Mo Steel Using Friction Stir Dovetailing

Md. Reza-E-Rabby, Scott Whalen, Ken Ross and Martin McDonnell

Abstract Friction stir dovetailing (FSD) was used to join 0.5 in. (12.7 mm) AA7099 to 0.5 in. (12.7 mm) Ni-Cr-Mo steel in a lap configuration. Two new FSD approaches are reported that significantly reduce zinc embrittlement of Fe–Al intermetallic compounds (IMCs) which form during conventional friction stir welding (FSW). The first method uses the general FSD approach where a custom designed tool is employed to extrude the AA7099 into the pre-machined dovetail groove of underlying steel by forming mechanical interlocking and metallurgical bonding simultaneously. The second method uses a two-step approach where FSD of AA6061 is first used to form a silicon-rich Fe-Al IMC within the dovetail groove. AA7099 plate is then joined to the AA6061 within the dovetail using conventional FSW. A discussion of the new FSD technique, joint configurations, and process parameters are provided along with joint microstructural analyses and mechanical performance.

Keywords Friction stir dovetailing · FSD · AA7099 · AA6061
Rolled homogenous armor · Dissimilar metals

Md. Reza-E-Rabby (✉) · S. Whalen · K. Ross
Pacific Northwest National Laboratory, Applied Materials and Performance Group,
902 Battelle Blvd., Richland, WA 99352, USA
e-mail: md.reza-e-rabby@pnnl.gov

Md. Reza-E-Rabby
Pacific Northwest National Laboratory, 902 Battelle Boulevard,
Richland, WA 999, MSIN K2-03, 99352, USA

M. McDonnell
U.S. Army Tank Automotive Research, Development and Engineering Center,
6501 E 11 Mile Road, Warren, MI 48397, USA

Y. Hovanski et al. (eds.), *Friction Stir Welding and Processing X*, The Minerals, Metals & Materials Series, https://doi.org/10.1007/978-3-030-05752-7_16

Introduction

Dissimilar metal joining between aluminum and steel has become essential in many applications, such as light-weighing automotive components for energy efficiency [1], cryogenic applications [2], improvement in mobility of an armor vehicle without compromising ballistic performance [3], and bridge structures [4]. A solid phase joining technique such as friction stir welding (FSW) has shown promises in this regard for thick section assemblies. However, there are some specific challenges associated with FSW, especially in lap joint arrangement of aluminum to steel, such as narrow metallurgical bonded area with brittle intermetallic compounds (IMCs), FSW tool survivability (if not using expensive polycrystalline boron nitride tool), and formation of hooks (arguable how hooks affect the joint performance in terms of material mixing versus stress concentration site). In order to mitigate these challenges, as well as to obtain higher joining efficiency, some derivative technologies of the FSW process have been developed in recent years for joining dissimilar material lap joints, such as friction stir soldering [5], friction stir scribe welding [6], FSW with the assistance of filler interlayer [7], friction stir knead welding [8], friction stir extrusion [9], and friction stir dovetailing (FSD) [10]. Among these derivative techniques, few have shown promise in joining thick section aluminum (12.7 mm or higher) to steel [9–11].

The FSD process is one approach that successfully demonstrated the joining capability of thick AA6061 to rolled homogenous armor (RHA) plates. The FSD study also revealed the formation of silicon-rich $FeAl_3$ IMCs and dovetail mechanical interlocking simultaneously that resulted in a high ductile joint performance with maximized load-carrying capacity [10]. It is now essential to investigate the capability of the FSD process for precipitation hardened 7XXX aluminum alloys. However, it is well known that the effect of zinc embrittlement of Fe-Al IMCs system during the FSW process is detrimental to strength and elongation [12, 13]. This paper further explores the study of FSD to join AA7099 to a Ni-Cr-Mo steel (RHA) using two approaches: (a) single-pass FSD technique by plastically deforming AA7099 into dovetail grooves machined into the RHA to form mechanical interlocks while simultaneously producing an Al-Fe IMCs layer; and (b) double-pass FSD and FSW approach in which the first pass FSD is conducted to form high-strength metallurgical bonding of AA6061 to RHA with silicon-enriched IMCs within the dovetail followed by a second-pass FSW process to produce lap joint between AA7099 and AA6061. A set of welding parameters were examined to investigate the microstructural and mechanical properties of joints.

Materials and Experimental Procedure

Two types of precipitation hardened aluminum alloys (AA6061-T651 and AA7099-T7451) having the nominal thickness of 0.5 in. (12.7 mm) were used in this study for joining with RHA using FSD. The RHA plates were procured to satisfy the

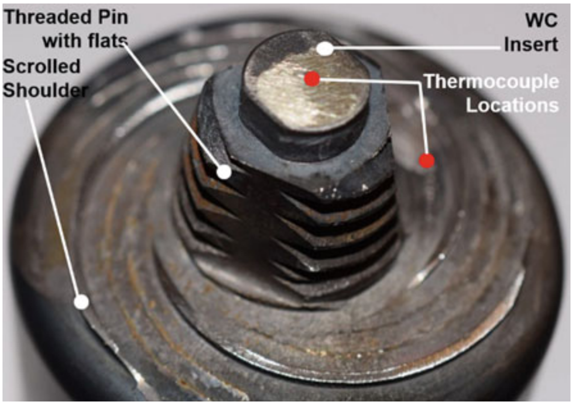

Fig. 1 FSD tool used in this study

Table 1 Summary of welding parameters in single-pass FSD and double-passes FSD/FSW joints

Lap joint configuration single and double pass	Trial #	Forge force	Shoulder temperature (controlled)	Tool rotational speed	WC temperature
		kN	°C	RPM	°C
Single pass: FSD joint of AA7099 to RHA	A	62	440	91	450
	B	69	440	86	445
	C	77	440	88	448
	D	74	420	85	430
	E	82	410	70	413
Double passes: 1st **Pass-FSD of AA6061 to RHA** [10] and 2nd Pass-FSW of AA7099 to AA6061	F	**57**	**470**	**150**	**485**
		74	420	85	–
	G	**57**	**470**	**150**	**485**
		83	410	74	–

MIL-DTL-12560J specification and the thickness of 0.5 in. (12.7 mm) was obtained by dual disc grinding. The RHA plates were also prepared for FSD by machining dovetail grooves. For a single-pass joint between AA7099 and RHA, FSD was preformed using a customized FSW tool shown in the Fig. 1. The tool features (shoulder scrolls and thread with flats in pin) with tungsten carbide (WC) insert and location of thermocouples are also shown. The process control parameters and key response variables are presented in Table 1.

The FSD tool and the dovetail geometry details were described in Refs. [10, 14]; therefore, were not repeated here for brevity. Since joining AA7XXX to steel always produces zinc-rich brittle IMCs using the conventional FSW process, a second approach of joining AA7099 to RHA in this study was introduced by incorporating an intermediate layer of AA6061 to link RHA and AA7090. Figure 2 summarizes the steps of joining AA7099 to RHA via AA6061 interlayer using a double-pass joint in which: (a) Step 1: FSD joining of AA6061 to RHA were produced using the process described in Ref. [10], (b) Step 2: AA6061 was machined off

Fig. 2 Steps of joining AA7099 to RHA using an intermediate layer of AA6061

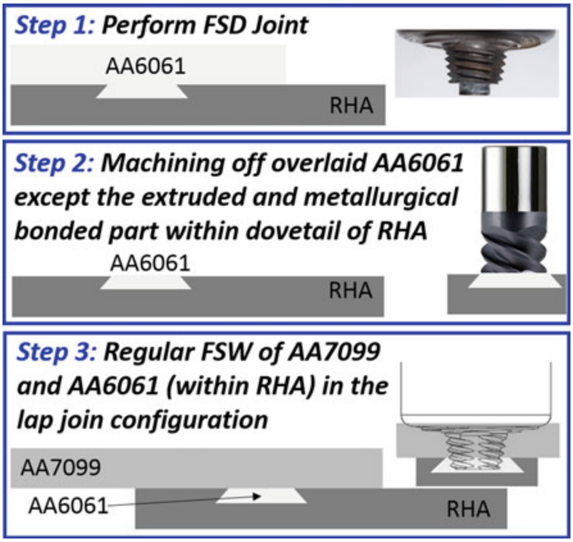

from the AA6061-RHA FSD joints except the extruded and metallurgical bonded part of AA6061 within dovetail, and (c) Step 3: perform FSW to form lap joint between overlaid AA7099 and extruded AA6061 using a conventional FSW. All welding was preformed using a temperature control algorithm which modulates spindle torque [15] to control the tool shoulder temperature with electronic displacement control (EDC) of the commanded plunge depth. Therefore, the tool rotational speed, WC tip temperature, and forge force mentioned in Table 1 are the response variable in this study. All the welds were performed at welding speed of 76.2 mm/min.

The lap shear tensile specimens were cut from the welded aluminum-steel to an average thickness of 15.0 mm using a water jet. Standard grinding and polishing sequences were followed for metallographic sample preparation and final polished surface was obtained using colloidal silica (<0.05 μm). A scanning electron microscope (SEM) equipped with energy dispersive spectroscopy (EDS) was employed to investigate the dovetail interfaces. The lap shear tensile testing was performed using a 50 kip MTS test frame.

Results and Discussion

Weld Microstructural Analysis of AA7099 to RHA Using FSD

Figure 3 presents the montages of low-resolution SEM images of five trials of AA7099 to RHA FSD joints at the dovetail interface. It is obvious in all trials that the interfaces within the dovetails are disrupted by the WC tip of the FSD tool. However,

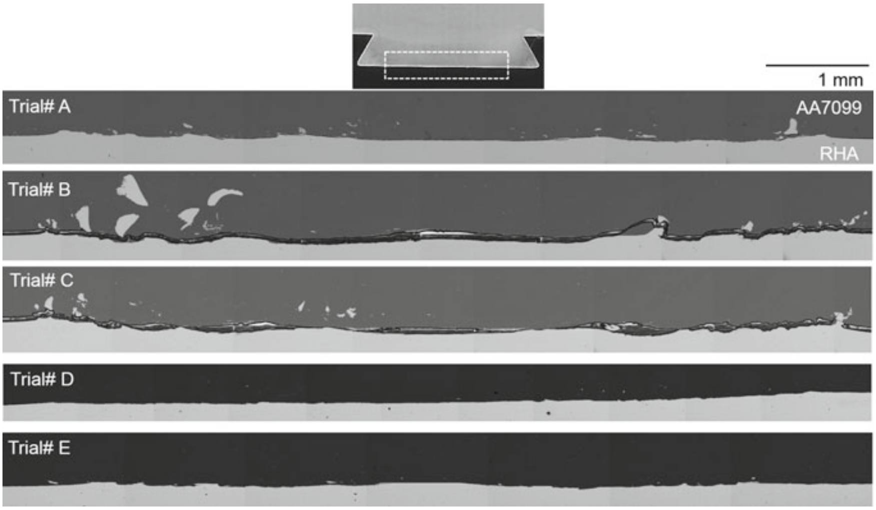

Fig. 3 Weld transverse section and SEM montage images of the FSD joints of AA7099 and RHA with different parameters

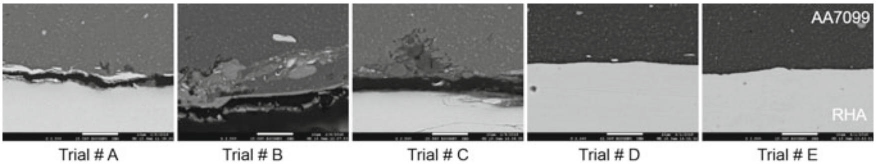

Fig. 4 High-resolution SEM images to investigate the interface of AA7099 and RHA

no continuous metallurgical bonding (IMCs) was revealed at the interface for trial A, B, and C at or above 445 °C. However, trials D and E in Fig. 3 indicate continuous metallurgical bonding at the interface.

The high-resolution SEM micrographs at the middle of dovetail interface in Fig. 4 also confirm the absence of a continuous IMC for trials A, B, and C as well as presence of continuous metallurgical bonding for trials D and E. As noticed, the dark area at the AA7099 and RHA interface in trials A, B, and C are the voids/gaps which indicate no continuous interlayer. Moreover, a further detailed SEM-EDS investigation revealed that the intermetallic which is formed eventually broke down in case of trial A, B, and C, but the metallurgical bonding was evident between AA7099 and RHA for trials D and E when the recorded tool temperature at the interface was below 430 °C. However, the interlayer thicknesses and phases were not resolved by SEM for trials D and E.

Attempts have also been made to quantify the interlayer that is formed in different trials using SEM-EDS. Figure 5 illustrates the SEM micrographs with area elemental analyses using EDS. It was observed that magnesium- and zinc-rich Fe-Al IMCs (atomic % in the table of Fig. 5) are formed in each case; however, these interlayers

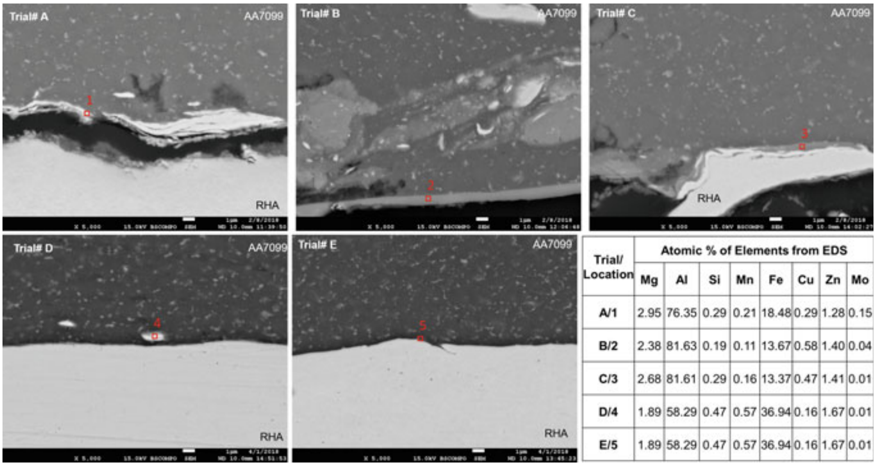

Trial/ Location	Atomic % of Elements from EDS							
	Mg	Al	Si	Mn	Fe	Cu	Zn	Mo
A/1	2.95	76.35	0.29	0.21	18.48	0.29	1.28	0.15
B/2	2.38	81.63	0.19	0.11	13.67	0.58	1.40	0.04
C/3	2.68	81.61	0.29	0.16	13.37	0.47	1.41	0.01
D/4	1.89	58.29	0.47	0.57	36.94	0.16	1.67	0.01
E/5	1.89	58.29	0.47	0.57	36.94	0.16	1.67	0.01

Fig. 5 SEM-EDS analysis at the dovetail interface

were broken down in trials A, B, and C mostly because of the high temperature at which the IMCs are formed and over engagement of the WC with the RHA. A continuous IMCs layer, the thickness of which was not detectable with current SEM resolution in this study, was observed in trials D and E. Apart from the interfaces, it is also interesting to note the microstructure of the aluminum-rich region in which coarsening of precipitates near the aluminum grain boundary were evident in the SEM micrographs of Fig. 5.

Lap Shear Tensile Test of AA7099 to RHA Using FSD

The lap shear tensile test was conducted for at least four specimens of each trial and the normalized load (load per weld length) as a function of displacement was plotted with representative test data for each trial. It should be noted here that the load-carrying capacity for trials A, B, and C are governed by the mechanical interlocking through the dovetails and disrupted dovetail interfaces since no continuous metallurgical bonding is observed in these trials. Therefore, it is observed in Fig. 6 that the load increases with displacement up to the maximum value followed by a sharp change in load when the corner of the extruded aluminum within the dovetail fails for trials A, B, and C. In trials D and E, the load increases linearly up to the maximum value and suddenly drops at constant displacement; however, the load increases somewhat after each drop before complete failure of the specimens. The first portion of the load displacement curve (linear up to the maximum value) is attributed to the combined action of metallurgical bonding and mechanical interlocking that govern the load-carrying capacity of trials D and E specimens. The sudden drop in load,

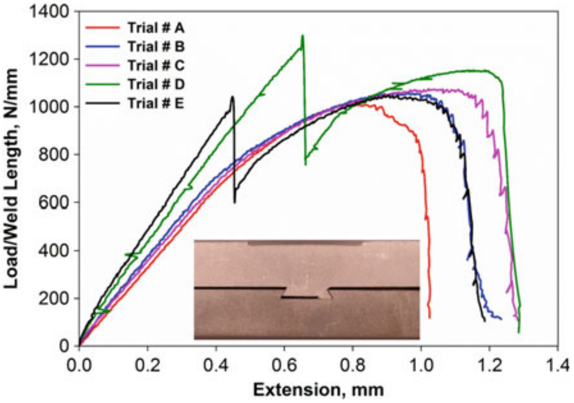

Fig. 6 Lap shear tensile specimens (load versus extension curve)

when the IMCs fail and load afterward, is being carried by the dovetail mechanical interlocking solely. This is consistent with the brittleness of the zinc-rich IMCs layer where load drops suddenly at the time of IMCs failure [12, 13]. However, after the failure of IMCs, load increases with displacement until the corner of AA7099 within the dovetail fails (similar to trials A, B, and C). Therefore, the load-carrying capacity of the lap shear tensile specimen for trials D and E is predominated by dovetail interlock in the second phase of the curve. The maximum load of 1257 N/mm was observed for trial D, which is 17–25% higher than other trials. It is also interesting to note that in all trials of AA7099 to RHA FSD process, the failure location of the lap shear tensile test are observed in similar location with initial separation of disrupted metallurgical interface followed by the failure of the corner of aluminum within the dovetail on the loading side.

AA7099 to RHA Joint with AA6061 Intermediate Layer at the Dovetail

Figure 7 presents the weld transverse macro sections of double-pass FSD and FSW joints of AA7099 to RHA with AA6061 as an intermediate layer. In each image the advancing side is on the left and the retreating side is on the right. Each column of the images show the cross sections for a particular trial (trial F on the left and trial G on the right) in which the process parameters of the second pass were varied (refer Table 1). The interface of AA6061 and RHA near the dovetail root was metallurgically bonded to a length of about 8 mm [10]. It is interesting to note the difference in the mixing of AA7099 and AA6061 at different commanded plunge depth for trials F and G (trial G was 0.12 mm higher than trial F).

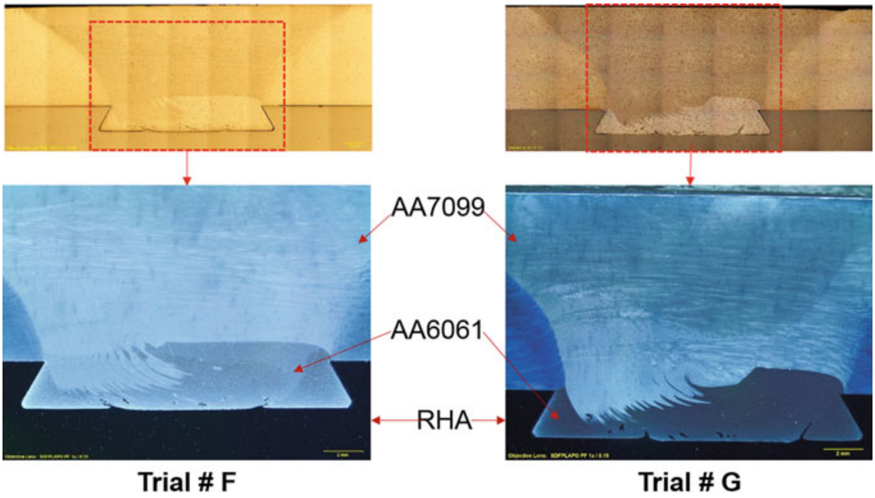

Fig. 7 Weld macro cross sections of AA7099 to RHA joints via AA6061 interlayer

It is evident from the weld cross sections that the mixing of two materials within the dovetail is higher with less plunge (trial F) than higher plunge (trial G). This resulted in a higher protrusion of AA6061 into AA7099 on the retreating side in trial G compared to trial F, leaving less AA6061 in the dovetail. This asymmetric nature of material flow in the advancing and retreating sides is generally common in FSW.

The asymmetrical material flow of AA6061 in the weld cross sections unequal joint strength depends on the loading direction. As such, lap shear tensile test with AA7099 loaded on both the advancing and retreating sides was performed. Figure 8 presents the load versus displacement curve for trial F (dark lines) and trial G (gray lines), with load being applied on the advancing side (continuous line) and retreating side (dashed lines). The ascending part of the curve up to peak loads for similar loading configurations is identical for trials F and G as seen in Fig. 8. However, the descending part of the curve differs between trials F and G. This data suggests that failure in the aluminum is governed by the extent to which AA7099 is extruded down below the top of the dovetail. It is also observed from Fig. 8 that the peak load in the case of pulling from the advancing side is about 35% higher compared to loading the retreating side. This data shows that the two-step process of first performing FSD of AA6061 to the RHA, and then FSW of AA7099 to AA6061 results in a stronger joint than only performing FSD of AA7099. This improvement is attributed to the elimination of the brittle zinc-rich IMC despite the lower strength of the AA6061 interlayer.

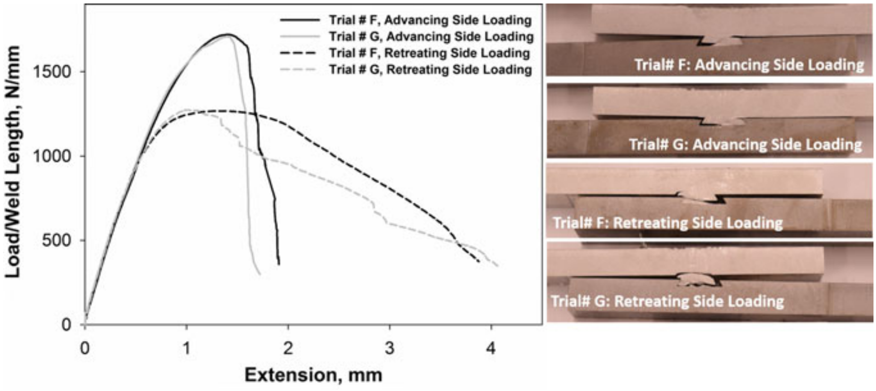

Fig. 8 Load versus displacement curve of AA7099 to RHA FSD lap shear tensile test specimens having AA6061 at intermediate layer

Conclusions

The following concluding remarks can be drawn from this study:

(1) FSD is capable of extruding different aluminum alloys (AA7099, AA6061) into dovetail grooves within RHA plates to from lap joints by introducing mechanical interlocking and metallurgical bonding simultaneously.
(2) The load-carrying capacity and ductility of lap joints produced between AA7099 and RHA is degraded by the zinc-rich Fe-Al IMCs formed during the FSD process.
(3) Introduction of an intermediate layer of AA6061 within the dovetail drastically improves the joint performance of AA7099 to RHA.
(4) The asymmetric material flow of AA6061 in the advancing and retreating sides resulted in an asymmetric joint performance.

Acknowledgements This work was supported by the U.S. Army Tank Automotive Research, Development, and Engineering Center [Military Interdepartmental Purchase Request 10834736, 11008837, 11079043]. Pacific Northwest National Laboratory is operated by the Battelle Memorial Institute for the U.S. Department of Energy under contract DE-AC06-76LO1830. The authors would like to thank Mr. Jason Scheuring, Application Engineer at Kaiser Aluminum, for providing the AA7099 alloy.

References

1. Dilthey U, Stein L (2006) Multimaterial car body design: challenge for welding and joining. Sci Technol Weld Joining 11(2):135–142
2. David E (2003) Materials for cryogenics applications. In: 12th international scientific conference on achievements in mechanical and materials engineering, AMME 2003

3. Polsen E, Krogsrud L, Carter R, Oberle W, Haines C, Littlefield A (2014) Lightweight Combat Vehicle S and T Campaign. In: US Army TARDEC/Ground System Survivability Warren United States
4. Siwowski T (2006) Aluminium bridges–past, present and future. Struct Eng Int 16(4):286–293
5. Ebrahimian A, Kokabi A (2017) Friction stir soldering: a novel route to produce graphite-copper dissimilar joints. Mater Des 116:599–608
6. Upadhyay P, Hovanski Y, Jana S, Fifield LS (2017) Joining dissimilar materials using friction stir scribe technique. J Manuf Sci Eng 139(3):034501
7. Zheng Q, Feng X, Shen Y, Huang G, Zhao P (2016) Dissimilar friction stir welding of 6061 Al to 316 stainless steel using Zn as a filler metal. J Alloy Compd 686:693–701
8. Geiger M, Micari F, Merklein M, Fratini L, Contorno D, Giera A, Staud D (2008) Friction stir knead welding of steel aluminium butt joints. Int J Mach Tools Manuf 48(5):515–521
9. Evans WT, Gibson BT, Reynolds JT, Strauss AM, Cook GE (2015) Friction stir extrusion: a new process for joining dissimilar materials. Manuf Lett 5:25–28
10. Reza-E-Rabby M, Ross K, Overman NR, Olszta MJ, McDonnell M, Whalen SA (2018) Joining thick section aluminum to steel with suppressed FeAl intermetallic formation via friction stir dovetailing. Scr Mater 148:63–67
11. Patterson EE, Hovanski Y, Field DP (2016) Microstructural characterization of friction stir welded aluminum-steel joints. Metall Mater Trans A 47(6):2815–2829
12. Ratanathavorn W, Melander A, Magnusson H (2016) Intermetallic compounds in friction stirred lap joints between AA5754/galvanised ultra-high strength steel. Sci Technol Weld Joining 21(8):653–659
13. Tanaka T, Morishige T, Hirata T (2009) Comprehensive analysis of joint strength for dissimilar friction stir welds of mild steel to aluminum alloys. Scr Mater 61(7):756–759
14. Reza-E-Rabby M, Ross K, Whalen S, Hovanski Y, McDonnell M (2017) Solid-state joining of thick-section dissimilar materials using a new friction stir dovetailing (FSD) process. In: Friction stir welding and processing IX, pp 67–77. Springer
15. Ross K, Sorensen C (2013) Advances in temperature control for FSP. In: Friction stir welding and processing VII, pp 301–310. Springer

Material Flow and Microstructure Evolution in Corner Friction Stir Welding of 5083 Al Alloy Using AdStir Technique

Kunitaka Masaki, Hiroshi Saito, Koji Nezaki, Shoko Kitamoto, Yutaka S. Sato and Hiroyuki Kokawa

Abstract During corner AdStir fillet stationary shoulder friction stir welding (FSW), filler material with surface oxide is fed into the stir zone. In this study, the material flow of the filler material and surface oxide layer during the process was investigated by microstructure observation. To visualize the material flow, a marker insert technique was employed. Similar to conventional FSW, fine and equiaxed grain structure was observed in the stir zone. EBSD investigation revealed that the material flow was governed by the simple shear deformation induced by the rotating probe. The filler material was widely distributed in the stir zone, suggesting that some amount of the filler material moved downward due to the vertical material flow. The initial surface layer on the filler material was finely broken up by the material flow, achieving metallic bonding between the filler wire and the plates. Any harmful effects by adding the filler material were not found in the mechanical tests in this study.

Keywords Friction stir welding · AdStir · Material flow

K. Masaki (✉) · H. Kokawa
Welding Technology Department, Production Engineering Center, Corporate Research and Development, IHI Corporation, 1, Shi-Nakahara-Cho, Isogo-ku, Yokohama 235-8501, Japan
e-mail: kunitaka_masaki@ihi.co.jp

H. Saito
Mechanical Technology Department, Products Development Center, Corporate Research and Development, IHI Corporation, 1, Shi-Nakahara-Cho, Isogo-ku, Yokohama 235-8501, Japan

K. Nezaki
Production Engineering Center, Corporate Research and Development, IHI Corporation, 1, Shi-Nakahara-Cho, Isogo-ku, Yokohama 235-8501, Japan

S. Kitamoto · Y. S. Sato
Department of Materials Processing, Graduate School of Engineering, Tohoku University, 6-6-02 Aramaki-aza-Aoba, Aoba-Ku, Sendai 980-8579, Japan

Y. Hovanski et al. (eds.), *Friction Stir Welding and Processing X*, The Minerals, Metals & Materials Series, https://doi.org/10.1007/978-3-030-05752-7_17

Introduction

Applications of friction stir welding (FSW) are now wide-spreading due to the many advantages. One of the advantages of FSW is no requirements of the filler material to make a weld. However, this may be disadvantageous in some cases. FSW of the materials with large gap is not easy. Since conventional FSW doesn't use the filler material, welding of the reinforced fillet joint requires complex and unpractical joint preparation [1].

Recently, corner AdStir fillet Stationary Shoulder FSW (SSFSW) process has been developed [2, 3]. In this process, very smooth reinforced fillet welds between flat plates can be obtained. To form the reinforcement, an additional filler material is used to produce the fillet shape during the process. A smooth reinforced fillet weld having a low stress concentration can be easily obtained.

Since AdStir technique is recently invented process, some fundamental knowledge still remains unclear. The stir zone obtained by AdStir should be composed of mixture of the base material and the filler material. It is generally known that dissimilar conventional FS weld sometimes exhibits heterogeneous material distribution [4], i.e., the filler material might heterogeneously distribute in the stir zone of AdStir FS weld, affecting the joint properties. In addition, the filler material should be covered by the surface oxide layer. It is also known that the initial surface oxide layer on the base material can be broken up during FSW, but most of the broken oxide particles are left in the stir zone. The oxide particles remaining in the stir zone sometimes affect mechanical properties of the weld [5]. Therefore, the surface oxide on the filler material might affect the mechanical properties of the FS weld by AdStir. To understand the microstructure and mechanical properties of the AdStir weld, the material flow of the filler material and surface oxide layer should be examined.

In this study, the material flow during AdStir FSW was examined. To visualize the material flow during FSW, a marker insert technique [6] was employed. Material flow of the filler material was studied using the dissimilar filler material, and surface oxide layer distribution was examined using the similar filler material with coating of the dissimilar metal as a marker. These results were discussed with the mechanical properties of the weld.

Experimental Procedures

The materials used in this study are listed in Table 1. For the microstructure and mechanical property examinations, Al alloy 5083-O supplied in 12 mm thick plates and 5183 Al alloy cylindrical wires were used. To examine the material flow of the

Table 1 List of materials combination used

Examination item	Base material	Filler material
Filler material flow	5083-O plate	7075-T6511 wire
Surface oxide distribution on filler wire	5083-O plate	Ni-coated 5183 wire
Microstructure in stir zone	5083-O plate	5183 wire
Mechanical properties	5083-O plate	5183 wire

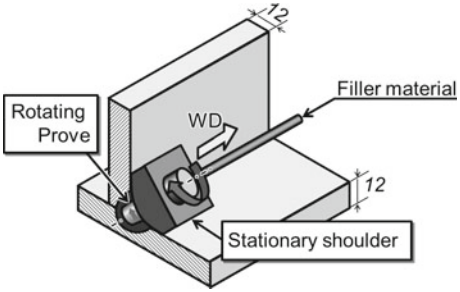

Fig. 1 Schematic illustration of the corner SSFSW

filler material, Al alloy 7075-T6511 cylindrical wires are used as the filler material. To examine the distribution of surface oxide on the filler wire, Ni-coated 5183 wire was employed. The threaded welding probes and stationary shoulders with a chamfered corner shape were used. These tools were made from a tool steel. Figure 1 shows the schematic illustration of the corner SSFSW in this study.

Corner SSFSW welds were produced at the travel speed of 200 mm/min and the rotational speed of 750 rpm. At the end of FSW, the welding tool was immediately extracted from the weld to “freeze” the material flow around the tool during FSW.

Following FSW, the transverse cross sections of the weld, and horizontal cross sections with various depths around the keyhole left at the end of FSW were cut by electric discharge machine for the material flow examination. For the filler material flow examination, the stir zone macrostructure was characterized by optical microscopy. To distinguish the regions originated from the filler wire, EPMA technique was employed. For examination of initial surface oxide, SEM observation was employed. Furthermore, the microstructure in the stir zone was examined by EBSD technique. Mechanical properties of the weld were also examined. To examine static mechanical properties, tensile test was performed. To examine the effect of surface oxide on fracture path, fracture test was performed.

Results and Discussion

Figure 2 shows the typical cross-sectional overview of the weld of 5083 plates with 5183 filler wire. The advancing and retreating sides are expressed as “AS” and “RS”,

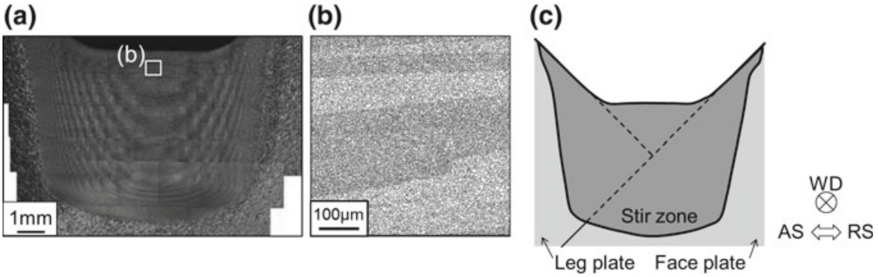

Fig. 2 A typical cross section of the weld: **a** optical macrograph by Barker's reagent, **b** high angle grain boundary map obtained by EBSD technique, and **c** schematic illustration of the cross section

respectively. Sound corner FS weld with smooth fillet was obtained. Clear onion-ring structure was observed in Fig. 2a. EBSD measurement revealed that the stir zone exhibited fine and equiaxed grain structure similar to that of conventional FSW. It is also worth noting that a moderate simple shear texture was observed. This result suggests that the material flow was governed by the simple shear deformation induced by the rotating probe.

The stir zone shape was visible by optical microscopy, as shown in Fig. 2a, but the regions originated from the filler wire couldn't be distinguished. Furthermore, oxide particles remaining in the stir zone cannot be recognized in this experiment. To distinguish those microstructural features, a marker insert technique was employed in this study.

The cross sections of the weld of 5083 plates with 7075 filler wire after etching by Barker's and Keller's reagents are shown in Fig. 3. By Barker's reagent etching, clear onion-ring structure similar to that in the weld with 5183 filler wire was obtained (Figs. 2a and 3a). The microstructure in the stir zone also looked close to that in the weld with 5183 filler wire. By Keller's reagent etching, dark regions are observed in the stir zone as shown in Fig. 3b. EPMA measurement revealed that the dark regions contained high Zn, and other regions hardly contained Zn. Since only 7075 contains Zn in this study, this result implies that the dark regions are originated from the filler wire. The dark regions originated from the filler wire distribute throughout all depth in the stir zone. It is found that the dark regions at upper part contained high Zn close to Zn content of 7075 Al alloy, but those in middle and bottom parts contained the lower amount of Zn than the surface area.

To examine the movement of the surface oxide layer in the stir zone during welding, FSW of no-coated plates and Ni-coated filler wire was conducted. The backscattered electron (BSE) images on the cross section of the welds of no-coated plates and Ni-coated filler wire obtained by SEM is shown in Fig. 4. The initial surface with Ni was clearly visible as white phases in BSE images due to the high atomic number. The initial surface oxide distribution at the upper part area was denser than the middle and bottom parts.

To examine the material flow during FSW, the cross sections perpendicular to the probe around keyhole were observed at several depths. The cross-sectional overview

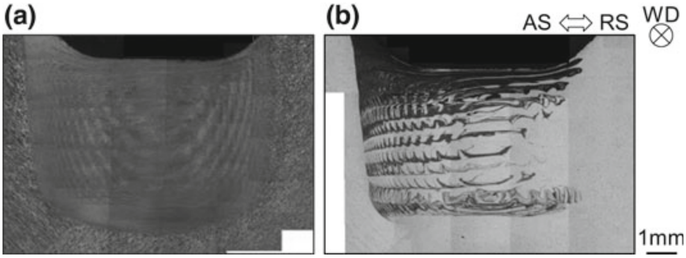

Fig. 3 Cross-sectional overviews of the weld with 7075 filler wire etched by **a** Barker's reagent and **b** Keller's reagent

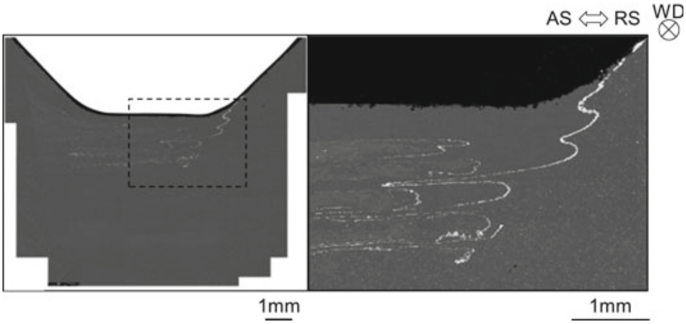

Fig. 4 BSE images on cross section of the weld with no-coated plate and Ni-coated filler wire

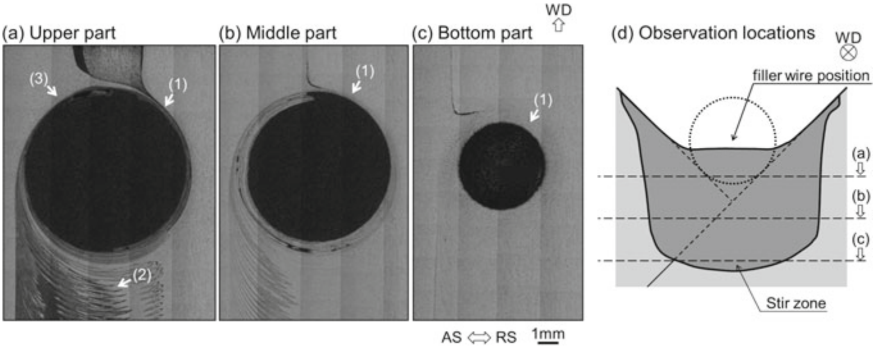

Fig. 5 Filler material flow around keyhole at several depths

of the weld of 5083 plates with 7075 filler wire and Ni-coated 5183 wire is shown in Fig. 5 and Fig. 6, respectively.

At the upper part, it was found that the filler wire experienced severe shear deformation and moved to retreating side ((1) in Fig. 5a). During the deformation, the filler wire was extremely thinned, and the surface oxide on the filler wire was broken up to fine particles ((1) in Fig. 6a). Fragmentation of the oxide layer generates the

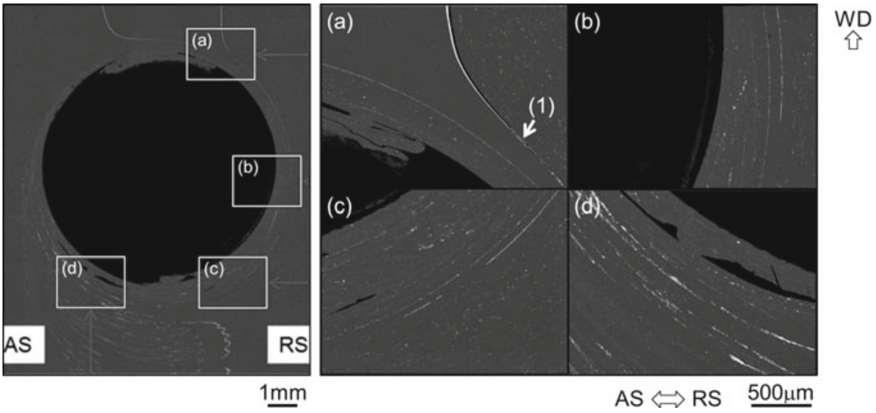

Fig. 6 Surface layer on the filler material flow around keyhole at upper part

oxide-free surface, so that metallic bonding between the filler wire and the plates would be achieved behind the probe, as like conventional FSW process [5]. Behind the tool, a large amount of the filler material was released with the base material ((2) in Fig. 5a). However, it seems that some amount of the filler material moved ahead of the probe through advancing side ((3) in Fig. 5a).

At the middle and bottom parts, the filler material can be found around the probe ((1) in Fig. 5b, c), although the filler wire was not located initially at these depths (Fig. 5d), suggesting that the filler material around the probe moved downward from the upper part due to the vertical material flow induced by the screwed probe rotation. This material flow may result in distribution of the filler material on these parts in the stir zone. During such material flow, compositional mixing between the base material and the filler material could also occur, causing the low Zn content in the middle and bottom parts, as shown in Fig. 3b.

Finally, static mechanical property of the weld was examined by tensile test. Figure 7a shows the schematic illustration of the tensile test in this study. All specimens failed at the location with the minimum throat in the stir zone. No brittle fracture surface was observed. The tensile strength of the weld satisfied the strength limit of the base material (275 MPa).

Additionally, the effect of the oxide layer remnant of the stir zone on fracture was examined by a fracture test. In the fracture test, corner FSW specimen was torn by tensile test machine, as shown in Fig. 7b. Figure 8 shows the fracture test result. The samples failed in the base material, not through the stir zone. Any harmful effects weren't found in this study.

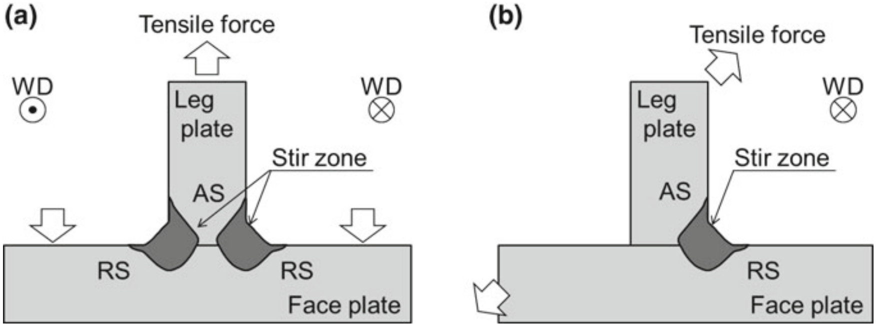

Fig. 7 Schematic illustrations of mechanical properties test: **a** tensile test and **b** fracture test. White arrows indicate force directions during the tests

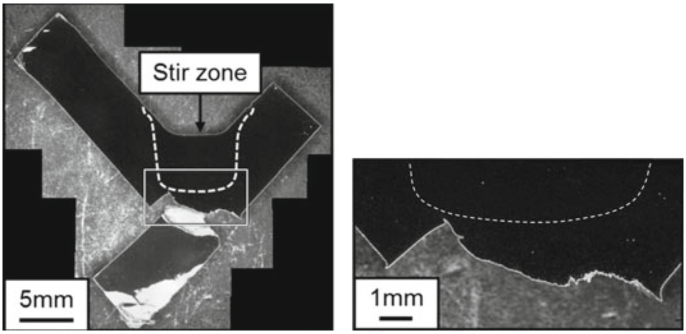

Fig. 8 Appearance of fracture test specimen after the test

Conclusions

The material flow of the filler material and surface oxide layer during corner friction stir welding of 5083 Al alloy using AdStir technique were examined.

The stir zone exhibited fine and equiaxed grain structure similar to that of conventional FSW. The regions originated from the filler material were widely distributed in the stir zone. It was found that the filler material experienced severe shear deformation during FSW. The shear deformation might break up the initial surface oxide layer, achieving metallic bonding. Some amount of the filler material moved downward due to the vertical material flow. This material flow may result in the wide distribution of the filler material in the stir zone. In this study, any harmful effects by adding filler material were not found in mechanical tests.

Acknowledgements The authors are grateful to Mr. Y. Ishii for technical assistance and Dr. S. Mironov and Dr. K. Kobayashi for technical support. Thanks also go to Dr. N. Oiwa and Mr. K. Kojima for helpful discussion.

References

1. Mishra RS, Ma ZY (2005) Mater Sci Eng R 50:1
2. Makita S (1998). Patent JP 4240579 1998
3. Martin JP (2013) In: Proceedings of 1st international joint symposium on joining and welding, Osaka, Japan, pp 477–482
4. Srinivasan PB et al (2005) Mater Sci Eng A 392:292–300
5. Sato YS et al (2005) Mater Sci Eng A 405:333–358
6. Liu FC et al (2016) Mater Des 110:354–364

Joining of Lightweight Dissimilar Materials by Friction Self-Piercing Riveting

Yong Chae Lim, Charles David Warren, Jian Chen and Zhili Feng

Abstract In this work, we employed a unique solid-state joining process, friction self-piercing riveting (F-SPR), to join carbon fiber composites to the low-ductility magnesium alloy AZ31B. The localized frictional heat generated between the rotating rivet and the underside of the magnesium sheet softened and prevented crack generation in AZ31B. A consumable joining rivet was designed to join the selected material stacks by F-SPR. Lap shear tensile testing was used to assess the joint quality of specimens produced by F-SPR. The joint interface from the cross-sectioned F-SPR specimen was evaluated by optical microscopy.

Keywords Friction self-piercing riveting · Carbon-fiber-reinforced polymer AZ31B

This manuscript has been authored by UT-Battelle, LLC, under contract DE-AC05-00OR22725 with the US Department of Energy (DOE). The US government retains and the publisher, by accepting the article for publication, acknowledges that the US government retains a nonexclusive, paid-up, irrevocable, worldwide license to publish or reproduce the published form of this manuscript, or allow others to do so, for US government purposes. DOE will provide public access to these results of federally sponsored research in accordance with the DOE Public Access Plan (http://energy.gov/downloads/doe-public-access-plan).

Y. C. Lim (✉) · C. D. Warren · J. Chen · Z. Feng (✉)
Oak Ridge National Laboratory, Materials Science and Technology Division,
One Bethel Valley Road, Oak Ridge, TN 37831, USA
e-mail: limy@ornl.gov

Z. Feng
e-mail: fengz@ornl.gov

C. D. Warren
e-mail: warrencd@ornl.gov

J. Chen
e-mail: chenj@ornl.gov

Y. Hovanski et al. (eds.), *Friction Stir Welding and Processing X*, The Minerals, Metals & Materials Series, https://doi.org/10.1007/978-3-030-05752-7_18

Introduction

Multi-material lightweight vehicles have been targeted by the automotive industry as a way to comply with government regulations while producing safer, more fuel efficient, and more durable vehicles. One general approach to achieving this goal is to integrate high specific strength (i.e., strength divided by density) materials—-such as aluminum, magnesium alloys, carbon fiber (CF) composites, and advanced high-strength steels—into the unified vehicle structure. However, joining of the individual materials has been a critical challenge because of the physical and chemical incompatibilities between the materials.

Extensive research has been conducted on joining dissimilar lightweight materials using fusion welding, solid-state joining, and mechanical fastening [1–5]. Although hybrid vehicle structures using CF composites and magnesium alloys have good potential for future lightweight vehicle applications, only limited work has been reported for joining CF-reinforced composites (CFRCs) to magnesium alloys [6]. For this reason, the authors focused on developing a process for joining CFRCs to the magnesium alloy AZ31B. Magnesium has low ductility and formability at room temperature [7], so it is hard to achieve the required plasticity even for mechanical fastening, such as self-piercing riveting. To overcome the issue of low ductility at room temperature, we employed a unique friction self-piercing riveting (F-SPR) process. This process has recently been used for joining dissimilar materials, such as joining aluminum to magnesium alloys [8, 9] and aluminum to steel [10].

Experiment

Materials

For a top sheet material, a 3-mm-thick thermoplastic CF-reinforced polymer (polyamide [PA] 66 with 40% random and short CFs) was provided by BASF. Another top sheet was purchased for this work—a 1.86-mm-thick thermoset CF-reinforced polymer (Clearwater Composites, Minnesota, USA) with G-83 prepreg laminated reinforced with 50 wt% of unidirectional CFs (T700, Toray). The stacking sequence of the CF layers was (0°/90°) with nine plies. A 2.3-mm-thick AZ31B alloy sheet was used as the bottom material. Figure 1 shows a magnified cross-sectional view of both the thermoplastic and thermoset CF composites. For the F-SPR process, 5.3 mm diameter special semi-tube rivets with hexagonal heads were designed and fabricated. The rivet shank length was 6 mm. The rivets were made of Japanese Industrial Standard G3507-2 carbon steel without heat treatment or coating. Table 1 shows the chemical compositions of AZ31B and the rivets. The mechanical properties of both materials are summarized in Table 2. Finally, a DZ series pip die with a 1.7 mm cavity depth was used, based on previous work [8].

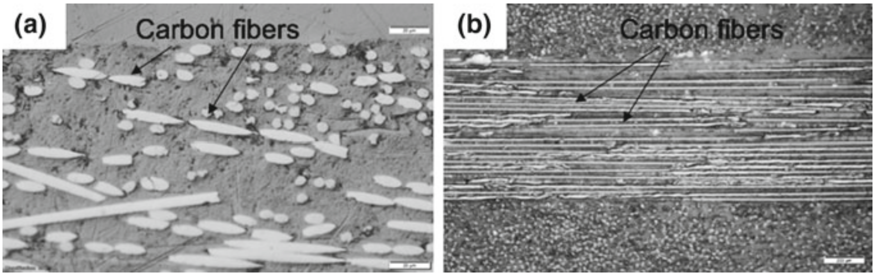

Fig. 1 Magnified cross-sectional optical image of **a** thermoplastic CFRP (PA66-40% CF), **b** thermoset CFRP with (0°/90°) CF layers

Table 1 Chemical compositions of AZ31B and rivet

Element	C	Al	Zn	Mn	Ca	Cu	Fe	Ni	Si	P	S	Others	Mg
AZ31B	–	2.5–3.5	0.7–1.3	0.2–1.0	0.04	0.05	0.005	0.005	0.05	–	–	0.4	Balance
Rivet	0.14	0.0005	–	0.71	–	–	Balance	–	0.04	0.011	0.004	–	–

Table 2 Mechanical properties of each material

Material	Tensile strength (MPa)	Elongation (%)
CFRP (PA66-40%CF)	154	–
CFRP (G-83 prepreg)	827	–
AZ31B	285	8
Rivet	463	26.4

A water jet was used to cut all sheets into coupons of 25 mm wide and 100 mm long for lap shear coupons. A 25 mm overlap was used for the lap shear coupons. Then, acetone, followed by isopropyl alcohol, was used to clean the surfaces of both sheets before joining. The material stacks for F-SPR were 3-mm-thick CFRP (PA66-40% CF) joined to 2.3-mm-thick AZ31B, and 1.86-mm-thick CFRP (G-83 prepreg) joined to 2.3-mm-thick AZ31B.

Friction Self-Piercing Riveting

In the F-SPR process, a semi-hollow rivet is rotated and plunged into the top and bottom materials to create a joint, as illustrated in Fig. 2. Frictional heat is generated by the rotating rivet and underneath the material, leading to local softening of the material. This local heating can produce a crack-free joint for a low-ductility material such as a magnesium alloy. Finally, mechanical interlocking between the rivet and bottom sheet is achieved by outward flaring of the rivet leg based on the geometry of the supporting die. The joint quality is governed by the interlock distance and the remaining material thickness of the bottom sheet. Figure 3 shows a specially

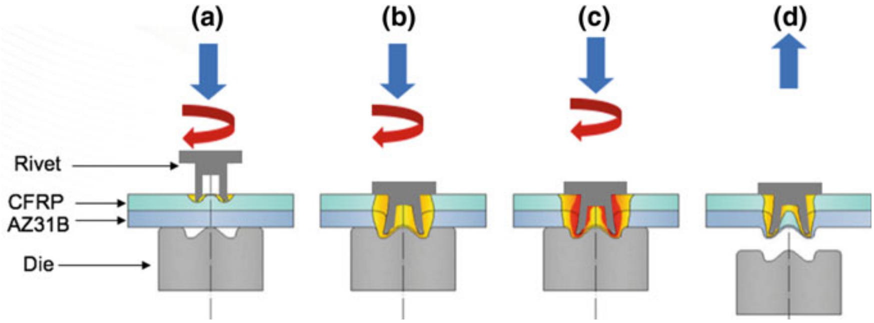

Fig. 2 Schematic of F-SPR process

Fig. 3 **a** Overview of friction self-piercing riveting machine. **b** Magnified image showing rivet holder, steel rivet, and pip die

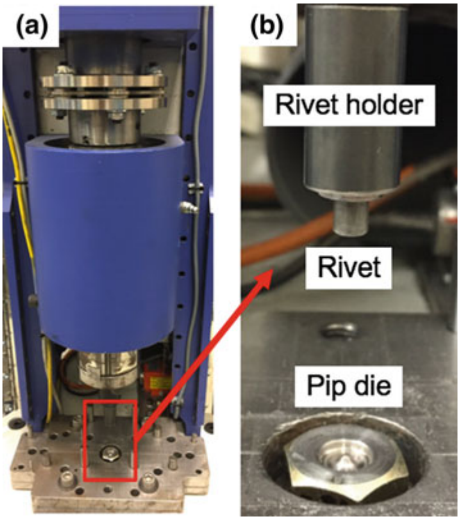

Table 3 Summary of F-SPR process parameters for each material stack

Material stack	Spindle speed (rpm)	Z-axis plunge depth (mm)	Z-axis plunge speed (mm min^{-1})
CFRP (PA66-40%CF)—AZ31B	2000	6.7	101.6
CFRP (G-83 prepreg)—AZA31B	2000	6.65	101.6

designed piece of welding equipment for the F-SPR process along with a rivet, its holder, and the pip die. The F-SPR process parameters initially used for the material stacks are summarized in Table 3.

Mechanical Testing

To evaluate the joint integrity of F-SPR specimens, lap shear tensile testing was performed using an MTS tensile machine with a constant crosshead speed of 10 mm min^{-1} at room temperature. Spacers were used to grip the lap shear coupons to align them.

Results and Discussion

Figure 4 shows an example of thermoset CFRP (G-83 prepreg) joined to AZ31B by F-SPR. No surface damage was observed on the CFRP when the rivet is plunged into the top sheet. In addition, visual observation of the backside of the AZ31B after F-SPR showed no crack formation on the low-ductility magnesium alloy. Frictional heat generated during F-SPR softened the AZ31B so that crack formation was avoided. Previous work also demonstrated that preheating AZ31B up to 200 °C before self-piercing riveting effectively prevented cracking [11].

Load and displacement curves from lap shear tensile testing of the different material stacks are plotted in Fig. 5. The peak failure load for the thermoplastic CFRP (PA66-40%CF)–AZ31B stack was 3.2 kN, and a failure load of 5.12 kN was obtained for the thermoset CFRP (G-83 prepreg)–AZ32B stack. Note that the lap shear peak load obtained was comparable to that found in previous reported work (~1.5 kN) for AZ31B joined to a polyphenylene sulfide CF composite by friction spot welding [6]. The peak loads obtained for the different material stacks were normalized using the cross-sectional area of the rivet shank diameter (5.3 mm), resulting in load values of 145.1 MPa and 231.96 MPa for the thermoplastic CFRP–AZ31B and the thermoset CFRP–AZ31B, respectively. The normalized tensile shear strengths for both cases were close to the tensile strengths of the base materials, such as thermoplastic CFRP (PA66-40%CF) and AZ31B, respectively.

Different failure modes were observed for each material stack. Net tension failure of the CFRP was observed for the CFRP (PA66-40%CF)–AZ31B specimen, as shown in Fig. 6a. The failure could be due to stress concentration around the hole produced by the F-SPR process. In the CFRP (G-83 prepreg)–AZ31B specimen, a large hole was observed in the AZ31B sheet because the mechanical interlock pulled out from the bottom magnesium sheet, as seen in Fig. 6b. From the cross-sectional view, the

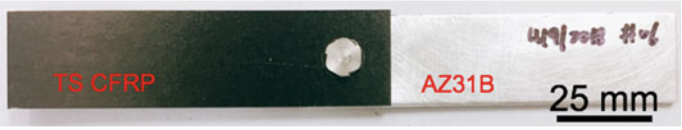

Fig. 4 Example of thermoset CFRP joined to AZ31B by friction self-piercing riveting

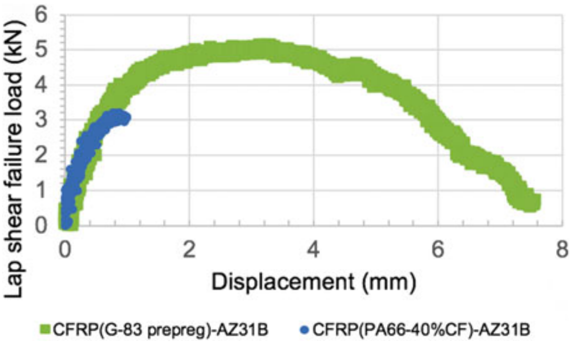

Fig. 5 Load and displacement curves of different material stacks

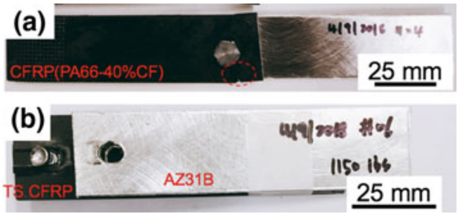

Fig. 6 **a** Fractography of thermoplastic CFRP (PA66-40%CF) joined to AZ31B by friction self-piercing riveting, showing net tension failure of the composite (red-dotted circle). **b** Fractography of thermoset CFRP (G-83 prepreg) joined to AZ31B showing pullout from the AZ31B

mechanical interlock was measured at around 0.4 mm. This failure mode can indicate good mechanical interlocking between the rivet and the magnesium alloy.

Conclusions

In quick summary, F-SPR was successfully demonstrated for joining CF composites to the magnesium alloy AZ31B. No cracking of AZ31B was found after the joining process, because localized friction heat generated during F-SPR softened the magnesium alloy, leading to improved ductility and formability of the material. Lap shear tensile peak loads of 3.2 kN and 5.12 kN, respectively, were achieved for thermoplastic CFRP (PA66-40%CF) joined to AZ31B and thermoset CFRP (G-83 prepreg) joined to AZ31B. Net tension failure was observed for the thermoplastic CFRP joined to AZ31B, and mechanical interlocking pullout from the bottom magnesium sheet was seen for thermoset CFRP joined to AZ31B. In future work, other process parameters should be further studied for optimization of the F-SPR process.

Acknowledgements This research was financially sponsored by the US Department Energy, Vehicle Technologies Office, as part of the Joining Core Program. Oak Ridge National Laboratory is managed by UT-Battelle, LLC, for the US Department of Energy under Contract DE-AC05-00OR22725. The authors would like to thank to Kevin Simmons at Pacific Northwest National Laboratory for an optical microscopy of carbonfiber composites.

References

1. Jung KW, Kawahito Y, Takahashi M, Katayama S (2013) Laser direct joining of carbon fiber reinforced plastic to zinc-coated steel. Mater Des 47:179–188
2. Min J, Li Y, Li J, Carlson BE, Lin J (2015) Friction stir blind riveting of carbon fiber-reinforced polymer composite and aluminum alloy sheets. Int J Adv Manuf Technol 76:1403–1410
3. Abibe AB, Sonego M, dos Santos JF, Canto LB, Amancio-Filho ST (2016) On the feasibility of a friction-based staking joining method for polymer-metal hybrid structures. Mater Des 92:632–642
4. Zhang J, Yang S (2014) Self-piercing riveting of aluminum alloy and thermoplastic composites. J Compos Mater 49:1493–1502
5. Lim YC, Squires L, Pan T-Y, Miles M, Song G-L, Wang Y, Feng Z (2015) Study of mechanical joint strength of aluminum alloy 7075-T6 and dual phase steel 980 welded by friction bit joining and weld-bonding under corrosion medium. Mater Des 69:37–43
6. Amancio-Filho ST, Bueno C, dos Santos JF, Huber N, Hage E Jr (2011) On the feasibility of friction spot joining in magnesium/fiber-reinforced polymer composite hybrid structures. Mater Sci Eng A 528:3841–3848
7. Doege E, Droder K (2001) Sheet metal forming of magnesium wrought alloys—formability and process technology. J Mater Process Technol 171:10–20
8. Liu X, Lim YC, Li Y, Tang W, Ma Y, Feng Z, Ni J (2016) Effects of process parameters on friction self-piercing riveting of dissimilar materials. J Mater Proc Technol 237:19–30
9. Li YB, Wei ZY, Wang ZZ, Li YT (2013) Friction self-piercing riveting of aluminum alloy AA6061-T6 to magnesium alloy AZ31B. J Manuf Sci Eng 135:061007
10. Ma YW, Xian XR, Lou M, Li YB, Lin ZQ (2017) Friction self-piercing riveting (F-SPR) of dissimilar Materials. Proc Eng 207:950–955
11. Wang JW, Liu ZX, Shang Y, Liu AL, Wang MX, Sun RN, Wang P-C (2011) Self-piercing riveting of wrought magnesium AZ31B sheets. J Manuf Sci Eng 133:031009

Part VII
Friction Stir Processing

Achieving Forced Mixing in Cu-Based Immiscible Alloys via Friction Stir Processing

Mageshwari Komarasamy, Ryan Tharp, Subhasis Sinha, Saket Thapliyal and Rajiv Mishra

Abstract Cu-based binary and ternary immiscible alloys were synthesized from elemental powders via friction stir processing (FSP) as a pathway to obtain thermally stable bulk nanostructured alloys with forced miscibility. The processed alloys were characterized using scanning electron microscopy (SEM). High magnification SEM confirmed the formation of forced mixing in the friction stir processed layer. Forced miscibility in immiscible alloys systems was possible due to high temperature intense severe plastic deformation during FSP. Mixing characteristics in Cu–Ag–Nb and Cu–Fe immiscible alloys were carried out and a mixing mechanism was proposed. As-processed alloys exhibited hardness in the range of 215–320 HV0.3.

Keywords Immiscible alloys · Friction stir processing · Forced mixing
Microstructural evolution · Hardness

Introduction

One driver for the immense interest in nanocrystalline materials over the last few decades stems from the well-known Hall–Petch prediction of increasing the strength with reduction in grain size [1] and also the realization of manufacturing nanocrystalline materials in bulk [2]. The high volume fraction of grain boundaries increases the total free energy of the material tremendously and the nanocrystalline grains grow to reduce the free energy [3]. The degree of instability can be clearly recognized from a study on nanocrystalline Cu, where a significant grain growth was

---

M. Komarasamy (✉) · R. Tharp · S. Sinha · S. Thapliyal · R. Mishra
Department of Materials Science and Engineering, Center for Friction Stir Processing,
University of North Texas, Denton, TX 76203, USA
e-mail: Mageshwari.Komarasamy@unt.edu

R. Mishra
Department of Materials Science and Engineering, Center for Friction Stir Processing,
Advanced Materials and Manufacturing Processes Institute, University of North Texas,
Denton, TX 76203, USA

Y. Hovanski et al. (eds.), *Friction Stir Welding and Processing X*, The Minerals,
Metals & Materials Series, https://doi.org/10.1007/978-3-030-05752-7_19

observed in the sample after one month of storage at ambient temperature [4]. Additionally, deformation-induced stress-assisted grain growth was extensively observed in nanocrystalline materials [5]. Therefore, it is important to limit or reduce the grain growth to maintain the benefit of nanocrystalline grains in achieving high strength material.

In nanocrystalline materials, two approaches are followed to reduce the grain growth. One is energetics based where the grain boundary energy is reduced due to the presence of solutes at the boundary and the second one is kinetics based where second phase particles pin the boundary thereby restricting grain growth, also known as “Zener pinning” [3]. To effectively control the growth of nanocrystalline grains, it is imperative to make use of both thermodynamic and kinetic approaches toward grain boundary stabilization. The abovementioned approach can be accomplished by careful selection of alloying elements, where the solute elements can form stable nano-sized precipitates to pin the grain boundaries and/or the solute elements can be in solid solution with the matrix, which can either pin the boundary via solute drag or reduce the boundary energy. Various immiscible alloying elements that are usually added to Cu are Nb, Ta, W, Cr, and Fe [3]. Methods such as high energy ball milling and severe plastic deformation (SPD) techniques are generally employed in creating forced miscibility in immiscible systems [6, 7]. Through this method of incorporating immiscible elements, nanocrystalline Cu grains were stable even at very high temperature (>0.5 Tm) and high stress conditions [8]. Forced shear mixing across Cu–X interface during various SPD techniques depends on various factors such as, differences in (1) crystal structure, (2) elastic moduli, (3) atomic size and (4) mutual solubility, (5) heat of mixing between the solute and the solvent, and (6) interface structure [9–12]. For instance, in coherent or semi-coherent interfaces, extensive chemical mixing due to slip transfer across the interface was observed [10]. Furthermore, a large difference in shear modulus would lead to severe strain localization in the soft phase and the hard phase not deforming plastically thereby limiting the intermixing of the two phases. Overall, there are a number of factors that can affect the extent of mixing in immiscible systems, ranging from intrinsic material properties to the deformation conditions.

Friction stir processing (FSP) is a high-temperature SPD technique and further details of the process can be found in [13, 14]. High temperature, intense shear strain, and high strain rate deformation conditions are imparted by the tool onto the sheared volume. For the first time, the authors have shown the ability of FSP to force shear mix immiscible elements in Cu–Ag–Nb alloy [15] and to obtain nanostructural features. In this investigation, mixing characteristics and microstructural evolution of two friction stir processed Cu-based immiscible alloys were carried.

Experimental Procedure

Elemental Cu, Ag, Nb, and Fe in ~99.9% purity and in the size range of 1–5 μm was purchased from Atlantic Equipment Engineers. Figure 1 shows various steps involved in fabricating the forced mixed immiscible Cu–X alloys. Mixture of the elemental powders in the nominal compositions of Cu-5 wt% Ag-3 wt% Nb, Cu-5 at.% Fe (Cu–5Fe), and Cu-10 at.% Fe (Cu–10Fe) were weighed and then mixed mechanically with the help of roller mixer. The mixed powders were then cold pressed into a 10 mm diameter pellet using a dry pressing die set and hydraulic press. The cold pressed pellet was placed in a slightly larger diameter hole made in a pure Cu block. Then, friction stirring without translational movement was performed at 600 rpm and for differing stirring times. Two different tools were used to investigate the effect of tool features on the forced mixing. First, lanthanated Tungsten (La_2O_3W) tool (tool 1) with a featureless cylindrical pin of 6 mm diameter and 3 mm length and a flat, featureless shoulder of 12 mm diameter, and second, a tool (tool 2) made up of tool steel with concave shoulder and conical pin with step-spiral profile was used. The shoulder diameter, pin length, pin diameter at the root and tip were 12, 2.25, 6 and 3.75 mm. Both the tools were used for processing the Cu–Ag–Nb composition. Furthermore, in the case of tool 1, stirring time was 10 s while stirring time in tool 2 was increased to 60 s. For the processing of Cu–Fe alloy, tool 2 was used with the stirring time of 60 s. Top view of the processed volume is shown in Fig. 1. Scanning electron microscopy (SEM) of both Cu–Ag–Nb and Cu–Fe alloys was done with FEI Nova NanoSEM 230 in back scattered electron mode. Samples for SEM were polished down to 0.02 μm surface finish using colloidal silica suspension.

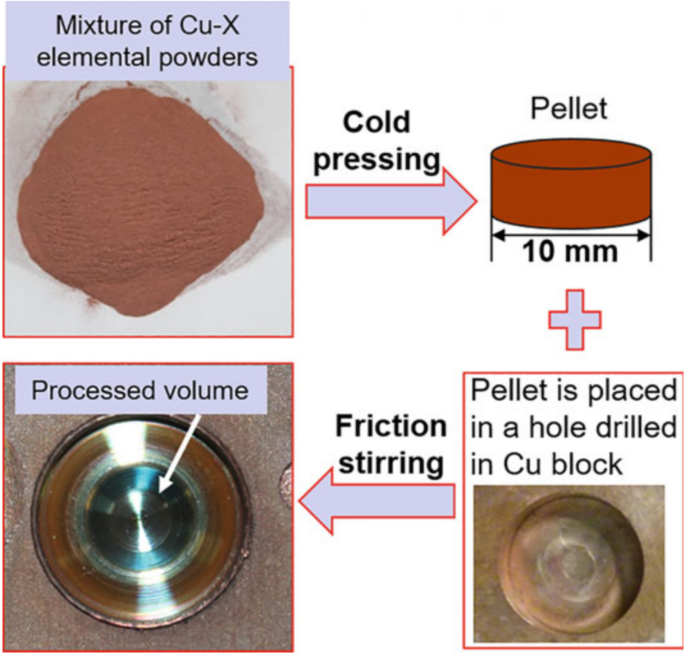

Fig. 1 Complete process description of creating bulk, force mixed nanocrystalline, or ultrafine-grained Cu–X alloy systems from elemental powders

The Vickers microhardness of the processed volume was obtained at a load of 300 g and 10 s dwell time. Transmission electron microscopy (TEM) of Cu–5Fe sample was done to investigate grain size and the TEM sample was prepared via Focused Ion Beam milling process using FEI Nova 200 NanoLab Dual Beam FIB/FESEM. TEM was done in FEI Tecnai G2 F20 S-Twin 200 keV field emission scanning TEM.

Results and Discussion

Effect of Tool and FSP Parameters

Figure 2 shows the effect of both tool features and the stirring time on the extent of mixing in the processed volume. Figure 2a–c is for tool 1 with 10 s of stirring time, while Fig. 2d–f is for tool 2 with 60 s of stirring time. As noted from the overall cross-section view in (b) and (c), tool 1 with featureless cylindrical pin did not result in good mixing. A sliver of processed volume consisting of slight mixing between the elements can be observed (Fig. 2c). On the other hand, tool 2 led to a good forced mixed layer (Fig. 2e, f). The step-spiral conical pin enhanced the material flow of the powders and intensified the deformation conditions, due to which a relatively thick processed volume was obtained. Figure 2f shows both the unmixed and force mixed region, and the absence of coarse particles in the processed volume signifies the mixing of elemental powders. Detailed analysis of the mixing is presented in the upcoming sections.

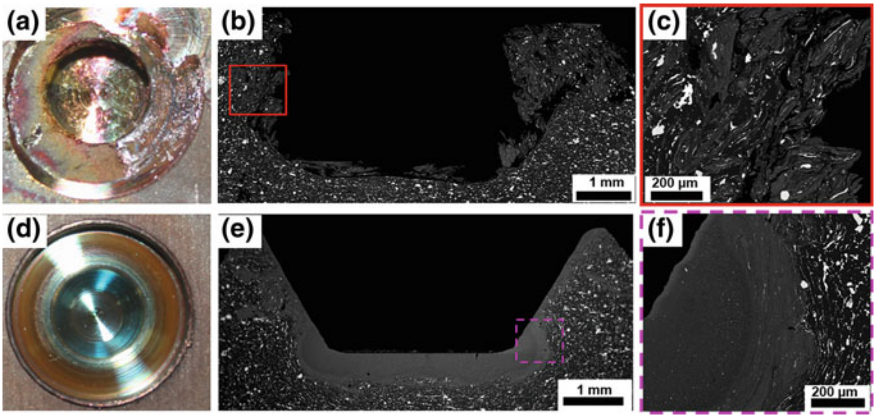

Fig. 2 Effect of tool features and processing parameters on the mixing extent in Cu–Ag–Nb alloy. **a**–**c** and **d**–**f** are for tool 1 with 10 s of stirring time and tool 2 with 60 s of stirring time, respectively

Microstructural Evolution in Cu–Ag–Nb System

Figure 3 shows the deformation and subsequent mixing behavior in various zones. Figure 3a is the overview of the processed volume and the region marked by the red square box is presented in Fig. 3b. Figure 3b, c shows the thermomechanically affected zone (TMAZ). Figure 3d, e shows processed volume and the high magnification view of the mixed zone, respectively. Furthermore, EDS analysis of the region denoted in Fig. 3f is presented in Fig. 3g–i to understand the deformation behavior of Ag and Nb particles. A quick summary of various observations is presented here. Note the absence of coarse secondary particles and the presence of extremely fine particles and nanocrystalline Cu–Ag–Nb grains. In addition, a few scattered fine particles were also noted as denoted by red arrows which essentially are refined particles after the high-temperature severe plastic deformation during FSP. As well known, FSP is a high strain rate, strain, and high temperature process [13, 14]. Initially, fric-

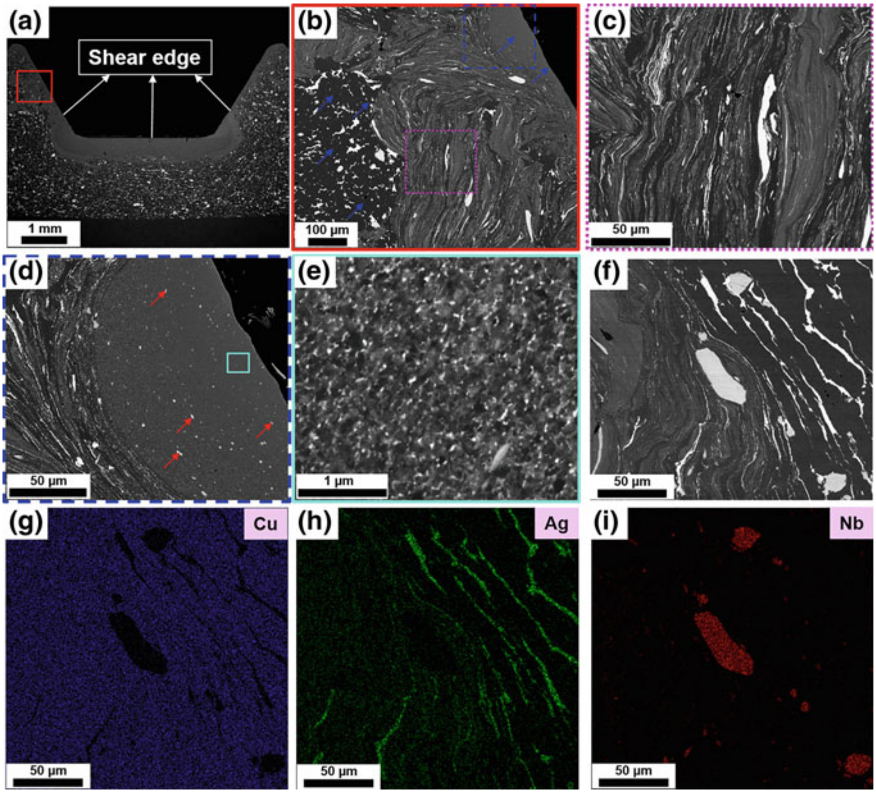

Fig. 3 Microstructural evolution in the stirred region and TMAZ. **a** Cross-sectional overview, **b**, **c** TMAZ region showing deformation characteristics of various particles, **d**, **e** mixing in the stirred region, **f**–**i** EDS analysis of the TMAZ region

tion generated at the specimen–tool interface would be limited due to cold compacted powders, but with continued stirring and subsequent formation of the solid material, friction would increase resulting in high temperature in the processing volume. The average grain size in the processed volume near the shear edge was approximately 100 nm. Shear edge is marked on Fig. 3a. Note the significant contrast change in the processed volume as compared to the unmixed base material as denoted by blue arrows in Fig. 3b. This was due to the forced introduction of high atomic number elements (Ag and Nb) into solid solution with Cu. Next, the co-deformation behavior of Ag and Nb relative to Cu can be understood based on the microstructural evolution in TMAZ. Note that Ag particles were deformed extensively as compared with Nb particles. Both Nb (38 GPa) and Ag (30 GPa) exhibit a comparable shear modulus to Cu (48 GPa), hence shear modulus difference is not the determining factor. In addition, crystal structure difference also exerts significant impact on the co-deformation characteristics. Nb and Ag have body-centered cubic (BCC) and face-centered cubic (FCC) crystal structures, respectively. Extensive co-deformation of two materials was observed in materials with similar crystal structure (Cu–Ag) and in the case of FCC-BCC combination, the co-deformability was limited [10]. The current investigation clearly demonstrates such expected co-deformation behavior in Cu–Ag–Nb system. A similar phenomenon was observed in the friction stir processed Cu–Cr immiscible alloy as well. In this case, in addition to the differences in crystal structure, Cr has high shear modulus (115 GPa) as compared to Cu (48 GPa), overall, leading to a limited mixing for the same deformation conditions (not shown here).

Microstructural Evolution in Cu–Fe System

In addition to Cu–Ag–Nb immiscible alloy, mixing behavior and microstructural evolution in Cu–Fe immiscible alloy were carried out. Figure 4a–f shows the microstructural evolution in Cu–5Fe and Cu–10Fe immiscible alloys, respectively. Note that both the compositions were processed with the tool rotation rate 600 rpm for 60 s. In both the alloys, coarse Fe particles in the cold pressed pellet were deformed extensively during FSP, and resulted in Cu–Fe solid solution and submicron Fe particles as denoted by magenta arrows in Fig. 4. Cu–10Fe had more submicron Fe particles as compared to Cu–5Fe. This was due mainly to the increased Fe particle fraction and also reaching the solubility limit even under forced shear mixing. In the case of Cu–5Fe, both high magnification SEM (Fig. 4b) and TEM (Fig. 4c) showed the presence of ultrafine grains. Furthermore, friction stirred Cu–10Fe alloy also exhibited ultrafine grains (SEM image not shown here). The limited presence of submicron particles in the case of Cu–5Fe indicated the existence of Fe in solid solution with Cu, which could be precipitated out with an appropriate aging heat treatment. The impact of the presence of solid solution or large fraction of submicron Fe particles can be understood from the hardness results which are presented in the next subsection.

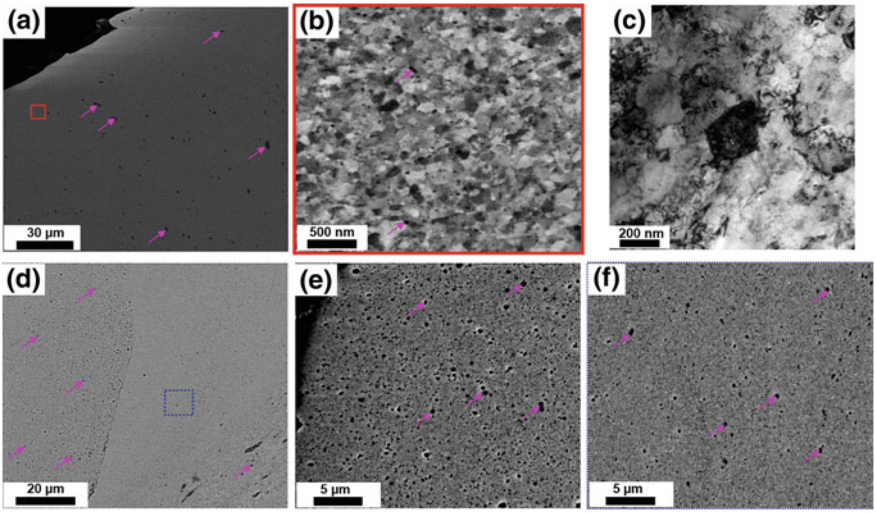

Fig. 4 Microstructural evolution after friction stirring in **a**–**c** Cu–5Fe and **d**–**f** Cu–10Fe alloys, respectively

Vickers Microhardness

Vickers hardness measurements of various alloys in as-processed condition are shown in Table 1. Among the five compositions, alloys with high fraction of alloying element exhibited the highest hardness. As noted in the case of Cu–10Fe, a large fraction of submicron Fe particles were noted in the high magnification SEM image. Similar observations were made in the Cu–10Cr alloys as well. Therefore, the presence of micron-sized or submicron particles increased the hardness of the alloy due may be to composite strengthening. In addition to that, Cu–Ag–Nb alloy exhibited an intermediate hardness, which could be due to the combination of nanocrystalline grains and extremely fine Ag and Nb-rich particles. A relatively low hardness in the case of Cu–5Fe immiscible alloy could be due to the existence of Fe in solid solution with Cu and the limited presence of Fe-rich particles. Overall, as-processed Cu-based immiscible alloys show the potential for postprocessing aging treatment which would enhance the strength/hardness of such material system.

Table 1 Vickers microhardness for various Cu-based immiscible alloys fabricated via friction stir processing

Alloys	Cu–Ag–Nb	Cu–5Fe	Cu–10Fe	Cu–5Cr	Cu–10Cr
Hardness HV0.3	245 ± 32	223 ± 19	318 ± 15	214 ± 10	312 ± 10

Mixing Mechanism

Figure 5 explains the extent of deformation and subsequent mixing of various particles in the Cu matrix. The example contains Ag, Fe, Nb, and Cr particles in Cu matrix. As discussed earlier, among the four immiscible alloying additions, differences in crystal structure and shear modulus exist as compared with Cu base. Due to the force exerted by the FSP tool in the deformation zone, the particles underwent extensive shearing and extrusion deformation. Once the fracture strain was reached, the elongated particles fragmented into fine particles. Due to continued stirring, the fragmented particles subjected to further deformation that again elongated them. The continuation of these processes led to extremely fine particles and also the forced creation of solid solution in Cu–X immiscible alloy systems. The abovementioned process is presented in Fig. 5. Also, note that the extent of deformation was determined by the characteristics of the particles and varied between, for instance, Ag and Cr particles. Furthermore, in the case of Cu–Ag system, dislocation transfer across the FCC/FCC was observed which aided in the forced mixing process [10]. However, in the case of FCC/BCC interface, no such dislocation transfer across the interface was noted [10]. As mentioned earlier, with continued stirring, friction between the tool and workpiece would also increase that would increase the process temperature. Therefore, high temperature would enhance the defect-assisted diffusion processes

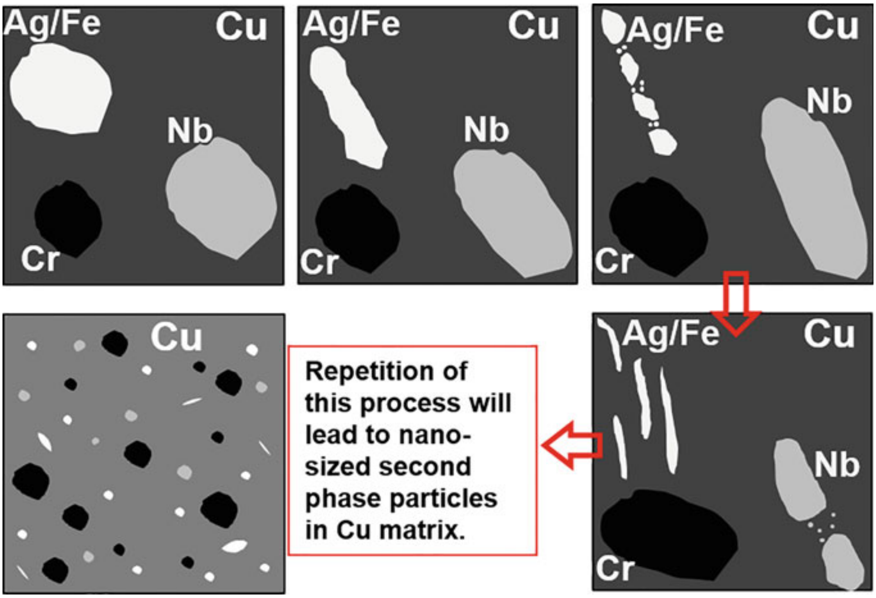

Fig. 5 Schematic of forced shear mixing mechanism is explained for particles with different physical properties

in FSP due to high density of vacancies and dislocations present in the shear deformation zone. Overall, all these mechanisms would aid in the mixing of immiscible elements in Cu matrix.

Conclusion

In this investigation, the viability of friction stir processing in creating miscibility in various Cu-based immiscible alloys was investigated and following are the conclusions:

1. Both tool features such as concave shoulders and conical, step-spiral pin, and processing parameters are critical factors in attaining relatively bulk processed volume consisting of forced mixed solid solution.
2. High magnification SEM analysis proved the presence of mixing in both Cu–Ag–Nb and Cu–Fe alloys.
3. In Cu–Ag–Nb alloy, Ag particles deformed much more extensively as compared to Nb particles, as observed in the TMAZ region.
4. In Cu–Fe alloys, large fraction of submicron Fe particles were present in Cu–10Fe composition as compared to Cu–5Fe.
5. Vickers microhardness varied from 215 to 320 HV0.3, which was dependent on whether the processed volume contained primarily solid solution or submicron second phase particles.

Acknowledgements Authors acknowledge the help of Maya Duffy and Smruthi Senthil in sample preparation. Authors also acknowledge Material Research Facility (MRF) at University of North Texas for the microscopy facilities.

References

1. Gleiter H (1989) Nanocrystalline materials. Prog Mater Sci 33:223–315
2. Meyers MA, Mishra A, Benson DJ (2006) Mechanical properties of nanocrystalline materials. Prog Mater Sci 51(4):427–556
3. Tschopp MA, Murdoch HA, Kecskes LJ, Darling KA (2014) Bulk nanocrystalline metals: review of the current state of the art and future opportunities for copper and copper alloys. JOM 66(6):1000–1019
4. Gertsman VY, Birringer R (1994) On the room-temperature grain growth in nanocrystalline copper. Scr Metall Mater 30(5):577–581
5. Boyce BL, Padilla HA (2011) Anomalous fatigue behavior and fatigue-induced grain growth in nanocrystalline nickel alloys. Metall Mater Trans A Phys Metall. Mater Sci 42(7):1793–1804
6. Suryanarayana C (2001) Mechanical alloying and milling. Prog Mater Sci 46(1–2):1–184
7. Ma E (2005) Alloys created between immiscible elements. Prog Mater Sci 50(4):413–509
8. Darling KA, Rajagopalan M, Komarasamy M, Bhatia MA, Hornbuckle BC, Mishra RS, Solanki KN (2016) Extreme creep resistance in a microstructurally stable nanocrystalline alloy. Nature 537:378–381

9. Vo NQ, Zhou J, Ashkenazy Y, Schwen D, Averback RS, Bellon P (2013) Atomic mixing in metals under shear deformation. JOM 65(3):382–389
10. Ashkenazy Y, Vo NQ, Schwen D, Averback RS, Bellon P (2012) Shear induced chemical mixing in heterogeneous systems. Acta Mater 60(3):984–993
11. Odunuga S, Li Y, Krasnochtchekov P, Bellon P, Averback RS (2005) Forced chemical mixing in alloys driven by plastic deformation. Phys Rev Lett 95(4):93–96
12. Botcharova E, Freudenberger J, Schultz L (2004) Mechanical alloying of copper with niobium and molybdenum. J Mater Sci 39(16–17):5287–5290
13. Mishra RS, Ma ZY (2005) Friction stir welding and processing. Mater Sci Eng R Rep 50(1–2):1–78
14. Mishra RS, De PS, Kumar N (2014) Friction stir welding and processing. Springer International Publishing, Switzerland
15. Mageshwari K, Mishra RS, Mukherjee S, Young ML (2015) Friction stir-processed thermally stable immiscible nanostructured alloys. JOM 67(12):2820–2827

Stationary Shoulder Friction Stir Processing: A Low Heat Input Grain Refinement Technique for Magnesium Alloy

Vivek Patel, Wenya Li, Quan Wen, Yu Su and Na Li

Abstract Stationary shoulder friction stir processing (SSFSP) as a low heat input grain refinement technique is projected in this study. SSFSP can be considered as a variant of friction stir processing (FSP) with modified tooling system. It uses stationary shoulder tool and rotating probe, which helps to reduce heat input in great manner during process. Present work aims to refine grain size in thick AZ31B magnesium alloy using SSFSP without using external cooling at different tool rotational speeds (700–1300 rpm). The smooth surface with little flash without any defect was obtained in all the samples, which had confirmed the wide processing range of SSFSP. Probe-dominated stir zone (SZ) achieved for all rotational speeds, which confirmed smaller temperature gradient throughout the SZ thickness. SZ produced at the lowest rotational speed (700 rpm) exhibited reduction in grain size and subsequently enhancement in mechanical properties (hardness and tensile).

Keywords Grain refinement · Friction stir processing · Magnesium
Stationary shoulder

V. Patel (✉) · W. Li · Q. Wen · Y. Su · N. Li
Shaanxi Key Laboratory of Friction Welding Technologies, School of Materials
Science and Engineering, Northwestern Polytechnical University, Xi'an 710072, Shaanxi,
People's Republic of China
e-mail: profvvp@yahoo.com

W. Li
e-mail: liwy@nwpu.edu.cn

Y. Hovanski et al. (eds.), *Friction Stir Welding and Processing X*, The Minerals,
Metals & Materials Series, https://doi.org/10.1007/978-3-030-05752-7_20

Introduction

Friction stir processing (FSP) is a promising method to modify the microstructural features of the base metal (BM) in such a way that improves the properties of it [1, 2]. FSP has shown different material processing applications like grain refinement [3, 4], superplasticity [5–8], surface composite [9], fusion weld repair [10], and coating modification [11, 12]. FSP uses conventional tooling system of rotating shoulder and probe to create severe plastic deformation into BM. During plastic deformation, the shoulder of tool mainly contributes to the heat generation due to its larger dimensions in comparison to that of probe. The microstructural refinement is preferred at low heat input so that grain growth could be minimized during FSP. The heat input is lower by either adopting low rotational and high travel speeds or additional cooling of processed material. In case of heat-sensitive alloy like magnesium, the conventional tooling system is quite difficult to conduct FSP. Therefore, magnesium alloys, especially AZ31 has been investigated mostly using additional cooling during FSP [13–15]. To eliminate the additional cooling, the tooling system can be modified in such a way that shoulder of tool remains nonrotating like stationary shoulder friction stir welding (SSFSW) tooling system. Use of stationary shoulder tool in welding has already demonstrated sound weld quality due to low heat input, smaller temperature gradient across the weld thickness, no or little flashes and arc corrugations [16–18]. Such a low heat input and smaller temperature gradient characteristics are desired in FSP to enhance the grain refinement by producing uniform grained microstructure in SZ. Therefore, stationary shoulder tooling system can also be used in FSP to lower the heat input for processing magnesium alloys without using additional cooling. We propose stationary shoulder friction stir processing (SSFSP) as a variant of FSP for microstructure refinement and properties enhancement. The present work is a feasibility check of SSFSP on thick AZ31B magnesium alloy at different rotational speeds.

Experimental Procedures

6.35-mm-thick, rolled Mg plate as BM was used for SSFSP. The chemical composition of BM is displayed in Table 1. The self-designed stationary shoulder tooling assembly at the Shaanxi key laboratory of friction welding technologies, NWPU, was used to install the stationary shoulder and rotating probe or pin. Stationary shoulder and probe assembly are shown in Fig. 1. The tool dimensions consist of stationary shoulder of 18 mm, threaded probe diameter of 6 mm root and 3.5 mm tip, and probe length of 6 mm. The single-pass SSFSP was conducted at three different rotational speeds of 700, 1000, and 1300 rpm. The travel speed of 150 mm/min and tool tilt of 2.5° was maintained for all three samples. After SSFSP, the cross section of the processing zone was cut to prepare specimen for optical microscopy. The cut specimens were mechanically ground, polished, and etched (4.2 g picric acid + 10 ml glacial

Table 1 Chemical composition of AZ31B magnesium alloy

Al	Zn	Mn	Fe	Cu	Si	Mg
2.5–3.5	0.60–1.4	0.20–1.0	≤0.003	≤0.001	≤0.008	Balance

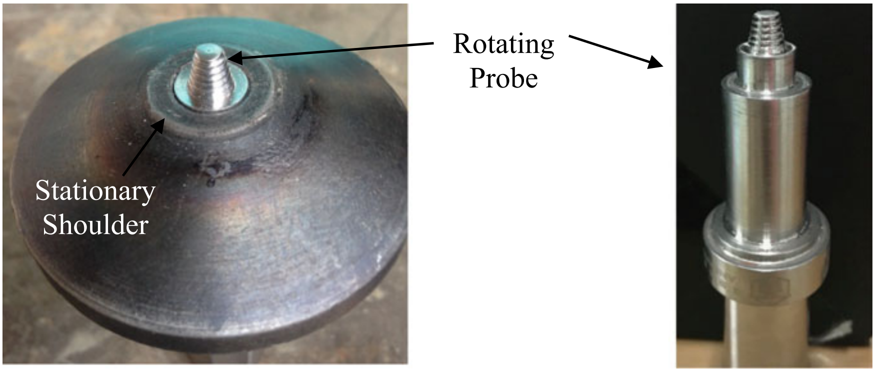

Fig. 1 Stationary shoulder tooling system

acetic acid + 10 ml distilled water + 70 ml ethanol). Microhardness measurement across the thickness of SZ under 200 gm load and 10 s dwell time was carried out. Tensile specimens were cut using wire cut electro-discharge machining in longitudinal direction of the processing zone in such a way that gage dimensions (25 mm length, 1.5 mm thickness, 2 mm width) coincide with SZ only. The room temperature tensile testing was conducted at cross-head speed of 0.5 mm/min.

Results and Discussion

The cross section of the processing zone produced at different rotational speeds is shown in Fig. 2. The macrostructure clearly represents defect-free SZ for all rotational speeds. Moreover, the SZ shape confirms probe-dominated material flow due to nonrotating action of the shoulder during processing. Hence, stationary shoulder allows wide operating range of tool rotational speeds to process heat-sensitive Mg alloy without the use of external cooling. It is also worth to note that the absence of shoulder deformation in SZ minimizes the temperature gradient across the thickness, i.e., top to bottom. So, stationary shoulder contributes to the combined effect of low heat input and smaller temperature gradient, which benefits to produce uniform microstructure across the SZ.

Further characterization was carried out only for low heat input SZ produced at the lowest rotational speed, i.e., 700 rpm. The surface analysis is performed using 3D digital in-depth microscopy to evaluate the surface finish of processing zone, since stationary shoulder produces smooth surface finish in comparison to the conventional

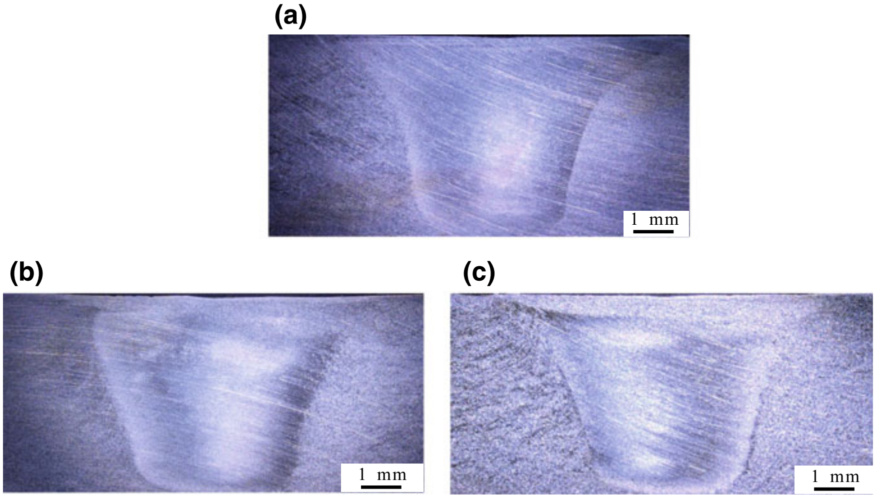

Fig. 2 Macrostructure of the cross section of FSP at different parameters

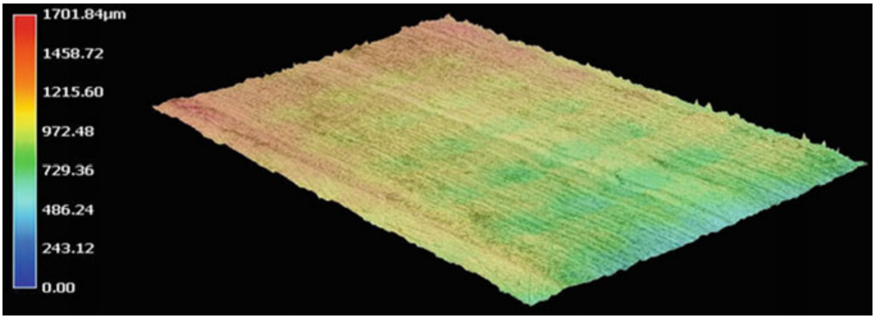

Fig. 3 Surface mapping of the FSP region

tooling system. The surface mapping of the processing zone produced at low heat input (700 rpm tool rotation) is presented in Fig. 3. The little flashes can be seen on the both sides in the form of red color densities in the 3D image. Overall, the surface finish of the entire surface is found reasonably well due to sliding action instead of rotating the shoulder on the BM during processing.

A typical fine-grained microstructure of the SZ produced at 700 rpm tool rotation is shown in Fig. 4a. This fine grain microstructure is attributed to the dynamic recrystallization during FSP. The grain size was reduced to 5.16 ± 0.63 µm in comparison to that of BM (~25 µm). Despite using external cooling, significant grain refinement is achieved due to low heat input characteristics of stationary shoulder tool. Microhardness distribution across the SZ thickness is presented in Fig. 4b, showing noticeable enhancement in the hardness across the thickness in comparison to that of BM. This enhancement in the hardness is attributed to the grain refinement.

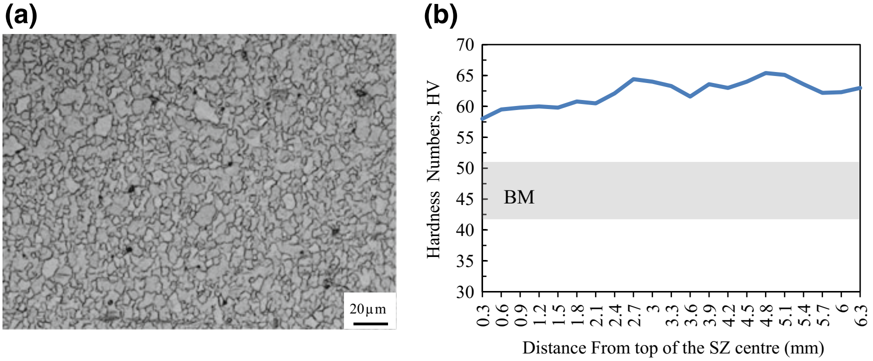

Fig. 4 **a** Optical micrograph of SZ and **b** Hardness distribution across the thickness of SZ at 700 rpm tool rotational speed

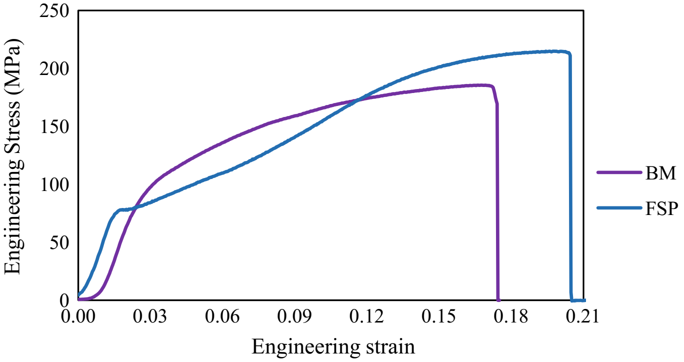

Fig. 5 Tensile behavior of BM and FSPed SZ at 700 rpm tool rotational speed

The peak hardness value is recorded of 65 HV and distribution of hardness was found with little anisotropy due to complex thermomechanical coupling through thickness during processing. However, this little anisotropy of hardness is higher in conventional FSP.

Tensile deformation behavior of the SZ produced at 700 rpm is presented as stress–strain curve in Fig. 5. The good combination of strength and ductility enhancement for FSP compared to BM is obtained. The ultimate tensile strength (UTS) of the FSPed sample is increased to 214 MPa from 185 MPa of BM. Similarly, the ductility of FSP specimen is also improved to 20.48% from 17.44% of BM. Moreover, Yuan and Mishra [19] reported the effect of texture on grain refinement and resultant mechanical properties in FSPed AZ31 magnesium alloy. They found the presence of strong basal fiber texture in the processing direction of SZ, which favors the formation of extension twinning during tensile deformation for strain accommodation. At the beginning of tensile testing, the formation of extension of twinning can reduce the stress concentration and accommodate strain incompatibility arising from basal slip dislocation movement, which can accommodate further dislocations [20]. Hence, twinning effect induced by basal slip contributes to the strain hardening and high ductility in the processed samples.

Conclusions

SSFSP of Mg alloy demonstrated wide range of tool rotational speeds (700–1300 rpm) to produce defect-free SZ. SZ is completely dominated by probe deformation due to nonrotating action of the shoulder. SSFSP achieves smooth surface finish with little flashes on the processing zone. Because of low heat input and small temperature gradient in SZ during SSFSP, significant enhancement in grain refinement followed by hardness and tensile properties enhancement in the SZ without the use of additional cooling during FSP is achieved. Hence, SSFSP would eliminate the need of additional cooling, which makes processing of Mg alloys simple and economic.

Acknowledgements The authors would like to thank for the financial support from the National Key Research and Development Program of China (2016YFB1100104). We also want to acknowledge the editorial committee, organizer(s) of Friction Stir Welding and Processing X, and TMS for recognizing our research work.

References

1. Nene SS, Liu K, Frank M, Mishra RS, Brennan RE, Cho KC, Li Z, Raabe D (2017) Enhanced strength and ductility in a friction stir processing engineered dual phase high entropy alloy. Sci Rep 7(1):161–167. https://doi.org/10.1038/s41598-017-16509-9
2. Komarasamy M, Mishra RS, Baumann JA, Grant G, Hovanski Y (2013) Processing, microstructure and mechanical property correlation in Al-B4C surface composite produced via friction stir processing. In: Friction stir welding and processing VII. Springer, pp 39–46
3. Ma ZY, Feng AH, Chen DL, Shen J (2018) Recent advances in friction stir welding/processing of aluminum alloys: microstructural evolution and mechanical properties. Crit Rev Solid State Mater Sci 43(4):269–333. https://doi.org/10.1080/10408436.2017.1358145
4. Patel VV, Li WY, Vairis A, Badheka VJ (2018) Recent development in friction stir processing as a solid-state grain refinement technique: microstructural evolution and property enhancement. Crit Rev Solid State Mater Sci (In Press)
5. Mishra RS, Mahoney M, McFadden S, Mara N, Mukherjee A (1999) High strain rate superplasticity in a friction stir processed 7075 Al alloy. Scripta Mater 42(2):163–168
6. Patel VV, Badheka V, Kumar A (2016) Influence of friction stir processed parameters on superplasticity of Al–Zn–Mg–Cu alloy. Mater Manuf Process 31(12):1573–1582. https://doi.org/10.1080/10426914.2015.1103868
7. Patel VV, Badheka V, Kumar A (2017) Effect of polygonal pin profiles on friction stir processed superplasticity of AA7075 alloy. J Mater Process Technol 240:68–76. https://doi.org/10.1016/j.jmatprotec.2016.09.009
8. Patel VV, Badheka V, Kumar A (2016) Friction stir processing as a novel technique to achieve superplasticity in aluminum alloys: process variables, variants, and applications. Metallogr Microstruct Anal 5(4):278–293

9. Rathee S, Maheshwari S, Siddiquee AN, Srivastava M (2017) A review of recent progress in solid state fabrication of composites and functionally graded systems via friction stir processing. Crit Rev Solid State Mater Sci 1–33. https://doi.org/10.1080/10408436.2017.1358146
10. Jesus JS, Costa JM, Loureiro A, Ferreira JM (2017) Fatigue strength improvement of GMAW T-welds in AA 5083 by friction-stir processing. Int J Fatigue 97(Supp C):124–134. https://doi.org/10.1016/j.ijfatigue.2016.12.034
11. Yang K, Li WY, Niu PL, Yang XW, Xu YX (2018) Cold sprayed AA2024/Al2O3 metal matrix composites improved by friction stir processing: microstructure characterization, mechanical performance and strengthening mechanisms. J Alloy Compd 736:115–123. https://doi.org/10.1016/j.jallcom.2017.11.132
12. Yang K, Li WY, Huang CJ, Yang XW, Xu YX (2018) Optimization of cold-sprayed AA2024/Al2O3 metal matrix composites via friction stir processing: effect of rotation speeds. J Mater Sci Technol 34(11):2167–2177. https://doi.org/10.1016/j.jmst.2018.03.016
13. Alavi Nia A, Omidvar H, Nourbakhsh SH (2014) Effects of an overlapping multi-pass friction stir process and rapid cooling on the mechanical properties and microstructure of AZ31 magnesium alloy. Mater Des 58(Supp C):298–304. https://doi.org/10.1016/j.matdes.2014.01.069
14. Darras B, Kishta E (2013) Submerged friction stir processing of AZ31 Magnesium alloy. Mater Des 47(Supp C):133–137. https://doi.org/10.1016/j.matdes.2012.12.026
15. Chang CI, Du XH, Huang JC (2008) Producing nanograined microstructure in Mg–Al–Zn alloy by two-step friction stir processing. Scripta Mater 59(3):356–359. https://doi.org/10.1016/j.scriptamat.2008.04.003
16. Zhou Z, Yue Y, Ji S, Li Z, Zhang L (2017) Effect of rotating speed on joint morphology and lap shear properties of stationary shoulder friction stir lap welded 6061-T6 aluminum alloy. Int J Adv Manuf Technol 88(5–8):2135–2141
17. Wen Q, Li WY, Wang WB, Wang FF, Gao YJ, Patel V (2018) Experimental and numerical investigations of bonding interface behavior in stationary shoulder friction stir lap welding. J Mater Sci Technol (In Press). https://doi.org/10.1016/j.jmst.2018.09.028
18. Ji S, Meng X, Liu J, Zhang L, Gao S (2014) Formation and mechanical properties of stationary shoulder friction stir welded 6005A-T6 aluminum alloy. Mater Des 1980–2015(62):113–117
19. Yuan W, Mishra RS, Carlson B, Mishra R, Verma R, Kubic R (2011) Effect of texture on the mechanical behavior of ultrafine grained magnesium alloy. Scripta Mater 64(6):580–583
20. Yuan W, Mishra RS (2012) Grain size and texture effects on deformation behavior of AZ31 magnesium alloy. Mater Sci Eng 558(Supp C):716–724. https://doi.org/10.1016/j.msea.2012.08.080

Friction Stir Processing (FSP) of Multiwall Carbon Nanotubes and Boron Carbide Reinforced Aluminum Alloy (Al 5083) Composites

Mahmood Khan, Wilayat Husain Syed, Shahid Akhtar and Ragnhild E. Aune

Abstract Friction Stir Processing (FSP) is a novel solid-state processing technique for fabrication of high strength surface composites. In present study, FSP was used to compare the cold formability of individually reinforced, hybrid and reference FSP samples of aluminum alloy Al5083. A plate of alloy containing MultiWall Carbon NanoTubes (MWCNTs) and boron carbide particles (B_4C) was processed by FSP and characterized. FSP composite containing MWCNTs was found to fracture during the bend-ductility test, while boron carbide particles reinforced FSP composites had superior cold bending formability along with the reference FSP sample. Cracking was also observed in hybrid FSP composite samples in lesser extent as compared to individually reinforced MWCNTs FSP composite. Possible cause of failure was identified as clustering of MWCNTs and weak interfacial bonding with the aluminum alloy matrix. Detailed metallographic and mechanical testing investigations revealed that the distribution of reinforcement at nanoscale and single pass processing played a vital role in generating defects and sinking of reinforcement particles in Al5083 matrix.

Keywords Friction Stir Processing (FSP) · MWCNTs · B_4C · Aluminum composite

---

M. Khan (✉) · W. H. Syed
Department of Materials Science and Engineering, Institute of Space Technology, Islamabad, Pakistan
e-mail: mahmood.khan@ntnu.no; mahmoodkhan77@gmail.com

W. H. Syed
e-mail: wilayat.hussain@ist.edu.pk

M. Khan · R. E. Aune
Department of Materials Science and Engineering, Norwegian University of Science and Technology (NTNU), Trondheim, Norway
e-mail: ragnhild.aune@ntnu.no

S. Akhtar
Norsk Hydro, Karmåy Primary Production, Håvik, Norway
e-mail: shahid.akhtar@hydro.com

Y. Hovanski et al. (eds.), *Friction Stir Welding and Processing X*, The Minerals, Metals & Materials Series, https://doi.org/10.1007/978-3-030-05752-7_21

Introduction

FSP is a method of changing the properties of a metal through intense, localized plastic deformation, and it is a modification of friction stir welding used to produce solid-state composites. Through FSP the microstructure of the processed surface is modified under action of a rotating tool by a mechanically induced sliding motion [1], and it is the movement/action of the tool that normally results in frictional heat and severe plastic deformation. Microstructural modification subsequently affects the mechanical properties of the base metal, i.e. hardness, tensile and compression strength [2]. Strength is often among the properties reported in literature [3] to have been improved by FSP as a result of elimination of microstructural defects like cracking and porosity. This makes friction stirred processed material more stress resistant [4].

Different types and morphologies of reinforcements have been incorporated by FSP in base metals such as aluminum oxide, silicon carbide, boron carbide, MWCNTs, etc. to prepare surface composites. In the case of aluminum and its alloys, range of particles from nanometer [5] to micrometer [6] have been reported to be incorporated by FSP, i.e. silicon carbide [7], aluminum oxide [8], boron carbide [9] and cerium oxide [10] are among the carbonaceous nanoreinforcements incorporated [11] as well as carbon nanotubes [5] and graphene nanoplatelets [12]. The combination of two chemically and morphologically dissimilar reinforcements has been less explored from the perspective of dispersion and effect of processing parameters of FSP.

Most of the studies on FSP reported in literature have focused on tooling and processing parameters along with general trend of improvement in mechanical properties of the resulting composites. Formability of the FSP composite in comparison with a nano and micro combination of reinforcements has, however, rarely been explored. Based on this, the present study focuses on the use of FSP to develop surface composites of Al5083 containing MWCNTs and B_4C particles. The B_4C particles, which are ceramic particles, possess high hardness [13] along with the MWCNTs which have exceptionally high strength and stiffness [14]. The baseline data for the hybrid composites was obtained by preparing FSP samples without the addition of any reinforcements. Microstructural observation and reinforcement distribution were examined by optical and scanning electron microscope. Micro Vickers hardness, tensile test and bending tests were carried out to characterize the mechanical performance. Finally, the results are critically reviewed in the light of available related data in literature.

Table 1 Aluminum alloy 5083 chemical composition obtained from X-ray fluorescence examination

Element	Mg	Fe	Mn	Cu	Si	Cr	Zn	Other	Al
wt%	4–4.9	≥0.4	0.4–1	≥0.1	0–0.4	0.05–0.25	0–0.1	0–0.05	Balance

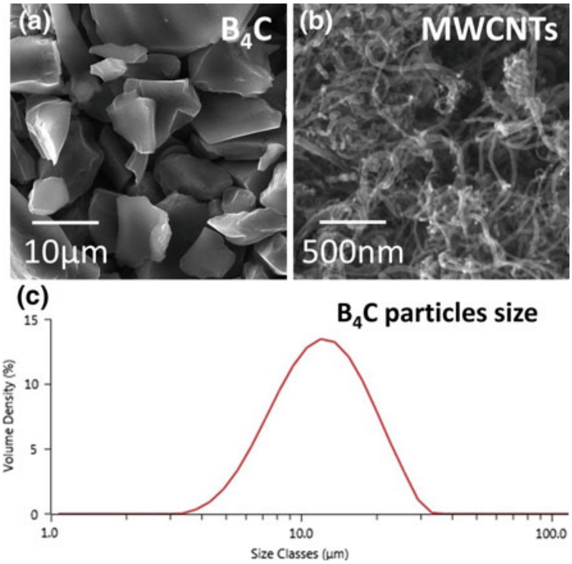

Fig. 1 SEM images of reinforcements using **a** B_4C particles, **b** Multiwall CNTs, and **c** particle size test results of B_4C particles

Experimental

Materials

Commercially rolled plate of Al5083, 6 mm thick was used with nominal composition shown in Table 1. 10 μm sized B_4C particles as shown in Fig. 1a, c, and MWCNTs with average length and diameter of 1–2 μm and 10–20 nm, respectively, were procured from Hongwu International Group, China, see Fig. 1b. H-13 tool steel with a diameter of 16 mm and 4.5–6.0 mm conical pin was used as a tool. A taper angle of 5° was made for the conical pin with a length of 4.5 mm (Fig. 2).

Manufacturing

Holes were drilled in the base plate of A15083 with a diameter of 2.0 mm and a depth of 3.0 mm. SI-3 M drilling machine (Siddhapura Enterprise, India) was used to drill holes ~10 mm apart. Each hole was filled with MWCNTs or B_4C particles, followed by manual compaction using a 1.8 mm diameter flat bottom face tool. Mixture of

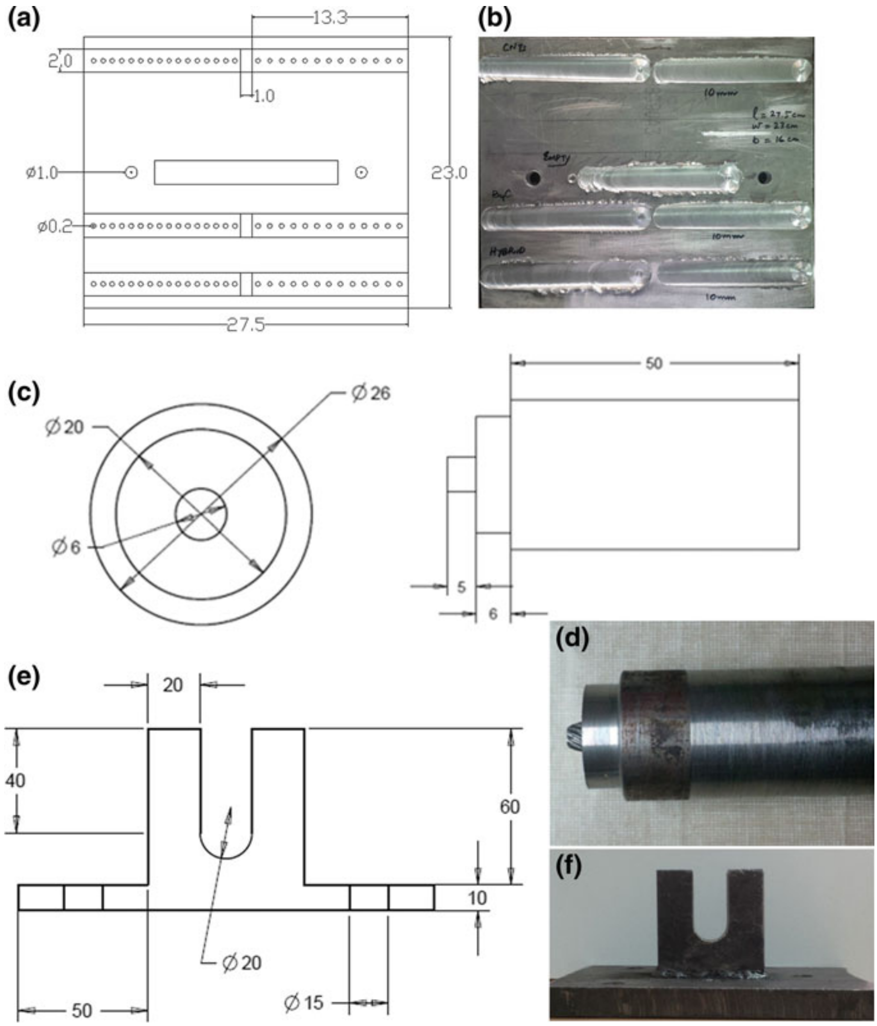

Fig. 2 Drawings and images of **a** Al5083 plate dimension, **b** Al5083 plate after FSP, **c** drawing H-13 tool, **d** image of FSP tool after machining [15], **e** customize bend-ductility die, and **f** Die after fabrication

equal weights of B_4C and MWCNTs were mixed at 100 rpm in ball mill for 30 min to prepare hybrid mixtures. In Fig. 3, schematics of FSP process and bend-ductility test is presented. Single pass FSP at rotational speed of 750 rpm, traverse speed of 16 mm/min, and tilt angle of 2 was selected for milling operation on LK5 N milling machine (Pakistan Machine Tool Factory).

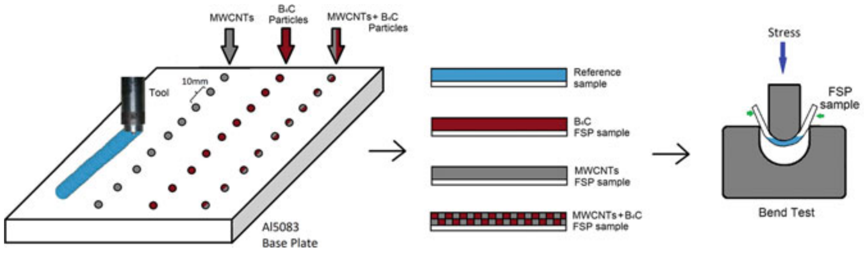

Fig. 3 Schematics of the FSP process showing reference and composite samples used for bend-ductility tests

Characterization

Radiography was performed on all FSP samples for detection of any major internal defects due to processing, using Andrex Smart X-ray machine (225 kV, 88527, Denmark). Macroscopic images were collected from stereoscope (3M05766, Olympus SZX7, Japan), and microstructure examinations was carried out using IMM 901 microscope (Metkon Instruments, Turkey). The metallographic study was carried out on mirror like surfaces after etching and polishing using a Keller's reagent (3 ml HCl, 2 ml HF, 5 ml HNO_3 and 150 ml distilled water). Scanning Electron Microscope (SEM) was also used to examine the fractured surfaces, using a MIRA-III (TESCAN, Czech Republic) in secondary electron imaging mode.

Hardness testing was carried out according to the standard ASTM E-384 on 550 g test load with 5 s dwell time, using Karl Frank microhardness tester. A hardness profile was made from the cross section of each FSP sample, and later used to record the variations from the FSP tool leading and trailing end. For tensile testing, sample were cut across the FSP area so as to allow for testing of FSP area specifically in the gauge length of the specimen. Four samples of each FSP combination were tested with a dimension of 25 mm in length, 2 mm in thickness, and 5 mm in width. Bend-ductility tests were performed using a custom made U-shaped die, see Fig. 2e, f, under guidelines of the ASTM E-190 standard. Convex surfaces of the bend FSP samples were examined; firstly with the naked eyes then using a stereoscope for fractured surfaces.

Results and Discussion

Radiography

Figure 4, shows radiographs of the FSP sample and composites. Excessive beads formed on sample surface, due to tool forward and rotating motion were removed with a tool to avoid perky ripples in radiographs of the FSP composites. The green

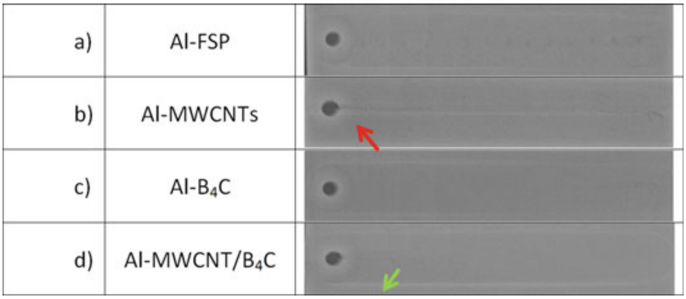

Fig. 4 Radiograph images of **a** Reference A15083 sample, **b** Al-MWCNTs composite sample, **c** the Al-B_4C composite sample and **d** the Al-MWCNT/B_4C composite sample

arrow in Fig. 4d shows an example of such a bright line at the edge of the FSP area. No defects in the radiography were detected in any other FSP samples, see Fig. 4a, c and d. A short dark line can however be seen in Fig. 4b representing the Al-MWCNTs FSP composite, see red arrow. It is a well-known fact that in radiography, loss of material can often be seen as a dark area/zone due to the lack of fusion in this specific area. Lack of fusion originates from microstructure under the influence of (1) type of reinforcement used and (2) distribution of reinforcement present in the matrix. No dark lines similar to the line seen in Fig. 4b was observed in the plain FSP, B_4C and hybrid FSP composites. Presence of MWCNTs in Al-MWCNTs FSP sample did, however, have an effect on the macrostructure. The lack of fusion can in other words be related to single pas FSP processing which is process parameter.

Microstructure

In Fig. 5, micrographs of the cross section of FSP samples are presented. As can be seen from the figure, three distinct areas/zones can be seen, i.e. the base metal (BM) zone where as received Al5083 rolled structure is present, the stir zone (SZ) zone which is in direct influence of the FSP tool and a Thermomechanically Affected Zone (TMAZ). Predominantly the affected areas/zones have the same dimensions as the tool pin, except for a fractional spread due to the rotation of conical threaded pin. No visible discontinuity can be observed in the bare reinforcement FSP samples, see Fig. 5a. The Al-MWCNTs composites showed, however, a distinct type of defect, see Fig. 5b that is believed to originate from stirring action of the tool and lack of compensation for the base metal to fill the drilled holes cavity filled with MWCNTs. The FSP composite with B_4C showed darker shades related to the distribution of microsized reinforcement, but no other defects, see Fig. 5c. The hybrid FSP composites, Al-MWCNT/B_4C, showed no defects, see Fig. 5d. It is believed that the ceramic B_4C reinforcement lowered the defect intensity by compensating the loss of material by effectively filling the empty volume of the drilled holes.

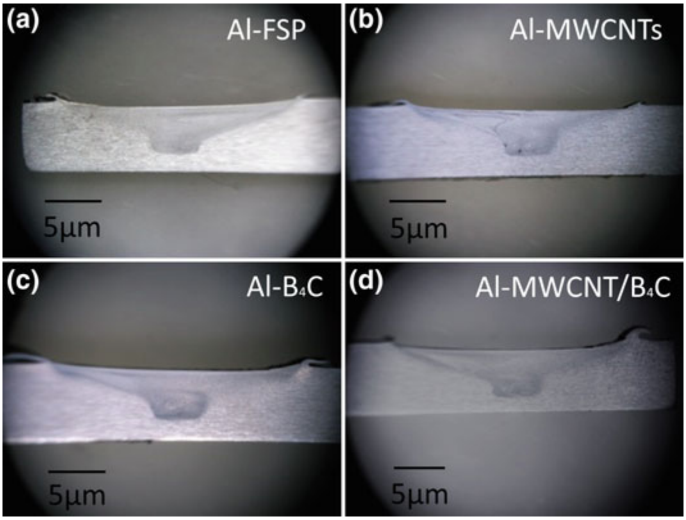

Fig. 5 Cross-sectional stereoscopic images of **a** reference Al5083 sample, **b** Al-MWCNTs composite sample, **c** the Al-B_4C composite sample, and **d** the Al-MWCNT/B_4C composite sample

FSP processing is usually characterized by using tool traversing zones. In Fig. 6 optical images of the reference FSP sample and composites are presented. The cross section views of the microstructures are identified by leading and trailing sides of SZ zone in all the FSP samples, see Fig. 6a. Grain size and morphological changes has been reported in an earlier study by McNelley et al. [16], confirming as rolled lamellar grains of the base plate Al5083 modified due to tool stirring action. As severe plastic deformation takes place the finer grains emerge, see Fig. 6b. This behavior is in good agreement with the findings of Lee et al. [17], who investigated the effect of MWCNTs on tensile properties of FSP composite. Presence of Heat- Affected Zone (HAZ) have also been reported in a study by Taban and Kaluc [18] where they proposed that HAZ usually exists between stirred, TMAZ regions and BM zones. In the present study grain coursing was not observed, and as a result nor was HAZ. In Fig. 6c the microstructure of Al-MWCNTs sample is presented. As can be seen from the figure, prominently dark lines of MWCNTs clusters exist, visible at TMAZ regions between BM and SZ zones. Compared to the Al-B_4C composite, see Fig. 6d, the appearance of the SZ and BM zones clearly differentiates from the FSP composite with MWCNTs. As low free volume was present in the micrometer size B_4C particle reinforced composites used to fill in the drill holes, thus better distribution of the reinforcement at single pass was observed as compared to nanoreinforcement, i.e. MWCNTs. The B_4C particles were found mainly trapped in the TMAZ region. The hybrid FSP composite Al-MWCNT/B_4C was observed to be dominated by the B_4C dispersion trend, see Fig. 6e. Lack of MWCNT-clustering in the TMAZ region is believed to be due to presence of B_4C particles in the TMAZ region with thinner

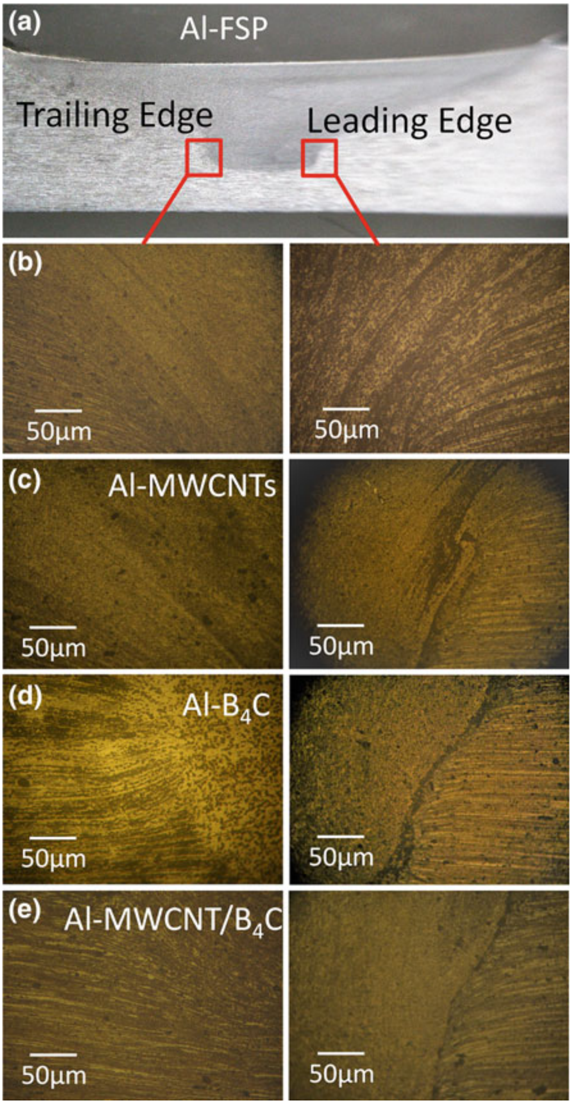

Fig. 6 Optical microstructures of FSP reference and composite sample's cross sections, showing tool's leading and trailing edges of FSP zones; **a** reference sample, **b** high magnification SZ and BZ zones, **c** Al-MWCNTs sample, **d** Al-B_4C sample, and **e** Al-MWCNT/B_4C sample [15]

lamellas as a result of the lower volume presence and in responds to the better stirring action at a single pass.

To perform a detailed optical examination of the FSP reference and composite samples the microstructural evolution at higher magnification was studied, see Fig. 7. In Fig. 7a clear transformation line of the grains orientation due to tool stirring can be seen in the Al-FSP sample, and the MWCNTs clustered in the TMAZ region in Fig. 7b. As can be seen from Fig. 7b, MWCNT's clustering takes place in lamellae region which exists between SZ zone and BM zone. The interface strengthening is

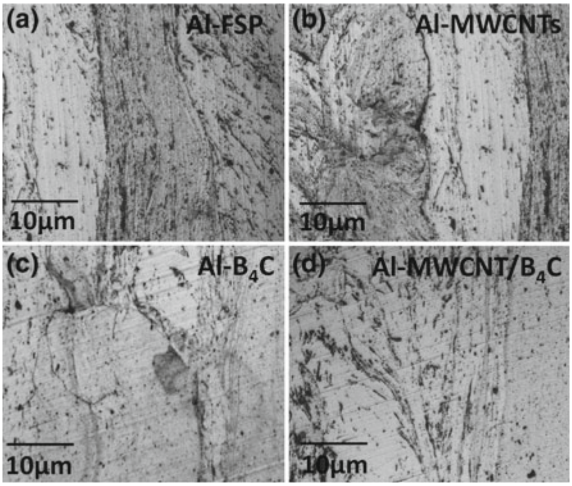

Fig. 7 Optical images of: **a** reference FSP sample, **b** Al-MWCNTs sample, **c** Al-B$_4$C sample, and **d** Al-MWCNT/B$_4$C sample

caused by the presence of MWCNTs which are restricted by their diffusion in the BM zone. The microstructure of the Al-B$_4$C composite is characterized by entrapped B$_4$C particles at the interface of the TMAZ region and BM zone, see the blue arrows in Fig. 7c. The hybrid FSP composite Al-MWCNT/B$_4$C and MWCNTs proved to have lower concentration of both reinforcements as compared to the individually reinforced FSP composites. As a result, a lower tendency on clustering, as well as entrapment of B$_4$C particles, was observed, see the red and blue arrows in Fig. 7d.

Hardness Profile

In Fig. 8a the cross sectional harness profile of FSP samples is presented, and in Table 2 the combined mechanical properties of the FSP samples summarized. Moving across from the BM zone to the SZ zone passing through the TMAZ region, noticeable variations in hardness is recorded. Maximum hardness was achieved for Al-B$_4$C composite, i.e. 107 ± 2 HV. Reference FSP sample and Al-MWCNTs composite exhibited minimum values, respectively 91 ± 1 HV and 93 ± 2 HV. However, the hybrid Al-MWCNT/B$_4$C composite revealed an intermediate value of 100 ± 1 HV. Within the FSP sample there is also variations of hardness along the cross sectional zones, which confirms earlier findings by Mahmood et al. [19]. The distinct feature of FSP resulting in grain refinement is obviously the cause of the increase in hardness. It is a well- known fact, that grain refinement originates from tool stirring, causing severe plastic deformation. Grain size reduction is best explained by Hall-Petch equation as referred by Hansen [20]:

$$H_c = H_o + K \cdot D^{-1/2} \tag{1}$$

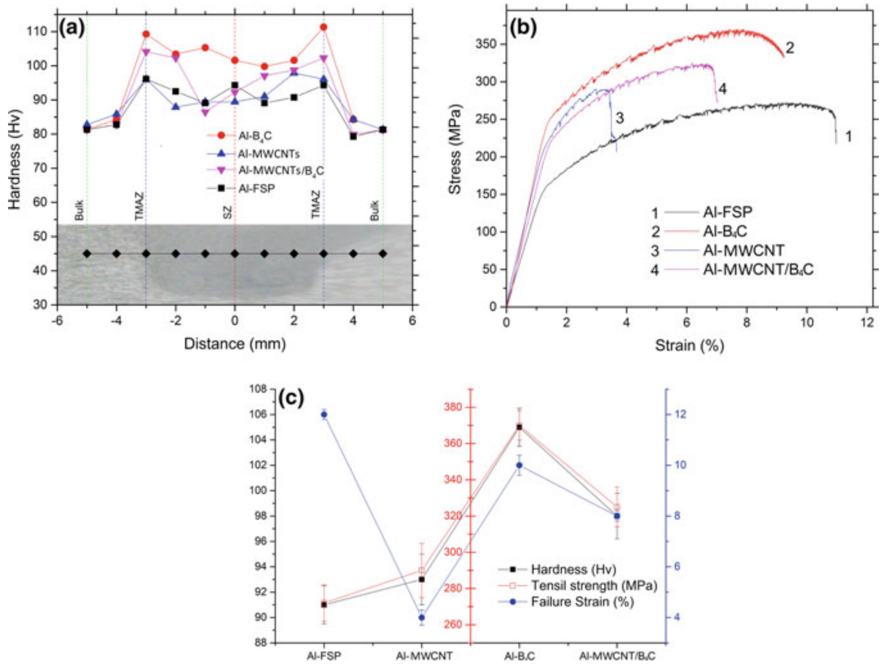

Fig. 8 **a** Hardness profile across the FSP cross section in all the samples [15], **b** tensile testing curves of the FSP samples [15], and **c** graph showing mechanical testing data of FSP samples

Table 2 Designations of FSP composites with hardness, and tensile properties

S. no.	Name	Description	Hardness HV	Ultimate tensile strength MPa	Strain (%)
1	Al-FSP	Al5083 FSP reference sample	91 ± 1	272 ± 10	11
3	Al-MWCNTs	Al5083 + MWCNTs FSP composite	93 ± 2	290 ± 15	3.7
5	Al-B_4C	Al5083 + B_4C FSP composite	107 ± 2	370 ± 8	9.2
7	Al-MWCNT/B_4C	Al5083 + MWCNTs/B_4C FSP composite	100 ± 1	325 ± 11	7

where; H_c is the hardness of material, grain diameter D. H_o is hardness of the base metal, and K a constant.

The BM zone generally presents the rolled condition as a result of the preliminary grain structure, unless treated otherwise. In contrast to any as received condition of the BM zone, it usually has minimum values of hardness. In present study the interface between SZ zone and BM zone showed highest hardness values. Dislocations pinning and presence of entrapped reinforcements can be attributed as the principle strengthening mechanism. In other words, the severe plastic deformation caused by the tool rotation interlocked the dislocations and they got piled up at the interface restricting further movement, which in turn caused the hardness to increase. TMAZ region exhibited maximum hardness value all FSP samples.

As per results of the microhardness profiling (see Fig. 8a and Table 2), the Al-B_4C composite showed the greatest increase in hardness (~18%). An increase in hardness can be related to the FSP processing and/or the presence of second phase particles. In the case of the Al-MWCNTs composite, an increase in hardness was observed at the interface of the FSP zone confirming the earlier findings of Hosseini et al. [21] and Lim et al. [11]. Even in this case the pinning effect of the dislocation movement is believed to be the reason for the observed increase in hardness. However, the clustering of the MWCNTs composite caused a decrease in hardness in the SZ zone compared to at the interface. The hybrid composite Al-MWCNT/B_4C proved to have the greatest variance in the hardness values, which can be seen in Fig. 8a. Localized synergic effect of dual reinforcement and thermal mismatch of the MWCNTs with B_4C particles is believed to be a possible reason for this severe variance of the hardness in the SZ zone.

Tensile Properties

In Fig. 8b, tensile stress-strain graphs of the different samples is presented, while their tensile properties are plotted in Fig. 8c and summarized in Table 2. As can be seen from the figures and the table, the reference Al-FSP sample shows the ultimate tensile strength of 271 ± 9 MPa with maximum fracture strain of ~ 11%. It can also be seen that the incorporation of MWCNTs did not significantly enhance the tensile strength value, which was 290 ± 15 MPa but they decreased fracture strain to ~4%. The addition of B_4C particles in the alloy matrix did also result in a significant increase in the tensile strength to 370 ± 10 MPa but with the fracture strain reduced to ~9%. By combining equal amounts of both reinforcements the ultimate tensile strength increased to an appreciable value of 325 ± 11 MPa and a failure strain of ~7%. This value is, however, lower than the value obtained for the FSP composite reinforced only with B_4C particles, and higher than the value obtained when reinforced only with MWCNTs. It has been reported in literature that incorporation of either MWCNTs or B_4C particles to the matrix has shown enhanced tensile strength and comparatively reduced fracture strain. Liu et al. [22] described in their study that strength of material increases with decrease in grain size during dynamic recrystallization. In other words, entrapment of reinforcements at the interface to restrict heat dissipation and elimination of HAZ has also contributed to strengthening the matrix. In a study by Shahraki et al. [23], they discoursed the presence of dislocations due to reinforcements result in pinning and grain size they also concluded that presence of hard particles and grain refinement augments the mechanical behavior of the FSP composite. Another investigation by Guo et al. [24] advocated that Orowan effect is prime reason, responsible for enhanced mechanical properties in FSP composites. However, the clustering of MWCNTs was reported to have deleterious effects on the failure strain at single pass FSP. Du et al. [25] reported that MWCNTs may break down into smaller lengths and disperse into the aluminum matrix inhibiting the dislocation movement, and resulted in a slight increase in strength at cost of the fracture strain, see Fig. 8b.

Base on present results it is believed that the difference in thermal expansion coefficient values of MWCNTs (1.0×10^{-6} K^{-1}), B_4C (5.7×10^{-6} K^{-1}) and the matrix, i.e. aluminum: 23.6×10^{-6} K^{-1}, may have produced residual stresses in the final material around the reinforcements, which may have generated dislocations [26]. Dislocation density in matrix depends on the surface area of reinforcement. Thus presence of MWCNTs is expected to produce higher dislocation density which results in increase of strength of final material. The single pass FSP was, however, proven not to be effective in dispersion of nanoreinforcement as compared to the mircosized B_4C particles. As a result, the FSP composite with B_4C particles have shown greater strength than the composites with MWCNTs, which is in agreement with the results reported by Liu et al. [27]. The premature failure of the FSP composites with MWCNTs can also be related to the clustering of nanoreinforcements. This reduces the effective surface area of MWCNTs and increases the porosity in FSP area.

Fractography

The fractographs of all the FSP samples after tensile test are shown in Fig. 9. Typical ductile fractures corresponding to aluminum and its alloys can be seen for the Al-FSP samples, see Fig. 9a. The inset in the figure presents the higher magnification area for better illustration of the Al-MWCNTs composite. As can be seen from the figure, the Al-MWCNTs composite was observed with cleavage failure dominated by clusters of MWCNTs. These clusters deleteriously damaged the mechanical properties of the final material by presenting lack of fusion defects, as discussed in the radiography section, as shown in Fig. 4b. In the high magnification inset of Fig. 9b, vertically aligned MWCNTs are seen from the region marked by red. The bridging effect, earlier reported by Deng et al. [28], is believed to be related to the slight increase observed in the ultimate tensile strength of the FSP composite, as well as the premature failure headed by the MWCNTs clustering. The clustering in the Al5083 matrix enables the metal to slide over to fail the composite at low strain values. The single pass FSP stirring action is also believed to be a possible reason for insufficient distribution

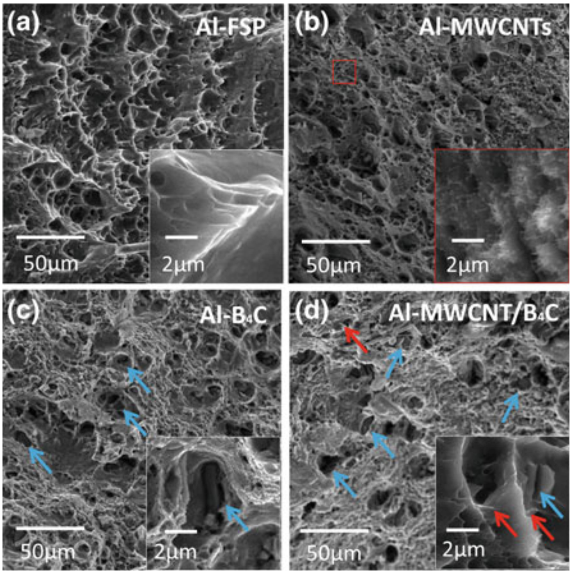

Fig. 9 SEM fractographs of FSP specimens after tensile test: **a** reference FSP sample, **b** Al-MWCNTs, **c** Al-B_4C and **d** M-MWCNT/B_4C

of MWCNTs in the Al5083 matrix. The FSP composite incorporating B_4C particles showed, however, uniform distribution of reinforcement and the fracture surface showed micro-cracks initiated by the ceramic reinforcement/matrix interface, see the blue arrow in Fig. 9c. The B_4C particles are seen surrounded with matrix alloy dimples, which is visualized as deep wells, due to the peening effect. Uniform distribution of B4C is believed to be the main reason for obtaining the highest strength in the FSP composites tested. The hybrid FSP composite with MWCNTs and B_4C particles, showed MWCNTs bridging at the crack tips, as shown with red arrow in Fig. 9c, and at wells of ceramic B_4C. The intermediate mechanical properties of the FSP hybrid composite indicated the dominance of micro sized ceramic reinforcement in comparison to the poor distribution of the nano-scale MWCNTs single pass FSPs. It should in this context be mentioned that synergic behavior was not prominent at the presently selected processing parameters.

Bend-Ductility Test

The Al-FSP reference sample presented in Fig. 10a proved to have the maximum fracture strain of all the materials tested (see Table 2). The same was found in regards to the bend ductility test, which revealed the maximum cold formability. The curved surface of reference FSP specimen showed no evidence of any cracking by the naked eye nor under microscopic examination on either sides of the sample, as shown in Fig. 10b, c. The bend-ductility samples with MWCNTs, see Fig. 10d, was possible

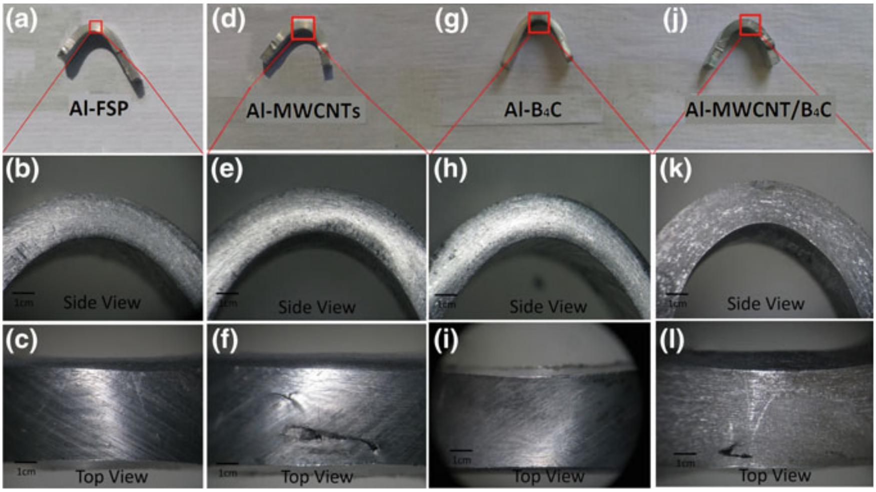

Fig. 10 Images of the side and top view of the bend-ductility samples; **a–c** reference Al-FSP samples **d–f** Al-MWCNTs samples, **g–i** Al-B_4C samples, and **k–i** hybrid Al-MWCNT/B_4C composite samples [15]

to bend up to full limits of the die, but distinct cracks were obtained alongside the SZ zone starting from the TMAZ region resulting in a cracked surface, see Fig. 10f. No visible evidences of any cracks appeared on either sides and convex surface of the B_4C containing FSP sample, see Fig. 10d–f, nor on the side of the hybrid FSP composite specimen, as shown in Fig. 10j, k. However, a ~12 mm crack surface appeared was observed on top view of the hybrid FSP composite specimen, as shown in Fig. 10i.

The overall results of the bend-ductility tests showed that the cold formability of the FSP samples corresponded to the cracking regardless of the mechanical strength. Among the four FSP samples tested in the present study only the Al-MWCNTs composite and the hybrid composite showed cracking in the bend area curvature under tensile stresses. The maximum recorded fracture strain of the FSP reference sample can be related to the maximum formability exhibited during the bend-ductility tests. Similarly, no cracking appeared on the surfaces of FSP composite with B_4C particles, and its failure strain was recorded as the second highest to reference the FSP sample. It is believed that the FSP composite with MWCNTs could not survive bend test and failed due to: (a) clustering of the MWCNTs near the TMAZ region, (b) poor mechanical bonding with the alloy matrix, and (c) retention of voids/porosity generated due to drilled holes for incorporating the MWCNTs in the base plate. The second FSP composite to fail in bend test was hybrid Al-MWCNT/B_4C composite, where cracks appeared on convex side of the sample, as shown in Fig. 10l. Unlike the fracture in the MWCNTs FSP composite, the length of crack was ~1/5th in the case of the hybrid composite. The behavior of the MWCNTs to cluster at single pass FSP seems to dominate the cold formability in the alloy matrix. However, the B_4C

particles restricted the crack propagation as a result of second phase strengthening which is evident from the fracture strain values obtained (~7%).

Conclusions

FSP is among emerging versatile surface modification techniques to yield promising properties in aluminum matrix composites. In the present study cold formability was determined for FSP composites with reference, individually and hybrid reinforcements, and microstructure evolution was studied using optical and SEM. Increase in average hardness was recorded for all the FSP composites with a maximum of ~18% for B_4C reinforced composite samples. Tensile test was carried out to determine effects of processing on mechanical properties of the FSP reference and composite samples. An improvement in ultimate tensile strength of ~36% at the cost of ~3% failure strain was recorded for the B_4C reinforced FSP composite samples. In the case of the Al-MWCNTs composite clusters was identified due to an uneven distribution in the alloy matrix resulting in inferior mechanical properties. Composite containing MWCNTs showed minimum fracture strain (3.7%) while its hardness and tensile strength values were comparable to the reference FSP sample. Additionally, it failed in bend test as cracks appeared on curved surface. Hybrid Al-MWCNT/B_4C samples showed comparatively higher tensile strength, hardness and fracture strain than MWCNTs composite samples. Poor MWCNTs distribution and weak interfacial MWCNT/Al bonding are concluded to be the possible reasons. Multiple-pass friction stir processing can be employed to enhance MWCNTs distribution. Based on the bend-ductility test of the Al5083 single pass FSP composites, an approximate threshold of ~8% failure strain in the tensile test can be proposed for cold formability without cracking.

Acknowledgements The authors acknowledge the financial support from the Higher Education Commission of Pakistan (Grant No. 213-53249-2EG2-102) provided under the Ph.D. indigenous fellowship; Phase-II Batch-II and Norwegian University of Science and Technology (NTNU), Norway for use of their laboratory facilities for characterization of all material properties.

References

1. Mishra RS, Ma ZY (2005) Materials science and engineering: R. Reports 2005, vol 50, pp 1–78
2. Nascimento F, Santos T, Vilaga P, Miranda RM, Quintino L (2009) Mater Sci Eng A 506:16–22
3. Khan M, Rehman A, Aziz T, Naveed K, Ahmad I, Subhani T (2017) Mater Sci Eng A 696:552–557
4. Guru PR, Khan Md F, Panigrahi SK, Janaki Ram GD (2015) J Manufact Process 18:67–74
5. Maurya R, Kumar B, Ariharan S, Ramkumar J, Kantesh B (2016) Mater Design 98:155–166
6. Joyson Abraham S, Chandra Rao Madane S, Dinaharan I, John Baruch L (2016) J Asian Ceramic Soc 4:381–389

7. Wang W, Shi Q-Y, Liu P, Li HK, Li T (2009) J Mater Process Technol 209:2099–2103
8. Azizieh M, Kokabi AH, Abachi P (2011) Mater Des 32:2034–2041
9. Srinivasu R, Sambasiva Rao A, Madhusudhan Reddy G, Srinivasa Rao K (2014) Defence Technol
10. Hosseini SA, Ranjbar K, Dehmolaei R, Amirani AR (2015) J Alloys Comp 622:725–733
11. Lim DK, Shibayanagi T, Gerlich AP (2009) Mater Sci Eng, A 507:194–199
12. Jeon CH, Jeong YH, Seo JJ, Tien HN, Hong ST, Yum YJ, Hur SH, Lee KJ (2014) Int J Precision Eng Manufact 15:1235–1239
13. Suri AK, Subramanian C, Sonber JK, Ch Murthy TSR (2010) Int Mater Rev 55:4–40
14. Salvetat J-P, Bonard J-M, Thomson NH, Kulik AJ, Forro L, Benoit W, Zuppiroli L (1999) Appl Phys A 69:255–260
15. Khan M, Rehman A, Aziz T, Shahzad M, Naveed K, Subhani T (2018) J Mater Process Technol 253:72–85
16. McNelley TR (2010) Revista de metalurgia 46:149–156
17. Lee IS, Hsu CJ, Chen CF, Ho NJ, Kao PW (2011) Composites Sci Technol 71:693–698
18. Taban E, Kaluc E (2007) Kovove Mater 45:241
19. Mahmoud ERI, Ikeuchi K, Takahashi M (2008) Sci Technol Weld Joining 13:607–618
20. Hansen N (2004) Scripta Mater 51:801–806
21. Hosseini SA, Ranjbar K, Dehmolaei R, Amirani AR (2015) J Alloys Compounds 622:725–733
22. Liu Q, Ke L, Liu F, Huang C, Xing L (2013) Mater Des 45:343–348
23. Shahraki S, Khorasani S, Behnagh RA, Fotouhi Y, Bisadi H (2013) Metallurg Mater Trans B 44:1546–1553
24. Guo JF, Liu J, Sun CN, Maleksaeedi S, Bi G, Tan MJ, Wei J (2014) Mater Sci Eng A 602:143–149
25. Du Z, Tan MJ, Guo JF, Bi G, Wei J (2016) Mater Sci Eng A 667:125–131
26. George R, Kashyap KT, Rahul R, Yamdagni S (2005) Scripta Mater 53:1159–1163
27. Liu ZY, Xiao BL, Wang WG, Ma ZY (2014) Carbon 69:264–274
28. Deng C, Zhang X, Wang D, Lin Q, Li A (2007) Mater Lett 61:1725–1728

Production of AlSi12CuNiMg/Al_2O_3 Micro/Nanodispersed Surface Composites Using Friction Stir Processing for Automotive Applications

L. Tonelli, M. Refat, S. Toschi, M. M. Z. Ahmed, Essam Ahmed, A. Morri, I. El-Mahallawi and L. Ceschini

Abstract The service life of automotive components often depends on their surface properties. Consequently, improved surface properties with the retainment of bulk characteristics are necessary for such components to guarantee enhanced mechanical and tribological properties. In this research, friction stir processing (FSP) is used to produce surface composites characterized by extruded AlSi12CuNiMg matrix and micro and nano-sized Al_2O_3 particles as reinforcing phase. Multiple passes of FSP using two different strategies were applied to distribute the Al_2O_3 particles. The effect of the different FSP parameters and sequence of rotation direction for the applied passes was investigated. The processed surface layers were analyzed through optical and scanning electron microscopy, hardness, and wear testing. The properties of the processed composite surface showed to be affected by both the size of reinforcing particles and the processing direction sequence. A comparison between properties of the produced surface composites and the base metal was also carried out. Bench-type test developed to measure the weight loss of samples under sand erosion conditions.

L. Tonelli · S. Toschi · A. Morri
Department of Industrial Engineering, University of Bologna, Bologna, Italy

M. Refat (✉)
Centre for Simulation Innovation and Advanced Manufacturing, The British University in Egypt, El-Shorouk 11837, Egypt
e-mail: mohamedrefatramadan@hotmail.com

M. M. Z. Ahmed
Mechanical Engineering Department, The British University in Egypt, El-Shorouk 11837, Egypt

M. M. Z. Ahmed · E. Ahmed
Metallurgical and Materials Engineering Department, Suez University, Suez 43111, Egypt

I. El-Mahallawi
Metallurgy and Materials Engineering Department, Cairo University, Giza 12316, Egypt

L. Ceschini
Department of Civil, Chemical, Environmental and Materials Engineering, University of Bologna, Bologna, Italy

Y. Hovanski et al. (eds.), *Friction Stir Welding and Processing X*, The Minerals, Metals & Materials Series, https://doi.org/10.1007/978-3-030-05752-7_22

Keywords Friction Stir Processing (FSP)
Surface Metal Matrix Composite (SMMC) · Microstructure · Hardness
Tribological properties · AlSi12CuNiMg

Introduction

The expanding demands to reduce the weight of vehicles with more fuel efficiency have been provoked by increased oil prices and concerns about global warming as well as reduction of fossil fuels usage. To cope with these claims, several studies have been applied to develop new powertrains (e.g., hybrid system), and improve traditional engine efficiency, using lighter weighting in automotive industries [1]. Aluminum alloys have widely replaced steel parts in the automotive structures owing to their high specific strength, corrosion resistance, fatigue strength, modulus, and thermal shock, which can lead to more than 50% weight saving compared to other competing ferrous materials maintaining the safety in most applications [2, 3]. Lately, aluminum usage in automotive industries has been increased by 80%. The average car today is predicted to weigh 250–340 kg of aluminum, which was 1100 kg in the 1990s [1, 4]. Silicon is considered as the major element with content between 5 and 17 wt% in most of the common aluminum foundry alloys. This is due to their excellent corrosion resistance, castability, and high thermal conductivity [2, 5, 6]. In addition, it can be recycled after the end of the use.

Al–Si–Cu–Mg alloys are extensively used in the automotive industry due to their superior mechanical properties following the application of appropriate heat treatments. However, the use of these alloys shows some limitations when exposed to extreme environmental conditions. This is attributed to the coarsening of the Si phase, which results in detrimental consequences on the mechanical properties [2, 7, 8]. By increasing the temperature, the strength of the aluminum–silicon alloys is deteriorated as the resistance to dislocation movement is reduced. Also, when the temperature rises, the thermal vibrations cause dislocation slip and dislocation climb as well as diffusion of vacancies [2, 9]. Improving the high-temperature strength and wear resistance of these alloys via precipitation and dispersion of micro/nanoparticles is a challenging task for researchers. Recent investigations have included the addition of transition elements, which form thermally stable phases, that result in enhanced mechanical properties at elevated temperatures [2, 3, 10–12]. However, the addition of transition elements faces some challenges in manufacturing and consistency of resulting ductility properties.

On the other side, the application of friction stirs processing (FSP) as a surface treatment technique has gained the interest of researchers [13–17] as it results enhanced strength without harming toughness or ductility [18]. The new surface metal matrix composites (SMMCs) illustrated microstructure refinement, densification, and outstanding bonding with the substrates conferring hard surface with superior mechanical and physicochemical properties [14, 18–20]. This is attributed to severe thermal exposure, plastic deformation, and material mixing that occurs in the processed zone during FSP [13]. One of the most recent approaches to produce surface composites is adding ceramic particles to the metallic plates [13]. The beneficial effect of developing FSPed surfaces have been illustrated in literature widely [13, 17, 21, 22], however, the avoidance of particles agglomeration and their transfer to deeper and wider regions in the new SMMC still remains a challenge.

In view of the above, this study aims to assess the feasibility to produce Al–Si-based surface composite for piston applications by applying FSP technique, using two different strategies to integrate the reinforcing particles. In particular, surface composites were produced employing AlSi12CuNiMg alloy as substrate and Al_2O_3 micro and nanoparticles as reinforcing phase. Aiming to evaluate the effectiveness of Al_2O_3 particles to enhance the mechanical and tribological behavior of the alloy, the processed surface layers were analyzed through optical and scanning electron microscopy, hardness and wear testing. A comparison between different distribution strategies, as well as between composite and base metal, was also carried out.

Experimental

AlSi12CuNiMg extruded billets and Al_2O_3 micro (~60 μm) and nanoparticles (~40 nm) were used in the current study as the metal matrix and reinforcing phases, respectively. The chemical composition of AlSi12CuNiMg alloy, characterized by a hardness of 85 HV1, was estimated using GDOES (Glow-Discharge Optical Emission Spectroscopy), reported in Table 1.

Two different strategies were adopted to insert the reinforcing phase in the matrix: (i) a single central groove (2 mm width and 3 mm depth), (ii) small holes (2 mm diameter and 3 mm depth) machined on the surface along the whole length of the workpieces, as shown in Fig. 1. Al_2O_3 particles were packed into the groove or holes that were subsequently top closed using a probeless tool of 19 mm shoulder diameter;

Table 1 Chemical composition (wt%) of the AlSi12CuMg alloy, measured by GDOES

Al	Si	Cu	Ni	Mg	Fe	Mn	Zn	Ti	Pb	Sn
Balance	11.576	2.850	1.391	0.971	0.186	0.154	0.072	0.063	0.015	0.001

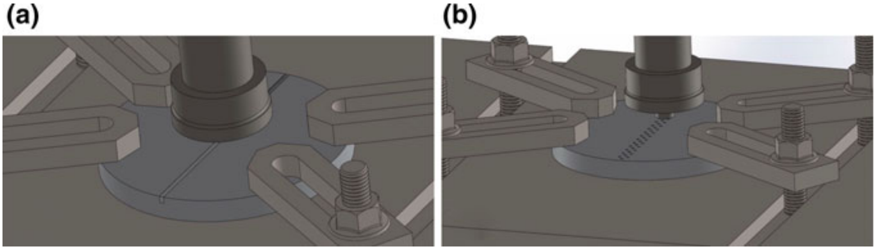

Fig. 1 Representation of FSP process: **a** groove strategy and **b** holes strategy

Table 2 Setting and parameters of FSP process

Sample	Al_2O_3	Strategy	Tool rotation (rpm)	Number of passes
G1	Micro	Groove	400	4
G2	Nano	Groove	400	4
H1	Nano	Holes	600	4
H2	Nano	Holes	600	2
H3	Nano	Holes	400	2

the FSP process was then carried out using a tool made of H13 steel with dimensions of 6.2 mm probe diameter, 5.3 mm probe length, and 19 mm shoulder diameter.

The workpieces were processed by different rotation rates, namely 400 and 600 rpm, with constant travel speed (50 mm/min) and a tool tilt angle of 3°. Process parameters, size of particles and the strategy adopted are summarized in Table 2.

FSPed samples were prepared following standard procedures for metallographic preparation, up to polishing with a 0.05 alumina suspension. Polished surfaces were chemically etched using diluted Keller's reagent (100 ml distilled water, 10 ml HNO_3, 10 ml HCL and 2 ml HF) for 15 s. The metallographic samples were characterized by optical (OM) and Scanning Electron Microscopy with Energy Dispersive X-ray Spectroscopy (SEM-EDS) for microstructural evaluation. Hardness investigation, dry sliding and erosion wear tests were also performed. Vickers hardness was measured across the transverse cross section of FSPed materials near the top surface of the nugget (NG) (at 0.2, 2.2, 4.2, 6.2 mm depth), using load of 1 Kg for 15 s dwell time. Samples extracted from the base material were subjected to the same microstructural and mechanical characterization, in order to compare FSP samples with the base material.

Results and Discussion

Base Material

A representative SEM micrograph of the AlSi12CuNiMg base material is reported in Fig. 2 along with the SEM-EDS spectra carried out on the intermetallic particles. It can be noticed that as a result of the extrusion process, all the intermetallic particles are oriented along the direction of the plastic deformation. According to the literature [23, 24], three major groups of intermetallic phases can be found in this alloy: Fe-based particles (β-Al_5FeSi and α-$Al_{15}(Mn,Fe)_3Si_2$), Cu-based intermetallics (Al_2Cu and AlSiCuMg) and phases containing Ni (Al(NiCuFe)Si and Al(CuNi)Si). In this work, Fe-based (lighter in Fig. 2) and Cu-based (darker) intermetallics were found on the base material.

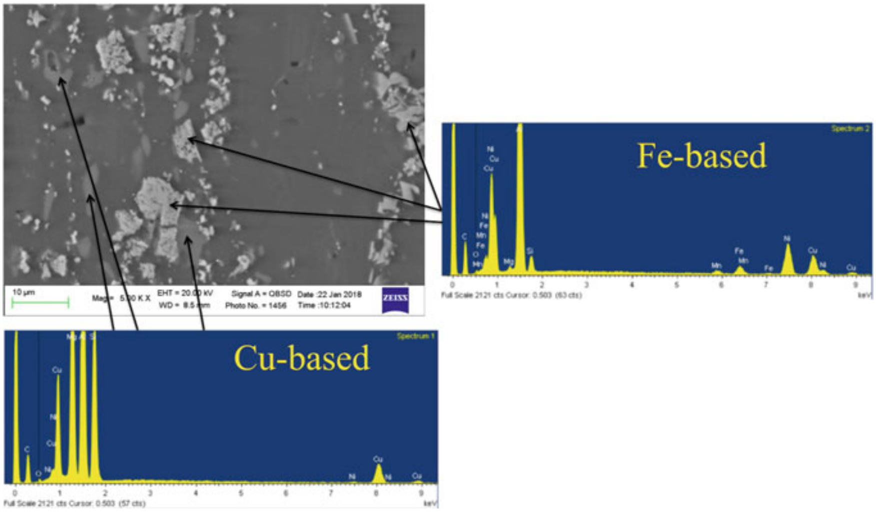

Fig. 2 SEM-EDS analyses of the unprocessed base material: representative micrograph and EDS spectra performed on intermetallic particles

FSP with Grooves' Strategy

The macroscopic investigation of the cross-section of FSP samples produced with the groove strategy (sample 1 and 2) reported in Fig. 3. It can be observed that the FSP zone clearly recognized by its typical concave shape. This strategy led to the formation of tunnel defects in both samples, as highlighted by white circles in Fig. 3. SEM-EDS investigation carried out on the FSP region revealed refining of the microstructure for both samples, leading to partial dissolution and combination and homogenous distribution of the particles in the matrix, as reported in Fig. 4.

Vickers hardness profiles carried out on samples 1 and 2 are reported in Fig. 5. The refinement of the microstructure resulting from the dynamic recrystallization occurring during FSP, along with the presence of hard Al_2O_3 reinforcing particles, resulted an increase in the hardness values for the FSP zone, with respect to the base material (85 HV1), up to 4.2 mm depth. As for samples reinforced with the micro-Al_2O_3 the increase is evenly distributed along the processed area, reaching a maximum of 100 HV1 in the outer layer. In the sample reinforced with nanoparticles, the hardness enhancement is located in the center of the FSP region, where a maximum value of approximately 120 HV1 was registered. In view of this, hardness enhancement in comparison to the surface composite reinforced by microparticles, samples produced with the holes strategy were reinforced only by Al_2O_3 nanoparticles.

The sliding wear test results (Fig. 6) illustrate the increase of the Coefficient of Friction (COF) for reinforced samples. Such an increase can be described to the presence of hard reinforcing ceramic particles that raise the abrasive component of the COF. Wear resistance of FSP samples is higher than the base material, as

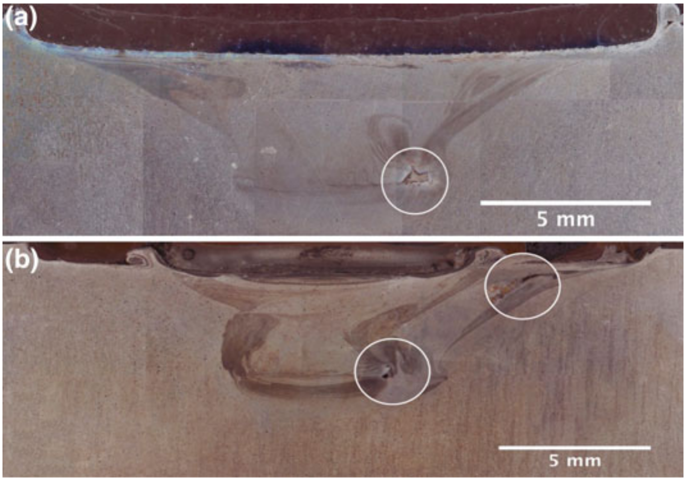

Fig. 3 Optical macrographs of the transverse cross-sections of the FSP with grooves of: **a** sample G1, **b** sample G2; white circles highlight tunnel defects

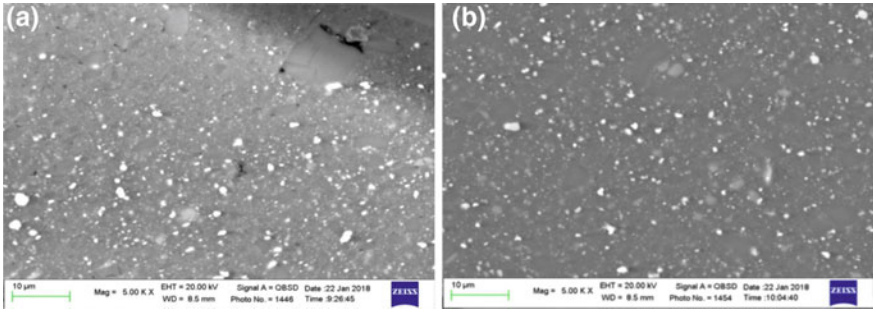

Fig. 4 SEM micrographs of the FSP zones: **a** sample 1, **b** sample 2

a consequence of higher hardness and Al_2O_3 acting as load-bearing phases. By comparing the results of FSP samples, the one reinforced with nano Al_2O_3 exhibited a slightly higher wear resistance than the microparticles reinforced one.

FSP with Holes' Strategy

Figure 7 shows the optical macrographs of the transverse cross-section of the samples H1 and H2 processed using holes' strategy. It can be observed that the processed zone is completely free of any type of defects with no signs of powder clustering either after four passes in (H1) or two passes in (H2). This suggests that the use of holes

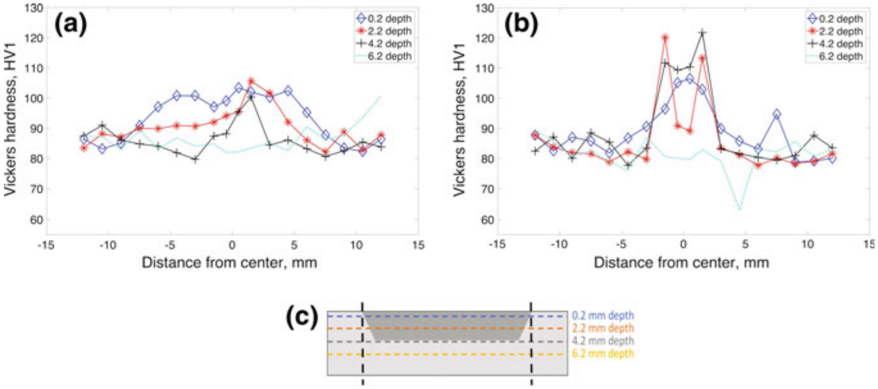

Fig. 5 Hardness profiles (HV1) carried out on samples cross-sections at incremental depths: **a** sample 1, **b** sample 2, **c** schematic representation of the regions investigated

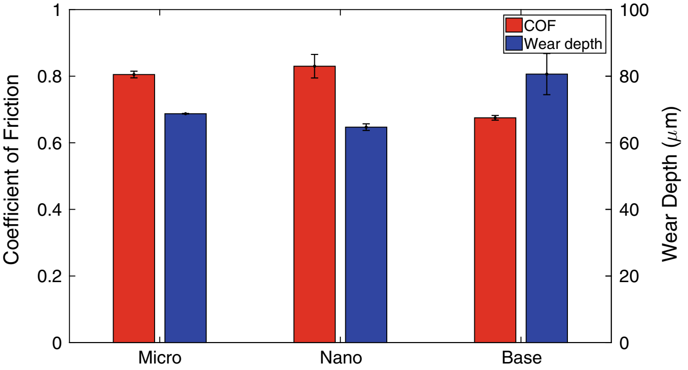

Fig. 6 Dry sliding wear test results: COF and wear depths of samples

instead of grooves can eliminate the tunnel-type defects and enhance the powder distribution as a result of the pre-distribution through the holes.

Figure 8 shows the optical microstructure of the FSP with holes' strategy (a) at the interface between the FSP zone and base material and (b) inside the FSP zone. Significant grain size reduction can be observed in addition to the typical features of onion rings inside the FSP zone. No clustering the powder can be observed also at this level. Figure 9 shows the wear results obtained by a bench-type test developed to measure the weight loss of samples under sand erosion conditions at an 20° angle.

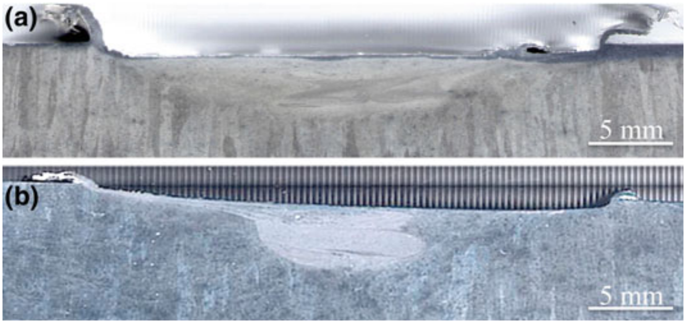

Fig. 7 Optical macrographs of the transverse cross-sections of the FSP with holes strategy of the FSPwith holes strategy of: **a** sample H1, and **b** sample H2

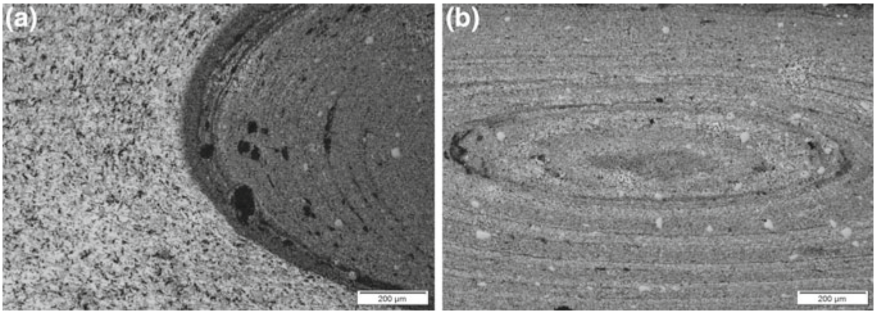

Fig. 8 Optical Microstructure of the FSP with holes' strategy **a** at the interface between the FSP zone and base material and **b** inside the FSP zone

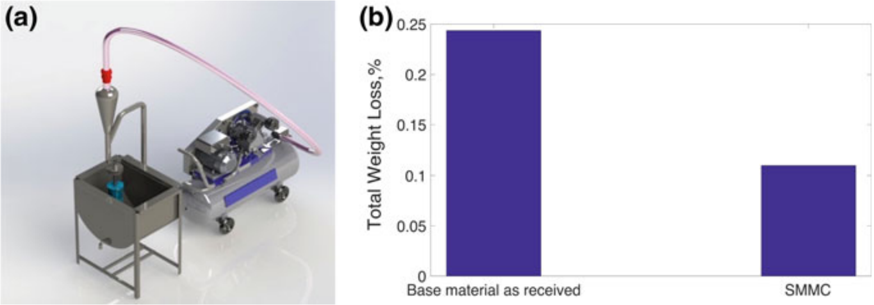

Fig. 9 Erosion wear test results: **a** schematic of rig and **b** weight loss% of samples

Comparison of Groove and Holes Strategy

Figure 10 shows the comparison of microhardness (HV1) profiles performed across cross-sections in correspondence of the outer reinforced layer (0.2 mm depth), for all FSP samples reinforced with nano Al_2O_3. It is clear that holes strategy; performed

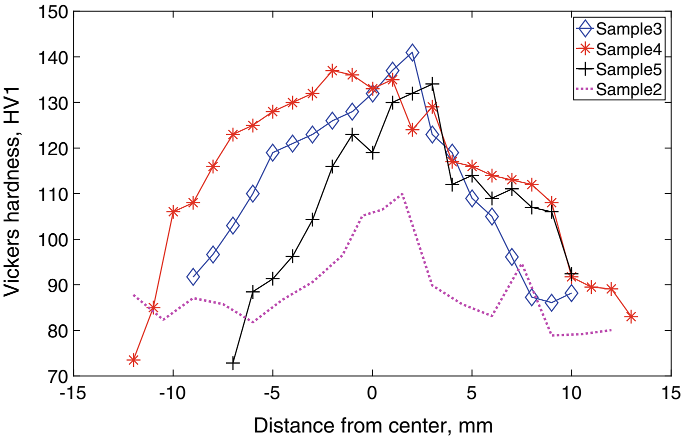

Fig. 10 Hardness profiles (HV1) carried out on samples cross-sections in the outer layer of FSP samples reinforced with nano Al_2O_3 adopting groove (sample 2) and holes strategy (samples 3, 4, 5)

with different process parameters, lead to higher hardness (up to 140 HV1). In addition, hardness enhancement is evenly distributed across the whole processed area. Moreover, by comparing samples 2 and 5, it is interesting to observe that at equal reinforcing particle size and tool rotation speed (400 rpm), the holes strategy allows to obtain higher and homogeneous hardness values with a lower number of passes.

Conclusions

1. The addition of micro-Al_2O_3 results in an even distribution of hardness along the processed area, reaching a maximum of 100 HV1 in the outer layer. While, the addition of nano-sized particles results in hardness enhancement located in the center of the FSP region, where a maximum value of approximately 120 HV1 was obtained.
2. Wear resistance of the surfaces after FSP using reinforcing particles is higher than base material for both dry sliding and sand erosion tests. However, the COF increases after FSP.
3. The addition of the reinforcing particles through holes strategy allows to obtain higher and homogeneous hardness values with a lower number of passes, compared to the addition through one central groove.

Acknowledgements The Italian Ministry of Foreign Affairs and International Cooperation (MAECI), and The Egyptian Science and Technology Development Fund (STDF) are deeply acknowledged for funding this work under the Executive Programme of Scientific and Technological Cooperation Between Arab Republic of Egypt and Italian Republic.

References

1. Miller W et al (2000) Recent development in aluminium alloys for the automotive industry. Mater Sci Eng A 280(1):37–49
2. Bogdanoff T (2017) Development of aluminium-silicon alloys with improved properties at elevated temperature
3. Rakhmonov J, Timelli G, Bonollo F (2016) The effect of transition elements on high-temperature mechanical properties of Al–Si foundry alloys–a review. Advanc Eng Mater
4. Sears K (1997) Autom Eng Strategic Overview 2(1):55–68
5. Kaufman JG, Rooy EL (2004) Aluminium alloy castings. American Foundry Society, Columbus, Ohio
6. Askeland DR, Phulé PP (2003) The science and engineering of materials
7. Stadler F et al (2012) Effect of main alloying elements on strength of Al–Si foundry alloys at elevated temperatures. Int J Cast Met Res 25(4):215–224
8. Tenekedjiev N, Gruzleski J (1990) Hypereutectic aluminium-silicon casting alloys—a review. Cast Metals 3(2):96–105
9. Dieter GE, Bacon DJ (1986) Mechanical metallurgy, vol 3. McGraw-Hill, New York
10. Zamani M et al (2017) The role of transition metal additions on the ambient and elevated temperature properties of Al–Si alloys. Mater Sci Eng A
11. Sepehrband P, Mahmudi R, Khomamizadeh F (2005) Effect of Zr addition on the aging behaviour of A319 aluminium cast alloy. Scriptamaterialia 52(4):253–257
12. Mahmudi R, Sepehrband P, Ghasemi H (2006) Improved properties of A319 aluminium casting alloy modified with Zr. Mater Lett 60(21):2606–2610
13. Ma ZY (2008) Friction stir processing technology: a review. Metallurg Mater Trans A 39(3):642–658
14. Zhu C, Lv Y, Qian C, Qian H, Jiao T, Wang L, Zhang F (2016) Proliferation and osteogenic differentiation of rat BMSCs on a novel Ti/SiC metal matrix nanocomposite modified by friction stir processing. Scientific Reports 6:38875
15. Refat M, Abdelmotagaly AMM, Ahmed MMZ, El-Mahallawi I (2015) The effect of heat treatment on the properties of friction stir processed AA7075-O with and without nano alumina additions. Friction Stir Welding and Processing VIII. Springer, Cham, pp 115–123
16. Mishra RS, Ma ZY (2005) Friction stir welding and processing. Mater Sci Eng R Reports 50(1–2):1–78
17. Mishra RS, Ma ZY, Charit I (2003) Friction stir processing: a novel technique for fabrication of surface composite. Mater Sci Eng A 341(1–2):307–310
18. El-Mahallawi I, Ahmed MMZ, Mahdy AA, Abdelmotagaly AMM, Hoziefa W, Refat M (2017). Effect of Heat treatment on friction-stir-processed nanodispersed AA7075 and 2024 Al Alloys. In: Friction Stir Welding and Processing IX. Springer, Cham, pp 297–309
19. Ahmed MMZ, Refat M, El-Mahallawi I (2014) Manufacturing of nano-surface AA7075 composites by friction stir processing. In: Light Metals. Springer, Cham, pp 1417–1422
20. Zahmatkesh B, Enayati MH (2010) A novel approach for development of surface nanocomposite by friction Stir processing. Mater Sci Eng A 527:6734–6740
21. Dixit Manisha, Newkirk Joseph W, Mishra Rajiv S (2007) Properties of friction stirprocessed Al 1100-NiTi composite. Scr Mater 56:541–544
22. Refat M, Elashery A, Toschi S, Ahmed MMZ, Morri A, El-Mahallawi I, Ceschini L (2016) Microstructure, hardness and impact toughness of heat-treated nanodispersed surface and friction stir-processed aluminum alloy AA7075. J Mater Eng Perform 25(11):5087–5101
23. Mohamed AMA, Samuel FH, Samuel AM, Doty HW (2009) Influence of additives on the impact toughness of Al–10.8% Si near-eutectic cast alloys. Mater Des 30:4218–4229
24. Konecˇná R, Nicoletto G, Kunz L, Riva E (2016) The role of elevated temperature exposure on structural evolution and fatigue strength of eutectic AlSi12 alloys. Int J Fatigue 83:24–35

Part VIII
Friction Stir Spot Welding

Welding Multilayer Materials by Refill Friction Stir Spot Welding

Uceu Suhuddin, Dennis Gera, Nelson Alcantara and Jorge dos Santos

Abstract In order to restrain global warming, automotive producers have adopted electric vehicle technology as one of the solutions to produce zero-emission cars as replacement for fuel combustion car. One of the challenges in production of the battery for electric vehicle is to weld thin electrode materials that have good electric conductivity, in multilayers configuration, which is challenging for conventional technologies. Refill friction stir spot welding is a spot-like joining process used as a nonconsumable tool to generate frictional heat during the process. Refill friction stir spot welding is able to weld various material combinations with good mechanical properties and surface quality. In this presentation, the capability of refill friction stir spot welding to join multilayer materials up to 80 layers of similar aluminum alloys will be presented. The presentation consists of the mechanical properties of the welds, electric conductivity/resistance of the welds and the temperature measurement data during welding process.

Keywords Friction welding · Refill FSSW · Multilayer · Foils · Battery
Contact resistance

Introduction

With global warming becoming an increasing threat throughout the years, scientists are evermore dedicated to searching new ways to mitigate its augmentation. In the twentieth century alone, the globe's mean surface temperature has risen 1.1 °C, causing an impact on the world's ecosystem [1]. Today, transportation is responsible for one-third of the GHG emissions [2], therefore attracting much attention from

---

U. Suhuddin (✉) · D. Gera · J. dos Santos
Helmholtz-Zentrum Geesthacht GmbH, Institute for Materials Research, Materials Mechanics, Solid State Joining Processes (WMP), Max-Planck-Str. 1, D-21502 Geesthacht, Germany
e-mail: uceu.suhuddin@hzg.de

D. Gera · N. Alcantara
Materials Engineering Department, Federal University of São Carlos, Sao Carlos, Brazil

Y. Hovanski et al. (eds.), *Friction Stir Welding and Processing X*, The Minerals, Metals & Materials Series, https://doi.org/10.1007/978-3-030-05752-7_23

researchers and developers around the world to replace gasoline-based vehicles. This has turned the spotlight of investments toward electric vehicles (EVs), for they do not depend on fossil fuel nor do they emit carbon-based compounds responsible for aggravating global warming. However, when compared to gasoline-based vehicles, EVs still present many limitations, such as limited range, long refueling time, and higher purchase cost. These downsides can be attributed to battery technology, which still has to improve to maintain itself competitively in the automotive industry.

The majority of EVs battery currently consists of Li-ion technology. There are three battery types in Li-ion batteries technology, which are cylindrical, prismatic and pouch cells. The joining process of a battery pack with a pouch cell configuration consists of some levels: cell, module, and pack, as presented in Fig. 1. In the cell level, the electrodes are welded to a tab followed by sealing of the case. This weld is usually carried out by ultrasonic welding, for it is an excellent technique for dissimilar materials, thin and multilayered sheets, and shows low heat affected zone. However, this technique has disadvantages, such as structural vibrations, upper limit in total joined materials, and may have severe knurl perforation at the top and bottom of the weld surface.

Refill Friction Stir Spot Welding (refill FSSW), also known as Friction Spot Welding (FSpW), is a solid-state joining process that produces a spot-like overlap connection between two or more sheets without bulk melting, therefore able to bypass many of the existing challenges related to the joining of high strength aluminum alloys. Refill FSSW is an alternative process for this application and does not present the referred limitations.

This work aims to analyze the use of RFSSW for welding 50 sheets of commercial aluminum foil in between two AA2024-T3 sheets, resembling the weld of electrodes to a tab. This analysis includes studying microstructure of the weld with regards to its mechanical and electrical properties, and the temperature reached during welding.

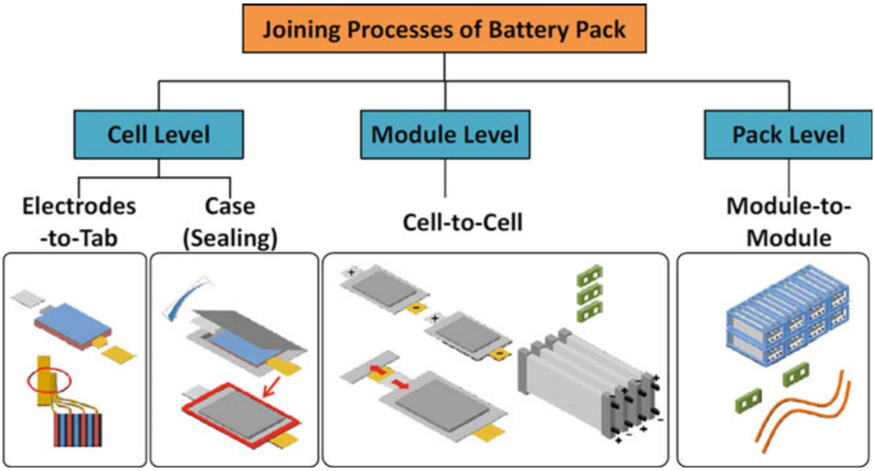

Fig. 1 Schematic illustration of pouch type battery pack production [3]

Experimental Procedure

In this study, 50 foils of commercial aluminum alloy between two sheets of AA2024-T3 aluminum alloy were welded. The aluminum sheets and foils were cut from larger sheets to attain a width, length, and thickness of 25.4 × 100 × 0.3 and 25.4 × 100 × 0.013 in millimeters, respectively. In this study, one set of the tool was used, and consists of a clamping ring, sleeve, and probe of 17 mm, 9 mm, and 6 mm diameters, respectively.

An initial study was conducted to assess the affecting welding parameters and their ranges. Based on a preliminary study, plunge depth (PD), rotational speed (RS), and feeding rate (FR) showed to be the most influential on surface quality and microstructure. PD represents the total depth achieved by the sleeve during plunging, RS is the number of rotations per minute undergone by the sleeve and probe, and FR is the speed at which the sleeve penetrates into the material and retracted from the weld. The statistical Box–Behnken model [4, 5] was used to analyze the influence of each parameter on the observed responses, and to obtain the combination of parameters that would generate the weld with the highest lap shear strength, lowest contact resistance, and heat input.

All friction spot welds were conducted using a Harms & Wende RPS100®. The welds were performed using the sleeve plunge variant with a fixed welding force of 14.8 kN. The lap shear specimens were produced with a 25.4 mm × 25.4 mm overlapped area. The equipment used for lap shear testing was a screw-driven Zwick/Roell®testing machine with a load capacity of 200 kN at room temperature and the displacement rate was 2 mm/s. All lap shear tests were done within 24 hours after welding. An INFRATEC ImageIR® 8300 infrared camera with the aid of IRBIS3 Professional® software was used to analyze the temperature throughout the sheet during and after welding. Dupli-Color Lackspray Tuning Supertherm Black, a high-temperature resistance spray, was used to paint the entire sheet and eliminate the influence of the sheets' reflectivity on the temperature measurement of the camera. For contact resistance measurement, welds were produced in the center of sheets with 50 mm length and 25.4 mm width. The current resistance was then measured by clamping one resistance lead on the edge of the upper sheet and the other resistance lead on the edge of the lower sheet. This configuration would, consequently, allow the current to pass through the weld. Three measures were taken for every sample, and the average was used for statistical analysis.

Results

Parameter Optimization

Given the Box–Behnken design, tests were conducted in the order given by the Minitab® software. Thirteen runs with different parameters were tested, and then two more with the center points. Some of the measurements are presented in Fig. 3.

Overall, the spot-welded samples presented good mechanical properties regarding the standard AWS D17.2 [6], used as reference. This standard establishes a minimum load requirement of 425 N for resistance spot welds in which the thinner welded sheet has a nominal thickness of 0.3 mm and the material used has an ultimate strength above 386 MPa. However, a large variability inside the process window can be observed, ranging roughly from 710 to 1891 N.

The temperature measurements obtained ranged from 163 to 283 °C. Therefore, it appears that all welds produced with parameters inside the chosen process window achieve temperatures above 80 °C. This becomes an issue because, in lithium-ion cells, the electrochemically active materials are in direct contact with the cell casing [7]. Accelerated rate calorimetry on various Li-ion technologies showed that the decomposition of electrochemically active materials starts at 80 °C [8]. For this reason, the highest temperatures achieved during any welding process conducted to join the electrodes to the tab have to be carefully analyzed to avoid reaching temperatures above 80 °C. However, it was also seen that the maximum temperature is achieved immediately outside the clamping ring and that the temperature of the sheet decreases significantly with the distance from the welding tool, see Fig. 2. It was decided, therefore, to measure the distance between the clamping ring and the location of the sheet that never reaches 80 °C to characterize the temperature's profile throughout the sheet. The distances varied from 32 to 89 mm, depending on the maximum temperature achieved during welding: the lowest maximum temperatures provided the smallest distances. Hence, this process may be used safely with the condition of using parameters that generate low heat input, and consequently, induces low overall temperatures of the sheet.

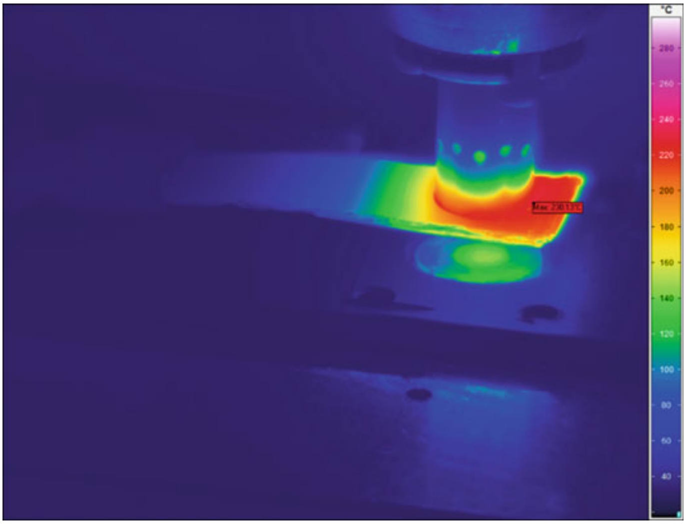

Fig. 2 Infrared image of temperature measurement during welding

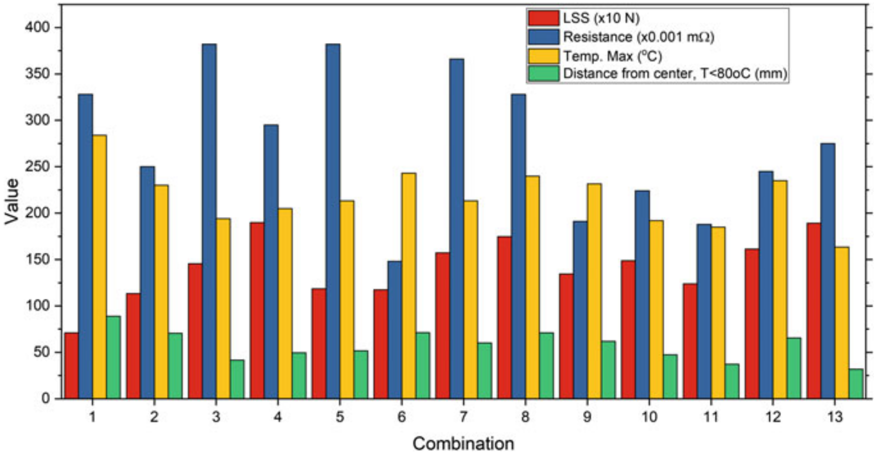

Fig. 3 Lap shear strength, contact resistance, and temperature measurements of welds produced by different welding parameters

Contact resistance analyzes the quality of weld regarding the difficulty of the current to pass through the weld. Given that this weld would be used in a battery, it is crucial that the weld presents low resistance. Since the values are given in milliohms, they would vary significantly due to the precision of the measurement. In light of that, three measurements were taken for every weld: at 3, 6, and 9 s of contact between the sheets and the measurement leads. The average between the measurements was then considered for statistical analysis. The measurements ranged from 0.145 to 0.382 mΩ, as shown in Fig. 3.

Microstructure

A macroscopic overview of a representative refill friction stir spot weld in this work is presented in Fig. 4. No defects, such as voids, lack of refill, and lack of bonding were observed, meaning that the screening process conducted to find a process window without defects was successful. However, this weld does not show the typical characteristics that are present on friction spot welds [9–11].

The macroscopic structure of a typical cross section of the friction-based process in aluminum alloys consists of four regions [12], i.e., stir zone (SZ), thermomechanically affected zone (TMAZ), heat affected zone (HAZ), and base material (BM). The HAZ corresponds to the region that is affected by the increase in temperature, therefore suffers a heat treatment, but does not undergo plastic deformation. The TMAZ is subjected to moderate strain rates and temperatures, characterized by deformed grains in the direction of the retracting sleeve. In the SZ, temperature, and strain

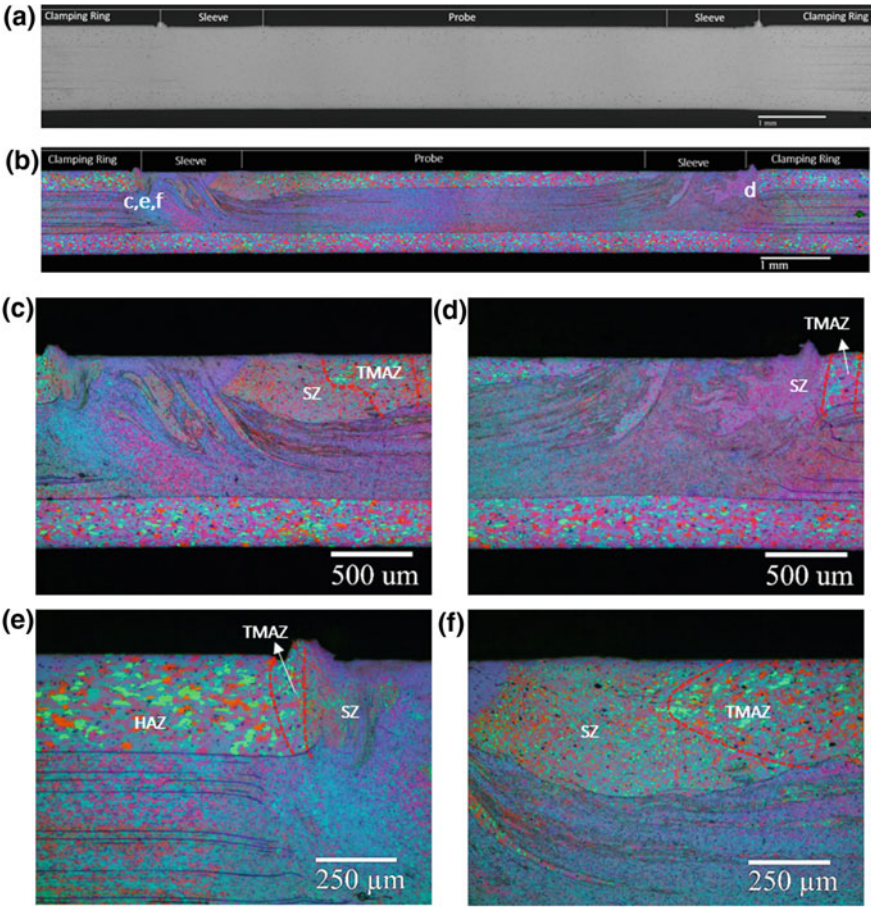

Fig. 4 Micrographs of a representative refill friction stir spot weld in aluminum foils between two AA2024-T3 sheets, etched with barker

rates are at their highest value, forcing the grains to recrystallize. Hence, this region is characterized by a fine grain microstructure.

As seen in Fig. 4, the representative weld of this work presents these regions. However, they are not well-defined. In typical friction spot welds, the stir zone appears in the center of the weld, that is, beneath the area occupied by the sleeve and probe, and the TMAZ and HAZ appear immediately outside the welded area and near the base material, respectively [9, 11–13]. Grains that are similar to those which are present in the heat affected and thermomechanically affected zones also appear in the center of the weld. Moreover, in the cross section, the stir zone seems to be divided into two regions, each located on different sides of the sleeve, separated by the center of the weld. However, this metallurgical configuration has not yet been reported in the available literature, and it is still under current investigation to correctly analyze and characterize these zones.

Micrographs of the region beneath the probe showed in Fig. 5, suggest that the material mixing during welding is not similar to what is observed in previous RFSSW studies [14–16], and therefore, presents a unique behavior.

The region of the upper sheet illustrated in Fig. 6 presents different grain morphologies. The grains located near the sheet's surface, the area that was in direct contact with the probe, shows fine grain microstructure. However, this fine grain morphology is only present in a layer of roughly 8 μm. A coarse and elongated grain microstructure characterizes the remaining of the upper sheet. Moreover, it is possible to see a very clear boundary line, which separates the AA2024 sheet from the aluminum foil, suggesting that there was almost no mixing between these materials. There is no clear evidence of why the microstructure appears to have these characteristics.

However, one possible explanation is that the upper sheet attaches itself to the surface of the probe during welding. Consequently, the material closest to the surface would suffer high heat input and strain rates, forcing localized recrystallization of the grains. The region immediately below this recrystallized layer, however, did not

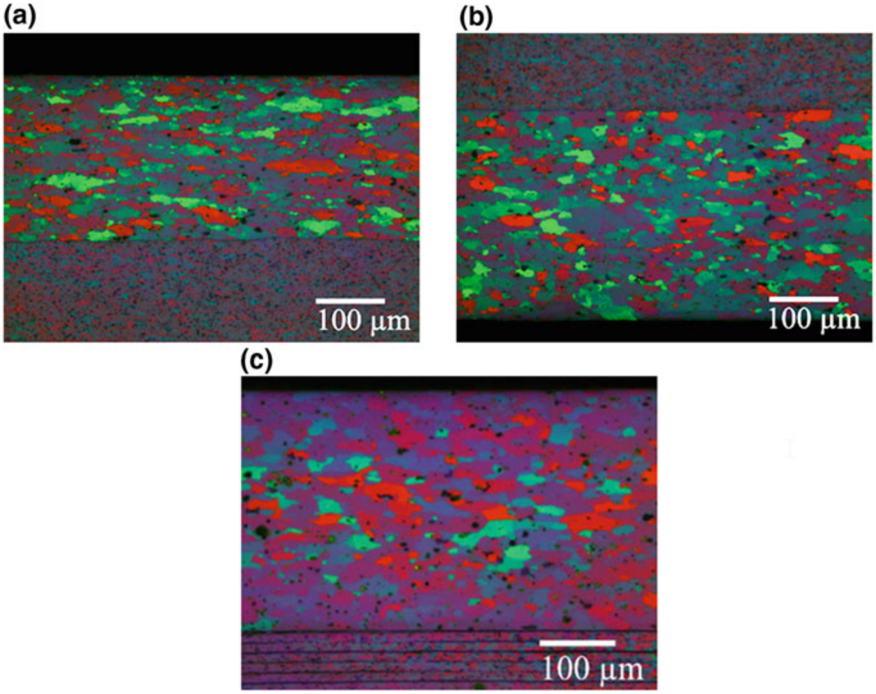

Fig. 5 Microstructure taken from regions under the probe on the upper sheet (**a**), on the bottom sheet (**b**) and base material (**c**)

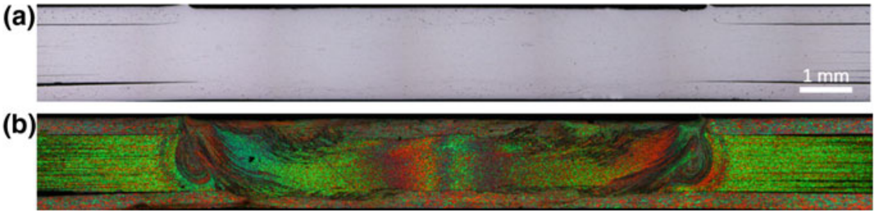

Fig. 6 A representative macrograph of dissimilar 80 foils and 2 thin sheets Al alloys welded by refill FSSW. Low magnification overview before (**a**) and after (**b**) etching process

undergo severe strain rates and high temperatures because the probe's rotation was unable to allow thorough mixing of the material, explaining the elongated grains. This would also explain the presence of a clear bonding line between the sheets and foils, for the material was not mixed enough to produce a stirred zone.

The grain morphology on the bottom sheet, however, is homogeneous. The grains are similar to those present in the base material, suggesting that the bottom sheet does not undergo high strain rates, and therefore does not participate in the mixture.

The aluminum foil below the probe also presents a fine grain microstructure when compared to its base material. This is an indication that the process induces high enough heat input and strain rates in the center of the weld to allow recrystallization of the aluminum foil grains in between the AA2024 sheets. Nevertheless, the microstructural behavior is still being investigated to assess what phenomena occur in each region of the weld.

Additionally, further experiments have been done to weld Al foils up to 80 layers. Free-defect weld can be obtained as presented in Fig. 6.

Conclusion

This work is investigating the mechanical properties, electrical resistance, heat input, and the microstructure of friction spot welds in AA2024-T3 with aluminum foil. The analysis produced the following observations so far:

1. Although the lap shear tests showed high variability, the studied weld presented good mechanical properties and is under current investigation to correlate the lap shear strength with the microstructure.
2. The heat input analysis showed that all welds produced with parameters inside the chosen process window present temperatures above 80 °C. However, the process is fast enough not to allow high temperatures to reach the entirety of the sheet.
3. Contact resistance has shown to be low and consistent, between 0.1 and 0.4 mΩ. Its correlation with the microstructure is also under current investigation.

4. The microstructure of the weld showed the presence of typical friction-based weld regions, such as stir, thermomechanically affected and heat affected zones. However, it was observed that these regions appear in sites not common to friction spot welds, and therefore, is still being investigated to better understand its formation.

References

1. Daly JL (2018) What's wrong with the surface record? https://www.john-daly.com/ges/surftmp/surftemp.htm. Accessed 15 Aug 2018
2. U.S.-EPA (2018) Sources of greenhouse gas emissions. https://www.epa.gov/ghgemissions/sources-greenhouse-gas-emissions. Accessed 13 Aug 2018
3. Cai W et al (2017) Analysis of Li-Ion battery joining technologies*
4. Hussein SH, Alzaidi M, Hasan QO (2016) A statistical approach for modelling of lightweight palm oil clinker reinforced concrete beams with openings 5(12):3390–3397
5. Montgomery DC (1984) Design and analysis of experiments eighth edition
6. American Welding Society (2013) AWS D17.2—specification for resistance welding for aerospace applications, no. 02016826
7. Brand MJ, Schmidt PA, Zaeh MF, Jossen A (2015) Welding techniques for battery cells and resulting electrical contact resistances. J Energy Storage 1(1):7–14
8. Brand M et al (2013) Electrical safety of commercial Li-ion cells based on NMC and NCA technology compared to LFP technology. World Electr Veh J 6(3):572–580
9. Rosendo T et al (2011) Mechanical and microstructural investigation of friction spot welded AA6181-T4 aluminium alloy. Mater Des 32(3):1094–1100
10. Santana LM, Suhuddin UFH, Ölscher MH, Strohaecker TR, dos Santos JF (2017) Process optimization and microstructure analysis in refill friction stir spot welding of 3-mm-thick Al-Mg-Si aluminum alloy. Int J Adv Manuf Technol 92(9–12):4213–4220
11. Suhuddin UFH, Piccolo D, Fischer V, dos Santos JF (2015) Friction spot welding of similar AA5754 to AA5754 aluminum alloys and dissimilar AA5754 aluminum to AZ31 magnesium alloys. Adv Mater Res 1112:485–488
12. Reimann M, Goebel J, dos Santos JF (2017) Microstructure and mechanical properties of keyhole repair welds in AA 7075-T651 using refill friction stir spot welding. Mater Des 132:283–294
13. Amancio-Filho ST, Camillo APC, Bergmann L, dos Santos JF, Kury SE, Machado NGA (2011) Preliminary investigation of the microstructure and mechanical behaviour of 2024 aluminium alloy friction spot welds. Mater Trans 52(5):985–991
14. Campanelli LC, Suhuddin UFH, Antonialli AÍS, Dos Santos JF, De Alcântara NG, Bolfarini C (2013) Metallurgy and mechanical performance of AZ31 magnesium alloy friction spot welds. J Mater Process Technol 213(4):515–521
15. Tier M et al (2008) The influence of weld microstructure on mechanical properties of refill friction spot welding of 5042 aluminium alloy. In: 7th international symposium friction stir welding, pp 20–22, May 2008
16. Suhuddin U, Fischer V, Kroeff F, dos Santos JF (2014) Microstructure and mechanical properties of friction spot welds of dissimilar AA5754 Al and AZ31 Mg alloys. Mater Sci Eng A 590:384–389

Improving Porous TC4/UHMWPE Friction Spot Welding Joint Through Controlling Welding Temperature and Force

Muyang Jiang, Ke Chen, Binxi Chen, Min Wang, Lanting Zhang and Aidang Shan

Abstract Joining between metal and polymer has attracted significant attention recently due to its advantage of great weight reduction and excellent integrated physical/chemical properties. In this study, specially designed biomedical additive manufactured porous TC4 titanium alloy plate was successfully joined to ultra-high molecular weight polyethylene (UHMWPE) plate by friction spot welding (FSpW). The z-axial load (F_z) evolution has been measured with load cell, and welding temperature (T_w) near TC4/UHMWPE interface has been measured with thermocouple. High tensile shear strength (~3000 N) has been realized through strong mechanical interlocking. Good macro-penetration of UHMWPE into TC4 porous structure (up to 80% filling rate) and sound micro-interlocking between metal and polymer were obtained. Relationship between T_w/F_z and joint quality has been unveiled for the fabrication of defect-less joints.

Keywords Friction spot welding · Metal–plastic joining · Coupling effect
Additive manufacturing

Introduction

Metal/polymer hybrid structures are increasingly demanded in biomedical, automobile, and aerospace industries due to its advantages of great weight reduction and excellent integrated physical/chemical properties. However, the differences between metal and polymer, including different melting points, mechanical and thermal properties, have brought a great difficulty to the joining process.

Commonly, there are three ways of metal/polymer joining: adhesive bonding [1], mechanical fastening [2], and welding [3–11]. However, as traditional joining techniques in industrial applications, adhesive bonding and mechanical fastening

---

M. Jiang · K. Chen (✉) · B. Chen · M. Wang · L. Zhang · A. Shan
School of Materials Science and Engineering,
Shanghai Jiao Tong University, Shanghai 200240, China
e-mail: chenke83@sjtu.edu.cn

Y. Hovanski et al. (eds.), *Friction Stir Welding and Processing X*, The Minerals,
Metals & Materials Series, https://doi.org/10.1007/978-3-030-05752-7_25

have their own disadvantages. The adhesive and primer used in adhesive bonding are usually unstable under extreme environment. Besides, the toxicity of adhesive is a potential threat when used in biomedical applications. Mechanical fastening leads to stress concentration. The use of screws and bolts not only has risk of loosening and corrosion, but also adds weight to the whole structure.

Meanwhile, some novel welding techniques which have been investigated in recent years, such as laser welding [3–5], ultrasonic welding [6–8], and friction stir welding [9–11] can avoid these problems. Katayama and Kawahito [5] and Chen et al. [3] studied laser joining of steel/PET and TC4/PET, respectively, and reported that hybrid joints can reach high tensile loads (failed at polymer). However, due to the high temperature at welding center (~1000 °C), the polymer inevitably degraded and thus bubbles formed at interface, which brought about potential risks for wear and fatigue properties in the long-term application. Wagner et al. [6–8] conducted many investigations on ultrasonic welding between aluminum alloys and carbon fiber reinforced polymers (CFRPs). High tensile shear strength (~25 MPa) and good interface bonding have been achieved. However, restricted by power limitation of equipment, ultrasonic welding is mainly applied to joining of thin plates. Friction stir welding (FSW) has advantages of relatively mild heat input rate and low process cost. Amancio-Filho et al. [11] and Esteves et al. [12] studied friction spot joining (FSpJ) of AZ31 Mg alloy/CF-PPS, AA2024-T3 Al alloy and AA6181-T4 Al alloy/CF-PPS. Joint strength reached 28 MPa, 27 MPa and 27 MPa, respectively, without metal surface treatment. Strength of the joint up to 43 MPa was achieved with surface treated Al alloy [11].

Among the above researches, the main metal/polymer joining mechanisms, as indicated by the authors [3, 4], are: (1) Mechanical interlocking in macro- and micro-scales, (2) Chemical bonding and interatomic/intermolecular force in micro-scale. Meanwhile, polymers studied in previous researches mainly have polar groups, such as thioether group and ester group, which can promote adhesion and chemical bonding between polymer and metal [13]. Few researches have studied joining between non-polar polymer and metal, since adhesion and bonding are difficult to realize [9]. One solution for this problem is to increase the surface roughness of metal [14], facilitating strong macro-scale interlocking. In our previous study [9], a 3D-printed TC4 plate was used to join with UHMWPE and achieved good joint performance (1300 N, failed at base material).

Additionally, previous researches mostly focused on influence of welding parameters on the joint properties. The force (F_z) and temperature (T_w) during welding received much less attention. Since the evolutions of temperature and force are key factors to the polymer property change during welding, it is fundamentally important to study their evolutions for purpose of achieving optimized metal/polymer joint.

In this research, based on our previous investigation, 3D-printed porous TC4 plates were produced for better interlocking with non-polar ultra-high molecular weight polyethylene (UHMWPE). The F_z and T_w evolution during welding were recorded, and macro-/micro-structures were characterized. Influence of F_z-T_w evolution on joint quality was studied and thus fed back to produce defect-less joints with good mechanical property. This study aims to promote the application of polymer/metal joints in biomedical prostheses.

Experimental Setup

Materials used in this work were 3D-printed porous TC4 titanium alloy and ultra-high molecular weight polyethylene (UHMWPE, *CHIRULEN 1050*). Sample dimensions were 60 × 20 × 4 mm^3 and 60 × 25 × 6 mm^3 for metal and polymer, respectively. Yield strength of UHMWPE plate is 20 MPa.

Figure 1a shows the 3D structure of the 3D printed TC4 alloy specimen (printed by *Arcam A1 EBM® machine*). The 4 mm-thick TC4 plate was specially designed into a 2-layer structure. The first layer was a 2 mm-thick bulk, while the second one is a 2 mm-thick diamond structure. The pore size of the structure is 0.9 mm, which was proved to be a suitable size based on previous welding. Tunnel for temperature measurement was opened at side of TC4 plate, with depth of 10 mm, as Fig. 1b shows. The thermogravimetric (TG) result of UHMWPE is shown in Fig. 1c. The polymer starts to degrade slowly from ~250 °C, while severe degradation occurs at 400 °C, which should be avoided. Note that UHMWPE has an essentially 0 melt flow index, and its fluidity remains very low even when it is melted [15, 16], rendering difficulty for the joining.

The welding system is shown in Fig. 2. TC4 plate overlapped 25 mm with UHMWPE plate. A probe-less FSpW welding tool made of WC–Co alloy was used in this study. The cylindrical shoulder has a 10 mm diameter. K-Type thermocouple was placed at the square tunnels for temperature measurement (Fig. 1a). A load cell (*Kistler 4578A®*) is fixed under the worktable to measure the load in Z-axis during welding.

The welding process was divided into 4 stages, which were preheating, pre-plunging, deep plunging, and cooling. During the preheating stage, the joint was

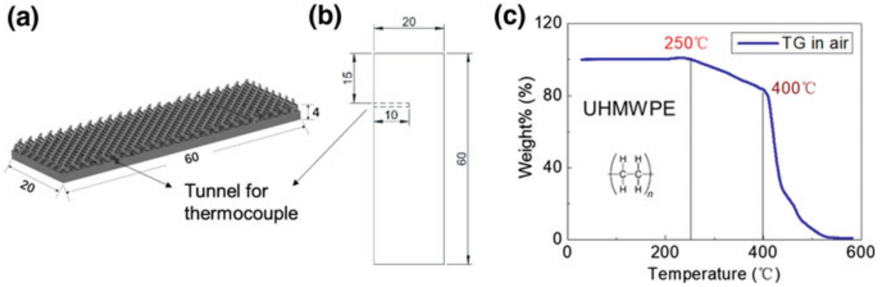

Fig. 1 **a** 3D structure of TC4 plate **b** front view of TC4 plate containing thermocouple tunnel **c** TG curve of UHMWPE

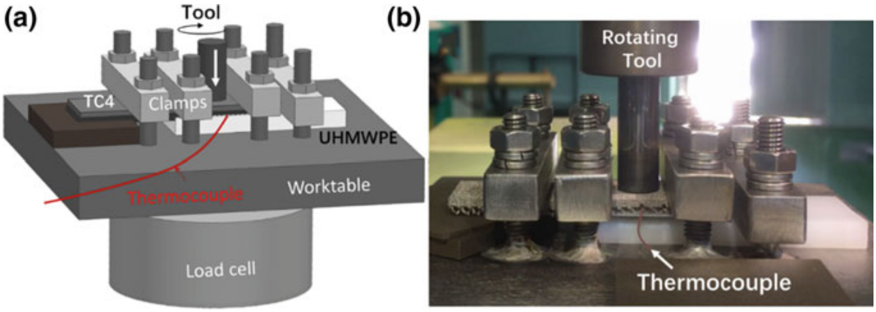

Fig. 2 **a** 3D structure of welding system **b** picture of welding process

Table 1 Welding parameters of different groups

Groups (designed heat input)	Welding time (s)	Plunge depth (mm)
R (reference)	20	0.8
L (low)	20 + 10	0.8 + 0.4 = 1.2
H (high)	20 + 30	
HD (high+)	20 + 30	0.8 + 0.6 = 1.4

heated to 160 °C by a heat gun in 60 s. After preheating, the welding tool starts to rotate at a speed of 555 rpm. In the pre-plunging stage, the tool was plunged into TC4 to a depth of 0.8 mm in 20 s. It is noteworthy that a relatively long pre-plunge time (20 s) is used here compared with other metal/polymer welding researches [11]. That is because the near 0 melt flow index of UHMWPE results to quite slow reptation of long chains even after melted [15], In this case, it needs not only high temperature and strong force, but also longer time to deform UHMWPE during joining. Besides, the thermal conductivity of both TC4 (6.7 W/m K) and UHMWPE (~0.4 W/m K) are relatively low. Longer welding time was needed for better heat conduction. In the deep-plunge stage, different welding time (10–30 s) and depth (1.2–1.4 mm) were used to study the influence of heat input on joint quality. At last, cooling stage marks the finish of the welding process. Four different sets of welding parameters are designed in the study, as shown in Table 1. Reference group (Group R) only undergoes pre-plunge stage to mark the start of interpenetration of TC4 and UHMWPE. Groups L, H, and HD are designed to have low, high, and ultra-high heat input through variation of welding time and plunge depth. 4 samples were welded for each group.

Lap shear testing was carried out using a Zwick testing machine (*Zwick Z200*). The clamping is shown schematically in Fig. 3a. Loading rate was set at 2 mm/min. Cross-section specimens were cut through the center of the joint, as Fig. 3b shows. A high CCD camera (*Leica DM 4000*) was used for macro-structure observation. A scanning electron microscope (*Phenom XL*) was used for micro-structure observation and local elemental composition analysis.

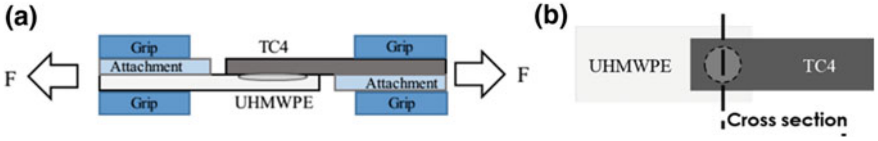

Fig. 3 **a** Schematic diagram of tensile testing **b** diagram showing cross-section cutting

Results and Discussion

Evolution of Welding Temperature and Load

The temperature and z-axial load evolution during welding process were recorded by thermocouple and load cell, respectively. Figure 4 shows the temperature and load history of all 4 groups of welding.

Since all samples were preheated to 160 °C for better fluidity, the temperature curves started from around 160 °C. The curves continued to decrease at first 15 s of welding, then started to rise. After welded for 20 s plunging to 0.8 mm depth, the peak temperature reached in Group R was 162 ± 10 °C. With a longer welding time, Groups L, H, and HD reached peak temperatures of 263 ± 13 °C, 344 ± 15 °C, and 385 ± 18 °C, respectively. However, during the welding process of Group HD, liquid with low fluidity flowed out from porous structure with bubble formation observed at the end of welding. It is a clear sign of severe degradation, in good agreement with the measured peak temperature approaching the severe degradation point of UHMWPE (400 °C, Fig. 1b).

Load curves all started to rise after 5 s of welding, which is related to the softening of polymer in the preheating stage. After pre-plunged for 20 s, the load surged quickly to ~1100 N. In the deep-plunge stage, the load curve with faster plunging speed (Group L) has a higher increasing rate than those with slower plunging speed (Groups H and HD). Peak load of Groups R, L, H, and HD reached 1224 ± 176 N,

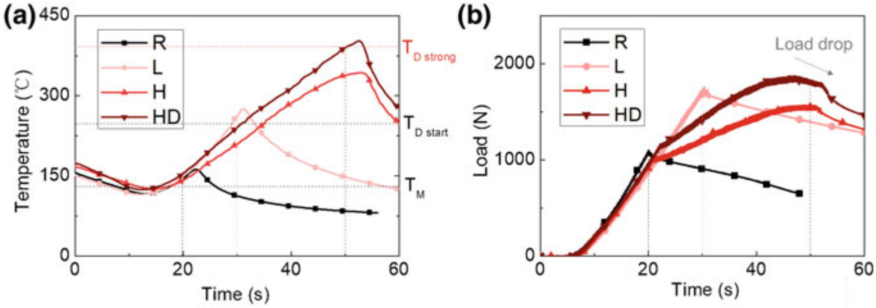

Fig. 4 **a** Temperature and **b** load evolution during welding process

1960 ± 140 N, 1602 ± 98 N, and 1806 ± 9 N, respectively. The rising trend of curves H and HD slowed down after 40 s of welding, indicating the softening and degradation of polymer at high temperature. All load curves kept increasing during welding, except for Group HD. The load curve of Group HD reached peak and then dropped for near 100 N in the deep-plunge stage. This phenomenon is possibly caused by the squeezing out of degraded polymer as mentioned above, which needs to be avoided. Relationships between T_w/F_z evolution and joint properties will be discussed in later sections.

Mechanical Properties

The lap shear load curves for all four groups are shown in Fig. 5a and the failed joints are shown in Fig. 5b. As shown in Fig. 5, only samples of Group R failed at TC4/UHMWPE interface, with elongation less than 8 mm. Other groups of samples, however, all failed at UHMWPE base material (BM).

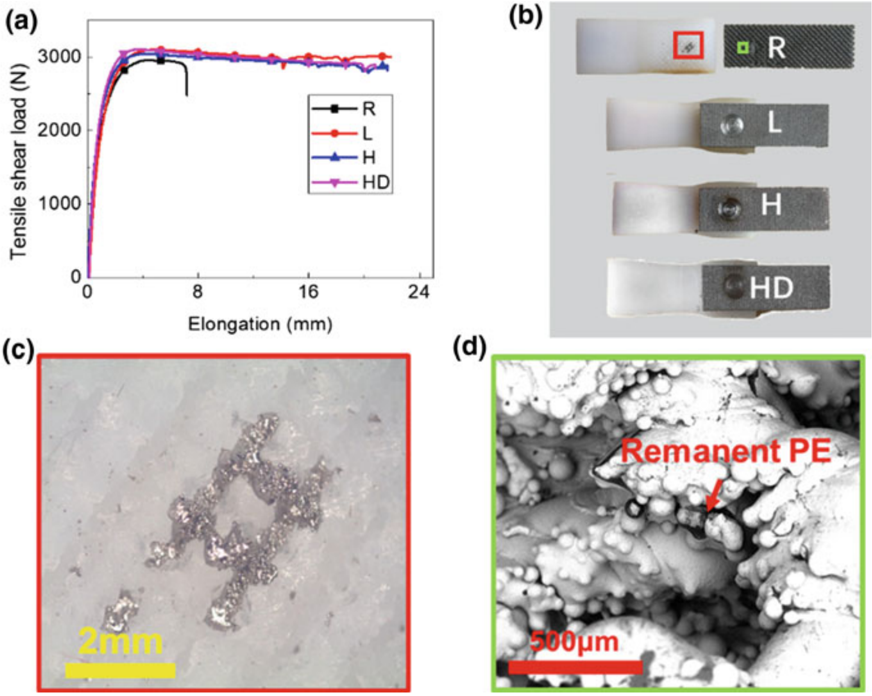

Fig. 5 **a** Tensile shear strength of four groups of samples, **b** failed joints after testing in which selected zones were magnified: **c** OM picture of TC4 embedded in PE, **d** SEM picture of TC4 surface after failure

The ultimate shear load of Group R was registered to be 2920 ± 40 N. The calculated UTS for group R (19.5 ± 0.3 MPa) was very close to the yield strength of UHMWPE BM (20 MPa). Magnification of failed regions on polymer side and TC4 side are shown in Fig. 5c, d. On the failure surface of UHMWPE plate, there remained some TC4 particles (Fig. 5c) torn off from TC4 plate. While much PE remanence can be observed on TC4 plate (Fig. 5d, black strips). The rough surface of 3D-printed TC4-enabled strong mechanical interlocking between the metal and polymer, which contributed to the strong property of joints.

Curves of other groups grew smoothly to the peak (yield of polymer) and slowly dropped. Meanwhile, obvious necking can be observed in these samples during test. The ultimate shear strength for these samples was calculated around 20 MPa, indicating ~100% joining efficiency. Joints after tensile testing were still undamaged.

Macro-/Micro-structure and Defects

Figure 6 shows the macro-structure of four groups of samples. The joint areas between TC4 porous structure and UHMWPE arSincee marked with red rectangles. The UHMWPE was darkened inside of rectangles to highlight the interpenetration between porous TC4 and UHMWPE.

To quantify the penetration of polymer into TC4 porous structure, filling rate (FR) is calculated for each cross-section. It is defined as the percentage of filled area to total joint area (including part of the ligaments) on the cross section: FR $= \frac{S_{filled}}{S_{total}} \times 100\%$. Group R has the lowest FR (42%). With the increasing of welding time, FRs of Groups L and H reached 67% and 74%, respectively, indicating the influence of welding time in the deep-plunge stage on the FR. In comparison, with a higher plunge depth, FR of Group HD reached 82%, ~10% higher than Groups L and H, implying the significant influence of plunge depth on the penetration between porous TC4 and UHMWPE. In Group L, the polymer could not fill to the top of porous layer, leaving insufficient filling at welding center (Fig. 6b). Meanwhile, in Group H and

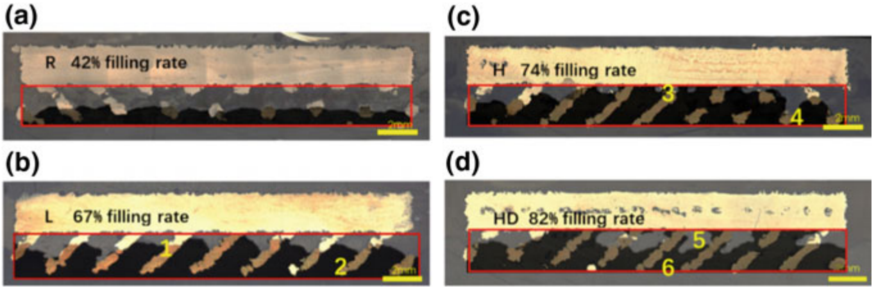

Fig. 6 a–d Macro-structure of the joints showing the interpenetration between porous TC4 and UHMWPE of Groups R, L, H, and HD

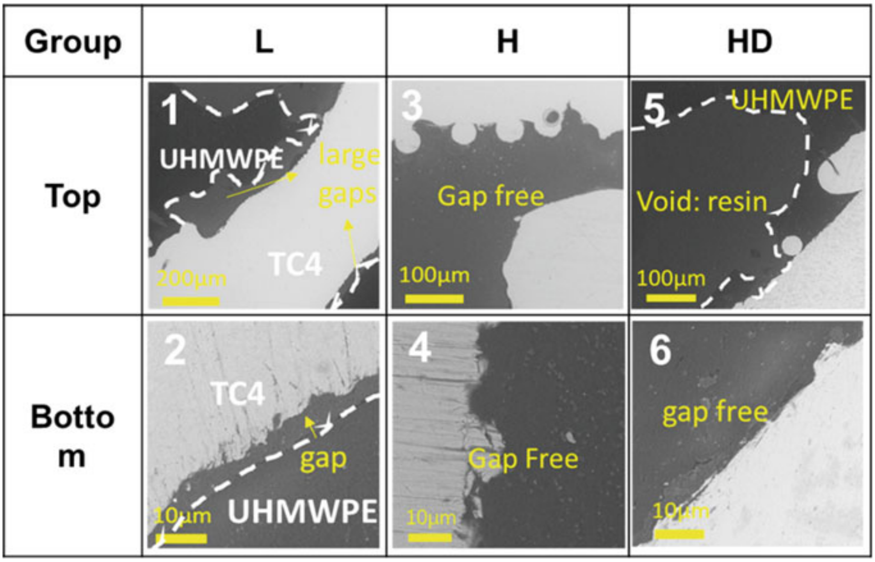

Fig. 7 Local microstructures of Groups L, H, HD from the selected regions marked in Fig. 6

HD, though the filling to the top at welding center were achieved and FR were higher, there were small voids at center of H and large voids at center of HD, which were clear signs of strong degradation of UHMWPE during welding, combined with the evidence that degradation products flowed out during welding process. This can be mainly attributed to too high welding temperature (~400 °C). Such large defects may influence the long-term use of the joint [3].

Micro-structures of the marked regions in Fig. 6 are shown in Fig. 7. Two pictures were taken from each sample (L, H, and HD), one at the top of porous layer and the other at the bottom. For Group R, since there is limited penetration of UHMWPE into the porous layer, the micro-structure is not compared here. With a relatively low heat input in group L (T_w reached 263 °C), gaps with width of 5–50 µm are dominant at the interface, as shown in Fig. 7(1) and (2). Even though the existence of these gaps did not influence much on the tensile property, they still have potential risks of early fatigue and bacterial infection in the long-term use of the joint for the biomedical application. With higher heat input (T_w reached 340 °C) in H, the interface between metal and polymer is mostly gap-free, indicating a good micro-scale interlocking. For Group HD (T_w reached 385 °C), though the interface was also gap-free, large macro-scale voids caused by degradation dominated the center of joint (Fig. 7(5)). Only a thin layer of UHMWPE (~100 µm) remained at the top of porous layer. Similar voids resulted from local polymer degradation were also reported in laser welding between metal and polymer [3].

The Formation Mechanisms of Defects

From the macro- and micro-structure observations, it is convincible that heat input has a strong influence on the macro-/micro-scale defects. The macro-scale defects include insufficient filling (Groups R and L) and degradation voids (Group HD), which have been described previously. Meanwhile, the micro-scale defects are mainly microgaps at TC4/UHMWPE interface shown in Fig. 7. The main cause of these gaps is cooling shrinkage of polymer. Note that TC4 and UHMWPE have linear expansivity of 9×10^{-6}/°C and 1.5×10^{-4}/°C, respectively, meaning that UHMWPE shrinks over 16 times more severely than TC4 during cooling stage with continuously decreasing temperature (dropping rate ~ 20 °C/s). The severe shrinkage formed internal stress both inside polymer and on metal/polymer interface. In case the interface interlocking is weak, gaps will be formed on the metal/polymer interface by the internal stress. Figure 8 shows the evolution of the macro- and micro-scale defects. The key to eliminate these kinds of defects is to find suitable welding condition during the process.

The formation of macro-scale interpenetration and micro-scale interlocking between UHMWPE and TC4 requires a good fluidity of polymer, which means a relatively low viscosity (η). However, the viscosity of UHMWPE is very high (~10^8 Pa s) at temperature around T_m, leading to an essentially zero melt flow index [15]. According to previous report [17], the viscosity of polymer has such a relationship with temperature:

$$\eta = B\exp\left[E_\eta/RT\right]$$

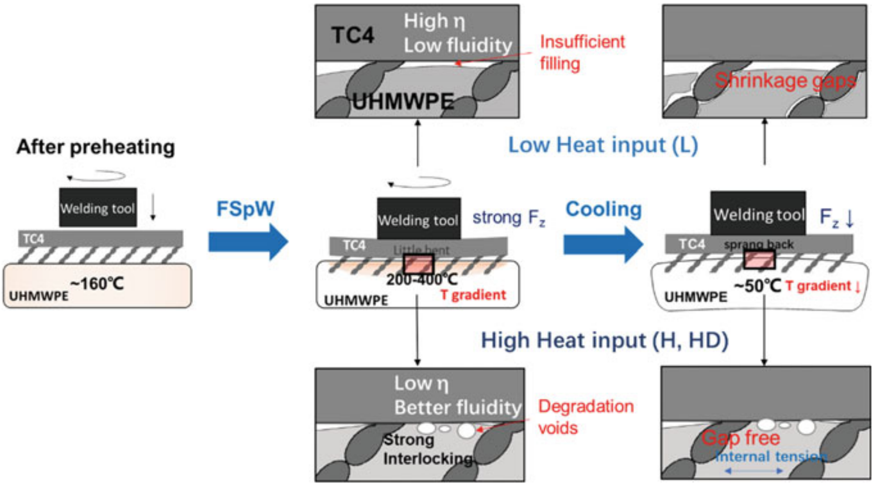

Fig. 8 Diagram of joint configuration evolution during welding process

In this equation, E_η is the activation energy for viscous flow (27 kJ/mol for UHMWPE), and B is a constant [17]. Since the peak T_w for Groups L and H were 263 °C and 340 °C, respectively, the viscosity difference for polymer in Groups L and H was: $\eta_L/\eta_H = 2.14$, which means that the fluidity of UHMWPE (at top layer where welding temperatures were measured) in Group H doubled that in Group L. Meanwhile, since the thermal conductivity for UHMWPE is very low (~0.4 W/m K), the temperature gradient within polymer was large during welding process, especially for groups with shorter welding time (Group L). This means the fluidity at the bottom layer is far lower than that at the top layer. In this case, in Group L, the polymer maintained relatively high viscosity during welding and the time for polymer penetrating into TC4 porous structure was short. As a result, the macro-scale interpenetration between TC4/UHMWPE was poor, causing insufficient filling defect. Besides, the micro-scale interlocking between TC4 and UHMWPE was weak, tending to form shrinkage gaps. In contrast, polymer in Groups H and HD had better fluidity and longer time to flow, thus formed enough macro- and micro-interlocking with metal, and kept a good interface contact even after cooling. In this case, the joint is more reliable in long-term application, such as prosthesis implantation. However, at too high temperature (Group HD, ~385 °C) severe degradation caused formation of large voids, adding potential risks for long-term application of the joints. In this perspective, parameters of Group H kept a good balance, avoiding both insufficient heating and severe degradation.

Conclusions

Non-polar UHMWPE was successfully joined to 3D printed porous TC4 plates (2 mm porous thickness) via friction spot welding. The following conclusions are summarized based on the study:

(1) Deep interpenetration and strong mechanical interlocking were achieved between porous TC4 and UHMWPE. Joining efficiency of 100% was reached.
(2) Two kinds of macro-scale defects showed up in TC4/UHMWPE joints. The first one is insufficient filling of UHMWPE, formed when the welding heat input was too low. Polymer with low fluidity could not reach top of porous layer within limited welding time. The other one is degradation void, formed when heat input was too high. Severe degradation of polymer resulted in large voids in the joint interface.
(3) Micro-scale gaps at the TC4/UHMWPE interfaces are mainly caused by shrinkage of UHMWPE during cooling stage. Gaps tend to form at the interface with poor micro-scale interlocking.
(4) With proper heat input control, both macro- and micro-scale defects can be reduced.

References

1. Gasparin AL et al (2013) An experimental method for the determination of metal-polymer adhesion. Thin Solid Films 534:356–362
2. Rodrigues C et al (2014) FricRiveting of aluminum 2024-T351 and polycarbonate: temperature evolution, microstructure and mechanical performance. J Mater Process Technol 214:2029–2039
3. Chen YJ, Yue TM, Guo ZN (2018) Fatigue behaviour of titanium/PET joints formed by ultrasound-aided laser welding. J Manuf Process 31:356–363
4. Lambiase F, Genna S (2017) Laser-assisted direct joining of AISI304 stainless steel with polycarbonate sheets: thermal analysis, mechanical characterization, and bonds morphology. Opt Laser Technol 88:205–214
5. Katayama S, Kawahito Y (2008) Laser direct joining of metal and plastic. Scr Mater 59(12):1247–1250
6. Wagner G, Balle F, Eifler D (2013) Ultrasonic welding of aluminum alloys to fiber reinforced polymers. Adv Eng Mater 15(9):792–803
7. Balle F et al (2013) Influence of heat treatments on the mechanical properties of ultrasonic welded AA 2024/CF-PA66-joints. Adv Eng Mater 15(9):837–845
8. Balle F et al (2013) Improvement of ultrasonically welded aluminum/carbon fiber reinforced polymer-joints by surface technology and high resolution analysis. Adv Eng Mater 15(9):814–820
9. Chen K et al (2017) Friction spot welding between porous TC4 titanium alloy and ultra high molecular weight polyethylene. Mater Des 132:178–187
10. Okada T, Nakata K, Enomoto M (2016) Joining mechanism of dissimilar materials such as metal and plastic sheets by friction lap joining. Key Eng Mater 710:149–154
11. Amancio-Filho ST et al (2011) On the feasibility of friction spot joining in magnesium/fiber-reinforced polymer composite hybrid structures. Mater Sci Eng A Struct Mater Prop Microstruct Process 528(10–11):3841–3848
12. Esteves J et al (2012) Friction spot joining of aluminum 6181-T4 and carbon fiber reinforced poly (phenylene sulfide). Mater Des 66:437–445
13. Fourche G (1995) An overview of the basic aspects of polymer adhesion. Part I: Fundamentals. Polym Eng Sci 35(12):957–967
14. Lambiase F et al (2017) Improving energy efficiency in friction assisted joining of metals and polymers. J Mater Process Technol 250:379–389
15. Pierangiola Bracco AB, Bistolfi Alessandro, Affatato Saverio (2017) Ultra-high molecular weight polyethylene: influence of the chemical, physical and mechanical properties on the wear behavior. A review. Materials 10:791
16. Fu J et al (2010) Ultra high molecular weight polyethylene with improved plasticity and toughness by high temperature melting. Polymer 51(12):2721–2731
17. Van Krevelen DW, Te Nijenhuis K (2009) Rheological properties of polymer melts. Properties of polymers, 4th edn. Elsevier, Amsterdam, pp 525–597

Part IX
Poster Session

Connecting Residual Stresses with Friction Stir Welding Conditions and Pseudo-Heat Index

N. Zhu and L. N. Brewer

Abstract This study examines the connections between friction stir welding (FSW) parameters, the simple pseudo-heat index (PHI) metric, and the prediction of resultant residual stresses on AA5052-H32 plates. A range of weldments was produced with different tool rotational speeds (283–1732 RPM) and traverse speeds (200–800 mm/min) to produce the same values of PHI with distinctly different FSW conditions. Residual stresses were measured on the surfaces of the welded plates using x-ray diffraction. All of the friction stir welds produced the typical, M-shaped longitudinal residual stress profiles across the weld. The largest tensile stresses were produced for low PHI conditions, which did not fully consolidate the material. For sound welds, increasing traverse speed with fixed rotational speed did systematically increase the residual stresses inside the stir zone. However, the simple metric of PHI was not a good predictor of the stir zone residual stress.

Keywords Friction stir welding · Residual stress · Pseudo-heat index · Heat input
AA5052

Introduction

Residual stresses stemming from friction stir welding (FSW) can significantly affect material performance. Large tensile residual stresses can promote various failure modes in materials including plastic collapse, monotonic fracture, fatigue cracking, creep cavitation cracking, and stress corrosion cracking [1]. Thus, low magnitude and symmetrically distributed residual stresses in welded materials are preferred. FSW parameters are optimized to control the microstructure and mechanical properties of the joint. Some of the key welding parameters, e.g., the tool traverse speed and

---

N. Zhu · L. N. Brewer (✉)
Department of Metallurgical and Materials Engineering, The University of Alabama,
Box 870202, Tuscaloosa, AL 35487, USA
e-mail: lnbrewer1@eng.ua.edu

Y. Hovanski et al. (eds.), *Friction Stir Welding and Processing X*, The Minerals,
Metals & Materials Series, https://doi.org/10.1007/978-3-030-05752-7_26

the tool rotational speed, have been studied specifically with respect to residual stress generation. For example, longitudinal residual stresses in friction stir welded AA5083 increased with increasing traverse speed [2], and decreased with increasing rotational speed [3, 4]. In industry, large traverse speed and low rotational speed are preferred for enhanced productivity and less tool wear.

Although there is literature examining the effects of FSW parameters on the generation of residual stresses [2–4] and separately on the effects of FSW parameters on the energy or heat input during FSW [5, 6], there is limited literature directly connecting FSW parameters with heat input and residual stress generation. Calculation of heat input from FSW parameters can be quite complex [7]. There has been work on using simplified heat input metrics to estimate relative changes in heat input when changing FSW parameters. The pseudo-heat index (PHI), which uses only rotational speed and traverse speed is an example of a simple heat input metric that attempts to correlate relative changes in heat input to welding parameters during FSW,

$$PHI = \frac{\omega^2}{10{,}000 * \mathrm{V}}$$

where ω is the tool rotational speed, revolutions per minute (RPM); and V is the traverse speed, millimeters per minute (MMPM) [8].

There has been little work that examines the ability of simple heat input metrics, such as PHI, to predict changes in residual stress levels from changes in FSW parameters. Moreover, many of the residual stress studies on aluminum alloys have been performed on complex, precipitation strengthened aluminum alloys such as AA7075 [9, 10] and AA6061 [11]. Residual stress distribution across friction stir welds in these alloys can be complex due to the evolution of the precipitate structures in the stir zone (SZ), thermomechanically affected zone (TMAZ), and heat affected zone (HAZ). This proceeding's contribution uses AA5052 as a solid solution strengthened model alloy (Al-2.5 wt% Mg) to examine how well PHI can be used to predict the level of residual stress in the stir zone over a range of FSW conditions.

Experimental Procedures

Bead-on-plate friction stir welds were produced on the aluminum alloy AA5052-H32 with dimensions of 305 mm × 152 mm × 6.35 mm (12 in. × 6 in. × 0.25 in.). The nominal chemical composition of AA5052 is shown in Table 1 [12]. FSW of AA5052 was performed on the RM7 three-axis friction stir welder using a monolithic tool made of H13 tool steel, both from Bond Technologies. The monolithic tool had a 5.7 mm threaded pin and an 18-mm-diameter shoulder with a concave surface (Fig. 1). The penetration depth was 5.90 mm, and the tilt angle was 1.5° for all welds. Upon achieving steady-state welding conditions, a 220 mm long FSW path

Table 1 Nominal chemical composition of AA5052 in wt% [12]

Alloy	Si	Fe	Cu	Mn	Mg	Cr	Zn	Other (each)	Others (total)
AA5052	0.25 max	0.40 max	0.10 max	0.10 max	2.2–2.8	0.15–0.35	0.10 max	0.05 max	0.15 max

Fig. 1 D10314A monolithic friction stir tool made of H13 tool steel by Bond Technologies

was produced. The longitudinal residual stress measurements were taken at 50% along this 220 mm long FSW path. Residual stress values shown in this proceedings article refer to the average value of 7 measurements of longitudinal residual stresses inside the SZ with a 2 mm spatial resolution along the transverse direction.

A series of friction stir welds was produced to generate a range of welding conditions with the same PHI. The traverse speed range was set from 200 to 800 mm/min (MMPM) in steps of 200 MMPM. The rotation speed range was varied from 283 to 1549 RPM and was set to generate PHI values ranging from 0.02 to 0.7 in approximate increments of 0.1. The naming convention for these welds is given by the rotation speed, the traverse speed, and whether this condition was a replicate weld

Table 2 Parameters of x-ray diffraction-based residual stresses measurement

Exposure time (s)	5
No. of exposures	5
Psi angle range	±(0.5°, 4.5°, 5.5°, 9.5°, 10.5°, 15.5°, 20.5°, 25.5°, 30.5°, 35.5°, 40.5°)
Psi oscillation	4°
Aperture (mm)	2

or not, e.g., ω1265V400-2 represents the welding parameters of $\omega = 1265$ RPM and $V = 400$ MMPM, and the weld being the second replicate.

Residual stress distributions were measured using the iXRD Residual Stress Analyzer from Proto Manufacturing. X-rays were generated by a Co X-ray tube with wavelength of 1.79 Å at a tube power of 20 kV and 4 mA. Peak shifts in the {331} reflections were used to calculate the residual strain and stress. The X-ray elastic constants used were 18.889×10^{-6} for $\frac{1}{2}S_2$ and 4.687×10^{-6} for $-S_1$. Other parameters for the residual stresses measurements are shown in Table 2.

Experimental Results

Sound welds were achieved for traverse speeds of 400 and 600 MMPM over a range of rotational speeds. Wormhole defects found inside weldments with the lowest rotational speed of 283 RPM (Fig. 2). Excessive flash was observed on the surface of weldments with the highest rotational speed (1897 RPM) for 600 MMPM. PHI for all welds varied from 0.02 to 0.7 through different combinations of traverse speed, V, and rotational speed, ω. At PHI = 0.02, associated with the lowest rotational speed for traverse speeds of 400 MMPM and 600 MMPM, wormholes were found at the root of the weld close to the penetration depth and the weld centerline (Fig. 3b). As PHI increased to 0.10 and beyond, sound welds were achieved for both traverse speeds of 400 and 600 MMPM (Fig. 3a). At PHI = 0.15, sound welds were also achieved for a traverse speed of 800 MMPM. Excess flash and surface grooves were observed on weldments with a low traverse speed of 200 MMPM (Fig. 3c, d). Similar welds defects in aluminum alloys caused by improper combinations of rotational speed and traverse speeds have been previously reported [13].

All of the residual stress profiles measured had the common "M"-shaped profile with peaks in the tensile residual stresses just outside of the tool shoulder (Fig. 4). For fixed traverse speed, increasing rotational speed did not produce a large change in the magnitude of the tensile residual stresses. The increased rotational speed did

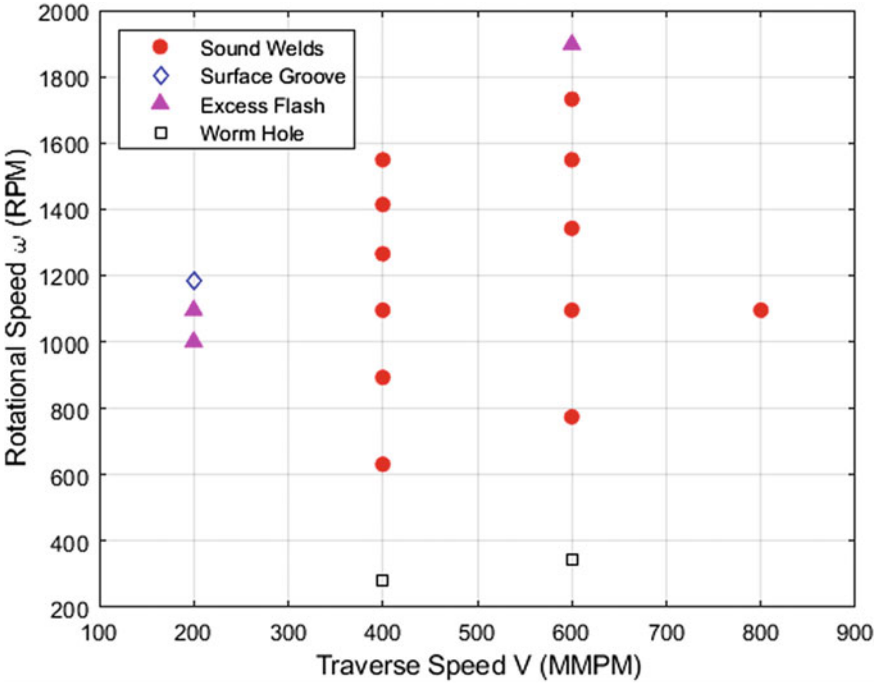

Fig. 2 Quality of welds as a function of combinations of rotational speed and traverse speed

increase the width of the tensile residual stress profile. This change in rotational speed for fixed traverse speed corresponds to an increase in the PHI value. In addition, the residual stresses outside the HAZ changed from slightly tensile to slightly compressive with increasing rotational speed. It should be noted that these x-ray diffraction measurements are from the top 100 μm of material. The depth distribution of residual stresses may well change with changing FSW conditions, but this information is not available from the surface x-ray diffraction measurements reported here.

Discussion

FSW conditions described by *the same PHI* produced similar residual stresses inside the SZ at PHI values between 0.1 and 0.3 (Fig. 5). That is to say, that in Fig. 5, the rotational speeds were selected so as to produce the same PHI values for different values of traverse speed, V. The differences in residual stresses for the same PHI values, but with different V, were quite small and almost within the error of the measurement. As PHI increased to 0.4, and particularly at 0.5, the difference in residual

(a) ω775V600, PHI=0.10, sound weld.

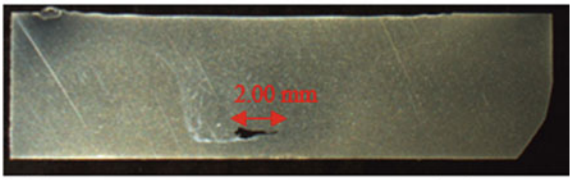

(b) ω346V600, PHI=0.02, worm hole.

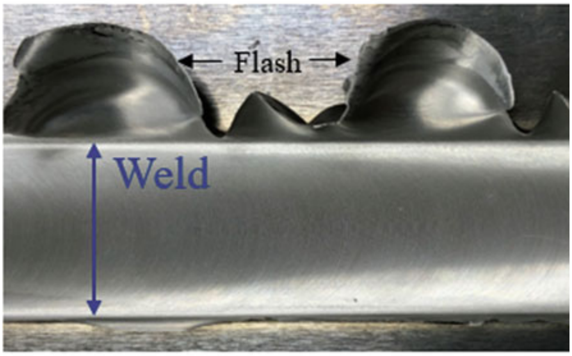

(c) ω1000V200, PHI=0.50, excess flash.

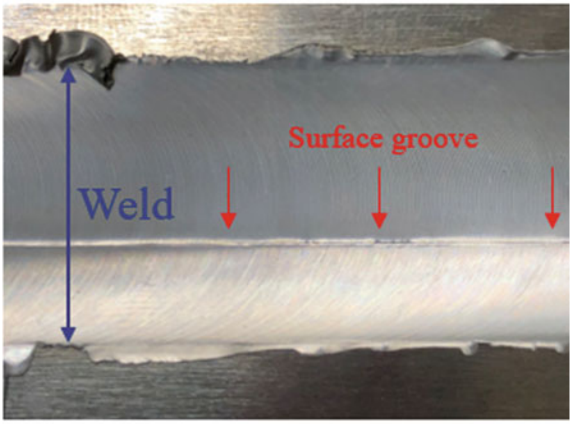

(d) ω1183V200, PHI=0.70, surface groove.

Fig. 3 Optical macrographs of AA5052 welds with different processing parameters. The cross-sectional plate thickness is 6.35 mm, and the width of welding path is 18 mm: **a** cross section of a sound weld; **b** cross section of a weld with wormhole defect; **c** plan view of excess flash on the weld surface on the retreating side; **d** plan view of surface groove on the weld surface on the advancing side inside the SZ

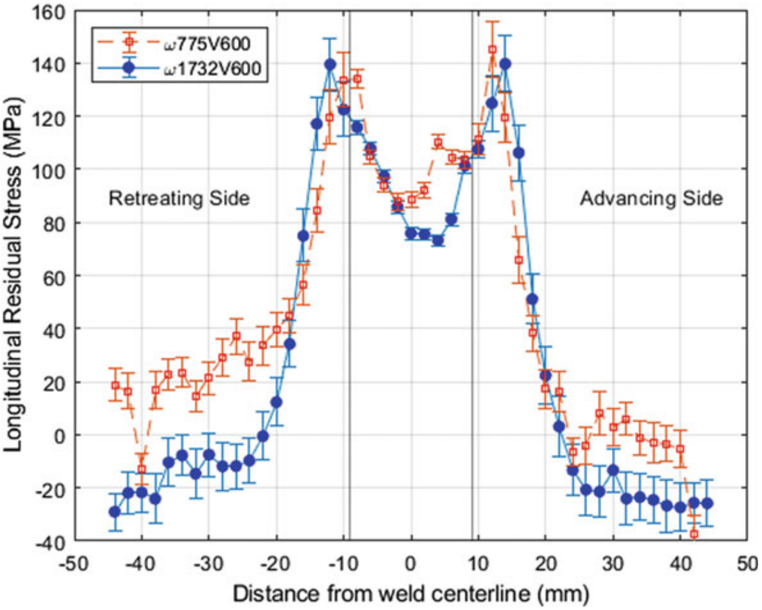

Fig. 4 Longitudinal residual stresses of weldment ω775V600 and ω1732V600

stresses for different traverse speeds (V) was much more noticeable. The residual stress produced with a traverse speed of 400 MMPM, and a resultant PHI of 0.5, was distinctly lower than the residual stresses measured for other FSW conditions. The quality of the x-ray diffraction data for this measurement was good. Both these FSW condition and the x-ray diffraction residual stress measurement were repeated. The residual stress inside the SZ for this replicate measurement was close to the previous result, around +60 MPa. At this point, there is no clear explanation for this 20–25 MPa drop in residual stress for this particular FSW condition. It should be noted that at PHI = 0.6, the residual stress level returned to a value of approximately +90 MPa. At the same PHI = 0.6, a traverse speed of 600 MMPM produced a weldment with excess flash, and its residual stress value is not shown in Fig. 5. The largest measured difference in residual stresses (blue circles versus red squares) was –13 MPa (10%) at PHI = 0.02. This lowest PHI condition generated both wormhole defects and the largest values of residual stress (+120 to 132 MPa).

The traverse speed did have a noticeable impact on the residual stress level. For weldments processed at the constant rotational speed of 1095 RPM, the residual stresses inside the SZ increased as the traverse speed increased from 200–800 MMPM (Fig. 6). This same correlation has been noted in the FSW literature [2]. In the current study, the magnitude of the residual stresses increased about 20%. Based upon their work on AA5083, Peel et al. suggested that the increase in residual stress could be a

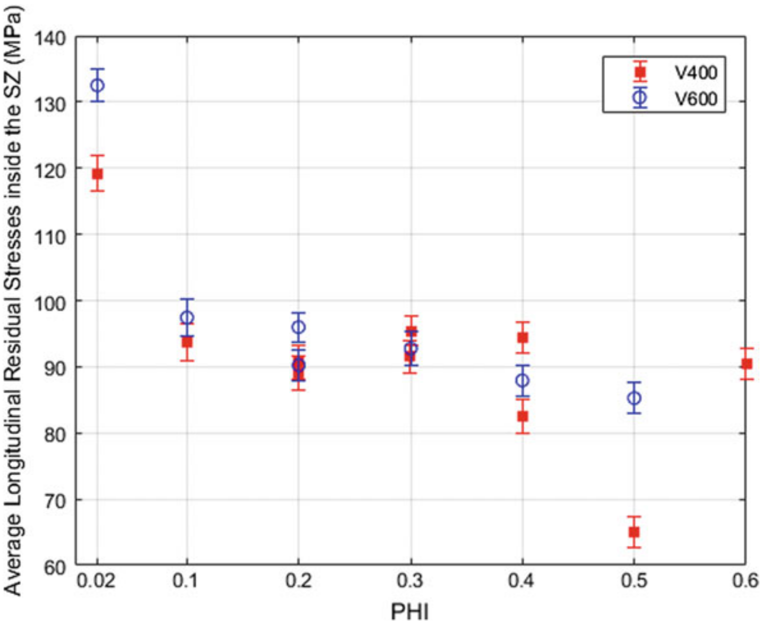

Fig. 5 Residual stresses inside the SZ as a function of PHI

result of the increased thermal gradients from increasing traverse speed [2]. Kumar suggests that high traverse speed does not allow sufficient time for relaxation of residual stresses inside weldments [4].

Conclusions

This study has investigated the connections between FSW parameters, a simple heat input metric, and the resultant residual stresses. The pseudo-heat index (PHI) was not a good predictor of residual stresses within the range of $0.1 < \text{PHI} < 0.5$; a range that produced sound welds. The largest tensile residual stresses were actually observed for defective welds with low values of PHI (0.02). Different ω-V combinations described by the same PHI produced similar residual stresses inside the SZ for sound welds. As has been noted in the literature, increasing the traverse speed, V, did systematically increase the residual stresses inside the SZ.

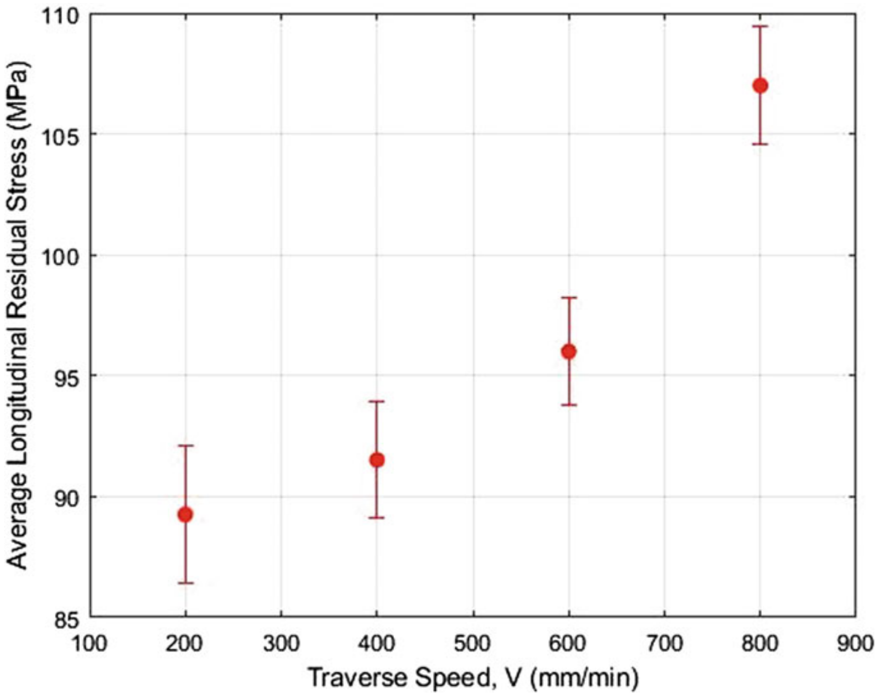

Fig. 6 Longitudinal residual stress inside the SZ for weldments with fixed rotational speed, ω, of 1095 RPM as a function of increasing traverse speed, V

References

1. Withers PJ (2007) Residual stress and its role in failure. Rep Prog Phys 70(12):2211–2264. https://doi.org/10.1088/0034-4885/70/12/r04
2. Peel M, Steuwer A, Preuss M, Withers PJ (2003) Microstructure, mechanical properties and residual stresses as a function of welding speed in aluminium AA5083 friction stir welds. Acta Mater 51(16):4791–4801. https://doi.org/10.1016/s1359-6454(03)00319-7
3. Lombard H, Hattingh DG, Steuwer A, James MN (2009) Effect of process parameters on the residual stresses in AA5083-H321 friction stir welds. Mater Sci Eng A Struct Mater Prop Microstruct Process 501(1–2):119–124. https://doi.org/10.1016/j.msea.2008.09.078
4. Kumar N, Baumann JA, Mishra RS (2013) Residual stresses in friction stir welding. Butterworth-Heinemann, Burlington
5. Peel MJ, Steuwer A, Withers PJ, Dickerson T, Shi Q, Shercliff H (2006) Dissimilar friction stir welds in AA5083-AA6082. Part I: process parameter effects on thermal history and weld properties. Metall Mater Trans A Phys Metall Mater Sci 37A(7):2183–2193. https://doi.org/10.1007/bf02586138
6. Rodrigues DM, Leitao C, Louro R, Gouveia H, Loureiro A (2010) High speed friction stir welding of aluminium alloys. Sci Technol Weld Join 15(8):676–681. https://doi.org/10.1179/136217110x12785889550181
7. Querin JA, Schneider JA (2012) Developing an alternative heat indexing equation for FSW. Weld J 91(3):76S–82S

8. Arbegast WJ, Baker KS, Hartley PJ (1998). Fracture toughness evaluations of 2195 Al-Cu-Li autogenous and hybrid friction stir welds. In: Proceedings of the 5th international conference on trends in welding research, pp 1–5
9. Mahoney MW, Rhodes CG, Flintoff JG, Spurling RA, Bingel WH (1998) Properties of friction-stir-welded 7075 T651 aluminum. Metall. Mater. Trans. A-Phys. Metall. Mater. Sci. 29(7):1955–1964. https://doi.org/10.1007/s11661-998-0021-5
10. Mishra RS, Ma ZY (2005) Friction stir welding and processing. Mater Sci Eng R Rep 50(1–2):1–78. https://doi.org/10.1016/j.mser.2005.07.001
11. Nandan R, DebRoy T, Bhadeshia H (2008) Recent advances in friction-stir welding—process, weldment structure and properties. Prog Mater Sci 53(6):980–1023. https://doi.org/10.1016/j.pmatsci.2008.05.001
12. ASM International Handbook C (2010) ASM handbook, Volume 02—properties and selection: nonferrous alloys and special-purpose materials. ASM International
13. Kim YG, Fujii H, Tsumura T, Komazaki T, Nakata K (2006) Three defect types in friction stir welding of aluminum die casting alloy. Mater Sci Eng A Struct Mater Prop Microstruct Process 415(1–2):250–254. https://doi.org/10.1016/j.msea.2005.09.072

Author Index

Y. Hovanski et al. (eds.), *Friction Stir Welding and Processing X*, The Minerals, Metals & Materials Series, https://doi.org/10.1007/978-3-030-05752-7

Subject Index

Y. Hovanski et al. (eds.), *Friction Stir Welding and Processing X*, The Minerals, Metals & Materials Series, https://doi.org/10.1007/978-3-030-05752-7